DONOSTIA INTERNATIONAL PHYSICS CENTER

D.I.P.C.

eman ta zabal zazu

Universidad del País Vasco

Euskal Herriko Unibertsitatea

First principles study of nanostructured surface reconstructions induced by the deposition of metals on vicinal Si(111) surfaces

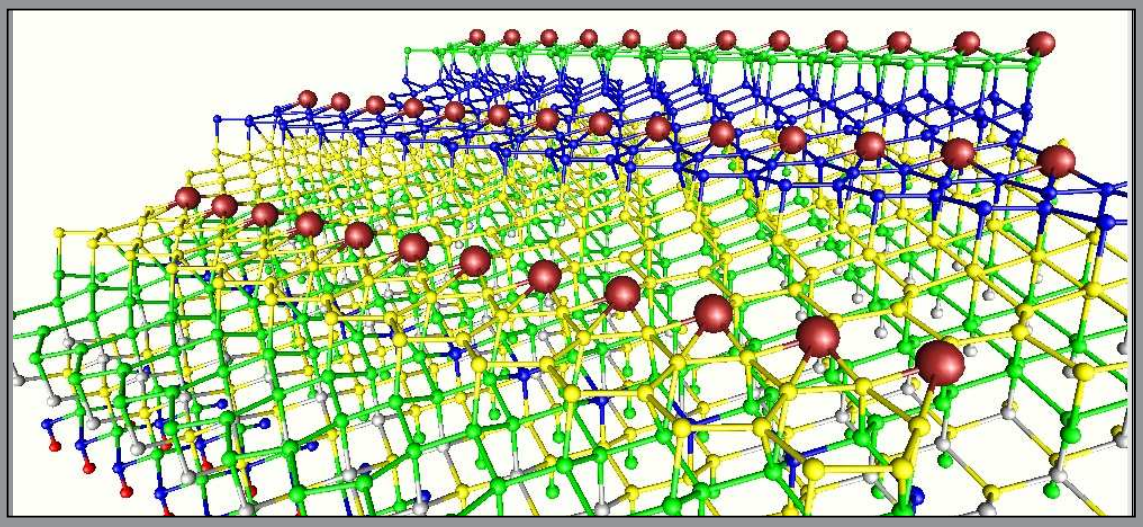

Doctoral Thesis submitted by

Sampsa Juhana Riikonen

for the degree of Doctor in Physics

June 2007

Cover picture: one of our models for the Si(553)/Au surface reconstruction

Resumen en castellano

Estudio teórico de las propiedades electrónicas y estructurales de reconstrucciones superficiales nanoestructuradas inducidas por la deposición de átomos metálicos sobre superficies de silicio

Tesis doctoral presentada por Sampsa Juhana Riikonen

Director de Tesis: Daniel Sánchez-Portal

Junio 2007

La presente tesis se centra en el estudio, utilizando cálculos de estructura electrónica dentro de la teoría del funcional de la densidad (DFT), de la estructura atómica y electrónica de varias reconstrucciones que se obtienen después de depositar diversos metales en Si(111) y superficies vecinales de Si(111). Muchas de estas estructuras forman reconstrucciones cuasi-unidimensionales donde los átomos de metal se agrupan formando cadenas monoatómicas o con secciones de unos pocos átomos. Por ello han sido propuestas como realizaciones experimentales de un metal unidimensional ideal, y se han buscado manifestaciones del comportamiento conocido como líquido de Tomonaga-Luttinger en sus espectros de fotoemisión, así como indicaciones de transiciones metal-aislante asociadas a distorsiones estructurales del tipo transición de Peierls. Casi todo nuestro estudio se ha centrado en las reconstrucciones inducidas por la deposición de oro Si(557)/Au, Si(553)/Au y Si(111)-(5x2)-Au. En nuestro trabajo hemos conseguido identificar los modelos estructurales energéticamente más estables y hemos estudiado sus propiedades electrónicas que, en general, están en buen acuerdo con lo observado en los experimentos de fotoemisión y de microscopía túnel. También hemos dedicado algún esfuerzo al sistema Si(111)/In. Para esta superficie hemos confirmado que el modelo para la transición 4x1$\rightarrow$ 4x2 $\rightarrow$ 8x2 basado en una deformación de cizalla seguido por una distorsión de Peierls, propuesto recientemente, es el más plausible y el que consigue un mejor acuerdo con la fenomenología experimental.

Las reconstrucciones inducidas por la deposición de diversas especies metálicas sobre superficies silicio han atraído la atención de muchos grupos de investigación en los últimos años. Metales como Au, Ag, Li, Na, Mg, K, Ca en recubrimientos inferiores a una monocapa, producen reconstrucciones en las que los átomos metálicos forman hilos monoatómicos separados por distancias del orden de 1 nm, de forma que la interacción entre ellas es, en principio, muy pequeña. En un modelo sencillo, olvidando por un momento los posibles efectos del substrato semiconductor, los electrones cerca del nivel de Fermi estarían confinados lateralmente en estas cadenas, siendo únicamente libres de moverse a lo largo de ellas. Los estados de superficie en estas reconstrucciones podrían por tanto constituir una realización experimental de un gas de electrones en una dimensión, uno de los modelos favoritos de la física cuántica durante décadas. En efecto, existe cierta evidencia experimental, basada en

fotoemisión y microscopia túnel, de la existencia de estados electrónicos de carácter fuertemente unidimensional en muchas de estas superficies. Desde un punto de vista teórico ha sido propuesto desde hace décadas que, debido a los efectos correlación, el comportamiento de los electrones en una dimensión (el llamado líquido de Luttinger) debe desviarse sensiblemente de la teoría del líquido de Fermi, válida normalmente en el volumen. Por ejemplo, a bajas temperaturas el sistema debe volverse aislante (i.e. se abre un "gap" para pequeñas excitaciones), las cuasipartículas son reemplazadas por excitaciones de espín y de carga (los denominados "spinons" y "holons"), y muchas de las propiedades del sistema debe ajustarse a ciertos comportamientos algebraicos. Sin embargo, la observación experimental de estos efectos ha demostrado ser muy complicada principalmente debido a la dificultad para encontrar sistemas "realmente" unidimensionales. En este contexto, las reconstrucciones de metales sobre silicio que hemos estudiado han sido propuestas como un sistema ideal para estudiar estos efectos, donde la magnitud de las interacciones laterales (i.e. distancia entre hilos) y de la interacción electrón-electrón (distintas especies metálicas adsorbidas y substratos) pueden variarse. El sistema Si(111)/Au es especialmente interesante en este sentido ya que existen datos de fotoemisión que parecen demostrar comportamientos inesperados, dentro de los modelos sencillos que se manejan, y que han sido interpretados utilizando las predicciones de la teoría de Tomonaga-Luttinger para una dimensión. Esta interpretación, sin embargo, ha sido discutida recientemente tanto teórica, como experimentalmente.

Hemos visto, por tanto, que en estos sistemas existen grandes expectativas de encontrar efectos exóticos relacionados con la correlación electrónica en una dimensión. Sin embargo, en muchos casos estas expectativas están basadas en interpretaciones muy simplificadas de las interacciones en estos sistemas. Por ejemplo, se desprecia el efecto de la interacción con los átomos del substrato en la estructura electrónica y geométrica del hilo. En muchos casos no se conoce la estructura atómica en detalle y no existen cálculos que refrenden la veracidad de los modelos estructurales, asociándoles una estructura de bandas que de forma aproximada puede ser comparada con los datos de fotoemisión.

En nuestro trabajo nos hemos centrado inicialmente en los sistemas Si(111)/Au que ha sido extensamente estudiados experimentalmente y para los cuales el debate está abierto, aunque hemos extendido nuestros cálculos a otros sistemas relacionados. Las fases seguidas en nuestra investigación han sido:

1. Estudiar distintos modelos estructurales de distintas reconstrucciones de Au sobre Si(111) y vicinales de Si(111) que exhiben hilos unidimensionales. Para ello hemos utilizado cálculos de primeros principios basados en la teoría del funcional de la densidad (DFT). En este primer periodo fue necesario familiarizarse con este aparato teórico y con las técnicas de simulación habitualmente utilizadas. Dado el gran número de átomos en estos cálculos, ha sido necesario utilizar un método eficiente, por lo que planeamos utilizar el código SIESTA, desarrollado por una colaboración de científicos españoles, entre los que se cuenta el director de la presente tesis (Dr. Daniel Sánchez Portal). Hemos obtenido resultados sobre los modelos estructurales de las siguientes superficies:

   (i) Si(111)-(5x2)-Au, esta reconstrucción ha sido estudiada durante décadas, y para ella existe un detallado modelo estructural basado en holografía con átomos pesados y microscopía electrónica de alta resolución. Sin embargo, pero existían muy pocos estudios basados en cálculos de primeros principios, y los que habían indicaban la posibilidad de una estructura diferente de la obtenida a partir del análisis de los datos experimen-

tales. Nosotros hemos encontrado con nuestros estudios que la estructura propuesta por los equipos experimentales no es en realidad la más estable. De hecho hemos propuesto el modelo estructural más estable de los conocidos hasta el momento. También hemos estudiado como cambia la estabilidad de las estructuras más estables en función de la concentración de ad-átomos de silicio sobre la superficie. Estos resultados han sido publicados en *First-principles study of the atomic and electronic structure of the Si(111)-(5x2)-Au surface reconstruction,* Sampsa Riikonen and Daniel Sánchez-Portal, Physical Review **B** 71, 235423 (2005)

(ii) En caso de la superficie escalonada Si(553)/Au hemos realizado una búsqueda exhaustiva de los modelos estructurales más estables y los hemos comparado con la información experimental existente. Este trabajo ha dado lugar a dos publicaciones: *Structural models for the Si(553)-Au atomic chain reconstruction,* Sampsa Riikonen and Daniel Sánchez-Portal, Nanotechnology **16** 218(2005); *Systematic investigation of the structure of the Si(553)-Au surface from first principles* Sampsa Riikonen and Daniel Sánchez-Portal, enviado a Physical Review B

(iii) Hemos comprobado que el modelo basado en una combinación de deformación de cizalla y distorsión tipo Peierls es el más apropiado para describir la transición de fase 4x1→4x2→8x2 observada en el sistema In/Si(111), confirmando los datos experimentales más recientes y en acuerdo con estudios teóricos realizados en la Univ. Autónoma de Madrid simultáneamente (e independientemente) a los nuestros. Estos resultados han sido publicados en *Metal-insulator transition in the In/Si(111) surface,* Sampsa Riikonen, Andres Ayuela Fernandez and Daniel Sánchez-Portal, Surface Science **600** 3821 (2006)

2. Los cálculos de estructura electrónica no sólo nos dan información sobre la estabilidad relativa de las distintas estructuras, si no que nos dan información sobre la estructura electrónica, esto significa que podemos obtener resultados sobre estructura de bandas, la densidad local de estados, la densidad electrónica, el tipo de enlace, etc.. Esto nos permite, entre otras cosas, el comparar los resultados teóricos con los experimentos de fotoemisión y de microscopía túnel de barrido. Esto nos ha permitido obtener los siguientes resultados:

   (i) Hemos identificado el origen de las dos bandas próximas que se observan cerca del nivel de Fermi en la superficie Si(557)/Au. Algunos autores habían propuesto que dichas bandas eran una prueba de la existencia de excitaciones separadas de espín y de carga como resultado del carácter unidimensional del sistema. Para otros autores no podían ser sino el resultado de la existencia de dos estructuras unidimensionales sobre la superficie: el borde del escalón y el hilo unidimensional de oro. En nuestro trabajo, publicado en: *Role of the spin-orbit splitting and the dynamical fluctuations in the Si(557) - Au surface,* Daniel Sánchez-Portal, Sampsa Riikonen and Richard M. Martin, Physical Review Letters **93** 146803 (2004), demostramos que en realidad las dos bandas se originan en la cadena de oro y que su aparición se debe a la rotura de degeneración entre distintos valores del espín asociada con la interacción espín-orbita inducida por la presencia de un elemento pesado como el oro.

   (ii) Tanto en el trabajo anterior, como en otro más reciente y detallado (S. Riikonen y D. Sánchez-portal, Interplay between the electronic and the atomic structure in the

Si(557)-Au reconstruction from first principles, aceptado para su publicación en Phys. Rev. B 2007), hemos estudiado en detalle el acoplamiento entre los grados de libertad electrónicos y estructurales. Hemos identificado a la distorsión del borde del escalón, que se estabiliza a bajas temperaturas como el origen de la transición metal-aislante y de los cambios de periodicidad en las imágenes de microscopía electrónica.

(iii) Hemos demostrado que el único modelo estructural existente para la superficie Si(553)-Au, obtenido a partir del análisis de los datos de difracción de rayos X, no sólo no es estable, sino que no produce imágenes STM ni bandas electrónicas en buen acuerdo con el experimento y por tanto debe ser revisado. Este resultado ha sido publicado en S. Riikonen, D. Sánchez-Portal, Ab initio study of the double row model of the Si(553)-Au reconstruction, Surf. Sci. 600 1201-1206 (2006)

3. Es sabido que la teoría del funcional de la densidad (DFT) en sus aproximaciones habituales, locales LDA o GGA, funciona bastante bien para predecir las geometrías de equilibrio de multitud de sistemas. El uso de las estructuras de bandas obtenidas como una aproximación a las excitaciones electrónicas elementales esta mucho menos justificado, aunque es una práctica habitual el comparar dichas bandas con los datos de fotoemisión. Nosotros hemos analizado en detalle las estructuras de bandas obtenidas en los cálculos, caracterizando los estados de superficie de acuerdo con su origen (asociados a los hilos metálicos o a otros átomos del substrato) y su dimensionalidad. Como un primer paso hacia una mejor descripción de la interacción electrón-electrón, hemos implementado el método LDA+U dentro del método de cálculo SIESTA. SIESTA es un programa que en la actualidad es utilizado por varios cientos de usuarios y que es distribuido libremente a la comunidad académica (ver http://www.uam.es/siesta). Por ello esperamos que nuestro trabajo tenga una amplia repercusión en la comunidad de ciencia de materiales, que usa este código como uno de sus estándares hoy en día. El esquema LDA+U es un método muy sencillo y, en principio, empírico de mejorar la descripción de las interacciones para estados electrónicos muy localizados. En particular, resuelve el problema de la autointeracción para estados con un fuerte carácter atómico. Este es uno de los principales problemas para describir estados muy localizados dentro de las aproximaciones locales de DFT. Hasta el momento hemos utilizado nuestro desarrollo para estudiar dos materiales cuyas propiedades electrónicas no son correctamente descritas por cálculos DFT a nivel LDA ni GGA: el FeO y el Sr2VO4. Se está preparando una publicación sobre este último material en colaboración con E. Canadell del Centro de Ciencia de Materiales del CSIC en Barcelona.

First principles study of nanostructured surface reconstructions induced by the deposition of metals on vicinal Si(111) surfaces

(2.nd, revised edition)

Sampsa Juhana Riikonen

Thesis supervisor:

Daniel Sánchez-Portal

author's e-mail: sampsa.riikonen@iki.fi

To Eva and Pulla

I owe my success to the fact that I never had a clock in my workroom.

-Thomas Alva Edison

Going slow does not prevent arriving.

-A nigerian proverb

Acknowledgements

First of all, this thesis being a professional matter, I would like to appreciate many of the people working at the Donostia International Physics Center (DIPC) and at the material physics department.

To begin with, I greatly appreciate my supervisor Daniel Sánchez-Portal who has been an excellent, one could say an ideal, instructor for a Ph. D. Thesis. He has always been available for responding my questions about physics and has devoted very generously his time for correcting the scientific articles in this thesis.

I would like to thank Prof. Pedro Echenique, for accepting me into his group and for creating such a good and stable atmosphere for the Ph. D. students and other scientists to work in San Sebastián and the secretaries of DIPC and the material physics department, in particular Ana López de Goicoechea, Francisco Vázquez Sánchez and Iñaki Juaristi for making everything to work so fluently.

Other important people for me in the DIPC have been Andres Ayuela, who I appreciate for useful discussions, both scientific and careerwise. The informatics staff, Txomin Romero and Belén Isla have always been available to fix immediately any kind of technical problem I might have had with the computers. I also appreciate Iñaki Silanes and Nora González for giving me some useful technical advices. I would like to thank Rene Gaudoin, Elton Jose Gomes Santos and Javier Aizpurua among others, for sharing with me so many excursions and so much *sidra* and Miguel Ruiz Osés and Javier Cordón for introducing me *torrente* and other essential things about the spanish way of life during my first two years in San Sebastián.

Outside the DIPC there are also many important people who have made these four years very pleasant time for me here in San Sebastián. It would be a formidable task to mention all of them here, so I only list a few names that come to my mind in this moment. The most important has been, since the past two years, my girlfriend Eva Larrarte. Of great support have also been my various roommates at *Avenida Navarra 30*, including Arturro Narros, Diana Ramos, Rajkumar Halder, Robert Keyling, just to name few, that have always been there for a friendly chat. Other people here or nearby include Eduardo Ogando, Remi Vincent, Julen Larrucea, the Salazar family, etc.

Going geographically further away from the DIPC, I must appreciate my friends and last but not the least my family in the far away Finland, for keeping on with their steady visits here and their continuos support.

Sampsa Riikonen
Donostia-San Sebastián, 5. June 2007

Contents

Chapter 1

Introduction

The main subject of this thesis are the surface reconstructions that form spontaneously when submonolayer amounts of metals are deposited on silicon. As we will see, on many occasions, the metal adsorbates stabilize reconstructions that have one-dimensional features. According to the latest geometrical models for these systems, the metals form (infinite) monatomic wires on the surface, an idea that seems to be in accordance with the experimental data. These reconstructions can also be formed on stepped silicon surfaces, allowing to tune the wire-wire interactions with the step width [1].

The fact that some metals form spontaneously one-dimensional structures on a semiconducting surface, is quite an extraordinary finding and there are still many open questions about the driving force for the formation of these structures and their properties.

As the miniturizion of electronic devices is approaching the atomic limit and the control of physical and chemical reactions on the nanometer-scale is very difficult, this kind of autoassembling becomes very desirable. Controlling and understanding it, is a strong motivation from a technological point of view. From a more fundamental point of view, the fact that these surfaces have one-dimensional features makes them attractive, because they might exhibit a completely a new kind of physical phenomena that could be exploited. One of these exciting phenomena is the so-called Tomonaga-Luttinger liquid, a novel phase of electrons where collective spin- and charge modes form the low-energy excitations of the system.

The *ab-initio* calculations are a powerful method to test different hypothesis about the origin of the physical phenomena observed in these surfaces. Although there exists numerous experimental studies about these surface reconstructions [2–64], the number of *ab-initio* calculations has remained quite small [1, 65–79]. One of the reasons for this is the large system size needed to properly simulate a surface reconstruction. In this thesis, we perform *ab-initio* calculations using the SIESTA method. It uses the localized-orbital formalism that is computationally less time-consuming than some other methods, allowing us to routinely simulate very large systems containing up to ~ 100 atoms. In this work we propose model geometries (i.e. the atomic coordinates) for many surface reconstructions, analyze their physical properties such as bond-forming, charge transfer, electronic band structure, etc. with first-principles calculations and then compare the results with the experimental data, mainly photoemission spectra and scanning-tunneling microscopy images. The systems studied in this thesis include metal-induced reconstruction on both flat and stepped silicon surfaces. Those on flat surfaces include the Si(111)/Au-5x2 [2–25, 67, 68] and Si(111)/In-4x1 [39–57, 72–79]. Systems with steps a few nanometers wide include the Si(557)/Au [26–38, 69–71] and Si(553)/Au

reconstructions [1, 58–64]. As we will see, we are able to reveal the origin of many physical phenomena seen on the experiments. These include the spin-orbit splitting of the one-dimensional bands in Si(557)/Au and Si(553)/Au, that was initially proposed by us and very recently backed-up by experimental data [62]. The metal-insulator transitions seen on many of these surfaces are also an interesting challenge for the *ab-initio* calculations that reflect how the atomic and electronic degrees of freedom couple to each other. We study this coupling for several systems and analyze the origin of some of these metal-insulator transitions.

A side subject of this thesis is the implementation of the LDA+U method into the SIESTA program package. We will discuss the origin of the failure of the Local Density Approximation (LDA) to deal with localized electrons (and their self-interaction), explain how this could be corrected and how this is implemented into SIESTA. We perform several tests with compounds such as FeO and Sr_2VO_4 [80–82]. In the case of Sr_2VO_4 we find that LDA+U breaks the symmetry of the vanadium d-orbitals and opens gaps in the electronic structure, correcting the metallic character of the LDA calculations.

List of publications

Part of the work described in this thesis has been published in the following publications:

- *Role of the spin-orbit splitting and the dynamical fluctuations in the Si(557) - Au surface,* Daniel Sánchez-Portal, Sampsa Riikonen and Richard M. Martin, Physical Review Letters **93** 146803 (2004)
- *Structural models for the Si(553)-Au atomic chain reconstruction,* Sampsa Riikonen and Daniel Sánchez-Portal, Nanotechnology **16** 218(2005)
- *First-principles study of the atomic and electronic structure of the Si(111)-(5x2)-Au surface reconstruction,* Sampsa Riikonen and Daniel Sánchez-Portal, Physical Review **B** 71, 235423 (2005)
- *Ab initio study of the double row model of the Si(553)-Au reconstruction* Sampsa Riikonen and Daniel Sánchez-Portal, Surface Science **600** 1201 (2006)
- *Metal-insulator transition in the In/Si(111) surface,* Sampsa Riikonen, Andres Ayuela Fernandez and Daniel Sánchez-Portal, Surface Science **600** 3821 (2006)
- *Interplay between electronic and atomic structures in the Si(557)-Au reconstruction from first principles,* Sampsa Riikonen and Daniel Sánchez-Portal, Physical Review B (in press)
- *Systematic investigation of the structure of the Si(553)-Au surface from first principles* Sampsa Riikonen and Daniel Sánchez-Portal, submitted to Physical Review B

Other publications written during the Ph. D. thesis:

- *Plasmon tunability in metallodielectric metamaterials,* Sampsa Riikonen, Isabel Romero and F. Javier Garcia de Abajo,
  Physical Review **B** 71, 235104 (2005)

Chapter 2

Methodology

In this chapter we discuss briefly about the Density Functional Theory (DFT) [83] and the SIESTA *ab-initio* program [84–86]. Some of the theory behind the SIESTA program is studied in detail.

The scope of this chapter is not to do a complete review on the SIESTA method, something already done elsewhere [84–86], but rather clarify some parts of the method that were relevant to this work. Formulas needed to implement new parts of the program, as well as various miscellaneous tools, are studied in detail. In addition to this, the pseudopotentials, basis sets and other "parameters" that were used throughout this work are presented.

2.1 Density Functional Theory

When solving for the ground state of the many-electron system, we have to minimize the total energy:

$$E = \langle \Psi | H | \Psi \rangle, \tag{2.1}$$

where $\Psi = \Psi(\mathbf{r}_1 s_1, \mathbf{r}_2 s_2, \mathbf{r}_3 s_3, ..., \mathbf{r}_N s_N)$ is the many-particle wavefunction of a system of N electrons. Since the electrons are fermions, the wavefunction has to be antisymmetric respect to the exchange of the coordinates for two particles. The simplest antisymmetric wavefunction can be constructed using the so-called Slater determinant:

$$\Psi = \begin{vmatrix} \psi_1(\mathbf{r}_1 s_1) & \psi_1(\mathbf{r}_2 s_2) & \dots \\ \psi_2(\mathbf{r}_1 s_1) & \psi_2(\mathbf{r}_2 s_2) & \dots \\ \vdots & \vdots & \ddots \end{vmatrix}. \tag{2.2}$$

Minimizing the energy using a wavefunction given by a single Slater determinant we obtain the so-called Hartree-Fock approximation that will be described in more detail in Chap. 8. Quantum chemistry methods rely on different approximations of the wavefunction which go beyond a single Slater determinant. The wavefunction is typically approximated by a collection of Slater determinants corresponding to the configurations with a stronger contribution to the ground state. These methods are referred to as multireference.

Density Functional Theory [87] provides a different approach to the problem. It states that the ground-state of the system is completely defined by its electron density and we may find

the ground-state density by minimizing the total energy:

$$\frac{\delta E[\rho]}{\delta \rho(\mathbf{r})} - \mu = 0, \tag{2.3}$$

where μ is a Lagrance multiplier that maintains a fixed number of electrons N. We must now express the total energy as functional of the electronic density:

$$E[\rho] = T[\rho] + E_{ee}[\rho] + E_{ext}[\rho], \tag{2.4}$$

where $T[\rho]$, $E_{ee}[\rho]$ and $E_{ext}[\rho]$ are the kinetic, electron-electron interaction and external potential, respectively. This can be further written as

$$E[\rho] = T_s[\rho] + (E_{xc}[\rho] + E_H[\rho] + E_{ext}[\rho]) \tag{2.5}$$

where $E_{xc}[\rho] = \Big((T[\rho] - T_s[\rho]) + (E_{ee} - E_H)\Big)$ is called the exchange and correlation energy. $T_s[\rho]$ is the kinetic-energy term of a non-interacting electron system, that has exactly the same electron density as the interacting electron system.

In going from Eq. (2.4) to Eq. (2.5), we have added and subtracted $T_s[\rho]$ from the right-hand side and the Hartree term

$$E_H = \frac{1}{2}\int \frac{\rho(\mathbf{r})\rho(\mathbf{r}')}{|\mathbf{r} - \mathbf{r}|} d^3\mathbf{r} d^3\mathbf{r}', \tag{2.6}$$

has been extracted from the total electron-electron interaction

$$E_{ee} = \langle \Psi | \sum_{i \neq j}^{N} \frac{e^2}{|\mathbf{r}_i - \mathbf{r}_j|} | \Psi \rangle. \tag{2.7}$$

We see that the original system of interacting electrons is substituted by a system of non-interacting quasi-particles. The energy Eq. (2.4) of this system has been divided in different parts, in such a way that all terms that could not be expressed exactly using the electron density (such as $\mathrm{E}_{ee}[\rho]$) are retained in $\mathrm{E}_{xc}[\rho]$. This problematic term is usually approximated in some way. The most widely used approximation is the Local Density Approximation (LDA), where $\mathrm{E}_{xc}[\rho]$ is taken from the calculations of the energy of the homogeneous electron gas using Many-Body Quantum Monte Carlo calculations. This results in a local functional $\mathrm{E}_{xc}[\rho]$ with respect to $\rho(\mathbf{r})$.

When applying Eq. (2.3) to Eq. (2.5), we come up with the Schrödinger equation:

$$\hat{T}\psi - (V_{xc} + V_H + V_{ext})\psi = \epsilon\psi, \tag{2.8}$$

where $\hat{T}$ is the kinetic energy operator. The potential terms have been obtained in the following way:

$$V_{xc} = \frac{\delta E_{xc}}{\delta \rho(\mathbf{r})}, \tag{2.9}$$

and similar for other potential terms. Notice that the V_{xc} potential is a "local" potential in contrast with the equations obtained in the Hartree-Fock method (see Chap. 8). This is *the* advantage allowed by DFT as discussed above. In order to solve the electronic ground-state, we solve Eq. (2.8), obtain the eigenstates ψ_n, then recalculate the electronic density and

potential terms and solve Eq. (2.8) again. This is called the self-consistency (SCF) cycle. Finding the ground-state of the system by SCF iteration is called the Kohn-Sham (KS) scheme [88].

In order to calculate the electron-density or the expectation values of other single-particle operators, we first write the wavefunction Ψ as a Slater determinant, using the eigenstates ψ_n and Eq. (2.2). Expectation value for a single-particle operator $\hat{f}$ of the form

$$\hat{f} = \sum_i \hat{f}(\mathbf{r}_i) \tag{2.10}$$

where the operator $\hat{f}(\mathbf{r}_i)$ is acting on coordinate i only, turns out to be:

$$\langle\Psi|\hat{f}|\Psi\rangle = \sum_\alpha \langle\psi_\alpha|\hat{f}|\psi_\alpha\rangle. \tag{2.11}$$

A widely used technique, to make the convergence of the self-consistency cycle faster especially in the case of metals, is to smooth the occupation between filled and empty states and write Eq. (2.11) as:

$$\langle\Psi|\hat{f}|\Psi\rangle = \sum_k \langle\psi_\alpha|\hat{f}|\psi_\alpha\rangle w_\alpha, \tag{2.12}$$

where w_α is the occupation number for the state $\psi_\alpha(\mathbf{r})$, given by the Fermi-Dirac distribution. If the operator $\hat{f}_i$ is simply

$$\hat{f}_i = f(\mathbf{r}_i), \tag{2.13}$$

i.e. a real valued function of $\mathbf{r}_i$, then

$$\langle\Psi|\hat{f}|\Psi\rangle = \int \rho(\mathbf{r}) f(\mathbf{r}) d^3\mathbf{r}, \tag{2.14}$$

where the electron density is calculated from

$$\rho(\mathbf{r}) = \sum_{\alpha=1}^{N} |\psi_\alpha(\mathbf{r})|^2 w_\alpha. \tag{2.15}$$

It is important to keep in mind that the eigenstates ψ_i and the eigenvalues ϵ_i of the non-interacting reference system are just auxiliary quantities. From now on, they are referred to as Kohn-Sham states (KS states). The only quantity that was assumed equivalent in both the actual system and the non-interacting reference system, is the electron density of Eq. (2.15). True physical quantities derived from this Kohn-Sham scheme and the DFT are thus the electron density and the total energy and also the derivatives of the total energy (i.e. the forces, response functions, etc.). Note here that we define the electron density as a positive quantity. This applies to other chapters as well.

2.2 Localized orbitals

2.2.1 Non-orthogonal basis sets

Most the calculations in this work were done using the SIESTA program package [84–86, 89]. In SIESTA, the wavefunctions are presented in a local orbital basis. In this section we study some details of the local orbital formalism.

We consider a set of non-orthogonal basis functions $\{|\phi_\mu\rangle\}$ and following the notation of Ref. [90], we define the dual of this basis as

$$|\phi^\nu\rangle = \sum_i S^{-1}_{\nu i}|\phi_i\rangle, \tag{2.16}$$

where $S^{-1}_{\nu i}$ is the inverse of the overlap matrix

$$S_{\nu i} = \langle\phi_\nu|\phi_i\rangle. \tag{2.17}$$

Then it is easy to show that

$$\langle\phi^\nu|\phi_\mu\rangle = \langle\phi_\nu|\phi^\mu\rangle = \delta_{\nu\mu}. \tag{2.18}$$

The dual $\langle\phi^\nu|$ is thus a projection operator, created as a linear combination of the basis functions. This linear combination is such that when the projector $\langle\phi^\mu|$ is applied to a function spanned by the space $\{|\phi_\mu\rangle\}$, only the coefficient corresponding to $|\phi_\mu\rangle$ is retained.

The systems we wish to solve, consist of a *unit cell* that is repeated periodically. In SIESTA it is also usefull to define a *supercell*, constructed by a few replicas of the unit cell. The supercell needs to be sufficiently large in order to catch all the interactions of the unit cell with its neighbouring cells. It must then contain all the periodical images of the unit cell that have orbitals overlapping with the orbitals of the unit cell. In the following, we refer with n and N to the total number of atomic orbitals in the unit and supercell, respectively.

Using localized orbitals we typically find various sums over different indices, each indice denoting the orbital, atomic site and cell. Occasionally, we would like to distinguish between different cells or atoms in the sums. For this reason we define a simplified notation to make the formalism more clear. We start by defining the basis set:

$$|\phi_{(un\mu)}\rangle = |\phi_{n\mu}(\mathbf{r} - (\mathbf{R_n} + \mathbf{R_u}))\rangle. \tag{2.19}$$

In Eq. (2.19) the $\phi_{n\mu}$ in the right-hand side refers to a set of orbitals, with a atom-index n (including the atom type), and with an orbital index μ. The indices of the basis set (left-hand side of Eq. (2.19)) are written in parenthesis in order to distinguish them from a set of orbitals. In Eq. (2.19), n refers also to the atomic site in the unit cell and each cell (i.e. repetition of the unit cell) is referred to with an index u. $\mathbf{R_n}$ is the vector to the atom n within the unit cell and $\mathbf{R_u}$ is a vector of the Bravais lattice. With the abbreviation

$$|\phi_{(..\mu)}\rangle, \tag{2.20}$$

we mean that the index μ refers to the "global" index of the orbitals in the supercell and runs from 1 to N. The idea of the notation is that we have grouped the indexes marked by "." into the index μ and the parenthesis indicate what has been grouped. For example, we can group indices n and μ within each cell u:

$$|\phi_{u(.\mu)}\rangle. \tag{2.21}$$

Now u refers to the cell number and μ is the index of all orbitals in a single cell. A more exotic example would be

$$|\phi_{(u.)\mu}\rangle, \tag{2.22}$$

where atomic site and cell index have been grouped into a single index u.

2.2.2 Bloch states

Now we wish to add the possibility to represent Bloch-states in our localized basis. Bloch-states allow us to calculate solutions for an infinite system, using only a finite one. A bloch-state $\psi^{\mathbf{k}}(\mathbf{r})$ with a k-vector $\mathbf{k}$ should satisfy the condition [91]:

$$\psi^{\mathbf{k}}(\mathbf{r}+\mathbf{R_v}) = \psi^{\mathbf{k}}(\mathbf{r})e^{i\mathbf{k}\cdot\mathbf{R_v}}, \tag{2.23}$$

where i is the imaginary unit $\sqrt{-1}$ and $\mathbf{R_v}$ a vector of the Bravais lattice.

In order to present bloch-states with our basis set, we add a phase factor into the basis functions of Eq. (2.19)

$$|\phi^{\mathbf{k}}_{(un\mu)}\rangle = |\phi_{n\mu}(\mathbf{r}-(\mathbf{R_n}+\mathbf{R_u}))\rangle e^{i\mathbf{k}\cdot\mathbf{R_u}} \tag{2.24}$$

and consider an eigenstate represented by this basis with index α and with k-vector $\mathbf{k}$:

$$\psi^{\mathbf{k}}_{\alpha}(\mathbf{r}) = \sum_{un\mu} a^{n\mu}_{\alpha\mathbf{k}}|\phi_{n\mu}(\mathbf{r}-(\mathbf{R_n}+\mathbf{R_u}))\rangle e^{i\mathbf{k}\cdot\mathbf{R_u}}. \tag{2.25}$$

It is easy to see that the wavefunction of Eq. (2.25) satisfies the Bloch condition:

$$\psi^{\mathbf{k}}_{\alpha}(\mathbf{r}+\mathbf{R_v}) = \sum_{un\mu} a^{n\mu}_{\alpha\mathbf{k}}|\phi_{n\mu}(\mathbf{R}-(\mathbf{R_n}+(\mathbf{R_u}-\mathbf{R_v})))\rangle e^{i\mathbf{k}\cdot\mathbf{R_u}}. \tag{2.26}$$

Now we substitute $R_u := R_u - R_v$, so

$$\sum_{un\mu} a^{n\mu}_{\alpha\mathbf{k}}|\phi_{n\mu}(\mathbf{R}-(\mathbf{R_n}+\mathbf{R_u}))\rangle e^{i\mathbf{k}\cdot(\mathbf{R_u}+\mathbf{R_v})} = \psi^{\mathbf{k}}_{\alpha}(\mathbf{r})e^{i\mathbf{k}\cdot\mathbf{R_v}}. \tag{2.27}$$

2.2.3 K-point sampling

When solving the Schrödinger equation 2.8 using basis functions 2.19, we use a finite unit cell, imposing the periodicity of this unit cell and obtaining this way the modes (eigenstates). This is the so-called Born-von Karman boundary condition. However, if we wish to solve a system where the unit cell is repeated to infinity, the correct boundary conditions are the zero boundary-conditions at the borders of the *infinite* cell. Each $\mathbf{k}$-vector and each bloch-state $\psi^{\mathbf{k}}(\mathbf{r})$ can be interpreted as a distinct mode of the infinite cell. Expectation value of any physical quantity should then be averaged over various solutions, each solution corresponding to a different $\mathbf{k}$-vector.

The values for the $\mathbf{k}$-vectors are chosen from the irreducible Brillouin-zone [91] with some reasonable scheme. Throughout this work, we use the Monkhorst-Pack (MP) notation [92], where M×N×L means a sampling of M, N and L equidistant points in the Brillouin-zone to the direction of the first, second and third reciprocal vectors, correspondingly.

2.2.4 Solving the Schrödinger equation

In this subsection we show how the Eq. (2.8) can be solved using the non-orthogonal basis functions of Eq. (2.24). We expand the wavefunction with the basis functions of Eq. (2.24) in the supercell and use the Schrödinger Eq. (2.8):

$$H|\psi^{\mathbf{k}}_{\alpha}\rangle = \varepsilon_{\alpha}|\psi^{\mathbf{k}}_{\alpha}\rangle, \tag{2.28}$$

where H is the Hamiltonian and α and k the eigenvalue and k-indexes, we create the matrix equations by multiplying with the ket $\langle\phi^{\mathbf{k}}_{1(.\nu)}|$:

$$\langle\phi^{\mathbf{k}}_{1(.\nu)}|H|\psi^{\mathbf{k}}_{\alpha}\rangle = \varepsilon_{\alpha}\langle\phi^{\mathbf{k}}_{1(.\nu)}|\psi^{\mathbf{k}}_{\alpha}\rangle. \tag{2.29}$$

Since the functions $\langle\phi^{\mathbf{k}}_{1(.\nu)}|$ are in the unit cell, the index k can be dropped. Writing Eq. (2.29) out gives:

$$\begin{aligned}\sum_{u\mu}\langle\phi_{1(.\nu)}|H|\phi_{u(.\mu)}\rangle e^{i\mathbf{k}\cdot\mathbf{R_u}}a^{\mu}_{\alpha\mathbf{k}} &= \epsilon_{\alpha}\sum_{u'\mu'}\langle\phi_{1(.\nu)}|\phi_{u'(.\mu')}\rangle e^{i\mathbf{k}\cdot\mathbf{R_{u'}}}\\ \Leftrightarrow \sum_{\mu}\Big(\sum_{u}H_{1(.\nu),u(.\mu)}(\mathbf{k})\Big)a^{\mu}_{\alpha\mathbf{k}} &= \sum_{\mu'}\epsilon_{\alpha}\Big(\sum_{u'}S_{(1(.\nu),u'(.\mu')}(\mathbf{k})\Big)a^{\mu'}_{\alpha\mathbf{k}}\\ \Leftrightarrow \mathbf{H}(\mathbf{k})\mathbf{a}_{\alpha\mathbf{k}} &= \epsilon_{\alpha}\mathbf{S}(\mathbf{k})\mathbf{a}_{\alpha\mathbf{k}},\end{aligned} \tag{2.30}$$

where we have defined:

$$H_{1(.\nu),u(.\mu)}(\mathbf{k}) = \langle\phi_{1(.\nu)}|H|\phi_{u(.\mu)}\rangle e^{i\mathbf{k}\cdot\mathbf{R_u}} \tag{2.31}$$

$$S_{1(.\nu),u'(.\mu')}(\mathbf{k}) = \langle\phi_{1(.\nu)}|\phi_{u'(.\mu')}\rangle e^{i\mathbf{k}\cdot\mathbf{R_{u'}}} \tag{2.32}$$

where $\mathbf{H}(\mathbf{k})$ and $\mathbf{S}(\mathbf{k})$ are matrices that depend on the k-index:

$$\Big[\mathbf{H}(\mathbf{k})\Big]_{\nu,\mu} = \sum_{u}H_{1(.\nu),u(.\mu)}(\mathbf{k}), \tag{2.33}$$

$$\Big[\mathbf{S}(\mathbf{k})\Big]_{\nu,\mu} = \sum_{u'}S_{1(.\nu),u'(.\mu)}(\mathbf{k}). \tag{2.34}$$

and $\mathbf{a}_{\alpha\mathbf{k}}$ is a vector:

$$\mathbf{a}_{\alpha\mathbf{k}} = (a^1_{\alpha\mathbf{k}}, a^2_{\alpha\mathbf{k}}, a^3_{\alpha\mathbf{k}}, ..., a^n_{\alpha\mathbf{k}}), \tag{2.35}$$

where n is the total number of orbitals in the unit cell.

We observe that the hamiltonian and overlap matrices of Eq. (2.31) and Eq. (2.32) have the dimensions n×N. The n×n matrices of Eq. (2.33) and Eq. (2.34) are created by summing up the n×n elements of the corresponding n×N matrices (Eqs. (2.31)-(2.32)) multiplied by a phase-factor that depends on the Bloch-index k. In SIESTA, each subroutine (say, local potentials, non-local potentials, etc.) adds its contribution to the Hamiltonian matrix of Eq. (2.31). After this, the matrices of Eqs. (2.33)-(2.34) are created and the eigenvalue problem of Eq. (2.30) is solved.

In SIESTA, the Hamiltonian matrix has some parts which - unfortunately - must be calculated in a real-space grid. The electron density $\rho(\mathbf{r})$ is projected into a real-space grid for various reasons: these are for example the exchange-correlation energy functional $E_{xc}[\rho(\mathbf{r})]$ that is a local, non-linear functional of the electron density and the usage of Fourier transforms in order to solve the poisson equation to get the Hartree potential. Three center integrals are also calculated using the real-space grid. All this creates the need for an extra parameter in the calculations, the cutoff energy E_c. It is defined as the energy of a plane-wave $\sim e^{k\cdot x}$ with the highest k that can be represented with the grid:

$$E = \frac{1}{2}\hbar k^2 = \frac{1}{2}\hbar\Big(\frac{\pi}{L}\Big)^2, \tag{2.36}$$

where L is the distance between neighboring grid points.

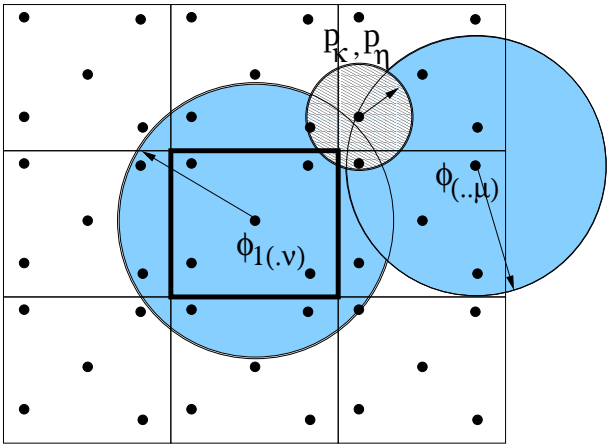

Figure 2.1: Calculation of Hamiltonian matrix elements and expectation values for localized projectors in a supercell scheme using localized orbitals. The orbital $\phi_{(.\nu)}$ is inside the unit cell (indicated by a thick box), while the orbital $\phi_{(..\mu)}$ can be anywhere in the supercell, this is also true for the projectors p_η and p_κ. The cutoff radii of orbitals and projectors are indicated by arrows.

2.2.5 The density matrix

The density matrix is a very useful concept; it encloses compactly all the information about the system and can be used to calculate the expectation values of operators. We can find the density matrix by considering the electronic density of the system:

$$\begin{aligned}\rho(\mathbf{r}) = \sum_{\mathbf{k}\alpha} \psi_\alpha^{\mathbf{k}*}(\mathbf{r})\psi_\alpha^{\mathbf{k}}(\mathbf{r}) &= \sum_{v u \nu \mu} \phi(\mathbf{r})^*_{v(.\nu)}\phi(\mathbf{r})_{u(.\mu)} \sum_{\mathbf{k}} (a^{\nu *}_{\alpha\mathbf{k}} a^{\mu}_{\alpha\mathbf{k}} e^{i\mathbf{k}\cdot(\mathbf{R}_u - \mathbf{R}_v)}) \\ &= \sum_{v u \nu \mu} \phi(\mathbf{r})^*_{v(.\nu)}\phi(\mathbf{r})_{u(.\mu)} D_{v(.\nu),u(.\mu)} \\ &= \sum_{v \nu \mu} \phi(\mathbf{r})^*_{v(.\nu)}\phi(\mathbf{r})_{(..\mu)} D_{v(.\nu),(..\mu)}, \end{aligned} \tag{2.37}$$

where we can easily see the definition of the density matrix $D_{v(.\nu),(..\mu)}$. Here the index $(..\mu)$ goes over all orbitals in the supercell. In order to express the electron density $\rho(\mathbf{r})$ inside the unit cell correctly the indexes v, ν do not have to run over the whole supercell, but over a small "buffer-zone" instead, that includes all overlapping orbitals at point $\mathbf{r}$. For many purposes (see below), it is sufficient that indexes v, ν retain in the unit cell. Then we can write the density matrix as $D_{1(.\nu),(..\mu)}$, having dimensions n×N.

2.2.6 Non-local projection terms in the Hamiltonian

As mentioned earlier, the matrix elements in Eq. (2.31) are created separately for each kind of potential term. Here we take a look how this is done in the case of non-local projectors. These are important in the case of pseudopotentials and the LDA+U method of Chap. 8 We consider projectors of the type:

$$P = \sum_{u,\eta,\kappa} |p_{(u.)\eta}\rangle V_{\eta\kappa} \langle p_{(u.)\kappa}|. \tag{2.38}$$

The projectors are similar to the basis functions of Eq. (2.19). Note that in Eq. (2.38) we have grouped both the atomic site and the cell index into the index u. Remembering Eq. (2.11) and

using the density matrix of Eq. (2.37) we write:

$$\begin{aligned}\bar{P} &= \sum_{\mathbf{k}} \langle \Psi^{\mathbf{k}} | P | \Psi^{\mathbf{k}} \rangle \\ &= \sum_{\alpha,\mathbf{k},u,\eta,\kappa} \langle \psi^{\mathbf{k}}_{\alpha} | p_{(u.)\eta} \rangle V_{\eta\kappa} \langle p_{(u.)\kappa} | \psi^{\mathbf{k}}_{\alpha} \rangle \\ &= \sum_{\nu,\mu,u,\eta,\kappa} D_{1(.\nu),(..\mu)} \langle \phi_{1(.\nu)} | p_{(u.)\eta} \rangle V_{\eta\kappa} \langle p_{(u.)\kappa} | \phi_{(..\mu)} \rangle . \end{aligned} \tag{2.39}$$

This sum is illustrated in Fig. 2.1.

The forces on atoms due to such projectors are the derivatives of the energy term Eq. (2.39) with respect to atom locations. They are calculated most easily by considering forces on each atom-projector pair and then summing over all pairs. One can then make the derivative of $\langle \phi_{1(.\nu)} | p_{(u.)\eta} \rangle$ with respect to the orbital-projector distance $\mathbf{R}_{\nu} - \mathbf{R}_{\mathbf{u}}$ and the force acting on each one of their corresponding atoms is:

$$\begin{aligned}\mathbf{F} = -\nabla \bar{P} &= -\sum_{\mu,\eta,\kappa} 2 D_{1(\nu.),(..\mu)} \nabla \Big(\langle \phi_{1(\nu.)} | p_{(u.)\eta} \rangle \Big) V_{\eta\kappa} \langle p_{(u.)\kappa} | \phi_{(..\mu)} \rangle \\ &= \sum_{\mu,\eta,\kappa} 2 D_{1(\nu.),(..\mu)} \Big(\langle \phi_{1(\nu.)} | \nabla | p_{(u.)\eta} \rangle \Big) V_{\eta\kappa} \langle p_{(u.)\kappa} | \phi_{(..\mu)} \rangle \end{aligned} \tag{2.40}$$

2.3 Pseudopotentials and Pseudo-orbitals

The pseudopotentials used by SIESTA are norm-conserving ab-initio pseudopotentials. We typically use those developed by Troullier and Martins (TM) [93] and apply them to the wavefunctions using the fully non-local formulation due to Kleynman and Bylander [94]. Using ab-initio pseudopotentials the wavefunction is projected into s-,p-,d- etc. orbitals and different potential terms are applied to each of these components. In Eq. (2.38) this corresponds to diagonal $V_{\eta\kappa}$ non-local potential terms. Rather than going into the details of the TM pseudopotentials, we simply present here the parameters used to generate the pseudopotentials used throughout this work. For more details, one can see Ref. [93, 94].

To generate the pseudopotentials, we used the ATOM program that comes with the standard SIESTA package. In addition to generate the pseudopotentials, ATOM program provides us with the pseudo-orbitals, which are the wavefunctions of an isolated atom, if the one-atom problem is solved using the pseudopotential. SIESTA uses these pseudo-orbitals as a natural basis when solving the Schrödinger equation. More complex basis sets can be generated using SIESTA. Individual orbitals can be "splitted" several times to obtain more variational freedom and excited-state orbitals can be generated. For more details, one can consult Refs. [84–86,89].

The pseudopotentials used in this work are listed in Tab. 2.1 and it has all the information needed to create these pseudopotentials with the ATOM program. As an example, the pseudopotentials and the wavefunctions for indium are illustrated in Fig. 2.2. Note that outside the matching radii, the wavefunctions are equal to the pseudo wavefunctions (which are used by SIESTA) and that the latter ones do not contain any nodes. By tuning the matching radii, we have been able to make the pseudopotentials if Fig. 2.2b relatively smooth, compared to the all-electron effective potential (not shown), and keep them in a reasonable energy range.

The bases used for all the elements in the course of this work are indicated in Tab. 2.2. In this table we have also calculated the bulk lattice constant in some cases. An example band structure from a bulk calculation of Au is illustrated in Fig. 2.3.

Element	E_{xc}	file	valence	matching radii
H (1)	LDA	H.psf	1s	1.25
H (1)	GGA	H2.psf	1s	1.25
O (8)	GGA	O_opt.psf	$2s^2 2p^4 3d^0$	1.14,1.14,1.14 (1.38)
Si (14)	LDA	Si.psf	$3s^2 3p^2$	1.89,1.89
Si (14)	GGA	Si2.psf	$3s^2 3p^2$	1.89,1.89, (3.00)
Fe (26)	GGA	Fe.vps	$3s^2 3p^6 3d^6 (4s^2)$	1.20,1.20,1.78, (1.37)
In (49)	GGA	In2.vps	$4d^{10} 5s^2 5p$	1.79,2.48,2.99,(3.56)
In (49)	GGA	In3.vps	$5s^2 5p$	2.48,2.99,(5.59)
Au (79)	LDA	Au.vps	$5d^{10} 6s$	2.00,2.47
Au (79)	GGA	Au2.vps	$5d^{10} 6s$	2.00,2.47,(4.03)
V (23)	GGA	V.psf	$3d^3 4s^2$	2.35, 2.70, (0.8)
Sr (38)	GGA	Sr.psf	$4s^2 4p^6 5s^2$	1.80, 1.80, 1.80 (1.3)
O (8)	GGA	O.psf	$2s^2 2p^4$	1.14, 1.14

Table 2.1: The pseudopotentials used in the calculations of this work. The functional used for LDA is due to Perdew and Zunger [95] and the one used for GGA due to Perdew, Burke and Ernzerhof [96]. Valence electronic configuration is shown, as well as the mathing radii. In the radii column, core-correction radius is indicated in parenthesis. In the case of iron, 4s orbitals were not included in the pseudopotential. Scalar-relativistic corrections were included for Au [97]. In the case of Sr, the 5s orbital was not explicitly generated, but we use the 4s orbital (very similar to 5s) instead, when generating the basis set in Tab. 2.2.

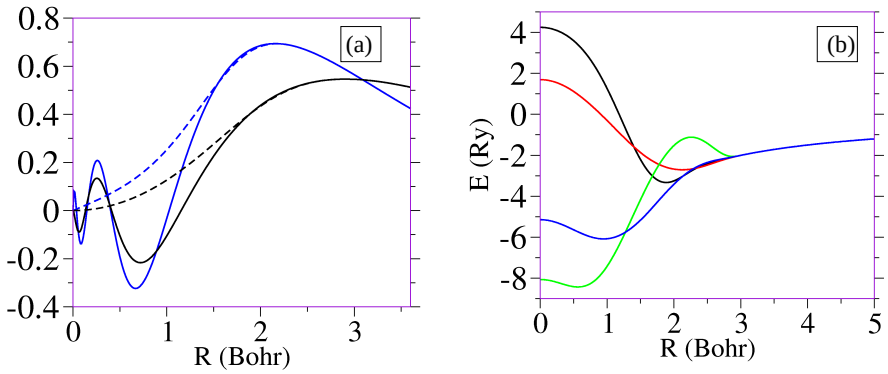

Figure 2.2: The Indium pseudopotential. (a) The all-electron (solid) and pseudo- (dashed) wavefunctions for 5s (black) and 5p (blue) atomic states. (b) Pseudopotentials for s (black), p (red), d (green) and f (blue) states.

In this work, we use mainly three type of basis sets: (i) the single-ζ (SZ), which includes just the plain pseudo-orbitals, (ii) the double-ζ (DZ) in which the plain pseudo-orbitals have been splitted once (DZ) and (iii) the double-ζ with polarization orbitals (DZP), in which wave-functions with angular momentum L+1 (L being the maximum angular momentum of the SZ and DZ basis sets) have been created by perturbation theory. In the SIESTA methodology, the confinement radii of the orbitals is defined by an excitation energy [86, 98]. This "energy shift" is indicated in column 2 and the resulting cutoff radii are listed in column 3 of Tab. 2.2.

2.4 Miscellaneous tools and implementations

In this work we used the ready-made SIESTA program package but there was also some implementation involved, as will be emphasized in Chap. 8. Apart from the programming work done in Chap. 8, we implemented numerous auxiliary programs (in awk, python, matlab, etc.) in order to handle band structure plots, create simulated STM/STS data, etc. We also modified some parts of the SIESTA code and made data post-processing programs in Fortran. We explain some of the most important modifications and tools in this section.

Pseudopotential file	ΔE (mev)	orbitals (cutoff radii / au)	basis	LC (Ang)
`Au.vps`	200	5d(4.51),6s(6.24), 6p(6.24)	DZP:6s-SZ:5d	4.12 (exp 4.08)
`Au2.vps`		5d(4.51),6s(6.24), 6p(6.24)	DZP:6s-SZ:5d	-
`In2.vps`		5s(5.95),5p(7.83), 5d(7.83)	SZ:4p-DZ:5s-DZP:5p	-
`In3.vps`		5s(5.95),5p(7.83), 5d(7.83)	DZP	-
`Si.psf`		3s(5.26),3p(6.43), 3d(6.43)	SZ	5.53
			DZ	5.48
			DZP	5.42 (exp 5.43)
`Si2.psf`		3s(5.13),3p(6.59), 3d(6.59)	SZ	5.62
			DZ	5.56
			DZP	5.50
`H.psf`		1s(5.08),2p(3.95)	DZP	-
`H2.psf`		1s(4.95),2p(4.95)	DZP	-
`Fe.vps`	50	3s(2.56),3p(2.91), 3d(4.23),4s(6.00), 4d(6.00)	DZ:3d,4s-SZ:3s,3p,4p	
`O_opt.psf`	-	2s(4.47,2.37), 2p(5.85,2.42), 3d(3.51)	DZ:2s,2p-SZ:3d	-
`V.psf`	-	3d(5.025,2.724), 4s(7.88,6.87)	DZP:4s-DZ:3d	-
`Sr.psf`	-	4s(3.62),4p(4.11), 5s(7.30,6.69), 4d(6.28)	SZ:4s,4p,4d-DZP:5s	-
`O.psf`	-	2s(3.65,2.51), 2p(4.57,2.64)	DZ:2s-DZP:2p	-

Table 2.2: Information about the basis sets used throughout this work. In the first two columns, the pseudopotential file (see Tab. 2.1) and the energyshift used to confine orbitals, respectively. In the third column the resulting pseudo-orbitals and their cutoff radii. In some cases (`Fe.vps` 4s and 4d orbitals, `O_opt.psf`, `V.psf`, `Sr.psf`, `O.psf`) the cutoff radii has been defined explicitly. For `O_opt.psf`, parameters (`PrefactorSoft,InnerRadSoft`) have been used: they are, for 2s, 2p and 3d orbitals, (58.20,3.47),(1.05,4.85),(69.65,0.30), respectively. The basis set (see also Sec. 2.3) is indicated in column "basis". Sometimes the basis set is a mixture of SZ, DZ and DZP. For example, in the case of gold, we have used a minimal basis for the 5d orbitals (SZ:5d), doubled 6s orbitals and the perturbation theory has been used to create the polarization 6p orbitals (DZP:6s). For some elements, bulk calculations were performed in order to obtain the lattice constant (LC). In these cases $8\times8\times8$ Monkhorst-Pack sampling and mesh cutoff $E_c \sim 100$ Ry were used. The experimental lattice constant values are from Ref. [91].

2.4.1 Simulated STM images

The simulated Scanning Tunneling Microscopy (STM) images are a very important tool for comparing theory and experiment in the case of surfaces. Experimental images are obtained by the STM apparatus that measures the tunneling current between the sample surface and the STM tip. As the tip is moved along the surface, the tunneling current is altered, depending on the local conductivity at that point on the surface. An STM topography is obtained by raising and lowering the STM tip in such a way that the tunneling current stays constant. In the simplest approximation the tunneling current depends on the Local Density Of electronic States (LDOS), so an STM topography then corresponds to a LDOS isosurface, which can be easily derived from calculations. Using the calculated LDOS and searching for its isosurface is a very simple and powerful approximation, first introduced by Tersoff and Haman [99].

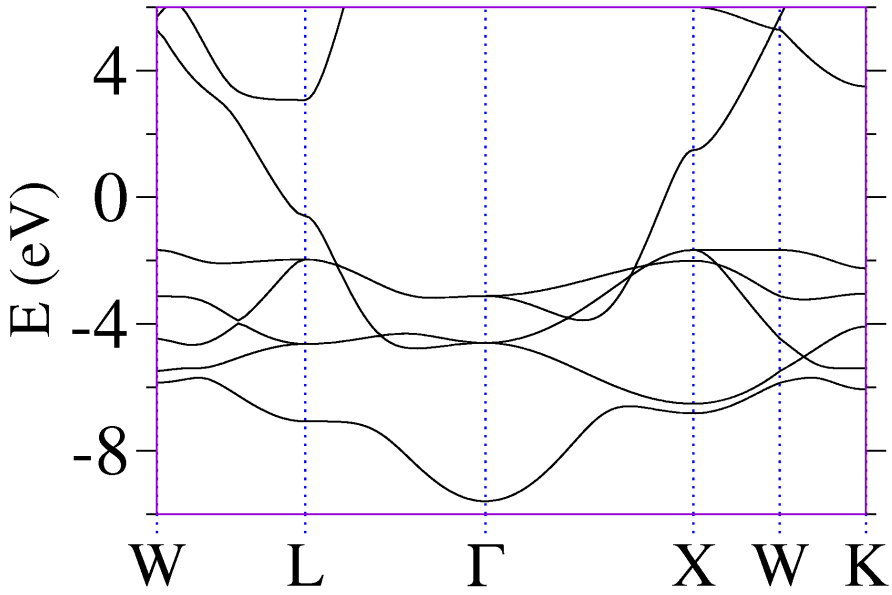

Figure 2.3: The band structure of Au using the basis set described in Tab. 2.2

The LDOS reduces to the electronic density of Eq. (2.37), but now the indice α runs over eigenstates that are within some energy-window ($\epsilon_1 < \epsilon < \epsilon_2$):

$$\rho(\mathbf{r}) = \sum_{v\nu\mu} \phi(\mathbf{r})^*_{v(.\nu)} \phi(\mathbf{r})_{(..\mu)} D_{v(.\nu),(..\mu)}(\epsilon_1, \epsilon_2) \tag{2.41}$$

where

$$D_{v(.\nu),u(.\mu)}(\epsilon_1, \epsilon_2) = \sum_{\mathbf{k},(\epsilon_1<\epsilon(\alpha)<\epsilon_2)} a^{\nu *}_{\alpha\mathbf{k}} a^{\mu}_{\alpha\mathbf{k}} e^{i\mathbf{k}\cdot(\mathbf{R}_u - \mathbf{R}_v)}. \tag{2.42}$$

By adjusting the energy-window, we are able to create filled- and empty-state LDOS data, with desired energy range.

The SIESTA code was modified in such a way that it permits us to save the density matrix of Eq. (2.42). Then we can use the DECHAR program, available with the SIESTA code to produce the LDOS data in a three-dimensional grid. This data is then processed with MATLAB and the isosurface can be searched using available MATLAB routines. Once we have the isosurface on a 2-dimensional grid (function values at grid points correspond to isosurface heights), we can transform it into grayscale colors, finally producing the simulated STM image.

2.4.2 Population analysis

When analyzing the chemical bonding of the system it is essential to know the number of electrons in different atoms and orbitals. One possible way of performing this analysis was introduced by Mulliken (1955) [100]. With Mulliken charges (or populations) one can draw conclusions about the ionic versus covalent character of the bonds and the charge-transfer taking place in the system. The latter helps to understand the behaviour of, for example, the metal-adsorbates and dangling bonds on a silicon surface.

In this work we are frequently interested in the origin of different surface bands seen both in the experiments and *ab-initio* calculations. In calculations, we are able to see the contribution of an individual atom (or an orbital) in the electronic band structure. We start by considering the total charge of a single one-electron state:

$$Q = 1 = \langle \psi_\alpha^{\mathbf{k}} | \psi_\alpha^{\mathbf{k}} \rangle = \sum_{\nu\mu} a_{\alpha\mathbf{k}}^{\nu *} a_{\alpha\mathbf{k}}^{\mu} S_{\nu\mu}(\mathbf{k}) = \sum_{\mu} q_\mu^{\alpha,\mathbf{k}}, \tag{2.43}$$

where we have defined the charge contribution $q_\mu^{\alpha,\mathbf{k}}$ of eigenstate α to orbital μ at k-point $\mathbf{k}$ as:

$$q_\mu^{\alpha,\mathbf{k}} = \sum_{\nu} a_{\alpha\mathbf{k}}^{\nu *} a_{\alpha\mathbf{k}}^{\mu} S_{\nu\mu}(\mathbf{k}) \tag{2.44}$$

To present this information in the band structure plots, one may proceed as follows: if the $q_\mu^{\alpha,\mathbf{k}}$ is greater than some treshold value, the eigenenergy of the state α is highlighted with a symbol in the band structure. The symbol size can also be made to correspond to the number $q_\mu^{\alpha,\mathbf{k}}$.

2.4.3 Constrained relaxations

During the course of this work we relax various surface structures using the Conju-gent-Gradient (CG) method. In some cases we want to fix some geometric entities, say, entire layers to keep the relaxation in accordance with an experimental proposal or individual atoms in order to force atomic distances, etc. We have implemented a few very simple constraints. Atoms can be collected into a group and atoms within the same group cannot move with one respect to another in a constrained direction. This can be achieved by "correcting" the forces on atom i in the following way:

$$\mathbf{f_i} := \mathbf{f_i} - (\mathbf{f_i} \cdot \mathbf{v^0})\mathbf{v^0} + \bar{\mathbf{f}}, \tag{2.45}$$

where v^0 is the constrained direction and $\bar{\mathbf{f}}$ the mean force of the whole group of atoms into this direction. We also implemented the possibility to set desired force components simply to zero.

Another possibility to implement such geometric boundary conditions would be to use the Z-matrices. In this approach, one uses the internal coordinates (bond lengths, bond angles, etc.) instead. The possibility to use Z-matrices has been implemented in SIESTA 2.1.

Chapter 3

1-D Metal-induced reconstructions on Si(111)

3.1 Introduction

An interesting class of surface reconstructions is created by the evaporation of small amounts (0.2-0.4 ML) of metal, usually alkali, rare-earth or noble metals on a silicon substrate. Depending on the amount of the deposited metal, and the annealing process (i.e. how the sample is heated and cooled), different surface patterns emerge and characteristic surface geometries are stabilized by the presence of the metallic atoms. In many cases, one-dimensional features are observed.

These reconstructions include the so-called Si(111)-(3x1) reconstruction (for a review, see [65, 66]) that is formed by the deposition of alkali metals or silver. Deposition of gold forms a variety of reconstructions depending on the miscut angle of the substrate (see Refs. [1, 31, 101] and references therein). Similar reconstructions result from the deposition of indium (see Ref. [55] and references therein).

These (quasi) one-dimensional metal-induced surface reconstructions are usually created *in-situ* in order to study them with Scanning-Tunneling Microscopy (STM), Angle-Resolved Photoemission (ARPES) and Low-Energy Electron Diffraction (LEED). Row-structures are observed with STM and (quasi-) one-dimensional electronic states can be seen in ARPES experiments. The periodicity of the reconstruction is observed with LEED. When the substrate has terraces (a "vicinal" substrate) the row-structures tend to form more easily because the reconstruction has a preferred direction. However, these reconstructions have also been observed for completely flat substrates.

According to recent theoretical models for many of these systems, the metal atoms tend to form monatomic wires [1, 67, 69–72, 101–103]. In the case of the vicinal surfaces, typically only one single or double-wire per terrace, running parallel to the step-edge, is present. One could then tune the coupling of the wires of neighboring terraces by changing the terrace-width and this way alter the one/two-dimensional character of the reconstruction [1].

A strong motivation for fabricating one-dimensional metallic structures on semiconducting surfaces, has been to observe the so-called *Luttinger liquid* behaviour. In a one-dimensional metal, the low-energy electronic spectrum is dominated by collective spin and charge excitations [104–106]. This is in contrast with the behavior of typical metals, that can be understood

in terms of independent particle-like excitations usually called quasiparticles. Unfortunately, one-dimensional metals are thought to be, in principle, unstable with respect to the Peierls distortion that drives them into an insulating ground state [107]. A possible route to avoid this limitation could be the fabrication of metallic chains absorbed on surfaces; the hope is that the rigidity of the substrate will make the energy cost for the structural distortions too large and, therefore, the one-dimensional chains would remain metallic. Semiconductor surfaces are specially attractive for this purpose: the existence of an energy gap prevents the coupling of the electronic states of the chain in the vicinity of the Fermi level with the substrate and the one-dimensional character of these states is preserved.

The Luttinger-liquid theory predicts a splitting of the band structure near the Fermi-level, where two different excitations, spinons and holons, should be observed (corresponding to separate spin- and charge excitations) [104–106]. In the case of the Si(557)/Au reconstruction, a clear band splitting was observed by Segovia, et. al. [27] and interpreted in terms of the Luttinger liquid. As the experimental [28–30, 32–34, 38, 62] and theoretical [69–71, 103] research of this surface increased, several other explanations for this behaviour were proposed. These are, the existence of two distinct metallic bands, based on a theoretical model and *ab-initio* calculations [69, 70]; the existence of two distinct metallic wires on the surface [30]; and the spin-orbit splitting [71].

The origin of the band-splitting observed by Segovia, et. al. [27] is very likely to be the spin-orbit interaction; after it was theoretically predicted by us [71], it was found in a very similar system, the Si(553)/Au reconstruction [62]. Not only the Si(557)/Au, but most of the gold-induced quasi one-dimensional surface reconstructions found up to date feature a similar band-splitting [1, 19, 28]. From the technological point of view this might make them interesting; one could use them in the future spintronic devices. The Si(557)/Au and the role of the spin-orbit interaction and its consequences are discussed in detail in Chap. 6.

Another very interesting feature observed in these surface reconstructions is the existence of metal-insulator transitions [30, 33, 45, 47, 52, 54, 59]. Transition from a metallic state to an insulating one has been observed for several of these surface reconstructions in ARPES and Scanning-Tunneling Spectroscopy (STS) experiments as the temperature is lowered below $\sim$ 100 K. This transition is accompanied with periodicity-doubling in the STM images.

According to Ahn and co-workers these transitions are Peierls-like displacive phase transitions [30, 33, 45, 52, 54, 56], between a highly symmetric high temperature phase and a low temperature structure with lower symmetry and/or higher periodicity. In the case of the Si(557)/Au we have initially proposed that the behaviour seen in the STM experiments could be explained by the disappearance of the dynamical fluctuations in the system as the temperature is lowered, corresponding to an order-disorder phase transition [71]. Gonzalez, et. al., have proposed a similar mechanism in the case of the Si(111)/In-4x1 reconstruction [77–79]. However, in Chap. 6 we also point out that there exist a continuous cross-over between these two different kind of transitions [108] and the two different ideas do not necessarily exclude one another. According to us, the metal-insulator transition in Si(557)/Au is dominated by the freezing of a mode that corresponds to the movements of atoms in the step-edge of the Si(557) terrace. In Chap. 6 we have simulated using *ab-initio* calculations STM and STS data based on the geometrical model of Si(557)/Au to test this idea and it seems that our results reproduce quite well the experimental data.

The metal-insulator transition is particularly interesting in the case of the Si(111)/In-4x2 and Si(553)/Au reconstructions. Both systems have a number of different bands crossing

the Fermi-level, each one with its characteristic fillings [52, 72]. These bands seem to suffer a metal-insulator transition, involving several different structural distortions and complex charge-transfer between them [52, 72, 77, 78, 109]. These effects are studied using a simplified model for the Si(111)/In-4x2 in Chap. 5.

A particularly interesting phenomena in many gold-induced reconstructions [1] is the presence of silicon adatoms which can be removed or added without strongly affecting the underlying surface reconstruction [20–22, 24]. For this reason it has been proposed that these reconstructions could be used as atomic-scale memory devices, individual adatoms acting as bits [20]. Also using adatoms, Yoon et. al. [25] were able to create alterning conducting and semiconducting segments in the Si(111)-5x2/Au surface, consisting of regions with excess or depletion of the adatom density.

The research on some of these systems started as early as the late sixties [2–4]. Only quite recently, *ab-initio* calculations have started to play important role in the research of these systems [67–69, 101]. They are a powerfull way for testing different hypothesis about the origin of observed phenomena. A good example is the Si(557)/Au reconstruction mentioned above. By now the origin of the metallic bands found with ARPES [19, 28] seem to be quite clear: the free-electron like metallic bands are a result of the hybridization of the gold 6p-states with the neighboring silicon orbitals [69, 70], the 6s-states of gold appearing well below the Fermi-energy. Another good example is the Si(111)-5x2/Au reconstruction. It has been studied with growing intensity during the last three decades (see refs. [14, 101] and references therein). From the experimental work, many different geometrical structure were proposed. Finally, the models based on theoretical calculations [67, 101] have been able to reproduce to some extent the theoretical results (see ref. [101] and references therein). In Chap. 4 we present some new models which agree quite well with the recent STM and ARPES data and which are predicted to be more stable than any other model proposed to date.

The theory behind the band structures and atomic geometries in all gold-induced surface reconstructions is quite similar and analogies between the different reconstructions can be found easily. Based on these analogies, in Chap. 7 we have created several trial geometries for the Si(553)/Au reconstruction. It is the "newest" of these reconstructions [58] and we consider that a reliable structural model has not yet been found [1].

In order to test hypothesis with *ab-initio* calculations, a model geometry is needed; in this scheme, one proposes a trial geometry and then produces the relevant physical properties of this geometry (total energy, electron-density, eigenstates, etc.) by an *ab-initio* method. By relaxing the trial geometry one also checks for its stability and by comparing total energies, one can make conclusions about its stability with respect to other geometries. From *ab-initio* calculations simulated STM data can be easily reproduced (see Sec. 2.4.1). The band structure is usually taken to represent the simulated ARPES spectra and Mulliken analysis can be performed in order to see the origin of the bands (see Sec. 2.4.2).

In order to create reasonable trial geometries, one needs some insight on the geometry, bonding and charge-transfer that takes place in the Si(111) surfaces (and in the silicon surfaces in general). For this reason we start, in Sec. 3.3 by introducing some very basic and famous silicon reconstructions and looking at their physical properties. In Sec. 3.4 we also consider the honeycomb model for the Si(111)(3×1)/X, X=Li,Na,K,Ag,Mg reconstructions which turns out to be also relevant for the surfaces we study in the course of this work. In Sec. 3.5 we consider some fundamental Si(111) stacking properties which are, together with the basic Si reconstructions the base for creating our trial geometries. Before all this, we take

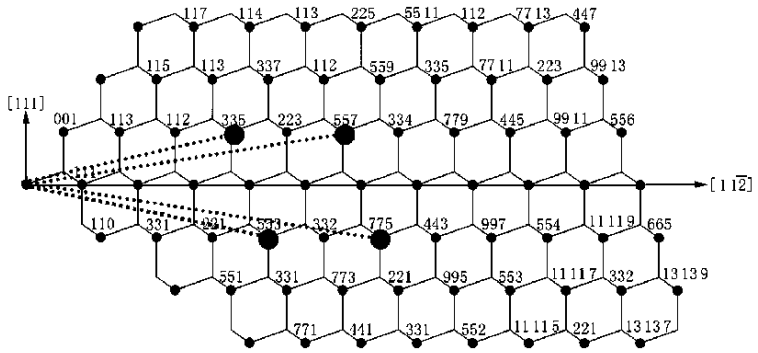

Figure 3.1: Cleaving of the Si(111) surface as function of the Miller indices. Each set of Miller indices corresponds to a different step width. Picture taken from Ref. [1].

a look at some basic concepts such as the notation of surface reconstructions.

3.2 Some basic concepts

A cleaved, unreconstructed Si(111) surface is presented in Fig. 3.2. We assume for the moment that the reconstruction takes place in the first double-layer (dbly), where we should relocate the atoms. The periodicity of the reconstruction is denoted by its two-dimensional lattice vectors, say N×M. This means that the lattice vectors of the reconstructions are N$\hat{v_1}$ and M$\hat{v_2}$, where $\hat{v_1}$ and $\hat{v_2}$ are the lattice vectors of the unreconstructed Si(111) surface (see Fig. 3.2a). In lattice constant units they are $\hat{v_1} = (0, 1/\sqrt{2})$ and $\hat{v_2} = (\sqrt{3/8}, 1/\sqrt{8})$. Here with (x,y) we refer to the $[\bar{1}\bar{1}2]$ and $[\bar{1}10]$ directions, correspondingly. With relative units we refer to a coordinate system that must be scaled by the lattice constant.

By a *vicinal* surface we refer to a surface that has been cleaved along some direction whose normal is close to the [111] direction. Typically these surfaces produce steps with terraces exhibiting [111] facets, the widths of the steps depending on the cleaving direction. The normal of the surface is denoted by the three Miller indices, so each set of indices corresponds to a certain step width. This is illustrated in Fig. 3.1, where a large set of Miller indices is considered.

Some Miller indices are - depending on the symmetry of the bulk material - equivalent. In the case of silicon, we are allowed to "scroll" the Miller indices, i.e. (557),(755) and (575) correspond to the same surface. This "scrolling" corresponds to a symmetry operation that leaves the silicon lattice vectors unaffected.

3.3 Basic Si(111) reconstructions

The natural geometry of cleaved and annealed Si(111) is the Si(111)7×7 reconstruction, also called the Dimer-Adatom-Stacking Fault (DAS) model [111, 112]. It was found after more than two decades of research and is quite complicated. We will not go into its details, but rather concentrate on some well known small-scale reconstructions that take place in the Si(111). Even the complex Si(111)7×7 reconstruction can be reduced to some extent to the basic silicon building blocks, say, mainly to the adatom 2×2 reconstruction and surface-dislocation

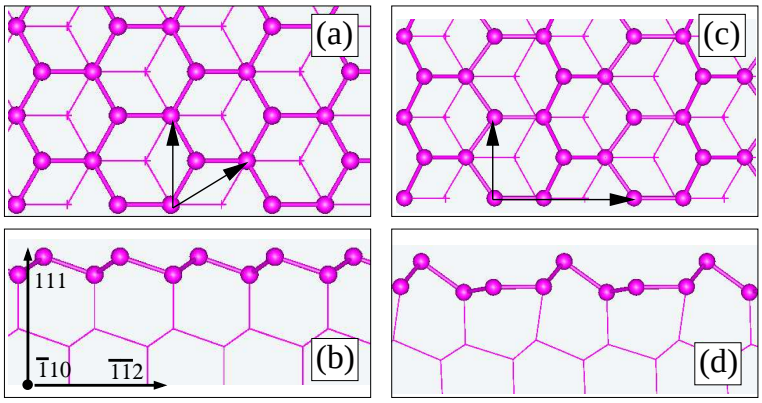

Figure 3.2: Silicon (111) surface without reconstruction, viewed from top (a) and from side (b). The inset of figure (b) shows the directions. The buckling (2×1) reconstruction of Si(111) [110], viewed from top (c) and from side (d). 2-dimensional lattice vectors are indicated in (a) and (c).

(that will be discussed below). A wide range of vicinal silicon surfaces have been studied in Ref. [113] and it seems that in the family of Si(111) surfaces (both flat and stepped), atoms reconstruct only inside the terrace - i.e. no strong rebonding of the step-edge is observed [113]. The building blocks we consider here are the buckling, pi-chain and the adatom reconstructions. For more details on the buckling model, see Haneman (1961) [110]. The pi-chain model was introduced by Pandey (1981) [114], see also Norhtrup et. al. (1982) [115]. For some of the first *ab-initio* calculations of the adatom model, see Northrup, et. al. (1984) [116] and Meade and Vanderbilt (1989) [117].

A cleaved Si(111) surface is illustrated in Fig. 3.2a-b. The driving force for the reconstruction are the dangling-bonds that are left to project into the vacuum, after the surface has been created from the bulk. The system tries to eliminate these dangling bonds by relocating the surface atoms. By hybridizing the dangling bonds with other orbitals, the system could open gaps and lower its total energy. During the relocation (or even removing) of the atoms, surface stress arises, due to the underlying silicon bulk that prefers unaffected atomic sites. The system with lowest total energy is the one that optimizes the competition of these two terms. Each one of the following simple building blocks we are about to consider, solves this problem in a different way.

3.3.1 The buckling model

In the buckling model [110], illustrated in Fig. 3.2c-d, the neighboring atoms "buckle", i.e. change their relative heights. This creates a surface with 2×1 periodicity, where the atoms have different z-positions alternating along the $[\bar{1}\bar{1}2]$ direction. By having different heights, the atoms achieve an important charge transfer. The lowered atom adopts the sp^2 hybridization and gives up the electron in its p_z orbital. This extra electron moves to the sp^3 dangling-bond of the elevated atom and thus saturates it. This eliminates one dangling bond per each 2×1 unit cell, and opens a gap in the surface bands associated with the dangling bonds.

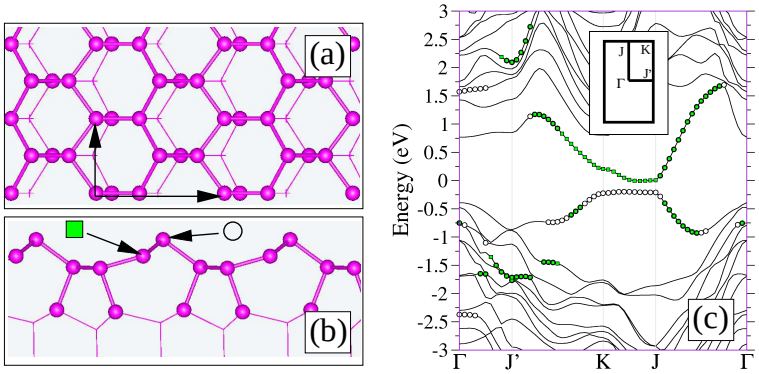

Figure 3.3: The pi-chain reconstruction of Si(111) [114] viewed from top (a) and side (b) and the band structure (c). 2-dimensional lattice vectors are indicated in (a). Inset of (c) shows the Brillouin-zone and the path in the k-space used to plot the bands. The atomic character of the bands has been marked with green squares and open circles. Corresponding atoms are marked with the same symbols in panel (b).

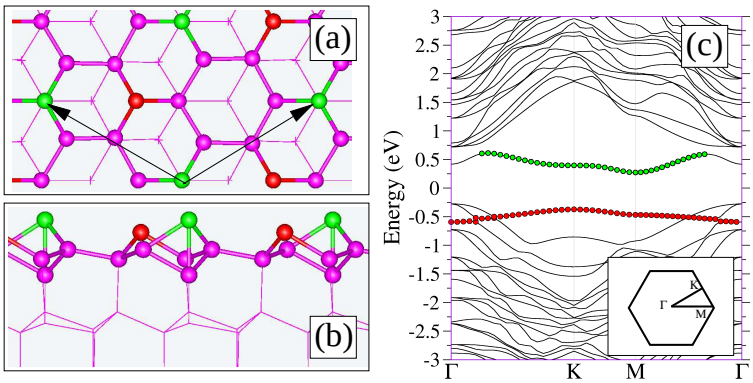

Figure 3.4: The adatom reconstruction of Si(111) [117] viewed from top (a) and side (b) and the band structure (c). 2-dimensional lattice vectors are indicated in (a). Inset of (c) shows the Brillouin-zone and the path in the k-space used to plot the bands. The states marked with red circles have a strong weight on the restatom, while the green ones are mainly from the adatom.

3.3.2 The pi-chain model

The energy barrier between the buckling and the pi-chain reconstructions is minimal [115]; in an *ab-initio* calculation, starting from the buckling reconstruction the system frequently relaxes spontaneously into the pi-chain configuration (due to small noise in the forces). Pi-chain reconstruction is illustrated in Fig. 3.3. We notice two elevated atoms that form a zigzag-chain into the $[\bar{1}10]$ direction. The p_z orbitals of these atoms are hybridized, creating a "pi-chain" while the rest of the orbitals adopt the sp^2 hybridization. A gap opens in the band associated with the π-chain due to the two inequivalent positions of the atoms along it. The lower atoms are in the sp^3 hybridization state, so there are no unsaturated dangling bonds. In the band structure of Fig. 3.3c we show our calculation of the band structure of this surface and observe how bands related to the elevated atoms develop a gap.

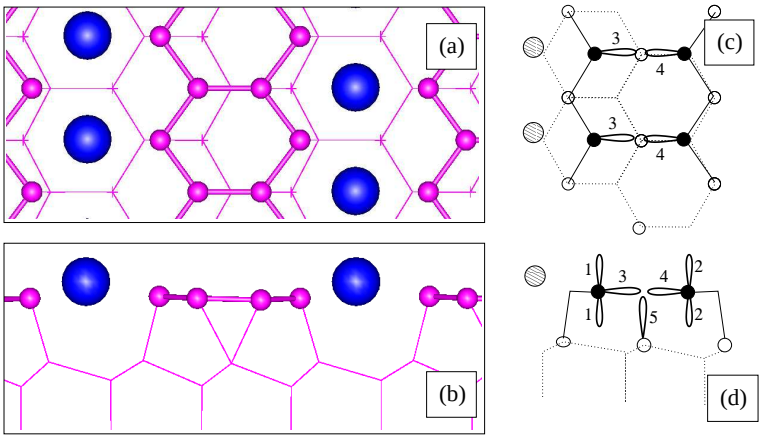

Figure 3.5: The Honeycomb Chain (HC) model of Si(111)(3×1)/X, X=Li,Na,K,Ag,Mg [66], viewed from top (a) and side (b). The honeycomb is indicated by a box in (b) and the 2-dimensional lattice vectors are plotted in (a). Schematic plot of the bonds, viewed from top (c) and side (d). The dashed lines present the bonds of the second dbly, while the solid ones the bonds of the first (topmost) dbly. The bonds of the honeycomb (not in clear sp^3 hybridization) are numerated from (1)-(5) (see text for details). The large filled circles present the metal adsorbate atoms.

3.3.3 The adatom model

In contrast to the two basic building blocks of the previous sections, in the adatom reconstruction we add atoms in top of the surface. This is illustrated in the Fig. 3.4. We observe that by adding one adatom every 2×2 supercell, we are able to saturate three dangling bonds, while creating only a single new one. We also observe a slightly elevated atom, the "restatom" that has a dangling bond not saturated by any of the adatoms. The dangling bond of the adatom gives up its electron that moves into the restatom, thus saturating it. The elevation of the restatom can be attributed to the repulsion between its negative charge and the underlying dangling-bonds. From the band structure of Fig. 3.4c we see how the adatom gives signal in the empty states while the restatom in the filled ones.

3.4 The honeycomb chain model

In the last section, some simple Si(111) building blocks, consisting purely of silicon, were considered. What happens when a small amount of metal is evaporated on the surface? When ≈ 0.2 ML of Li, Na, K, Ag or Mg are deposited on the flat Si(111) and annealed, a characteristic row-structured reconstruction, the Si(111)(3×1)/X, X=Li,Na,K,Ag,Mg is observed [66]. The theoretical model with the lowest total energy up-to-date according to *ab-initio* calculations is due to Erwin and Weitering [66] and is illustrated in Fig. 3.5. It is also called the "Honeycomb Chain" (HC) model.

First of all, one observes the metal adsorbate sitting inside the surface layer, in a situation that can be interpreted as a silicon substitutional site. Second, located next to the metal atom, the silicon bonds create a curious structure, which is the so-called honeycomb. Third, in order to create the honeycomb, one has to remove a silicon atom from the unreconstructed Si(111) surface.

The stability of the HC is explained as follows [66]: the Si-atoms of the HC create a

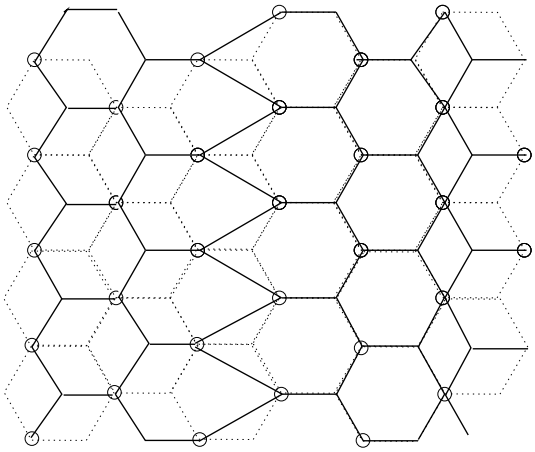

Figure 3.6: Different ways of stacking silicon. The dashed lines present the bonds of the second silicon dbly, while the solid lines those of the first (topmost) silicon dbly. Spheres correspond to the "up" atoms of the second silicon dbly.

double-pi bond (separate sp^2- and p_z-hybridization) and in order to saturate all the bonds, ionize the alkali-metal. This scheme is illustrated in Fig. 3.5c-d, where the bonds of the honeycomb are visualized. Bonds (1) and (2) hybridize, so does (3) and (4). The "molecular orbital" created by this hybridization, further hybridizes with the bond (5). The charge transfer can be explained by counting the electrons of the honeycomb: there is one electron available for each bond, so the total electron-count in Fig. 3.5c-d. is five. It can be made closed-shell (even electron count) if one electron is removed or added to it. The HC ionizes the alkali-metal, obtaining this way the extra electron.

In our case and in the following chapters, we are studying mainly surface reconstructions involving gold. Surprisingly, the (HC) forms spontaneously in most of the cases. Gold can act both as a donor and as an acceptor of electrons, so the charge transfer will not be as obvious as in the case of the Si(111)(3×1)/X, X=Li,Na,K,Ag,Mg . On the other hand, the silicon HC will obtain a closed-shell electronic structure even if it acts as a donor. Also both the gold and the silicon HC might act as acceptors, ionizing other parts of the surface reconstruction (for example, dangling bonds).

3.5 Stacking Silicon

By stacking silicon, we refer to the different ways of arranging the bonds in the Si(111) surface. Some of these ways are illustrated in Fig. 3.6. Starting from the very first row in the right, we first have silicon atoms in a similar coordination as in the unreconstructed Si(111) surface. We then remove a row of silicon atoms. In order to maintain the bond-lengths reasonable, this removing is accompanied by a translation of the remaining topmost double-layer to the right. First of all, this creates a so-called "surface-dislocation" (SD). A row of atoms becomes overcoordinated, so their position is obviously energetically unfavorable. We also observe that when going further to the left the atoms are in a "stacking-fault" (SF), where the bonds of the first dbly follow the bonds of the underlying silicon dbly. Going further to the left, this SF is corrected by removing an atom and creating two rows of silicon atoms with rather long bond-lengths. Continuying to the left, we observe that the perfect silicon stacking

has been recovered.

After removing or adding atoms to the surface the different combinations of SD and SF become important as one wishes to recover the perfect stacking. This happens for example when one wants to introduce a HC into the Si(553) surface; by introducing a HC, one creates stacking-faults which must be corrected by a surface-dislocation. This is discussed in more detail in Chap. 7. We also create a notation for defining the different combinations of SD, SF and HC in Chap. 7.

3.6 Surface calculations with SIESTA

The SIESTA *ab-initio* code [71, 84, 86] was used throughout this work to simulate the surface reconstructions. On some occasions, to test our results, the plane-wave code VASP [118, 119] was also used. The results of SIESTA and VASP were always almost identical.

In surface calculations, and in *ab-initio* calculations in general, one can adjust the trade off between computational speed and accuracy of the calculation by some key methodological parameters. For most DFT schemes, these are (i) the *autoconsistency* of the field equations of Eqs. (2.8)-(2.15), (ii) the *mesh density* (electronic density must be put on a real-space grid in order to calculate the exchange-correlation terms), (iii) the *k-point sampling* and (iv) *the basis-set*. In the case of surface calculations, key parameters are also (v) the *slab thickness* and (vi) the *slab-slab distance*.

(i) A less stringent autoconsistency condition speeds up the calculation, but may give inaccurate results, especially when there are lots of states very near/crossing the Fermi-energy. The autoconsistency in SIESTA calculations is measured from the density-matrix, for details, see Sec. 2.2.5. (ii) The mesh density is usually taken to be larger than 100 Ry. (iii) The k-point sampling is very important when calculating infinite systems; each k-point corresponds to a mode of the infinite system (in contrast to the modes adjusting to the periodicity of the unit cell) we are calculating, so using more k-points makes the calculated quantities more realistic. In the case of the quasi-one dimensional surface reconstructions, one typically uses more k-points in the "one-dimensional" direction, along which the electronic bands present a larger dispersion. (iv) The basis set is very important parameter in SIESTA calculations; one must consider in detail the limitations of the basis set used and how suitable it is to describe the known properties of each of the simulated elements. For the definition of different basis sets, see Sec. 2.3.

When calculating surfaces using standard methods like SIESTA or VASP, we are bound to calculate infinite systems (not semi-infinite, like a surface). We must then model the surface as a slab with a finite thickness that is repeated periodically along the normal direction of the slab. The bottom of the slab is saturated with hydrogen (alternatively, symmetric slabs can be used [117]) and the atoms in the lowermost layer are fixed to their initial bulk positions. One must then choose carefully (v) the slab thickness and (vi) the amount of vacuum between the slabs. A very thin slab has smaller number of atoms and is thus computationally very convenient. However, not using a sufficient amount of freely relaxing atoms in the slab results in artificial stresses. A good example is the adatom reconstruction of Fig. 3.4, where atoms move considerably from their bulk-positions also in the second dbly. A thin slab also polarizes easily and might create a strong dipole-moment. Using a slab instead of a real semi-infinite medium also implies that the electronic states become quantized due to the finite thickness;

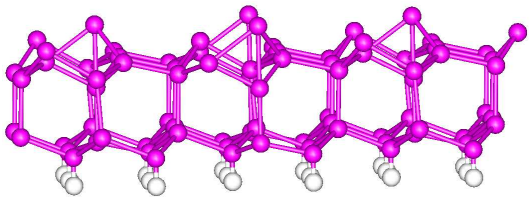

Figure 3.7: A small portion of the (infinite) adatom reconstruction, including only two dblys, viewed from an arbitrary angle.

basis-set	SZ	DZ	DZP
buckling	0.0	0.0	0.0
π-chain	-16.3 (-3.6)	-18.6 (-5.7)	-13.2 (0.0)
adatom	-4.4 (1.2)	-3.9 (1.8)	-5.9 (0.0)
Bulk Si Chemical potential (eV)	-107.013	-107.298	-107.752

Table 3.1: LDA total energies (meV/Å^2) of relaxed Si(111) reconstructions, calculated with different basis sets, using k-point sampling of 4×4 and 3-dblys. Relative energy values within each column are comparable. Relative energy values in parenthesis are comparable within each row.

thinner slabs result in less electronic states and poorer results.

We have calculated the systems presented in Sec. 3.3 as function of the most important key parameters (iii)-(vi) in order to see how they converge. The parameters (i) and (ii), i.e. the autoconsistency and the mesh cutoff, were set to 10^{-4} and 120 Ry, respectively. For (iii) the k-point sampling, we use the Monkhorst-Pack scheme, explained in Sec. 2.2.3.

By the number of dblys, we refer to the total number of dblys in the system, including the bottom layer saturated by hydrogen: an example of the 2×2 adatom model, with only two double-layers is presented Fig. 3.7. The basis for the hydrogen atoms was always taken to be DZP, in order to enhance the sp hybridization with the silicon. The distance of the hydrogen layer from the silicon layer was optimized, yielding the value of d≈0.217 (in units of lattice constant). The (vi) slab-slab distance was taken to be 15 Å.

The silicon basis-sets used in the test calculations are listed in Tab. 2.2. Calculations are performed with LDA. As explained in Sec. 2.3, the SZ basis includes (one) 3s and (three) 3p orbitals. DZ includes the same set of orbitals, but splits each of them in order to get more variation freedom (resulting in eight orbitals). DZP has the same orbitals as DZ, but adds also a shell of (five) d-orbitals, resulting in total of 13 orbitals per atom.

The bulk lattice constants for different basis sets can be found in Tab. 2.2. In Tab. 3.1 the silicon chemical potential μ (the energy of a Si atom in the bulk) have been calculated using each of the basis sets. It is very important to use the adequate lattice constant for each set of the computational parameters in order to avoid artifical stresses. When comparing total energies from systems involving different number of atoms, for the extra-atoms we will assign

slab thickness	2-dbly	3-dbly	4-dbly	5-dbly
buckling	0.0	0.0	0.0	0.0
π-chain	-21.6 (-2.4)	-18.6 (0.5)	-19.5 (-0.3)	-19.4 (0.0)
adatom	-4.1 (-3.4)	-3.9 (-3.2)	-3.0 (-2.2)	-0.8 (0.0)

Table 3.2: LDA total energies (meV/Å^2) of relaxed Si(111) reconstructions, calculated with different number of double-layers, using 4×4 k-point sampling and the DZ basis set. Relative energy values within each column are comparable. Relative energy values in parenthesis are comparable within each row.

k-point sampling	2×2	4×4	8×8	16×16
buckling	0.0	0.0	0.0	0.0
π-chain	-29.2 (-12.4)	-18.6 (-1.8)	-17.0 (-0.2)	-16.8 (0.0)
adatom	50.5 (60.1)	-3.9 (5.6)	-9.4 (0.2)	-9.5 (0.0)

Table 3.3: LDA total energies (meV/Å^2) of relaxed Si(111) reconstructions, calculated with varying k-point sampling, using 3-dblys and the DZ basis set. Relative energy values within each column are comparable. In the "adatom" row, the relative energies in parenthesis are comparable within the same row.

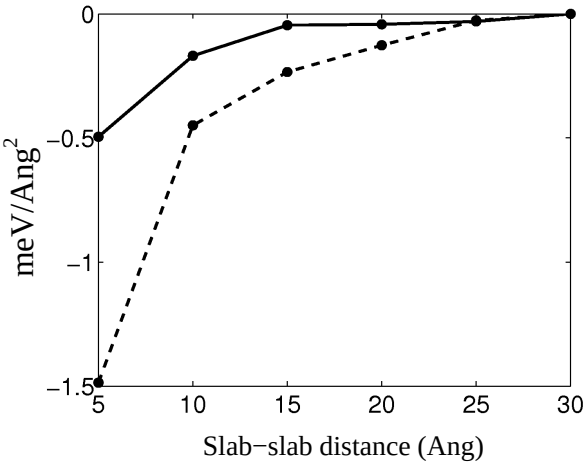

Figure 3.8: Energy difference as function of the slab-slab distance, for the pi-chain (solid) and the buckling (dashed) reconstructions.

the energy μ of a bulk silicon atom, since the surface should be in equilibrium with the corresponding bulk. The correction term is then ΔN$\times\mu$, where ΔN is the difference in the number of silicon atoms (one must keep in mind that the chemical potential μ changes as function of the computational parameters). For example, relative energy differences between the π-chain and the adatom models are calculated as follows:

$$\Delta E = \frac{\frac{1}{2}E_{2\times2} - \frac{1}{2}\mu - E_{2\times1}}{A_{2\times1}}, \tag{3.1}$$

where E's are the energies and A the area. Subscripts refer to the unit cell. In units of lattice constant, $A_{2\times1}$ ≈0.87.

When calculating the total energies of Tabs. 3.1-3.3, we systematically relax the atomic coordinates for each of the parameter sets. In order to accelerate the relaxation, we use the information (the relaxed coordinates) from previous calculations; for example, one first relaxes the system using the SZ basis then moves into more accurate basis sets. This systematic way of refining calculations will be fully developed in Chap. 7, where one refines step by step using also (i) the accuracy of the self-consistency and the (iii) size of the k-point sampling. When realizing this kind of an approach, we have found very usefull the python programming language.

From Tab. 3.1 we see that the relative energies change considerably when the d-orbitals are included in the basis set. For example for π-chain $\sim$ 2 meV/Å^2 when changing the basis from SZ to DZ and $\sim$ 6 meV/Å^2 when changing from DZ to DZP. This is consistent with earlier observations [86, 120] and shows the importance of the d-orbitals; silicon can lower

significantly its total energy with the d-orbitals (this way readjusting the relative energies). This becomes more important especially when the coordination becomes more complicated.

The energies in Tab. 3.1 are in accordance with earlier calculations [117], where the π-chain reconstruction is always energetically more favorable than the adatom one. As the basis set is made more complete, this energy difference becomes vanishingly small [117]. In the calculations of Meade and Vanderbilt [117], the π-chain is ~ 300 meV per 1×1 unit cell more favorable than the adatom reconstruction with a plane wave cutoff of 5 Ry and only ~ 25 meV per 1×1 unit cell more favorable when the plane wave cutoff is increased to 12 Ry. From Tab. 3.1 we can derive that this energy difference varies from ~ 160 meV per 1×1 unit cell, when using the SZ basis to ~ 93 meV per 1×1 unit cell when using the DZP basis. This difference further reduces when using a more complete k-sampling.

In order to see the convergence with respect to the basis set, one should compare them to a fully converved plane-wave basis set [90], a task that is out of the scope of the present chapter. However, in the following chapters we will present such tests and will see that a typical comparison between SIESTA and plane-wave results (VASP) is very satisfactory.

From the tables Tab. 3.1 we see that the relative energies as function of the number of dblys has converged (when compared to a slab containing 5 dblys), in the case of the π-chain, to less than ~ 1 meV/Å^2 already with 3 dblys. Already 2 dblys give a satisfactory convergence of ~ 2 meV/Å^2 . In the case of the adatom reconstruction, this convergence is much slower. The reason for this can be seen in Fig. 3.4, where we observe that also the atoms in the second topmost dbly move considerably. When systems include adatoms and strong modification of atomic heights, using 3-dblys, we can expect an error bar of ~ 3 meV/Å^2 from the data in Tab. 3.2.

Althought the results from different k-point sampling calculations in Tab. 3.3 are not directly comparable (the unit cells 2×1 and 2×2 have a different k-point density), we can see the importance of using a reasonable amount of k-points. This seems to be 4×4 in the case of the π-chain (convergence up to ~ 2 meV/Å^2) and 8×8 in the case of the adatom reconstruction (convergence up to ~ 0.2 meV/Å^2). From Fig. 3.8 we take the sufficient amount of vacuum to be ~ 15 Å; including more vacuum changes the energies less than 0.5 meV/Å^2

Chapter 4

Si(111)5x2-Au

4.1 Introduction

The deposition of gold in the monolayer (ML) range on the flat Si(111) surface results in a variety of phases [13], such as $\sqrt{3}\times\sqrt{3}$R30^o, 1×1 and 5×2. The 5×2 phase occurs at ∼0.4 ML gold coverage [8]. It was first discovered about thirty years ago [2–4] and has been investigated using many experimental techniques since then. This includes low energy electron diffraction (LEED) studies [2–4], x-ray diffraction [9] and x-ray standing wave analysis [5], scanning tunneling microscopy (STM) [6, 11, 15], angle resolved photoemission spectroscopy (ARPES) [12, 18, 19, 23, 24] and inverse photoemission [16], and high resolution electron microscopy (HREM) combined with heavy-atom holography [14].

Already the first structural models, based on LEED measurements, considered two atomic gold chains per 5×2 unit cell running in parallel [3,4]. This was later confirmed by HREM [14] and seems to be firmly established (see Fig. 4.3). The gold chains run along the $[\bar{1}10]$ and equivalent directions (parallel to the ×2 periodicity of the unit cell). Therefore, three different domains are possible for the 5×2 reconstruction on the flat Si(111) surface. Single-domain surfaces, necessary for ARPES, can be fabricated using vicinal surfaces with a slight cut-off angle [1, 11]. The presence of one-dimensional structures in this reconstruction has also been confirmed by the ARPES studies. Early studies found a strong anisotropic signal near the Fermi level [12, 16], but no evidence of Fermi-level crossing for this band was found [16]. Later studies at low temperature found a one-dimensional band with a strong dispersion along the direction of the gold chains [18, 19]. The top of this band appears near the 5×2 zone boundary and disperses downward, reaching its minimum close the 5×1 zone boundary. This band has been reported to change its dimensionality from strongly one-dimensional near the Fermi energy to two-dimensional at lower energies [18]. In these studies a gap of ∼0.3 eV was also identified for this band. The presence of this gap and its apparent closing with increasing temperature was related to a Peierls instability [18, 19]. More recent ARPES results [23, 24], both at low and room temperatures, have been able to identify some additional surface bands. However, the metallic or semiconducting character of the surface is still a matter of debate. In fact, it has been proposed that the metallic or semiconducting character can depend on the concentration of silicon adatoms [24, 67], and even that semiconducting and metallic segments can alternate along the gold chains in the surface [25].

The STM images (see Fig. 4.14) are characterized by the presence of bright, irregular

protrusions [6, 15] and "Y"-shaped features [11, 17] with a well defined orientation respect to the underlying substrate (see Fig. 4.15). The protrusions have been established to be silicon adatoms [21], which are present on the surface with an optimum coverage close to 1/4 adatoms per 5×2 unit cell (see Fig. 4.14).

In spite of all these experimental studies, the structure of the Si(111)-(5×2)-Au reconstruction has not been completely established yet. Earlier structural models only considered the adsorption sites of the gold atoms. Many of them could be ruled out on the bases of more detailed STM studies [6] and the knowledge of the exact gold coverage [8]. A few more refined models exist [14, 15]. They consider both the position of the gold atoms on the substrate and the rebonding of the silicon atoms in the surface layer. Probably the most detailed structural model proposed to date is the one by Marks and Plass (MP) [14]. The MP model is based on a combination off-zone HREM, transmission electron diffraction and heavy-atom holography data.

The first theoretical studies using first-principles electronic structure calculations appeared only quite recently. This is due to the complicated structure and the large unit cell of the Si(111)-(5×2)-Au reconstruction. Kang and Lee [68] studied the MP and the Hasegawa-Hosaka-Hosoki (HHH) [15] models using density functional theory. Their main conclusion is that both models fail to reproduce some of the key features of the STM images and the experimental band structures. Using a similar methodology, Erwin [67] proposed and studied new structures which are characterized by the presence of the so-called honeycomb-chain silicon structure [66]. One of these models (the so-called "5×2" model) seems to fulfill many of the constraints imposed by the empirical evidence. An interesting point raised by Erwin is that of the crucial role played by silicon adatoms in the stabilization of the different structures. According to Ref. [67], the surface energy of Erwin's "5×2" model is minimized for an optimum adatom coverage in agreement with recent experimental reports [21]. For lower adatom coverages other structures compete in stability. This is a very interesting result which, however, is based on approximate calculations. Due to the large size of the supercells necessary to simulate explicitly the effect of the different adatom concentrations, Erwin assumed that the main role played by the adatom is to dope the surface with electrons. He then analyzed the behavior of the total energy as a function of the number of extra-electrons in the substrate, obtaining a minimum for ∼0.25 electrons per 5×2 unit cell.

In this work, we present a comprehensive study of the atomic and electronic structure of different models of the Si(111)-(5×2)-Au reconstruction using electronic structure calculations based on the density functional theory. We have used two different methodologies, the SIESTA code [71, 84, 86] using a basis set of localized atomic orbitals and the VASP code [118, 119] using a basis set of plane-waves. We analyze the MP model [14], the models proposed by Erwin [67], and a new model that we found during our structural optimizations. We study in detail the energetics and the structural and electronic properties of the different models. We also calculate the change in the surface energy as a function of the content of silicon adatoms for the two most stable models. In order to do so, we perform calculations for large supercells containing realistic concentrations of adatoms: 5×4, 5×6, and 5×8 supercells. Our new model is the most favorable in the range of low adatom concentrations, while Erwin's "5×2" model becomes favorable for larger adatom concentrations. The crossing between the surface energy of both structures occurs close to 1/2 adatoms per 5×2 unit cell, i.e. near the maximum adatom concentration observed in the experiments. Both models, our new structure and Erwin's "5×2" model, seem to provide a good description of most of

the experimental data. Particularly, we find a general agreement between the calculated and measured band structures along the direction parallel to the gold chains.

In the next sections we present our results for the different models of the Si(111)-(5×2)-Au surface. We first focus on the energetics, relaxed geometries, and the electronic band structures. We then turn our attention to the effect of the different silicon adatom contents and the simulated STM images, which we only analyze in detail for the most stable structural models. A summary of the relative energies of the calculated configurations, accompanied with a brief description of each of them, can be found in Table 4.1.

Before starting with the description of the results, it is interesting to point out some brief comments about the concentration of silicon adatoms on the Si(111)-(5×2)-Au surface. A detailed study of the equilibrium situation has recently been performed by Kirakosian *et al.* [21, 22] using STM. Their results indicate that, at equilibrium, only one adatom site is occupied out of every four possible sites, corresponding to a 5×8 adatom periodicity (if all the adatom sites were occupied we would recover a perfect 5×2 periodicity). The analysis of the adatom-adatom correlation functions obtained from the STM images reveals a strong suppression of those configurations with small adatom-adatom distances, a clear maximum corresponding 5×4 periodicities, and a long range oscillatory tail [22]. This was interpreted in terms of a short range repulsion between adatoms plus a long range interaction term. In Ref. [21], Kirakosian and collaborators showed that the density of adatoms can be increased by depositing additional amounts of silicon reaching an almost perfect 5×4 arrangement of the silicon adatoms. Further deposition of silicon does not create a stable 5×2 adatom structure. Instead the extra silicon atoms decorate the step-edge of the terraces on the surface. These observations seem to have at least two implications: (i) the optimal adatom concentration must be certainly lower than one adatom per 5×2 cell and, (ii) the structure of the reconstruction must be stable against relatively large changes of the content of adatoms [1] since the density of silicon adatoms can be increased by a factor of two without, at least apparently, dramatic structural changes [21].

A systematic study of the energetics of the surface as a function of the adatom concentration by means of first-principles electronic structure calculations is quite complicated. This is for two main reasons. First, the energies involved are rather small, which implies the need of very well converged calculations. A more serious limitation, however, is the necessity to use large supercells consistent with the low adatom densities. For this reason we have concentrated most efforts in the two limiting cases, involving respectively 0 and 1 adatoms per 5×2 cell. The intermediate concentrations usually require drastic approximations. For example, Erwin [67] assumed that the main effect of the adatoms in the Si(111)-(5×2)-Au surface is to dope the gold chains with electrons and studied the energetics of the system as a function of this doping. Here we go a step beyond and present explicit calculations for adatom contents down to 1/4 adatoms per 5×2 cell, consistent with a 5×8 periodicity, which indeed can be reached in experimental conditions [21]. Due to the large size of these systems we limit this study to our two most stable models, and only use the smaller DZ basis set.

Results of this chapter have been published in Ref. [101].

[1] This observation does not contradict the recent proposal by Erwin [67] that a *minimum* adatom content may be necessary to stabilize the observed structure over other competing reconstructions.

4.2 Computational details

Most of the calculations were done using the SIESTA code (see Chap. 2), but also VASP [118, 119] was used. The pseudopotential and basis data can be found in Tab. 2.2, corresponding to the LDA versions `Si.psf`, `H.psf` and `Au.vps` (the generalized gradient approximation (GGA) has been also used for a few test calculations, i.e. using `Si2.psf`, `H2.psf` and `Au2.vps`). The bidimensional Brillouin-zone (BZ) sampling [92] (in N×M Monkhorst-Pack sampling, N refers to the direction parallel to the gold wires) contained 4×4 points for the 5×2 unit cell (and a consistent sampling for other cells [2]).

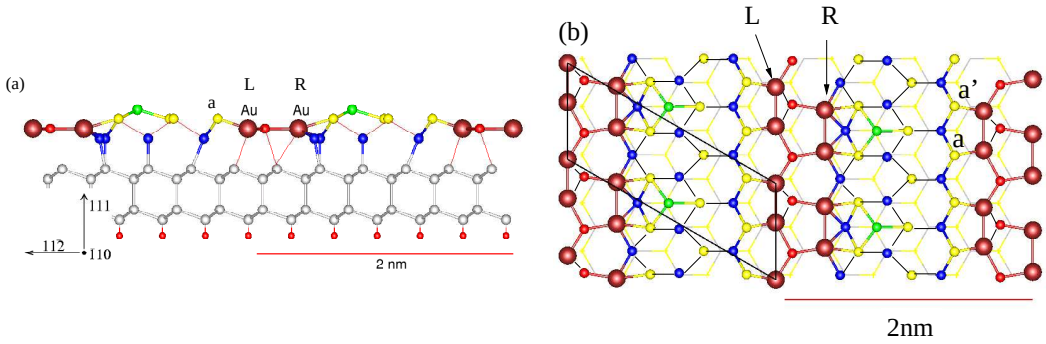

Figure 4.1: (color online). Schematic view of a typical slab used in our calculations. It shows the model proposed by Marks and Plass (MP^{+}) [14] for the Si(111)-(5×2)-Au surface reconstruction. Large circles in the surface layer represent the gold atoms. The bottom surface of the slab is saturated with hydrogen atoms. (a) Side view and (b) top view with some of the silicon atoms in the surface and the two gold chain labeled (see the text).

We modeled the surface using a finite slab, similar to that depicted in Fig. 4.1. For most calculations the slabs contained three silicon bilayers (the one at the surface and two underlying silicon bilayers) plus an additional layer of hydrogen atoms to saturate the silicon atoms in the bottom of the slab. This removes the surface bands associated to the bottom surface from the energy-range of interest, i.e. from the band-gap region. We have checked the convergence of the results using thicker slabs for the most stable structural models of the surface. We use periodic boundary conditions in all three directions. A vacuum region of 15 Å ensures negligible interactions between neighboring slabs (see Sec. 3.6). During the structural relaxations the positions of the silicon atoms in the bottom layer were kept at the bulk ideal positions. Unless otherwise stated all other degrees of freedom were optimized until all the components of the residual forces were smaller than 0.04 eV/Å. To avoid artificial stresses the lateral lattice parameter was adjusted to the theoretical bulk value calculated using similar approximations to those utilized in the slab calculations, i.e. the same basis set and grid cutoff, and a consistent k-sampling.

Due to the large number of atoms (∼70 atoms for typical slabs and up to 273 for the largest ones) and to the need to perform geometrical optimizations for many different structural models, we have decided to use a DZ basis set for silicon in most of our calculations, an approximation which according to our test calculations in Sec. 3.6 is well justified.

[2] More precisely, for the 5×4 supercells we have checked that k-samplings with 4×2 and 4×4 points produce almost identical results. k-samplings with 4×3 and 4×2 points have been used, respectively, for the 5×6 and 5×8 supercells.

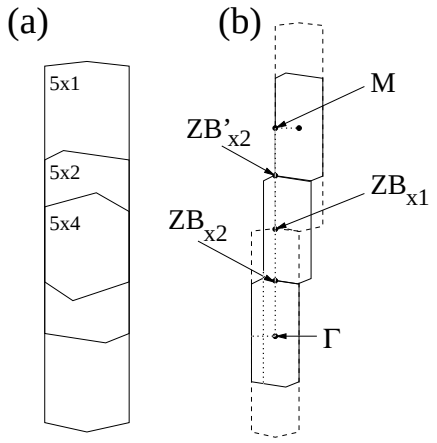

Figure 4.2: (a) Comparison of the bidimensional Brillouin zones corresponding to (5×1), (5×2) and (5×4) supercells on the Si(111) surface. (b) Schematic view of the path (dotted lines) used to plot the band structures in this work (Γ- $ZB_{\times 2}$-$ZB_{\times 1}$-$ZB'_{\times 2}$-M-Γ). Its relation with the (5×1) (dashed lines) and (5×2) (solid lines) Brillouin zones is indicated, and some special points are defined.

In this work we study the relaxed structures and the energetics of several models of the Si(111)-(5×2)-Au surface reconstruction. The energy differences between different models are of key importance since we would like to determine the most plausible structures. Whenever it is necessary to compare the energies of structures containing different numbers of silicon atoms, the silicon chemical potential is set to the total energy of bulk silicon at the equilibrium lattice parameter. This choice is justified by the fact that the surface should be in equilibrium with the bulk. A summary of our results can be found in Table 4.1. One can see that the relative energies are quite small in some cases. However, they are larger than the estimated error bar for the total energy (see above). Furthermore, the relative energies usually exhibit a faster convergence than the total energy of a single structure. It is also necessary to check the convergence of the results as a function of the slab thickness and the completeness of the basis set. Table 4.2 shows the results of these tests for the most stable structures. In one case, the slab thickness was increased by one silicon bilayer while, in the other, a DZP basis set was used for the silicon atoms. In both cases the systems were relaxed. The results are quite stable against the change of the slab thickness. In particular, the energy order of the structures is not changed and the variation of the relative surface energies is smaller than $\sim$0.5 meV/Å^2 in all the cases. The variations with the size of the basis set are somewhat larger. From the results in Table 4.2 we can estimate an error bar smaller than 2 meV/Å^2 for the relative surface energies of the different structures calculated using SIESTA.

In order to check the accuracy of our predictions we decided to perform calculations for some of the systems with another electronic structure code that utilizes a different methodology. We used the VASP code [118, 119] for this purpose. We used projected-augmented-wave potentials and a well converged plane-wave basis set with a cutoff of 312 eV. All structures were relaxed (the equilibrium lattice parameter of bulk silicon obtained with VASP is 5.41 Å). In Table 4.2 we can see some of the results obtained with VASP. They are in good agreement with the SIESTA results, especially with those obtained with the more complete DZP basis set. The order between our more stable models is preserved, although the energy difference is

somewhat decreased. In particular, the new structural model found in the present work (model N in Tables 4.1 and 4.2) is confirmed to be the most stable surface reconstruction between those studied here. It is also interesting to note that the energy associated with the addition and removal of adatoms for a particular structural model seems to be quite independent of the details of the calculation.

The surface BZs of the studied systems are shown in Fig. 4.2 (a). For the 5×1 system the BZ is a stretched hexagon while, for the remaining periodicities, the hexagons are distorted. We plot the electronic band structures of the different models along the Γ- $ZB_{\times2}$-$ZB_{\times1}$-$ZB'_{\times2}$ -M-Γ line (see the dotted line in Fig.4.2 (b)). The Γ-M path runs parallel to the gold wires in the surface, crossing the 5×2 BZ through three different regions. The M-Γ line is perpendicular to gold wires. The surface/bulk and main atomic character of the different bands is identified by means of a Mulliken population analysis [100].

Although a DZ basis is usually sufficient to obtain a quite good description of the occupied electronic states and the relaxed geometries in silicon systems, the use of a more complete basis set is necessary to describe the unoccupied part of the band structure even at low energies. For this reason all the band structures shown in the paper are calculated using a DZP basis set and slabs containing three underlying silicon bilayers (even if the relaxed geometry is obtained from a calculation using a DZ basis and/or a thinner slab).

Finally, the Scanning Tunneling Microscopy (STM) images are simulated using the theory of Tersoff and Hamann [99].

Model	Description	ΔE_{surf} (meV/Å^2)
MP^+	Marks and Plass model after a constrained relaxation	+46.8
RMP^+	Fully relaxed MP^+ structure	+5.4
RMP	Relaxed MP^+ structure without adatoms	+8.3
E(5×1)	Erwin "5×1"	+4.8
E(5×1)*	E(5×1) with adatoms on the Au-wires	+6.5
E(5×2)	Erwin "5×2"	+1.4
E(5×2)*	E(5×2) with adatoms on the Au-wires	0.0
N	New model	-3.3
N^+	N with silicon adatoms in H_3 positions	-0.6
$N^{+\prime}$	N with silicon adatoms in T_4 positions	+1.2
N*	N with adatoms on the Au-wires	+2.4

Table 4.1: Summary of the structural models studied here for the Si(111)-(5×2)-Au reconstruction and their relative surface energies (ΔE_{surf}). Those structures containing adatoms have one silicon adatom per 5×2 cell, i.e. the concentration of adatoms is maximum. Superscript $+$ indicates the presence of "conventional" adatoms saturating silicon dangling bonds in the surface. Labels H_3 and T_4 refer, respectively, to adatoms occupying hollow and top sites [121]. The presence of adatoms located on top of the Au wires is indicated by a $\star$ superscript. The data in this table have been calculated using the SIESTA code with a DZ basis for silicon and DZPs-SZd basis for gold. The slabs contained two silicon bilayers below the surface layer (see Fig. 4.1 (a)). All energies are referred to that of the structure recently proposed by Erwin in Ref. [67].

4.3 Marks and Plass model

We start our investigation of the structure of the Si(111)-(5×2)-Au surface using the model proposed by Marks and Plass [14] from experimental data obtained with heavy-atom holography and high resolution electron microscopy (HREM). An example HREM image can be seen in Fig. 4.3. We use the label MP^+ for this structure (see Table 4.1). The $+$ superscript indicates that the structure contains silicon adatoms saturating some of the silicon dangling-bonds in the

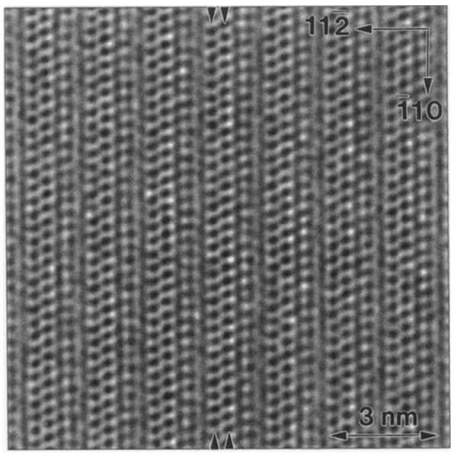

Figure 4.3: Near Schertzer defocus, noise filtered, off-zone HREM image of the Si(111)-5×2-Au surface. Clearly visible are two (arrowed) rows of dark features which correspond to gold atoms. Picture taken from Ref. [14].

structure, what we call "conventional" silicon adatoms. A schematic view of this structure, as proposed in Ref. [14], can be found in Fig. 4.1. It has to be taken into account that, due to the limitations of the experimental techniques, there are several uncertainties and assumptions in this structure. Only the atomic coordinates within the surface plane are accurate. The heights of the atoms over the substrate are only approximately resolved. The experimental beam error in combination with the size and complexity of the structure also limits the sensitivity to possible subsurface relaxations. As a consequence, the experimentally proposed structure only considers the reconstruction of the outermost bilayer and contains limited information about the registry between this surface bilayer and the underlying material. It is necessary to eliminate these uncertainties before one can undertake any serious study of the electronic structure of the MP^+ model. In order to do this while preserving all the information originally present in the MP^+ proposal, we started our study by performing constrained relaxations of the structure. The structure in Fig. 4.1 was relaxed using following degrees of freedom: (i) the height of the different layers and, (ii) the lateral position of the surface layers with respect to the underlying bulk slab. The grouping of the atoms in different layers given in Ref. [14] only implies approximately equal z-coordinates (the z-axis is taken here along the surface normal). For this reason, in a second step, the atoms were allowed to relax in the z-direction while keeping their coordinates within the xy-plane. The resulting geometry preserves the bonding pattern of the original MP^+ proposal, and provides a reasonable initial guess to start our search of the most stable models by performing full structural optimizations.

We now consider in detail some of the structural patterns appearing in the MP^+ model of the surface. For this analysis we find useful the comparison with the Si(557)-Au surface, a closely related reconstruction studied in more detail in Chap. 6 that has been quite well characterized during recent years [27–29, 69–71]. The stepped Si(557)-Au is formed after the deposition of $\sim$0.2 monolayers of gold on vicinal (111), with the misorientation chosen along the $[\bar{1}\bar{1}2]$ direction. The size and orientation of the terraces of the Si(557)-Au represent an analogous to the flat 5×2 unit cell but including a single silicon step [19]. With half the gold coverage than the Si(111)-(5×2)-Au surface, the terraces of the Si(557)-Au contain only one Au wire running parallel to the step edges. Gold atoms occupy silicon substitutional positions in the surface layer. This is supported both, by recent X-ray diffraction data [29], and density

functional calculations performed using a methodology similar to the one utilized here [70], which provide a consistent structural model of the surface. In particular, the highest stability of the silicon substitutional sites for gold has been unambiguously demonstrated by the *ab initio* calculations. For example, the substitutional site was determined to be at least 1 eV/Au more stable that adatom-like positions, where gold sits on the surface saturating one of the silicon dangling-bonds, or even $\sim$0.5 eV/Au more favorable than the adsorption decorating the step edges [70]. It seems, therefore, that the Au atoms on the Si(557)-Au surface exhibit a strong tendency towards three-fold silicon coordination. Gold atoms adapt to this situation without much strain, with typical Si-Au distances only a few percents larger than the bulk silicon bond length.

In the light of these observations the bonding pattern of some of the gold atoms in the MP$^+$ model (Fig. 4.1) seems quite peculiar. In particular, the gold atoms in the chain situated at the left side of the "gold trench" (marked with an L in Fig. 4.1) present a fourfold coordination. They are connected to three silicon atoms within the surface layer and, additionally, to the silicon atom immediately below. Furthermore, the Si atoms neighboring to the mentioned gold atoms (see atoms a and a' in Fig. 4.1) present an unsaturated dangling bond which might be avoided with a slight structural change.

It is interesting to note that the tendency of the gold atoms to occupy silicon substitutional positions in the top most layer cannot help to completely rationalize the structure. A three-fold bonding pattern of the gold atoms is inherently frustrated by the presence of a surface dislocation. In the MP$^+$ model this dislocation is located at the position of the right-hand gold wire (marked with R in Fig. 4.1). Due to the change of the bonding sequence there are not three unpaired silicon electrons available for each of these Au atoms, but rather two. Therefore, they do not occupy a normal three-fold position and are quite likely to be displaced from the initial symmetric positions after relaxation. As was discussed in Sec. 3.5, the surface dislocation can, in principle, be moved to different locations. In fact, we will see below that this provides a simple route to generate alternative structural models of the surface.

The comparison between the structure of the Si(557)-Au reconstruction of Chap. 6 and the MP$^+$ model of Fig.4.1 raises another interesting point. In the case of the Si(557)-Au surface the silicon atoms in the proximity of the step edge suffer a considerable rebonding. They form characteristic silicon structure which has been identified with the "honeycomb chain" (HC). As was explained in Sec. 3.4, the presence of the silicon HC seems instrumental to understand the stability of the Si(557)-Au and related reconstructions. It seems somewhat surprising that the silicon HC structure, common to the (3$\times$1) and Si(557)-Au metal induced reconstructions, is absent from the MP$^+$ model of the Si(111)-Au-(5$\times$2) surface. Indeed the MP$^+$ model seems to be based on an almost unreconstructed Si(111) surface with a row of adatoms on top, and the more clear disturbance from this bonding pattern being the presence of a surface dislocation.

We now proceed further with the structural relaxations of the MP$^+$ system. It is instructive to focus first on a optimization were only the silicon degrees of freedom are taken into account. The gold atoms are constrained to remain at their initial coordinates. Due to the more directional bonding of silicon we can expect the structural changes to be simpler to analyze and somewhat less dependent on the particular choice of the initial guess in this case. Besides, as a stronger scatterer, we can assume that the gold positions to be better resolved in the experiment. The resulting geometry is plotted in Fig. 4.4(a). We observe two main effects. On the one hand, the HC configuration clearly emerges. One of the driving forces behind this

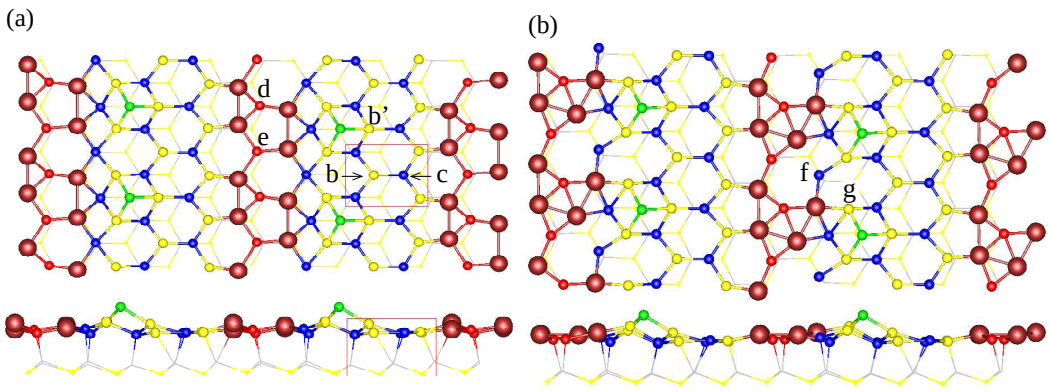

Figure 4.4: (color online). (a) MP^+ after the optimization of the position of the silicon atoms in the structure. The gold atoms are kept in the positions obtained after the initial contrained relaxation of the experimental coordinates. The silicon honeycomb chain (HC) structure has been highlighted. (b) The same structure after full relaxation (RMP^+). See the text for the labels of the different atoms.

rebonding is the movement forward of a and a' atoms in order to form an additional covalent bond with the silicon atoms in the underlying layer. The double-bonded “dimers" of the HC structure are formed by atoms b and c. This questions the location of the adatoms in the surface since, in principle, the dangling-bond associated with atom b' could disappear with the formation of a silicon double bond. We can observe the disturbing effect of the adatom on the HC structure. The appearance of the HC bonding pattern during the relaxation of the MP^+ structure confirms the results of recent density functional calculations by Kang and Lee [68], who also made a geometrical optimization of the MP^+ model. The electronic bands calculated for this structure (not shown here) are also in quite good agreement with those presented by these authors in Ref. [68]. Fig.4.4 (a) also shows clearly what could be classified as a “stacking fault" in the structure (bonds of atoms d and e coincide with those in the underlying silicon layer). This stacking fault, which probably is energetically unfavorable, can be easily avoided by moving the position of the surface dislocation from the right-hand to the left-hand of the gold trench. Alternatively we can visualize this change (at least approximately) as a 180^o rotation of the surface layer with respect to the underlying silicon structure. This transformation gives one of the structures discussed in the next section, which incidentally is almost identical to the “5×1" structure proposed recently by Erwin in Ref. [67].

When the relaxation of the MP^+ system is continued without any constraints, the monatomic gold wires are strongly distorted as can be seen in Fig. 4.4 (b). This distortion was not observed in the density functional calculations of Kang and Lee [68]. The reasons for this discrepancy are not completely clear at the moment. The break of the monatomic gold wires seems to be related with the presence of adatoms. If they are eliminated from the structure the gold atoms remain in two well separated parallel wires. Additionally, the strain introduced by the adatoms in the structure, results in the weakening of some Si-Si bonds in the surface layer (see the increased distance between atoms f and g). In spite of these strong structural distortions, the presence of adatoms in the structure is still energetically favorable as can be seen in Table 4.1. These structural distortions are reflected in the band structure: following the nomenclature used in Ref. [68], the band S_1 is shifted to higher energies respect to the S_2 and a gap of $\sim$0.3 eV is opened respect to the constrained case.

In summary, our results suggest that neither the silicon structure nor the positions of the

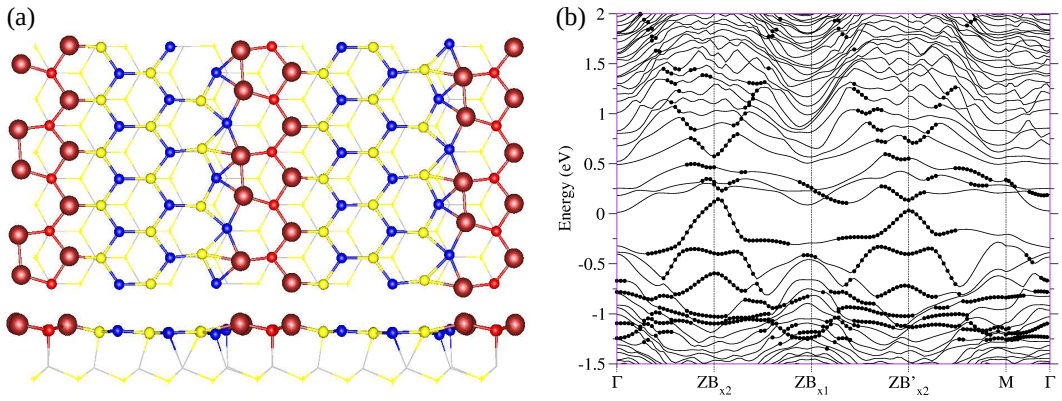

Figure 4.5: (color online). (a) Relaxed geometry of the E(5×1) model with zero adatom coverage and, (b) the corresponding band structure. Solid symbols indicate those bands with a larger weights in the atoms of the SiAu complex. The energies are referred to the Fermi level.

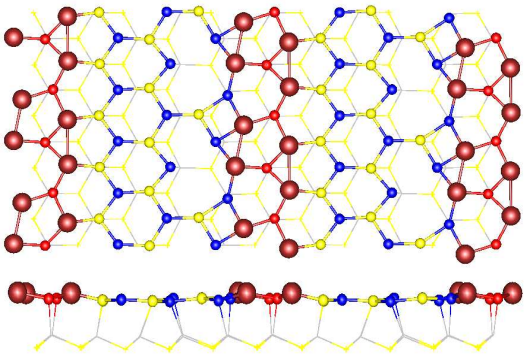

Figure 4.6: (color online). Relaxed geometry for the E(5×2) model.

gold atom in the structure proposed by Marks and Plass [14] are stable. Furthermore, in agreement with the general conclusions of Ref. [68], neither the STM images nor the band structure of the fully relaxed or the constrained relaxed MP^{+} model seem to be in agreement with the experimental information.

4.4 The Erwin models

As discussed in the previous section, the MP model of the Si(111)-(5×2)-Au surface reconstruction is characterized by the presence of a surface dislocation between one of gold wires and the neighboring silicon atoms. Other locations are possible for the surface dislocation. In particular, it can be translated to the *other* gold wire, this can also be assimilated to a rotation of the surface bilayer with respect to the underlying bulk silicon. This eliminates the “stacking fault" commented in the previous section, and produces a new structural model. This structure is very similar to the “5×1" model recently proposed by Erwin [67], and we refer to it as E(5×1). In Table 4.1 we can see that the E(5×1) model without silicon adatoms is slightly more stable than the relaxed MP structure. Fig. 4.5 (a) shows the relaxed structure of the E(5×1) model. The left (L) gold wire, where the surface dislocation is located, suffers a considerable dimerization, which is much smaller for the right (R) wire. The alternating

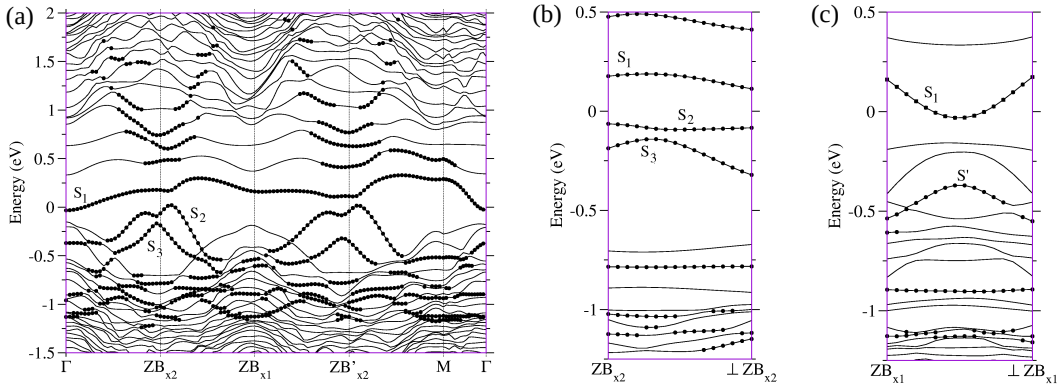

Figure 4.7: Band structure of the E(5×2) model with zero adatom coverage parallel (Γ-$ZB_{\times 2}$-$ZB_{\times 1}$-$ZB'_{\times 2}$ path in (a)) and perpendicular to the gold wires i (Γ-M path in (a) and panels (b) and (c)). Surface bands with the larger contributions coming from the atoms in the SiAu complex are indicated by filled circles. The energies are referred to the Fermi level.

Au-Au distances as obtained with VASP are, 4.06 Å and 3.59 Å for the L wire, and 3.82 Å and 3.83 Å for the R wire. The geometries obtained with SIESTA are very similar, specially those obtained with the more complete DZP basis set. Hereafter we name “SiAu complex" the structure formed by the two gold wires and the central silicon atom connecting them. The silicon structure in between two of such SiAu complexes is quite flat and resembles what could be described as a double honeycomb chain (DHC) silicon structure [67]. The band structure along the direction parallel to the gold wires is shown in Fig. 4.5 (b). It shows several surface bands and has a metallic character. Those surface bands mainly associated with the Si-Au complex has been highlighted using solid symbols. Most of these bands are occupied and appear in the gap region. The unoccupied surface bands appearing in the gap are mainly associated with the silicon DHC. The most prominent feature is a dispersive band associated with the weakly dimerized (right) gold wire and the central silicon atom in the SiAu complex. This band is, in principle, metallic and close to half occupied. Although small gaps are opened associated with the crossings with other bands and slight geometrical distortions, it can be easily followed in Fig. 4.5 (b) extending from ∼1.3 eV below to ∼2.3 eV above E_F. A similar band, with a similar origin, also dominates the band structure of the Si(557)-Au surface [69, 70]. This band comes mainly from the sp^3 lobes of the central silicon atom in the SiAu complex. There is also a strong hybridization with the 6p states of the gold atoms in the R wire. For this reason, they are better assigned to the Si-Au bonds connecting the central silicon with the R gold wire. Its large dispersion is due to the large overlap between these Si-Au bonds along the wire. The metallicity stems from the inability of gold (each gold atom only provides one valence electron) to saturate the bonds with all its silicon neighbors [69]. The other states in the Si-Au complex give rise to relatively flat surface bands associated either with weakly overlapping silicon states or with the gold dimers.

In Ref. [67] it was also proposed that, under certain conditions, it could be energetically favorable to remove some of the over coordinated silicon atoms in the neighborhood of the surface dislocation. Our relaxed structure for this model (hereafter E(5×2)) is shown in Fig. 4.6. In this case both gold wires present an appreciable dimerization with alternating Au-Au distances of 4.37 Å and 3.35 Å for the left gold wire, and 4.16 Å and 3.49 Å for the right wire. Our SIESTA calculations with the smaller DZ basis set predict the E(5×2) model to be more

stable, by at least 3.4 meV/Å^2, than both the E(5×1) model and the different variants of the MP model (see Table 4.1). However, the difference between the E(5×1) and E(5×2) models is reduced with the use of more complete basis set. In particular, our plane-wave calculations predict both models to be degenerate within 0.1 meV/Å^2 (the E(5×1) slightly more stable). This agrees with the results of Ref. [67] where the E(5×1) model is predicted to be more stable than the E(5×2) variant by less than 1 meV/Å^2, and only after the addition of silicon adatoms the E(5×2) structure becomes favorable.

The band structure of E(5×2) with zero adatom coverage is plotted in Fig. 4.7. The band structure along the wires is in good agreement with that reported in Ref. [67] for this structure. Again, the surface bands close to the Fermi energy come mainly from the SiAu complex. Like in the case of the E(5×1) model, the band structure is metallic. This is in disagreement with one of the latest and more detailed ARPES experiments which suggests that the Si(111)-Au-(5×2) surface is a semiconductor with a band gap of at least 0.2 eV (see Fig. 4.11). However, the metallic versus semiconducting character of this surface is still a matter of controversy. For example, the recent ARPES study by Himpsel and collaborators finds several metallic bands [24]. In fact, this reference and the scanning tunneling spectroscopy (STS) data of Ref. [25] indicate that the surface could be composed of alternate metallic and semiconducting regions along the gold wires. Our calculated band structure for the E(5×2) model is very close to being semiconducting. Just by shifting the S_1 band to higher energies by a few tenths of eV we could obtain a semiconducting surface. This might indicate that the metallic behavior is simply related to the limitations inherent to the local density approximation used here and the very simplified assumption that the monoelectronic eigenvalues can be directly identified with the photoemission peaks. In spite of its metallicity, several characteristics of the photoemission spectra are recovered by the band structure in Fig. 4.7. The most prominent band observed experimentally starts at the boundary of the 5×2 zone ($ZB_{\times 2}$) dispersing downwards until it reaches a minimum at the boundary of the 5×1 zone ($ZB_{\times 1}$) [18, 19, 23, 24]. This band appears at binding energies between ∼0.2 eV and ∼1.3 eV. Following Erwin [67], we can try to identify this band with our S_2 band, whose maximum appears close to E_F in the neighborhood of $ZB_{\times 2}$. However, it becomes difficult to follow the dispersion of this surface band as we move to higher binding energies for two reasons: *i)* the band enters the region of the projected bulk bands, becoming a surface resonance and, *ii)* other surface bands coming from the same region of the surface appear in the energy interval between -0.5 and -1.2 eV. This last point is widely consistent with the experimental data in Ref. [23], where three additional bands are identified for binding energies larger than 0.5 eV.

Losio and collaborators [18] reported an interesting effect, a continuous dimensionality transition of the main surface band. The character changes from strongly one-dimensional at the band maximum (i.e. only dispersing in the direction parallel to the gold wires) to two-dimensional at its minimum (i.e. with a non-negligible dispersion also in the perpendicular direction). The strong one-dimensional character of the surface states close to E_F has also been confirmed in the most recent ARPES measurements [23, 24]. The dispersions in the direction perpendicular to the wires can be found in Fig. 4.7 (b) and (c). The band widths are rather small for most surface bands. An effect similar to the reported dimensionality transition can be seen in the case of the S_1 band. It is tempting to assign the experimentally observed effect to the S_2 band (see the different dispersion of bands S_2 in panel (b) and S' in panel (c)). However, as commented above it is not so simple to follow the S_2 band as it disperses downwards. In fact, we can locate what seems to be an avoided crossing between the S_2 and

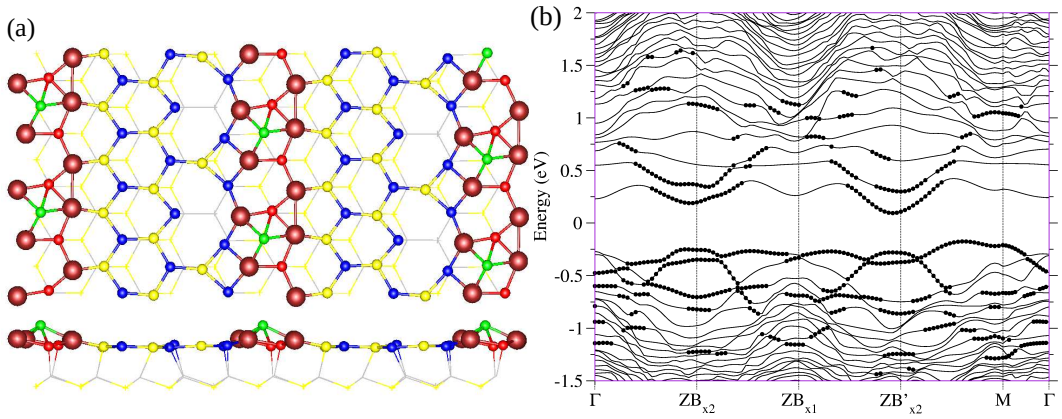

Figure 4.8: (color online). (a) Relaxed geometry of the E(5×2)* model (containing one adatom per 5×2 unit cell) and, (b) the corresponding band structure. Surface bands with a larger weight in the atoms of the SiAu complex are marked with filled circles. The energies are referred to the Fermi level.

the S_3 bands half way along the $ZB_{\times 2}$-$ZB_{\times 1}$ path in Fig. 4.7 (a). Therefore, we think that the S′ band in panel (c) is rather related to the S_3 band than to the S_2 band, and the dimensionality change would be absent from our results. Also the energy position of the band S′ (∼-0.5 eV) is quite far from the ∼-1.3 eV found experimentally for the band minimum. Therefore, in contrast to Erwin [67] we conclude that our calculated band structure for the E(5×2) model does not provide a direct explanation to the observation by Losio *et al.*.

Similarly to the surface bands of the E(5×1) model, the S_1, S_2 bands in Fig. 4.7 (a) have the largest weight in the central Si atom in the SiAu complex. The S_1 band can be associated with SiAu bonds connecting the central Si with the left gold wire. This SiAu bonds have a small overlap and this is translated in a quite flat band. The two dispersive S_2 and S_3 bands have a stronger weights in the other SiAu bonds, which have a larger overlap and, therefore, present a stronger dispersion.

We now explore the role of the silicon adatoms in these structures. We first studied the stability of the adatoms in the E(5×1) model when they are located over the silicon part of the surface reconstruction, i.e on sites equivalent to those occupied by the adatoms in the original MP proposal. It is interesting to note that the role of the silicon adatoms in such positions is indeed not very clear. The stability of the adatoms in typical silicon reconstructions stems from the fact that each adatom can saturate three dangling bonds in the surface at the expense of creating just an additional dangling bond. The energy gained in this process usually overcomes the strain energy caused by the addition of the adatoms. However, the E(5×1) model in Fig. 4.5 (a) does not have silicon dangling bonds. The appearance of unsaturated dangling bonds is avoided by the formation of the double-bonded silicon dimers that characterize the HC configuration. In fact, the only metallic band in this model comes from the SiAu complex as explained above. In accordance with these observations, we found extremely difficult to reach a stable configuration, i.e. with all the components of the forces below our threshold, for the silicon adatoms over the silicon sites of the E(5×1) model. Finally, after several hundreds of optimization steps this model spontaneously relaxed into a new structure. This structure, labeled N^+ in Table. 4.1, belongs to a new family of structural models for the Si(111)-Au-(5×2) surface found in this work for the first time and described in more detailed in the next subsection.

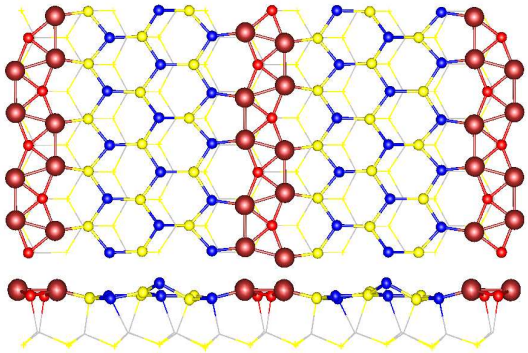

Figure 4.9: (color online). New structural model for the Si(111)-(5×2)-Au reconstruction. This is the most stable configuration of the surface according to our calculations (see Table 4.1).

In the light of the previous comments, a more stable adsorption site for the silicon adatoms would be on top of the SiAu complex. This has been previously proposed by Erwin [67], and is confirmed by our calculations. Table 4.1 shows the changes in surface energy after the addition of one silicon adatom per 5×2 unit cell. The behavior is opposite for the E(5×1) and E(5×2) models, with the addition being energetically favorable for the later model. The E(5×1) remains metallic after the addition of the adatom, and the dispersive band associated with the SiAu complex remains quite unchanged. The situation with the E(5×2) model is different. In agreement with the results in Ref. [67] we find that the band structure becomes semiconducting after the addition of the adatoms. The corresponding atomic and electronic structure can be found in Fig. 4.8 (a) and (b) respectively. The surfaces bands with a larger contribution from the atoms in the SiAu complex has been highlighted using solid symbols. It has been impossible to identify a band that can be solely assigned to the adatoms. We can see that the band structure of the E(5×2) suffers major modifications after the addition of adatoms, at least for the large concentrations considered here. Besides the fact that the structure becomes semiconducting, the agreement with the detailed photoemission experiments of references [23] and [24] seems to be somewhat degraded.

4.5 New structural model

In this section we present a novel structural model for the Si(111)-(5×2)-Au surface reconstruction that has been found during our investigation. Our slab spontaneously relaxed to this new structure while trying to optimize a modified version of the E(5×1) model commented in the previous section. The new structure can be found in Fig. 4.9, and will be referred here as model N. Table 4.1 shows that the energy of the new model compares favorably with those of the other structures proposed to date. In fact, within our calculational scheme it is the most favorable structure. The difference with the second most stable model without adatoms, the E(5×2), is 4.7 meV/Å^2. This difference is reduced to 4.1 meV/Å^2 when using a more complete DZP basis set as shown in Table 4.2. These energy differences are quite small, so further studies have been performed in order to drive more definitive conclusions. First, we have repeated our calculations using the PBE [96] GGA exchange and correlation functional instead of LDA. The new structure continues to be more stable by 3.6 and 5.1 meV/Å^2 using, respectively, a DZ and a DZP basis set. As a second step, the energy ordering between the N

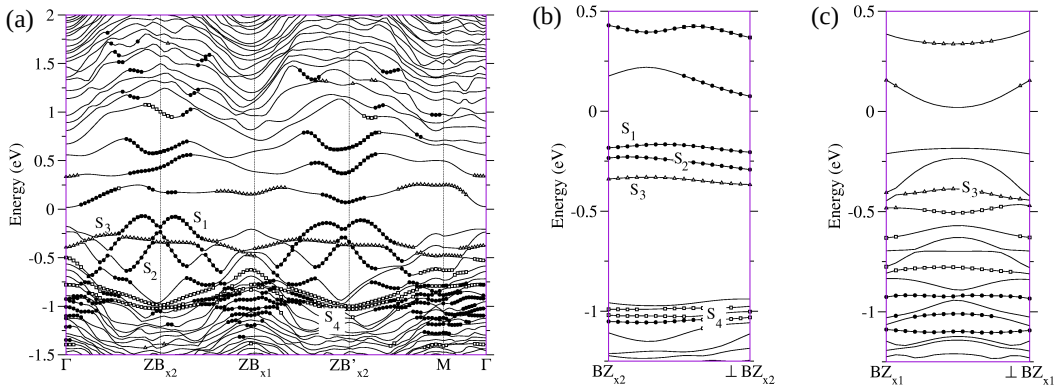

Figure 4.10: Band structure corresponding to the N model with zero adatom coverage parallel (Γ-ZB$_{\times 2}$-ZB$_{\times 1}$-ZB$'_{\times 2}$ path in (a)) and perpendicular to the gold wires (Γ-M path in (a) and panels (b) and (c)). Surface bands are marked according to its main atomic character: filled circles indicate a strong contribution from the atoms in the SiAu complex, open triangles from the silicon dangling bonds in the middle of the double honeycomb chain (DHC), and open cubes from those silicon atoms at the boundaries of the DHC stripes, neighboring to the gold wires. The energies are referred to the Fermi level.

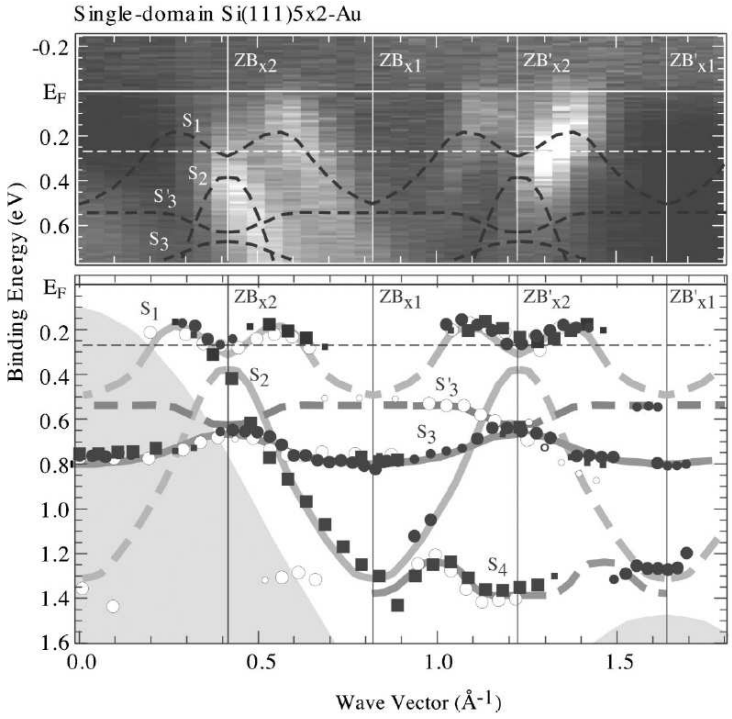

Figure 4.11: Experimental photoemission results. (upper panel) The gray-scale E_B-$k_{||}$ diagram for the single-domain Si(111)5x2-Au surface along the $\bar{\Gamma}_0 - \bar{X}_0$ direction taken from the ARPES scan with He II excitation. In the diagram, the intensities are represented by the brightness, white corresponding to high intensity. The dispersions for the surface states are depicted by black dashed curves. (lower panel) $\bar{\Gamma}_0 - \bar{X}_0$ Dispersions for the single-domain Si(111)5x2-Au surface along the direction. Large and small symbols represent rather distinctive and weak spectral features, respectively. Solid circles (squares) indicate peak positions obtained with the He Iα (He II) excitations. Peak positions taken along the $\bar{\Gamma}_3 - \bar{X}_3$ direction with the He Iα excitation are also shown as open circles. The shaded region is the bulk band structure projected onto the 1×1 surface Brillouin zone. The major surface state bands are traced by thick gray curves. Picture taken from Ref. [23].

and the E(5×2) structures has been confirmed using VASP and slabs containing three and four silicon double-layers. The new model is more stable than the E(5×2) by at least 2.6 meV/Å^2. These results convincingly establish, at least within the framework of density functional calculations, the larger stability of our new structural model compared to previous proposals in the limit of negligible adatom coverage

Model	ΔE_{surf} (meV/Å^2)			
	SIESTA			VASP
	DZ-3 blys	DZ-2 blys	DZP-2 blys	2 blys
E(5×2)	+1.3	+1.4	+1.6	+1.4
E(5×2)*	0.0	0.0	0.0	0.0
N	-3.4	-3.3	-2.5	-1.3
N$^+$	-1.0	-0.6	+0.9	+1.5

Table 4.2: Convergence of the relative surface energies (ΔE_{surf}) of the most stable structural models respect to the basis set and the thickness of the slabs used in the calculations. The first column shows the data obtained with the SIESTA code using a DZ basis for silicon and three silicon bilayers below the surface to construct the slab. In the second column a slab with only two underlying silicon bilayers was used. The third and four columns are obtained using the thinnest slab and, respectively, a DZP basis set for silicon and the VASP plane-wave code.

Model	ΔE_{surf} (meV/Å^2)				
	$x=0$	$x=\frac{1}{4}$	$x=\frac{1}{3}$	$x=\frac{1}{2}$	$x=1$
E(5×2)$^\star_x$	+1.39	+0.90	+0.86	+0.81	0.0
N^+_x	-3.35	-1.98	-1.72	-1.23	-0.60

Table 4.3: Relative surface energies (ΔE_{surf}) of the most stable structural models as a function of x, the number of silicon adatoms per 5×2 unit cell. The calculational parameters here are the same used in Table 4.1. Notice that E(5×2)$^\star_{x=0}$=E(5×2) and N$^+_{x=0}$=N.

Given the small energy differences between both models it may be interesting to estimate the effect of the vibrational degrees of freedom in the surface free energy $\gamma(T)$. The vibrational contribution can affect the energy ordering even at zero temperature due to the zero-point energy, and its importance grows with temperature. Unfortunately, an accurate estimation of the vibrational surface free energy $\gamma_{vib}(T)$ is a formidable task that would require the detailed calculation of the dynamical properties (phonon band structure) of the different surface models. This is a computationally very demanding calculation that is beyond the scope of the present work. We can obtain a rough estimation of the vibrational contribution to the difference of the surface free energies between the different structures $\Delta\gamma(T)$ following Ref. [122]. We have $\Delta\gamma(T) = \Delta E_{surf} + \Delta\gamma_{vib}(T)$, where $\Delta\gamma_{vib}(T) \approx 3N_{Si}^{E(5\times2)}[F(T,\omega_{surf}^{E(5\times2)}) - F(T,\omega_{bulk})]$ - $3N_{Si}^{N}[F(T,\omega_{surf}^{N}) - F(T,\omega_{bulk})]$ + $3N_{Au}[F(T,\omega_{Au}^{E(5\times2)}) - F(T,\omega_{Au}^{N})]$. Here ΔE_{surf} is given in Table 4.1 and is independent of the temperature T; $N_{Si}^{E(5\times2)}$ and N_{Si}^{N} are the number of silicon atoms per unit cell in both surface structures, and N_{Au} the number of gold atoms; $F(T,\omega)$, given in the Appendix of Ref. [122], is the free energy of a given vibrational mode ω; the frequencies ω_{surf}^{N}, $\omega_{surf}^{E(5\times2)}$, and ω_{bulk} characterize the average vibrational properties of the silicon atoms in both surface structures and in bulk silicon, while $\omega_{Au}^{E(5\times2)}$ and ω_{Au}^{N} those of the gold atoms in both surfaces. We take for ω_{bulk} values in the range of 50-70 meV, and ω_{surf} ranging from 0.5 to 1.5 the ω_{bulk} value. Within these range of parameters, if ω_{surf}^{N} and $\omega_{surf}^{E(5\times2)}$ differ less than a ∼10%, then $\Delta\gamma_{vib}(T)$ stays within $\sim \pm 2$ meV/Å^2 for temperatures up to 300 K. If the vibrational properties of both surface models differ more significantly, then

$\Delta\gamma_{vib}(T)$ can affect the relative order of the structures at much lower temperatures. However, we should not expect strong differences in the *average* vibrational frequencies of the E(5×2) and N models. Both models present very similar bonding patterns and structures. It is interesting to notice that $\Delta\gamma_{vib}(T)$ is nonzero even if the vibrational properties of both structures are identical, i.e. $\omega_{surf}^{E(5\times2)}$=$\omega_{surf}^{N}$ =ω_{surf} and $\omega_{Au}^{E(5\times2)}$=$\omega_{Au}^{N}$. This reflects the different number of silicon atoms in the unit cell of the two surface reconstructions. In this case we have $\Delta\gamma_{vib}(T) \approx 3(N_{Si}^{E(5\times2)} - N_{Si}^{N})[F(T,\omega_{surf}) - F(T,\omega_{bulk})]$. Using the same parameters as above we obtain $\Delta\gamma_{vib}(T)$ within $\pm$1.5 meV/Å^2 up to $\sim$1000 K. Thus we can conclude that the energy ordering obtained in the present total energy calculations is not altered by the vibrational contribution to the free energy up to, at least, room temperature.

In the new structure the gold wires along the $[\bar{1}10]$ direction present a dimerization comparable to the E(5×2) structure. The alternating Au-Au distances are 3.24 Å and 4.40 Å (3.19 Å and 4.45 Å) along the right (left) wires. The distance between nearest neighbor Au wires along the $[11\bar{2}]$ direction is smaller in the N structure (3 Å) than in the E(5×2) structure (3.8 Å). The later value being in better agreement with the $\sim$3.9 Å deduced from the HREM studies of the surface. [14]

Similarly to the E(5×1) structure, most of the surface of the N model is covered with a silicon double honeycomb chain structure [67]. One of the silicon atoms in the DHC appears at a higher position over the surface. This indicates that this atom has a charged dangling-bond and, therefore, is trying to develop a sp^3 hybridization. This atom is expected to be more visible in the STM images and to provide a preferential site for adsorption on the surface, in particular for possible silicon adatoms. The boundaries between the DHC stripes are occupied by the SiAu complex, in which a central silicon atom appears bonded with three gold dimers.

The band structure of the new structure is plotted in Fig. 4.10 and the spectra from a very recent photoemission study in Fig. 4.11. The general features are in good agreement with the most recent ARPES studies [23, 24], although some of the details are different. The most dispersive and prominent surface bands are quite similar to those found for the E(5×2) model. The surface is predicted to be semiconducting, which agrees with Fig. 4.11. The bands named S_1 and S_2 by Matsuda *et al.* in Fig. 4.11 can be easily identified in our calculation, and we use the same notation. Other less dispersive surface bands are also observed in our calculated band structure. These can be tentatively identified with those labeled S_3 and S_4 by Matsuda *et al.*. However, the S_3 band appears shifted to lower binding energies by a few tenths of eV. We can relate this upward energy shift to the use of the LDA in our calculations, which is likely to be less suited to describe more localized (less dispersive) states. Besides this energy shift, the sole major discrepancy with the experimental band structure in Ref. [23] is the absence of the S_3' band. However, this band is not so clearly resolved in the experiments as the others.

Different symbols are used in Fig. 4.10 according to the main atomic character of the bands. S_1 and S_2 come from the Si-Au bonds in the surface (solid symbols). This is common to most of the models studied in this paper: the most dispersive surface bands always originate in the Si-Au bonds, with the main character corresponding to the $3p$ states of the central Si atom, and a strong hybridization with the $6p$ states of the neighboring Au atoms. The flat S_3 band corresponds to the silicon dangling bonds in the middle of the DHC structure (open triangles). The also quite flat S_4 band is mainly associated with the bonds between the gold atoms and the silicon atoms in the border of the DHC structure (open squares). We find several unoccupied surface bands whose atomic character is difficult to determine. One of these bands is located at

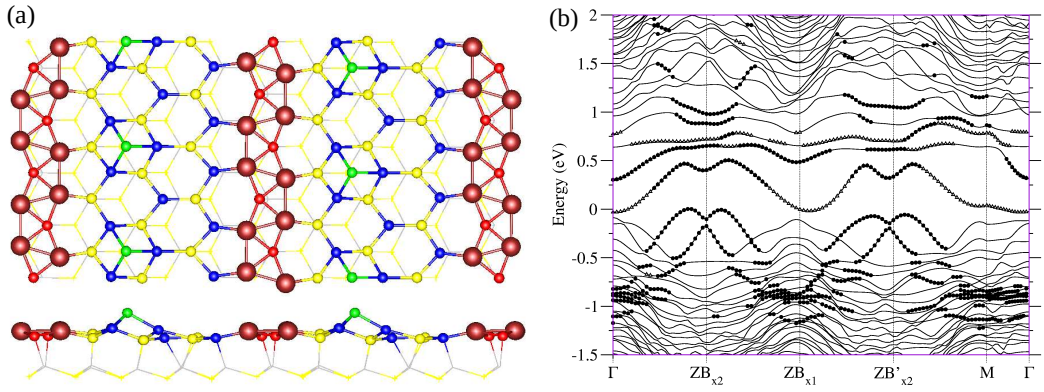

Figure 4.12: (color online). (a) Optimized geometry of the N^+ model (containing one adatom per 5×2 unit cell) and, (b) the corresponding band structure. Surface bands with strong contributions from the SiAu complex are indicated by filled circles, while the states associated to the adatom are marked with open triangles. The energies are referred to the Fermi level.

energies very close to E_F, particularly near the Γ point. The metallic/semiconducting character of the surface is thus governed by the position of this band. This situation is very similar to that already observed for the E(5×2) model, although in this case the band reaches to lower energies and becomes partially occupied driving the system to metallic.

In agreement with experiment, most surface bands show a strong 1D character in our new structural model as can be seen in Fig. 4.10 (b) and (c). This is particularly clear in panel (b), where most states are located within the bulk gap. In the region displayed in panel (c) (at the zone boundary of the 5×1 Brillouin zone) the S_2 and S_1 bands merge with the bulk bands, becoming surface resonances. It is no longer possible to identify the S_1 and S_2 resonances with a single band of our finite slab and, as a consequence, it is difficult to follow the band dispersion of these spectral features in the direction perpendicular to the gold wires. However, from the data in panel (c) it is clear that the combined effect of the possible dispersion, plus the broadening of the resonances extends over a range of $\sim$0.2 eV, much larger than its dispersion for energies closer to E_F. This is broadly consistent with the 1D to 2D transition reported in Ref. [18] for the most prominent photoemission feature as the binding energy increases.

We now explore the structure and energetics of the model N under the addition of one silicon adatom per 5×2 unit cell. We tried several different adsorption sites: directly on the SiAu wire following the proposal by Erwin [67] (referred as $N^\star$), and bonded to the prominent dangling bond in the DHC structure occupying hollow H_3 (N^+) or top T_4 ($N^{+\prime}$) sites [121]. As shown is Table 4.1, this high coverage of adatoms is energetically unfavorable in all cases by at least 2.7 meV/Å^2. This is in contrast with the situation for the E(5×2) model, where the addition of one silicon adatom per unit cell is slightly favorable. In the $N^\star$ structure (not shown) the silicon adatoms tend to locate in a peculiar bridge position between two gold dimers along the $[\bar{1}10]$ direction. The structure of the N^+ model is shown in Fig. 4.12 (a). The silicon atoms bonded to the adatom adopt a typical silicon configuration although, contrary to what is observed for the clean Si(111) surface, the hollow site is preferred over the top site [117].

The band structure of the N^+ surface is shown in Fig. 4.12 (b). It is very similar to that found for the model without adatoms. The S_1 and S_2 are largely unchanged, which clearly indicates its origin in the SiAu complex. The flat S_3 band disappears from the gap region as a

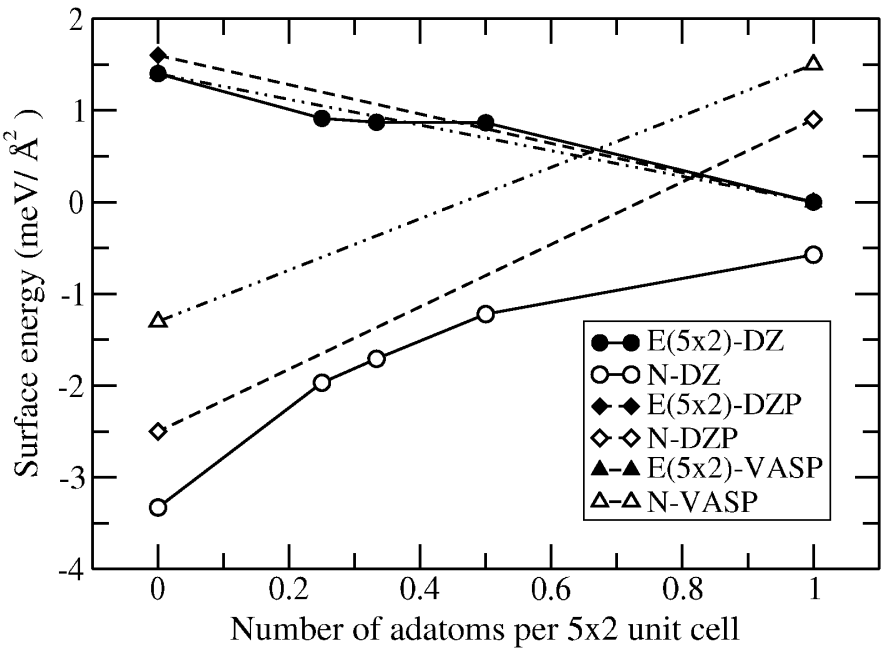

Figure 4.13: Relative surface energies as a function of the adatom content. Explicit calculations have been performed for several adatom concentrations using the smaller DZ basis set (circles). The results obtained with the DZP basis set (diamonds) and with plane-wave VASP calculations (triangles) for the two limiting cases are also shown for comparison. All energies are referred to those of the E(5×2)* model.

consequence of the saturation of the dangling bond with the adatom. A new unoccupied band, associated with the adatoms, appears instead. This new band can be found around ∼0.6 eV above E_F in Fig. 4.12 (b).

4.6 Adatom coverage

So far we have only considered the limiting cases with zero or maximum adatom coverage, which correspond to a number x of silicon adatoms per 5×2 unit cell equal, respectively, to 0 and 1. However, the experimental evidence indicates that the equilibrium concentration is $x \sim 1/4$, corresponding to one adatom per 5×8 supercell. Under silicon rich conditions the adatom coverage can be increased in the experiment only up to $x \sim 1/2$, consistent with a 5×4 periodicity (see Fig. 4.14). We have performed explicit calculations for $x = 1/2$, $x = 1/3$, and $x = 1/4$ for our two most stable models of the reconstruction in order to simulate these situations that can be reached experimentally. Due to the very large supercells necessary for these calculations (up to 273 atoms), we have performed them with the SIESTA code and restricted to the use of a DZ basis set for silicon. The results of the energetics as a function of the adatom content can be found in Table 4.3 and in Fig. 4.13. The behavior is opposite for both models, N and E(5×2). It should be kept in mind that model N favors the adatoms in hollow sites over the silicon surface, while in the E(5×2) structure the adatoms sit on the gold chains are more favorable.

The surface energy monotonously decreases as a function of the number of adatoms for the E(5×2) model. We do not find any evidence of an energy minimum as a function of the

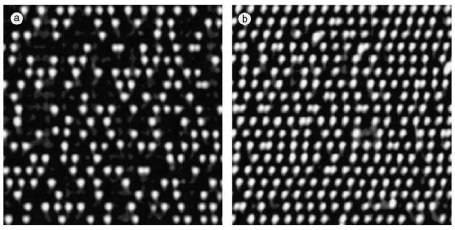

Figure 4.14: STM images of (a) Si(111)5x2-Au in thermal equilibrium and (b) after additional evaporation of 0.025 ML of silicon at 300 C. About 90% of all 5x4-cells are filled (-2 V, 0.2 nA, 30 x 30 nm^2). Picture taken from Ref. [21].

adatom concentration. This is in contrast with the suggestion made by Erwin in Ref. [67]. In that reference the addition of adatoms was studied using the following simplification: it was assumed that the sole effect of the adatoms is to dope the gold chains with electrons and the energy of the system was studied as a function of the doping. Erwin found a minimum of the total energy for 0.5 extra electrons per 5×2 unit cell. Since each adatom was found to donate two electrons to the surface, this would correspond to the observed adatom concentration at equilibrium of $x \sim 1/4$. However, our simulations introducing explicitly the adatoms in the structure do not confirm this behavior. The surface energy of the E(5×2) structure always decreases as the adatom concentration is increased. However, the slope of the curve becomes very small for intermediate adatom concentrations, showing a weak dependence of the surface energy in that region. We cannot completely rule out the presence of a minimum for the surface energy at very low adatom concentrations. However, it seems quite unlikely looking at Fig 4.13. It could also be argued that the DZ basis set is not flexible enough to produce the correct behavior. This seems quite improbable looking at the data in Table 4.2, which clearly show that the energy changes induced by the addition of adatoms are weakly dependent on the details of the calculation.

In the case of the new model N, the Fig. 4.13 shows that the surface energy systematically increases as a function of the adatom concentration. With the DZ basis set the N model is always more stable than the E(5×2) structure. Using a more complete basis set and a converged plane-wave calculation we find a crossing: the new model is always more stable at low adatom coverage, but becomes unstable compare with the Erwin “5×2" model at larger coverages. Scaling the data calculated with the DZ basis set to reproduce the VASP results at the end points (i.e. $x = 0$ and $x = 1$) we can estimate that the crossing occurs at $x \sim$1/2. We can conclude then that the N model is, at least in the framework of density functional calculations, more favorable than the E(5×2) model for adatom concentrations below ∼1/2 adatoms per 5×2 cell.

4.7 Simulated STM images

The STM images of the Si(111)-(5×2)-Au surface are characterized by the presence of bright “protrusions" (see Fig. 4.14 and Fig. 4.15) and “Y"-shaped features with a definite orientation respect to the underlying lattice [11, 17, 25]. This can be seen in Fig. 4.15, with the protrusions labelled by P. It seems quite well established that the protrusion correspond to silicon adatoms [20–22], illustrated in Fig. 4.14. However, the origin of the “Y"-shaped features,

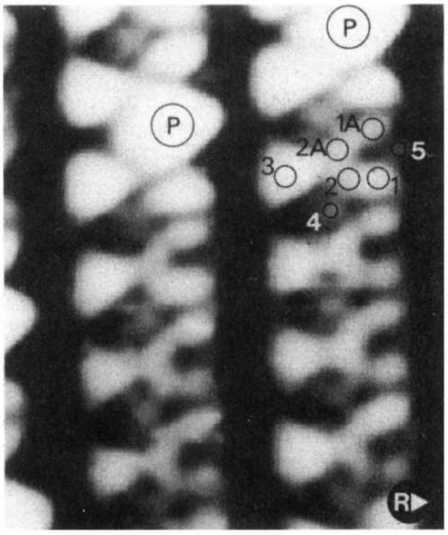

Figure 4.15: An experimental 35 Å×Å image of the slightly skewed Y structure unit seen in the filled states of the 5×2 rows. The topograph was taken at -0.4 V sample bias and 1.2 nA tunneling current. The main repeating features are labeled and R indicates the $[\bar{1}\bar{1}2]$ direction. Picture taken from Ref. [11].

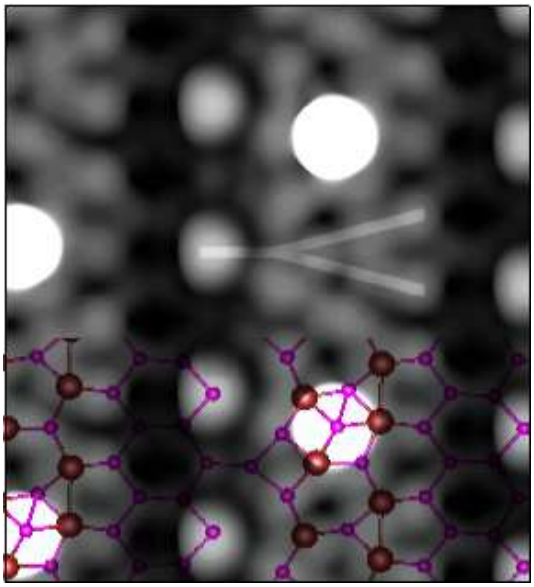

Figure 4.16: (color online). Simulated STM image of the E(5×2) model with a sample bias of -0.8 eV and an adatom concentration corresponding to a 5×4 periodicity. A possible candidate for the Y-shaped structure is schematically indicated. The atomic structure is superimposed with the simulated image in the lower part of the figure. Large circles indicate the positions of Au atoms.

illustrated in Fig. 4.15, is less clear.

Figures 4.16 and 4.17 present our simulations of the STM images for the E(5×2) model at -0.8 eV sample bias and the N model at -0.6 eV, respectively. The simulations have been performed for a 5×4 arrangement of the silicon adatoms, corresponding to concentration of adatoms that can be actually reached in the experiment. In agreement with Ref. [67] and the experiments the silicon adatoms show as very pronounced bright protrusions. With the adatoms directly sited on the gold chains, the bright spots appear in the middle of the under-

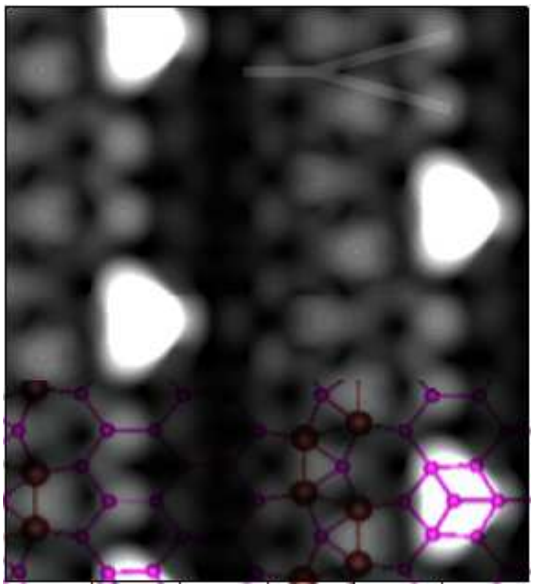

Figure 4.17: (color online). Same as Fig. 4.16 but for the new N structure and a sample bias of -0.6 eV.

lying row structures for the E(5×2) model. For the N model they appear in a more lateral position. This seems to be in somewhat better agreement with some of the experimental images (see, for example, the Figure 1 (b) in Ref. [22]). “Y"-shaped features can be identified in the simulated STM images of both N and E(5×2) models. The possible candidates have been highlighted in the Figures 4.16 and 4.17 (see also Ref. [67]). The identification is, however, more clear in the case of the less symmetric E(5×2) structure.

4.8 Conclusions

We have performed a systematic study of different models of the Si(111)-(5×2)-Au surface reconstruction by means of first-principles density-functional calculations using the SIESTA [84, 86] and the VASP [118, 119] codes. We start our investigation with the structural model proposed by Marks and Plass [14] (MP). This is the most detailed model of this surface reconstruction solely based on experimental information to date. Therefore, it provides a logical starting point for our study. We have also considered different variants of the relaxed MP model, including the structures recently proposed by Erwin [67], and a new structure found during our simulations. Within the computational schemes used here this new structure is the most favorable energetically, at least in the regime of low concentration of silicon adatoms. In general, we find a reasonable agreement between our results and those of the two existing theoretical studies of the surface [67, 68]. The energy differences between different models are quite small, with most structures lying in a narrow range of surface energies of less than 10 meV/Å^2 (the estimated error bar for our energies is of the order of 1-2 meV/Å^2). This, together with the uncertainties arising from the use of the local approximation to the density functional theory, make difficult to draw definitive conclusions solely based on the energetics. The comparison of the calculated band structures and local density of states, respectively, with the available ARPES data [18, 23, 24] and the STM images [6, 11, 25] becomes then instrumental in order to identify the most plausible candidates for the equilibrium structure. In the

following we summarized some our main conclusions:

i) Like in the case of the reconstructions formed by the deposition of gold on stepped silicon surfaces [1, 29, 69, 70], the silicon honeycomb chain (HC) [66] structure emerges as a fundamental building block of the reconstruction. In agreement with the result of Hang and Lee [68], the silicon HC is formed spontaneously during the relaxation of the MP model. The HC is also present in the optimized geometries of all the other structural models considered in our work.

ii) For the MP model we agree with the main conclusions of Ref. [68] that neither the simulated STM images nor the calculated band structure compare satisfactorily with the experimental data.

iii) We have studied in detail the models proposed in Ref. [67] by Erwin, the E(5×1) and E(5×2) structures. The E(5×1) model is quite similar to the MP structure: they correspond to two possible positions, at opposite sides of the SiAu complex, of the surface dislocation present in these structures. The E(5×1) model and its E(5×2) variant are energetically degenerate at zero adatom coverage. However, these two structures show a different behavior against the addition of silicon adatoms: it is always unfavorable for the E(5×1) model, while tends to increase the stability of the E(5×2) model.

iv) We have explored a different position of the surface dislocation: at the center of the SiAu complex. We arrive in this way to a new structure, the N model. According to our calculations this new structure is more stable, at least for low coverages of silicon adatoms, than any of the models proposed to date. The distance between the gold wires in this model is ∼3 Å, which seems somewhat small compared to the ∼3.9 Å deduced from the HREM measurements [14].

v) The calculated band structures of the E(5×2) and N models without adatoms are quite similar and appear to be in reasonable agreement with the available ARPES data [18, 23, 24]. The other models fail to reproduce the main features observed experimentally. The agreement seems to be particularly good in the case of the N model. According to our analysis the most prominent and dispersive surface bands, named S_1 and S_2 in Ref. [23], come from the atoms in the SiAu complex. In the case of the N model the silicon adatoms tend to adsorb on the silicon part of the surface, i.e. bonded to three silicon atoms in the surface layer. As a consequence, the topology and the energy position of these bands are quite insensitive to the coverage of silicon adatoms. This contrast with the situation found for the E(5×2) model. Here the silicon adatoms tend to adsorb directly on the SiAu complex, thus causing a notable modification of the surface bands that worsens the agreement with the experimental ARPES spectra.

vi) We have studied the energetics of the E(5×2) and the N models as a function of the concentration of silicon adatoms. Contrary to the suggestion of Ref. [67], we do not find any evidence of a minimum of the surface energy of the E(5×2) model as a function of the adatom coverage. The surface energy always decreases with the addition of adatoms, although the changes are very small in the range of x between 1/2 and 1/4, where x is the number of adatoms per 5×2 unit cell. For the N model the addition of the adatoms is always unfavorable. As a consequence of this opposite behavior, the E(5×2) structure becomes more stable than the N structure in the limit of relatively large adatom $x = 1/2$ corresponds to a 5×4 periodicity). According to this picture the exact content of adatoms is instrumental to determine the equilibrium structure of the reconstruction within the range of experimentally realizable adatom coverages. This introduces a new degree of complexity that should be taken into account when analyzing the experimental information. In particular, this might be behind the

observed phase separation into 5×4 and 5×2 patches [22, 24].

vii) The simulated STM images of the most stable models, N and E(5×2), are in broad agreement with the experimental images. The silicon atoms produce bright spots which are located in the middle of the underlying row structures for the E(5×2) and in a somewhat more lateral position for the N model. In both cases “Y"-shaped features similar to those observed in the experiment can be found. However, they are more clear in the case of the E(5×2) model [67] where the structure surrounding the gold chains is less symmetric.

Chapter 5

Si(111)4x1-In

5.1 Introduction

As was mentioned in Sec. 3.1, coupling between electronic and structural degrees of freedom are enhanced in one-dimension and, as a consequence, several electronic and structural phase transitons are observed in the metal-induced quasi one-dimensional surface reconstructions as the temperature is decreased. A nice example of this behaviour is found in the In/Si(111) system, which exhibits a $4\times1 \rightarrow 4\times2 \rightarrow 8\times2$ structural transition accompanied by a metal-insulator electronic transition.

The room-temperature (RT) 4×1 structure of the In/Si(111) surface is well established [43, 49]. It is illustrated in Fig. 5.1 and consists of two neighboring zigzag In wires along the $[11\bar{2}]$ direction. Each wire contains two In atoms per 4×1 cell and each In atom is bonded to one Si atom of the substrate. This model has been confirmed by *ab-initio* calculations [72–74] which reproduce the scanning tunneling microscopy (STM) images [41, 42], and the main features of the band structure.

At RT the system presents three metallic surface bands with similar dispersion [40]. However, when the temperature is lowered below ~ 130 K [45] photoemission shows the formation of a band gap (this is illustrated in Fig. 5.3). This transition is accompanied with a doubling of the unit cell in the STM images [45]. The low temperature (LT) phase has been widely studied experimentally [46, 48, 54, 55]. However, most *ab-initio* calculations have failed to reproduce the observed LT behaviour [72, 76].

Recently, an interesting mechanism for the gap opening has been proposed by Ahn *et al.* in Ref. [52]. The occupation of the surface bands in the 4×1 structure is quite close to two electrons. If one of these bands is depopulated (the upper one), the other two become very close to half-filled and thus are suitable to suffer a Peierls transition due to a periodicity doubling. If this is true, it seems to indicate that: (*i*) there are at least two types of surface bands that originate in different regions of the substrate or have different symmetries, and (*ii*) the metal-insulator transition is the result of a combination of two distinct structural distortions that couple with different bands. This last point is consistent with the recent first-principles calculations by González *et. al.* [77]. These authors find an insulating 4×2 structure (see Fig. 5.2) reminiscent of that proposed by Kumpf *et al.* [43], as a result of a combined shear and Peierls distortion of the 4×1 RT phase.

The objective of the present chapter is to understand in detail the origin and characteristics

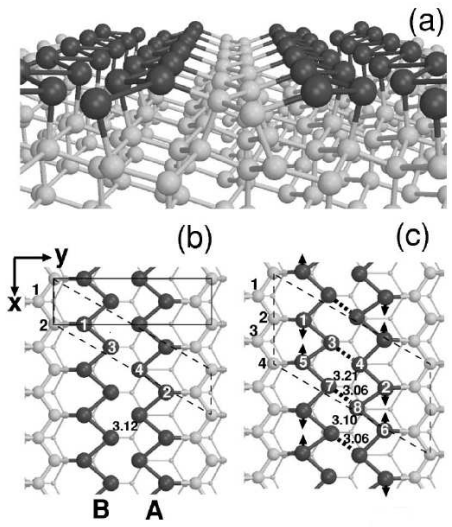

Figure 5.1: Equilibrium structure of In/Si(111): (a) the perspective view of the (4x1) structure and the top views of (b) the (4x1) structure, (c) a possible candidate of the (4x2) structure. The dark and grey circles represent In and Si atoms, respectively. The x and y directions are $[\bar{1}\bar{1}0]$ and $[11\bar{2}]$, respectively. Two different choices for the (4x1) unit cell are indicated by the thin solid and dashed lines. The arrows in (c) show pairing patterns of the outer indium atoms. The interatomic distances between the two zigzag indium rows are given in Å. Picture taken from Ref. [72].

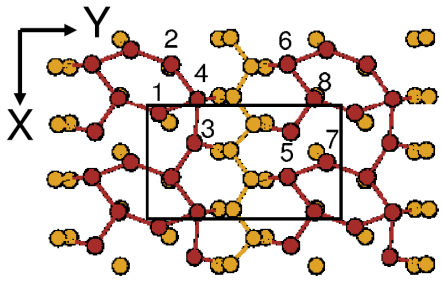

Figure 5.2: The low temperature Si(111)/In-4x2 surface according to González et. al. [78]. Top view of the surface, in which dark (pale) circles represent In (Si) atoms. The x and y directions are $[\bar{1}\bar{1}0]$ and $[11\bar{2}]$, respectively.

of the different electronic states involved in the metal-insulator transition, and how they couple to different structural distortions. The emphasis is on the electronic bands associated with the indium atoms in the substrate. We use a simplified model (shown in Fig. 5.4) that captures the essence of the system. Our results support the main conclusions of Ref. [77], and point to a primary electronic origin of the structural transition. Of course, in the real surface we can expect a delicate competition between the gain of electronic energy and the elastic energy associated with the different distortions.

The pseudopotentials and basis-set used in this chapter, are indicated in Tab. 2.2 and they correspond to the GGA versions `Si2.psf`, `H2.psf` and `In3.vps`. For the model system of Sec. 5.2, DZP bases were used. We typically used 12 inequivalent k-points along the axis of the wire (up to 250 in convergence tests, and 100 in the calculations shown in Fig. 5.7).

The results of this chapter have been published in Ref. [109].

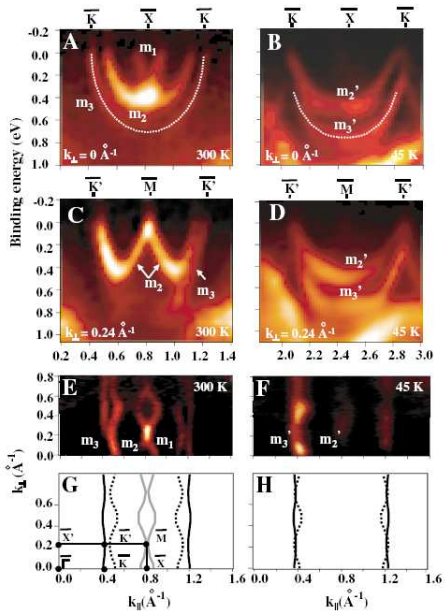

Figure 5.3: Measured energy bands of In/Si(111) along the wires ($k_{||}$) in the metallic state (RT) at two different $k_\perp$ of 0 (a) and 0.24 Å^{-1} (c) and in the insulating state (45 K) (b),(d). Constant-energy spectral density maps at EF showing the Fermi contours for the metallic states (e) and at a binding energy of 0.1 eV for the valence band maxima of the insulating phase (f), which are schematically depicted in (g) and (h), respectively. The first BZ of the 4×1 phase is drawn by the thin solid lines in (g). The wiggling Fermi contours (g) and the varying band dispersions at different $k_\perp$'s (a),(c) of m1 and m2 manifest the deviation from an ideal 1D nature in contrast with m3. Picture taken from Ref. [52].

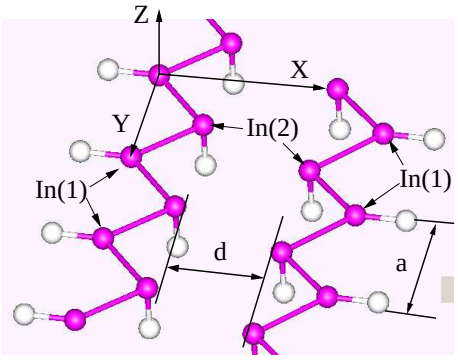

Figure 5.4: Our model of the In wires in the In/Si(111)-4×1 surface: it contains two zigzag indium wires saturated with hydrogen.

5.2 The Simplified model

Figure 5.4 presents the simple model used here to study the electronic properties of indium wires in the In/Si(111) surface. We keep the two zigzag In wires present in the 4×1 unit cell, and substitute the neighboring silicon atoms with hydrogen. The In-H distances were optimized (1.86 Å), and kept fixed for the rest of the study. The In-H bond is more ionic than the In-Si bond. However, we have checked that saturating with SiH_3 groups instead of H atoms leads to a very similar band structure.

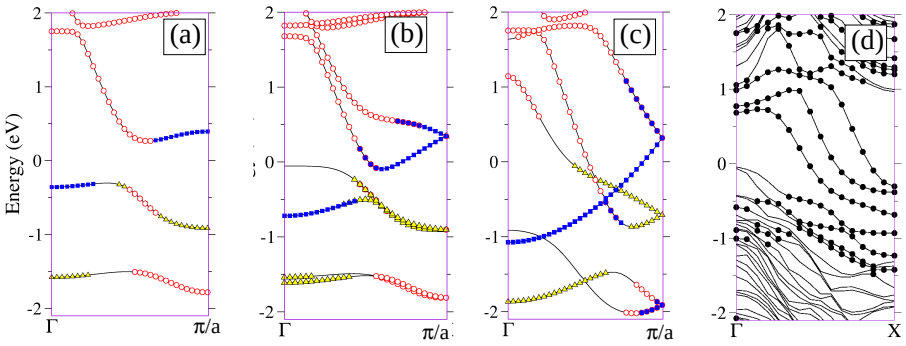

Figure 5.5: (a)-(c) Band structure (along the wires axes) of the system shown in Fig. 5.4 as a function of the wire-wire distance d: (a) isolated zigzag In wire (d=10.8 Å), (b) d=4.31 Å, and (c) d=2.15 Å. Different symbols indicate the distinct character of the bands as determined from a Mulliken population analysis [100]: In(1) and In(2)-p_y (circles), In(2)-p_x (squares), and In(1) and In(2)-p_z (triangles). (d) Band structure of the In/Si(111)-4×1 reconstruction (see Fig. 5.1) along the $[11\bar{2}]$ direction calculated with a slab containing four silicon bilayers, the bands with strong indium character are highlighted with circles. Energies are always referred to the Fermi level.

5.3 Coupling of Indium wires

Figure 5.5 shows the evolution of the band structure of our model as a function of the wire-wire distance d. There are two types of indium atoms in each wire, In(1) and In(2). The coordination of the In(2) atoms changes with d. Panel (a) corresponds to non-interacting (large d) zigzag wires, while panel (c) (d=2.15 Å) corresponds to a configuration similar to that found in the In/Si(111)-4×1 reconstruction. Although not completely evident due to appearance of interaction gaps, the band structure in Fig. 5.5 (a) can be rationalized in terms of three bands: (I) a strongly dispersive band associated with the In(1) atoms and the In(2)-p_y orbitals (circles), a flat band (II) with a clear contribution from In(1) and the In(2)-p_z orbitals (triangles), and another flat band (III) with large In(2)-p_x character (squares). Taken into account the hydrogen saturation, each In atom contributes with two valence electrons. Thus we have four electrons two distribute in these bands. Band (II) is doubly occupied and does not play any role in the argumentation below. Bands (I) and (III), however, are half-filled. Band (III) can be associated with the "dangling-bonds" in the In(2) atoms that project approximately into the x-direction and the vacuum.

As d is reduced, the interaction between the wires modifies the band structure. This can be seen in Fig. 5.5(b) and (c). Particularly, the dispersion of bands derived from band (III) largely increase as a result of the overlap of the dangling-bonds in the neighboring wires. Finally, the electronic states associated with this band become highly delocalized in the region between the two zigzag wires, and the band exhibits an almost free-electron dispersion. In the following we call this band the "interaction band".

Figure 5.5 (d) presents the band structure of the In/Si(111)-4×1 reconstruction calculated with a slab containing four silicon bilayers. Four surface bands can be located in the gap of the silicon substrate. Three of them cross the Fermi level with similar dispersions. This is qualitatively reproduced by our model. The agreement is improved if a small shift of the Fermi level is allowed (see Fig. 5.5 (c)). The information from our model allows to catalogue the surface bands in two types: (*i*) two bands that are derived from the band (I) of the right and left wires, and (*ii*) the interaction band. The first two bands have a larger weight *inside*

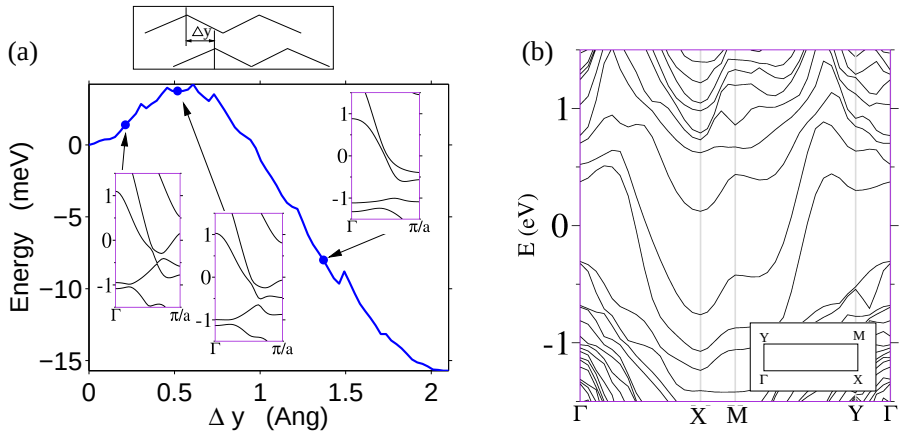

Figure 5.6: Shear distortion. (a) Energy per indium atom as a function of the relative displacement Δy of the indium wires along their axes (see the scheme in the upper part of panel (a)). The band structures for three different values of Δy are also shown. (b) Band structure of the In/Si(111)-4×1 reconstruction with Δy=1.65 Å. The inset shows the Brillouin zone, ΓX and YM run along the In wires. Energies in the band structures are referred to the Fermi level.

each of the wires and are quite sensitive to the structure of the zigzag chains. In contrast, the interaction band is localized in the region *between* the two zigzag wires and thus is more influenced by the relative positions of the wires.

This division allows to envision a two-step route for the observed metal-insulator transition. Step one: the dimerization of the dangling-bonds from neighboring zigzag chains opens a gap in the interaction-band. This effect can be obtained without doubling the periodicity of the system, the relative displacement of the wires along their axes (see Fig. 5.6) suffices. Notice that this corresponds to the shear distortion in Ref. [77]. Step two: the remaining metallic bands need to accommodate two valence electrons. Since these two bands have very similar dispersions, both become approximately half-filled. As a consequence, the system is now suitable to suffer a Peierls transition. This two-step mechanism is consistent with the calculations of Ref. [77] and the experimental evidence in Ref. [52].

Figure 5.6 (a) shows the evolution of the energy and the band structure of our system as function of the shear distortion. One of the zigzag wires was displaced along the y-direction by a magnitude Δy with respect to the other. For each displacement the distance between the wires d was optimized. A gap is opened in the interaction band which widens with increasing Δy. For distortions larger than Δy ∼0.5 Å the Fermi level enters in this gap. This is reflected in the behaviour of the energy that starts to decrease at this point. This behaviour translates in an energy barrier of ∼5 meV per In atom. The system is then left with two metallic bands that cross the Fermi level at nearby points in reciprocal space. This is also the case for the real In/Si(111)-4×1 surface as can be seen in Fig. 5.6 (b). However, in this case the behaviour of the total energy is different. Although still in the range of a few meV per In atom for moderate distortions, the shear deformation always increases the energy of the system.

5.4 Distortion of the wires

We now study the effect of doubling the periodicity along the wires. We consider a quite simple Peierls-like distortion: the length of one every four bonds is shorten (the undistorted

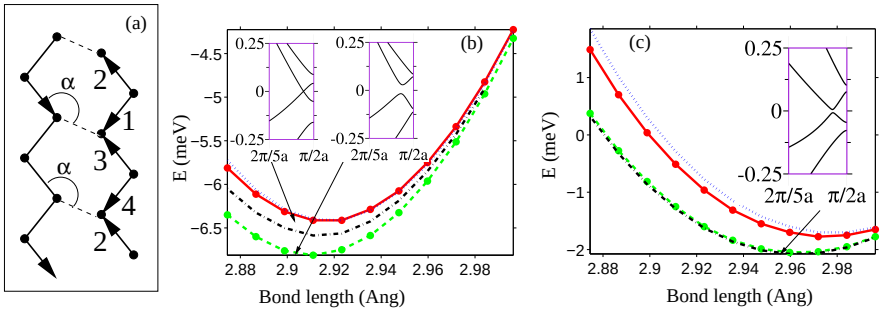

Figure 5.7: Peierls distortion. (a) Scheme showing four inequivalent Peierls-like distortions: the lenght of one of the bonds (indicated by an arrow) is modified by the same amount in both wires; different distortions correspond to different relative positions of the distorted bonds and are numbered according to the labels of the different bonds in the right wire. Panels (b) and (c) show the total energy per indium atom as a function of the modified bond length for distortions 1 (solid), 2 (dashed), 3 (dotted), 4 (dash-dotted). Panel (b) corresponds to α=90° (Δy=2.15 Å), while in panel (c) α=154° (Δy=1.05 Å). The insets show the band structures close to the Brillouin-zone boundary for distortions 1 and 2 in panel (b), and 2 in panel (c). Energies in the band structures are referred to the Fermi level.

bond length is 3.045 Å). The distortion is identical for both wires. Still we have four different possibilities according to the different relative locations of the distorted bonds in the neighboring wires. This is illustrated in Fig. 5.7 (a). While doubling the unit cell, the four distortions break the symmetry of the system in different ways. This detail is quite important. The distortions open a gap at $\frac{\pi}{2a}$ due to the periodicity doubling. However, since the Fermi points do not exactly lie in that position, this does not guarantee that the system will become semiconducting. This is more clear for the extreme shear distortion (Δy=2.15 Å, α=90°). In this case there is a mirror plane parallel to the axis of the wires which is only preserved by "distortion 1". As a consequence of this symmetry, the band structure of the system submitted to the "distortion 1" presents a band crossing and the system remains metallic. For the other three distortions the band crossing is avoided due to the break of symmetry and a gap opens at the Fermi level. This can be appreciated in Fig. 5.7 (b). For $\alpha \neq$90° the symmetry gap is always opened, although its magnitude depends again on each particular structural distortion. Figures 5.7 (b) and (c) present the total energy for the different Peierls-like distortions (a shear deformation has been previously applied to the system). "Distortion 2" and "distortion 4" are always the most favorables. It is worth noting that the structure proposed in Ref. [77] can be understood as the result of applying a combination of a shear distortion and the Peierls-like "distortion 2" presented above.

5.5 Conclusions

In summary, we have studied the electronic structure of the indium zigzag wires seen on the In/Si(111)-4x1 reconstruction. The different surface bands are identified and classified according to their origin and their response to different structural distortions. We confirm that the combination of a shear and a Peierls distortion, proposed in Ref. [77], provides a reasonable and robust route for the observed metal-insulator transition in this system. Our results also point to an electronic driving force of this transition.

Chapter 6

Si(557)/Au

6.1 Introduction

Probably, the first observation of gold-induced ordering on the Si(557) surface was performed by Jalochowski et. al. [26] and has attained lot of interest in recent years [19, 27, 29, 30, 32–34, 36–38, 58, 62, 69, 70]. The present geometrical model is base on x-ray diffraction studies [29] and *ab-initio* calculations [69, 70] and is illustrated in Fig. 6.1. The terraces of Si(557)/Au have a width of $\sim$19 Å (or 11 atoms) and each terrace contains a monatomic chain of gold atoms running parallel to the step-edge. Because of its one-dimensional features, the Si(557)-Au surface has been proposed as an experimental realization of a one-dimensional metal [27], one of the main motivations why it has been subject to such an intensive research. In spite of all the effort, the electronic structure of this system is not yet completely understood.

The first angle-resolved photoemission (ARP) study by Segovia *et al.* [27] found a spectrum dominated by a one-dimensional metallic band. This band was shown to split in two peaks near the Fermi level (E_F), and this was interpreted as signature of separated charge and spin low-energy excitations as predicted by Luttinger theory of the one-dimensional electron gas [105, 106]. However, later photoemission data seemed to discard this interpretation. According to Losio *et al.* [19] (see also Fig. 6.3 and Fig. 6.4) the observed splitting would correspond to two distinct proximal bands which cross E_F at neighboring, although different, positions of the surface Brillouin zone. However, the origin of these bands was unclear. Finally, Ahn *et al.* [30] have recently suggested that only one of the bands is truly metallic and suffers a metal-insulator transition upon cooling. This observation was correlated with the temperature dependence of the scanning tunneling microscopy (STM) images: the step-edge undergoes a periodicity doubling consistent with a Peierls-like instability (see Fig. 6.11). Thus these authors concluded that at least one of the two proximal bands should be associated with the atoms forming the step-edge.

In contrast with the electronic structure, the geometry of the Si(557)-Au reconstruction seems to be quite well established. A detailed model was proposed by Robinson *et al.* [29] on the basis of X-ray diffraction data, which has been corroborated by first-principles density functional (DFT) calculations [70] (see Fig. 6.1). Unfortunately, the calculated band structure only presents *one* one-dimensional metallic band exhibiting a considerable dispersion and a width consistent with the experimental observations [70]. Thus, the observed two-band photoemission spectrum remains unexplained from a theoretical point of view.

We will demonstrate in Sec. 6.2 with DFT calculations, that the observed ARP spectra is consistent after all with the model geometry and that the two proximal bands appear as a consequence of the spin-orbit (SO) splitting of the most dispersive surface state. The large effect of SO splitting on gold-derived surface states has been demonstrated previously by ARP experiments and calculations on Au(111) [123,124]. The origin and magnitude of the SO splitting is similar in the present case. The inversion symmetry is always broken at the surface, thus the spin splitting of bands with no spatial degeneracy becomes possible. This suggests that atomic wires formed by heavy atoms deposited on semiconducting surfaces could be used in the fabrication of spin transistors [125] and spin-filter devices [126]. Interesting phenomena can also appear associated with the competition between electron-electron interactions and SO coupling in one-dimension [127, 128].

The SO model has received some experimental support recently. Measurements of the plasmon dispersion in the Si(557)-Au surface by Nagao *et al.* [36] point to the importance of the SO interaction in this system. Furthermore, very recent photoemission measurements in the Si(553)-Au surface, which shows a band structure very similar to the Si(557)-Au reconstruction [1] (one can compare Figs. 6.3 and 7.1) seem to confirm that the origin of the two proximal bands is the SO splitting [62]. However, the authors of this reference arrived to this conclusion based on the observed pattern of avoided crossings in the band structure. This indirect method was used by Himpsel and coworkers [62] since the requirements of energy and angle resolution are difficult to combine with the low count rate imposed by spin detection. Thus the band structure of the Si(557)-Au surface is still a matter of certain debate that needs further experimental and theoretical work to be fully understood.

In Secs. 6.3-6.4 we show how the temperature dependence of several experimentally measurable quantities [30, 33, 34], such as Scanning-Tunneling Microscopy (STM) and Spectroscopy (STS) images, projected Density of States (PDOS) and Local Density of States (LDOS) could stem from the buckling of the step-edge whose atoms alternate between up and down positions. A given "up-down" configuration and the reverse one are separated by a small energy barrier. At room temperature the step-edge fluctuates between both structures, and for example the STM images only reflect the average surface electronic and atomic structure. Upon cooling the step-edge buckling can be revealed using STM, producing the apparent doubling of the periodicity. This implies a Peierls-like phase-transition. However, the order-disorder (freezing of “dynamical fluctuations”) or displacive (Peierls-like) character of this transition is still a matter of certain debate [33, 71, 103]. Due to the nature of the structure, we initially favored an order-disorder model. However, this might be in conflict with some of the observations made during the metal-insulator transition that accompanies the structural distortion [33, 71]. This aspect is discussed in detail in Sec. 6.3.

In Sec. 6.5 we also perform Molecular Dynamics (MD) simulations in the timescale of picoseconds and observe that the step-edge indeed fluctuates with the periodicity of ~ 0.5 ps. This movement is accompanied with several other atomic movements that contribute to the metallicity of the system at high temperatures, backing up our explanation of the metal-insulator transition.

In this chapter, both the DZ and DZP basis for silicon were used, while the DZP:s-SZ:d basis-set was used for gold. The pseudopotentials and pseudo-orbitals correspond to the LDA-flavour, i.e. to `Au.vps`,`Si.psf` and `H.psf` in Tab. 2.1.

The results presented in this chapter have been presented in two publications, Ref. [71, 103].

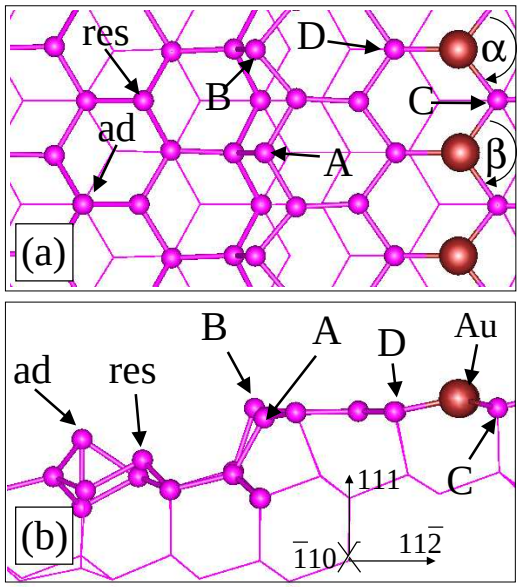

Figure 6.1: Top (a) and side (b) view of the structure of the Si(557)-Au reconstruction. The larger circles (Au) correspond to the gold atoms. The most prominent features of the surface are highlighted: a row of adatoms (*ad*), restatoms (*res*), a buckled step-edge with up-edge (B) and down-edge (A) Si atoms, and a chain of gold atoms with alternating Si-Au-Si bond angles (α and β).

6.2 Effect of the spin-orbit interaction

Fig. 6.1(a) shows the relaxed structure of the Si(557)-Au reconstruction [69, 70]. This structure is almost identical to the experimentally proposed model [29]. The atoms labelled with "Au" stand for the gold atoms occupying silicon substitutional positions on the middle of the terraces. The corresponding band structure, along the direction parallel to the steps, is shown in Fig. 6.2. Panel (a) shows the results from a non spin-polarized calculation, using the VASP [118] code, with the local density approximation (LDA) for the exchange-correlation potential. This band structure is almost identical to that reported in Ref. [70] using the SIESTA code. Several surface bands and resonances can be identified, all of them with negligible dispersion in the direction perpendicular to the steps. The different symbols reflect their main atomic character (see Sec. 2.4.2). The unoccupied band marked with open triangles comes from the adatoms (labeled *ad* in Fig. 6.1(a)), while the occupied one is related to the restatoms (labeled *res*). In principle, every atom in the step-edge has a dangling-bond pointing perpendicularly to the step, which would give rise to a very flat half-filled band. This unstable situation leads to a buckling of the step-edge that doubles the unit cell and forms two bands marked by open squares in Fig. 6.2. The band with larger weight in the "up" (B) atoms is fully occupied, while the band associated with the "down" (A) atoms has a small occupation. Notice that the step-edge bands have a very small dispersion. Thus they cannot explain the observed ARP spectra, as was recently suggested by Ahn *et al.* [30]. Contrary to the initial interpretation of the ARP data [27], none of the surface bands in the proximity of E_F has a clear Au 6*s* character. This is a direct consequence of the larger electron affinity of gold as compared to silicon: the 6*s* Au character appears several eV below E_F. The sole surface bands exhibiting an appreciable gold component in Fig. 6.2 are marked with circles.These bands mainly come from the 3*p* states of the silicon atoms neighboring to the Au chains (atoms D and C).

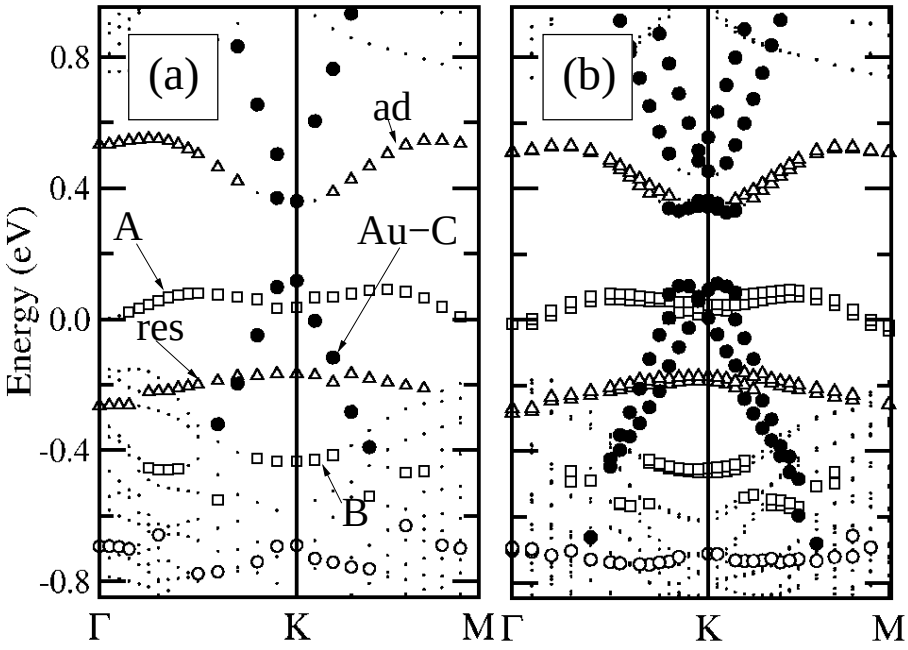

Figure 6.2: Electronic band structure for calculation not including (a), and including (b) the spin-orbit interaction. Energies are referred to the Fermi level. Surface states have been marked with different symbols according to their main atomic character (see text).

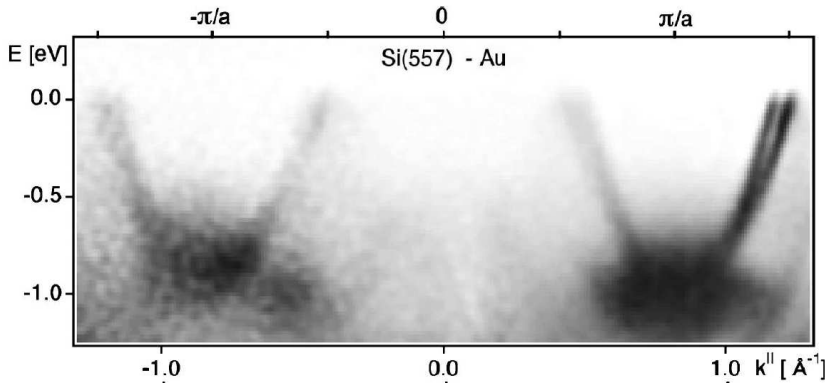

Figure 6.3: E($k^{||}$) band dispersions of surface states along the [1$\bar{1}$0] direction, which is parallel to the chains. High photoemission intensity is shown dark. The right/left asymmetry is due to different polarization of the photons, with the perpendicular component of A large at positive $k^{||}$. Picture taken from Ref. [19].

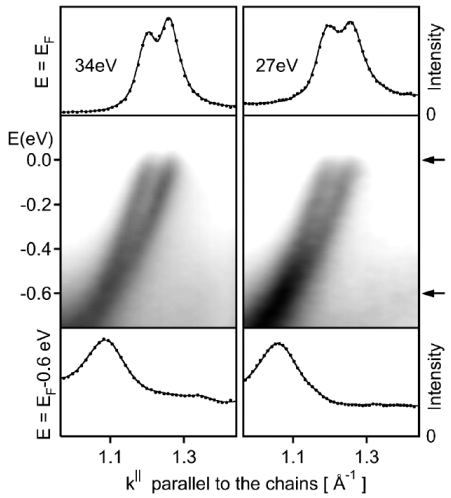

Figure 6.4: Experimental band dispersion of the metallic surface state on Si(557)-Au near the Fermi level E_F, measured by E, k multidetection (center). High photoemission intensity is shown dark. Two nearly degenerate bands are observed with a splitting that increases towards E_F. Picture taken from Ref. [28]

However, they also show a strong contribution from the 6*p* states of gold, so they are better assigned to the Si-Au bonds. We find a flat band (open circles) associated with the Au-Si_D bonds, and a dispersive (filled circles) corresponding to the Au-Si_C bonds. This last band is the *only one* that presents a dispersion and width consistent with the photoemission data.

Fig. 6.2(b) depicts the same band structure once the effect of the SO interaction has been included in a non-collinear spin calculation. We still get a non spin-polarized ground state. The changes are negligible for most surface bands. This is expected since most of them are localized in regions far from the gold atoms or have a very small dispersion, i.e. small group velocities. However, the dispersive Au-Si_C band develops a considerable SO splitting. This brings the calculated band structure in reasonable agreement with the experimental spectra. The experiments [19, 28, 30] show a $\sim$300 meV splitting near E_F (see Fig. 6.4). This splitting exhibits a linear dependence as a function of $k_{||}$ with a $\sim$1.2 eV Å slope. This can be compared with our calculated $\sim$200 meV splitting at E_F and $\sim$1.4 eV Å slope.

Even though the two SO-split bands are a robust feature predicted for this surface, the states at the Fermi energy are strongly affected by the other bands shown in Fig. 6.2(a) and (b). In our calculations both SO-split bands are metallic; however, there is a band gap just above E_F. This gap relates to the presence of a row of adatoms in the terrace, which induces an alternation of the Si_C-Au-Si_C bond angle between 101.8^o and 109.6^o. The presence of this gap drives the surface very close to becoming semiconducting. The metallicity of the system is due to the very small partial occupation of the upper step-edge band that pins the position of E_F.

If the step-edge band is lifted by $\sim$0.1 eV the surface becomes insulating in agreement with some of the most recent experimental observations [30, 32, 33]. Taking into account the use of LDA, and the very different origin of both bands, the existence of inaccuracies of a few hundreds of meV in their relative positions is not surprising. In fact, the limitations of LDA to describe the excitation spectra associated with the dangling bonds in silicon surfaces has been studied in detail by several authors. For example, in the case of the Si(001)-(2$\times$1) [129] and Si(111)-(2$\times$1) [130] the gap between the occupied and unoccupied surface bands is widened

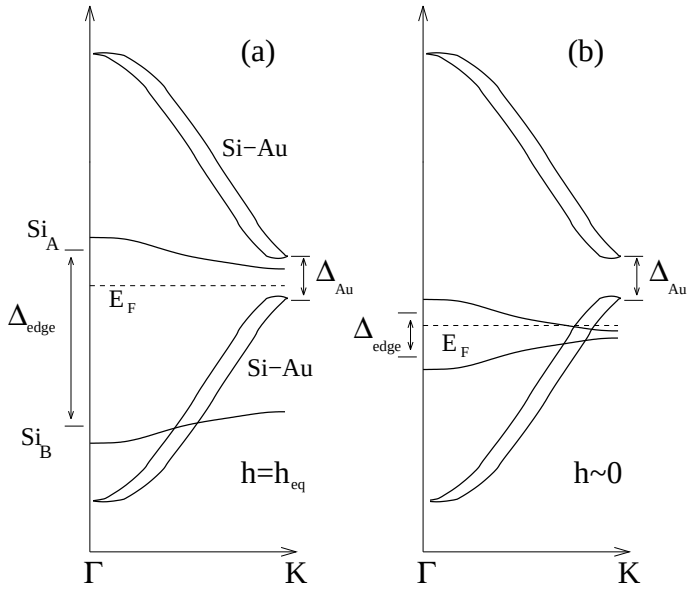

Figure 6.5: Schematic picture of a plausible model, based on the theoretical band structure, of the metal-insulator transition in the Si(557)-Au surface controlled by the buckling of the step-edge. (a) Shows the insulator situation for the equilibrium, low temperature, structure. The Si-Au label indicates the spin-split gold bands with a gap Δ_{Au} due to the periodicity doubling caused by the row of silicon adatoms in the terrace. The buckling of the step edge opens a gap Δ_{edge}, leaving an occupied band coming from the up-edge atoms (B) and an unoccupied band coming from the down-edge atoms (A). The position of the Fermi level is indicated by E_F, and $h = |h_B - h_A|$ is the height difference between the atoms B and A in the step edge. Panel (b) shows the metallic situation for $h \sim 0$. If the buckling of the step edge takes place through a displacive distortion, $h \sim 0$ corresponds to the high-temperature undistorted configuration. If the transition takes place through an order-disorder transition, configurations close to $h \sim 0$ will have a larger weight as the temperature is increased.

$\sim$0.5 eV using the GW approximation for the electron self-energy. The unoccupied surface bands appear shifted to higher energies with respect to the occupied surface and bulk states. The GW approximation provides a better description of the exchange and correlation effects than the LDA. In particular, the use of a non-local self-energy allows for a better description of the electronic exchange which is crucial for an appropriate treatment of the relatively localized silicon dangling-bonds. The origin of the step-edge bands in Si(557)-Au is very similar to, for example, the surface bands associated with the tilted dimers in the Si(001)-(2$\times$1) surface. Therefore, we can expect a shift of the unoccupied step-edge band to higher energies by a few tenths of eV using a description of the exchange and correlation beyond DFT-LDA.

6.3 Step-edge buckling and the metal-insulator transition

We proceed to demonstrate how the theoretical model of Figs. 6.2 and 6.1 contains all the necessary ingredients to justify the appearance of a metal-insulator transition driven by the step-edge distortion. Fig. 6.5 schematically presents the main ingredients and clarifies a possible mechanism for such transition. These are:

(*i*) due to the periodicity doubling imposed by the presence of a neighboring row of silicon adatoms, a band gap Δ_{Au} appears in the Si-Au bands at the Brillouin zone boundary;

(*ii*) the buckling opens a gap between occupied and unoccupied levels at the step edge

Δ_{step}, the size of this gap depends on the strength of the step-edge distortion, i.e. is a function of $|h| = |h_B - h_A|$ the difference between the height of up (B) and down-edge (A) atoms along the step edge (see Fig. 6.1);

(*iii*) the Fermi level position is controlled by the relative position of the upper step-edge band (this band is unoccupied at low temperature, its energy being dependent on the step-edge distortion) and the top of the occupied Si-Au bands;

(*iv*) if the alignment of the Si-Au and step-edge bands is appropriate, a change in size of Δ_{step} will drive a metal-insulator transition (compare Fig. 6.5 (a) and (b)).

If the band structure of Si(557)-Au is qualitatively similar to that in Fig. 6.5 (see Sec. 6.2), a displacive-like transition of the step edge between a distorted ($h = h_{eq}$) low-temperature and an undistorted ($h \sim 0$) high-temperature configurations will be accompanied by a transition from an insulator to a metallic state as the temperature is raised in agreement with the experimental observations [30]. Thus the connection between the step-edge distortion and the metal-insulator transition of the Si-Au bands has been established: the metallic/insulator character is determined by the position of E_F, the size of Δ_{step} controls E_F, and Δ_{step} is determined by the strength of the distortion h.

We could think the step-edge transition to be order-disorder, with the system fluctuating between two equivalent equilibrium configurations at room temperature. This is in complete analogy with the “dynamical fluctuation" model accepted for the Sn/Ge(111) and related surfaces [131] and was our first suggestion of the character of the transition [71]. On the other hand, such an order-disorder transition would make difficult the direct application of the model of the metal-insulator transition sketched in Fig. 6.5. The displacive or order-disorder character of the phase transition depends on the ratio between the energy gain associated with the local distortion and interaction between distortions created in nearby sites, and how such interaction decays with distance. As a function of these parameters, there is a continuous crossover between both types of phase transitions [108, 132, 133]. Unfortunately, the information necessary to fully characterize the step-edge structural transition in the Si(557)-Au cannot be obtained from *ab initio* calculations using small unit cells and thus is beyond the scope of the study. We notice, however, that the time spent by the system in configurations with small values of h (slightly distorted step edge), and thus metallic, increases as the temperature is raised even in the case of an order-disorder transition.

In the following sections we will analyze the changes of the electronic structure as a function of the step-edge distortion. We will see that these results support the plausibility of the model proposed in Fig. 6.5 and reproduce most of the features of the recent STM and STS experiments. [33, 34, 37]

6.4 Step-edge buckling: energetics and band structure

Fig. 6.6 presents the total energy as a function of the step-edge buckling h. With the DZP basis set the buckling distortion is favorable by at least 120 meV, with a DZ basis set, like the one that we used in our first study of this problem [71], these values are reduced to $\sim$30meV and 0.4Å. The value of the distortion at equilibrium h_{eq} is 0.65 Å. A value of h corresponds to a given up-down configuration along the step-edge, while $-h$ corresponds to the reverse arrangement. Therefore, with find equilibrium configurations at h_{eq} and $-h_{eq}$. Notice, however, that one of them is slightly more stable (by 11 meV). This asymmetry is due to the different

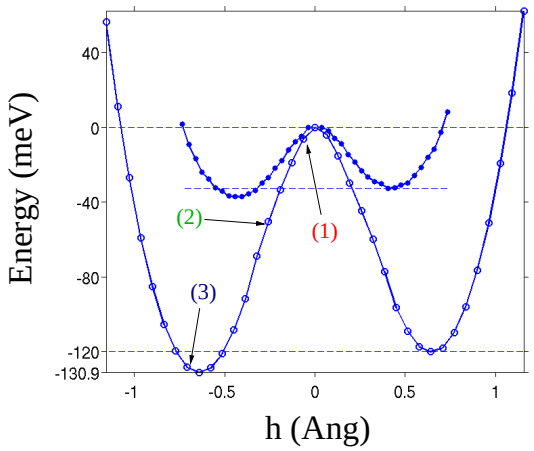

Figure 6.6: Total energy calculated with a DZP (open circles) and DZ (filled circles) basis sets as function of the relative height (h) of the step-edge atoms. Notice the slight asymmetry of the curve corresponding to the inequivalency of the two step-edge positions due to the presence of a row of adatoms in the *same* terrace. Three configurations, corresponding to different sizes of the step-edge buckling are selected: configuration (1) corresponds to a negligible buckling, (2) to an intermediate value and (3) is close to the optimum strength of the distortion. The local density of states and band structure of these configurations are analyzed and presented below in Figures 6.7, 6.8 and 6.12

registry of the two step-edge atoms with respect to the silicon adatoms on the *same* terrace, which are located $\sim$12 Å away. Both step-edge positions are equivalent respect to the closest adatom row, located $\sim$7 Å away from the step edge.

The results using the DZP basis for the energetics of the buckling distortion seem to be more consistent with the experimental observation. The value of 30 meV obtained with the DZ basis is too small to explain the observed stabilization of the step-edge buckling at temperatures of 78 K [33]. However, we should stress two points here. On the one hand, present theoretical methods [134] are probably not accurate enough to reliably estimate the small energy associated with the step-edge distortion in the Si(557)-Au surface. We can expect considerable inaccuracies associated with the use of approximate DFT functionals. On the other hand, this quantity is not sufficient to determine the apparent transition temperature in a real system with defects (see, for example, the “vacancies" in the step edge and the adatom row of the Si(557)-Au surface in Fig. 6.11 and Fig. 6.15). It has been shown [135] that the presence of defects can stabilize locally a reconstruction well above the phase transition temperature of the system. Given the very small energy differences between different reconstructions of the surface, the presence of defects is usually a very strong perturbation. Defects typically pin a particular surface configuration in their neighborhood. Therefore, the temperature at which a single step-edge configuration starts to be resolved in the STM images will depend critically on the type and the density of defects present on the Si(557)-Au surface. For example, the room temperature STM images of Krawiec *et al.* [34] resolve the step-edge modulation in clean sections of the step-edge of at least 10 nm limited by defects. The stabilization of the periodicity doubling of the step edge at room temperature nearby defects has also been observed by other authors [28, 33]. Since the appearance of a relatively large density of defects seems unavoidable in this surface, the estimation of the transition temperature from calculations of the “perfect" surface can be questionable.

In Fig. 6.6 we have selected three different configurations corresponding to, (1) a very

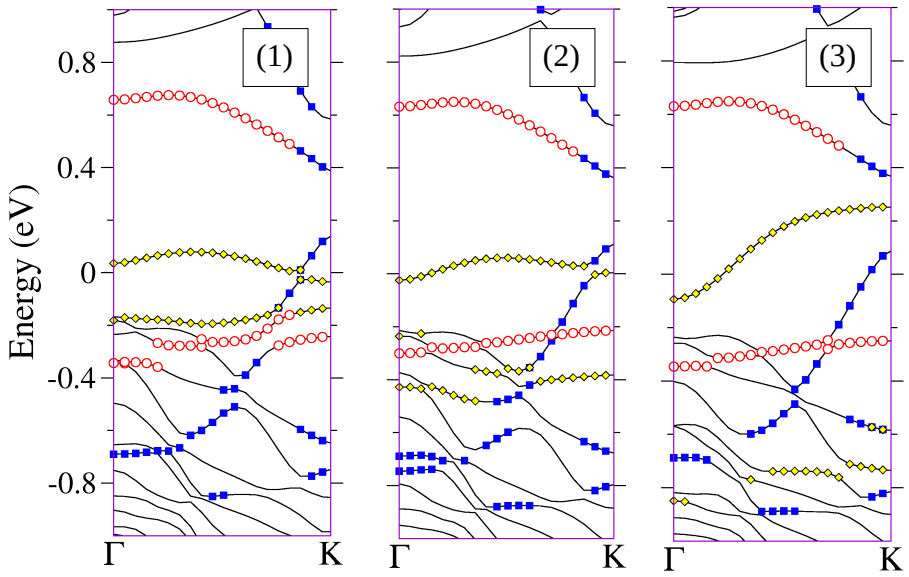

Figure 6.7: Band structures of the three configurations selected in Fig. 6.6. The different symbols indicate the main atomic character of the different surface bands. Filled squares for bands coming from the gold atoms and their neighboring silicon atoms, diamonds for the step-edge atoms, and open circles for the adatoms and restatoms. In the case of the step-edge, the (partially) unoccupied band corresponds to the down-edge atoms (A in Fig. 6.1), while the fully occupied one comes from the up-edge (B). As expected the band coming from the adatoms is unoccupied while the restatom band is fully occupied. Energies are referred to the Fermi level.

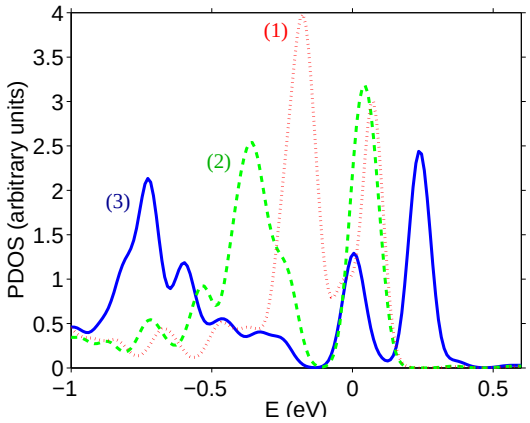

Figure 6.8: Density of states projected onto the step-edge atoms for the three configurations selected in Fig. 6.6. The energies are referred to the Fermi level.

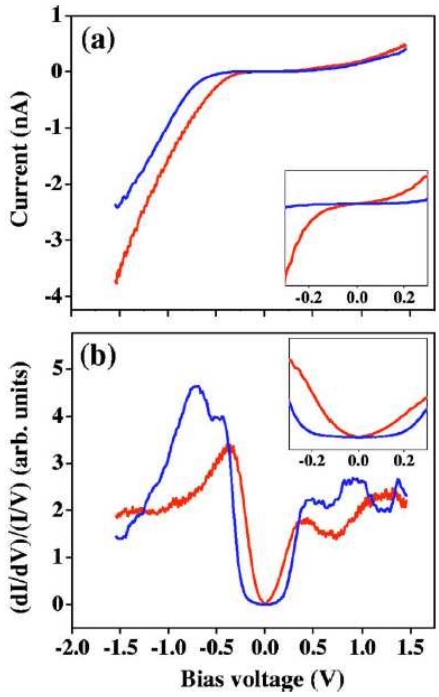

Figure 6.9: Experimental normalized dI /dV spectra on the step edges at 300 K (red) and 78 K (blue). The spectra near Fermi level (bias zero) are enlarged in the inset. Each spectrum is averaged over several equivalent positions along the step edges. Picture taken from Ref. [33].

small step-edge distortion (h=0.06Å), (2) an intermediate value (h=0.25Å) and, (3) close to the equilibrium configuration (h=0.70Å). The corresponding band structures along the direction of the step edge are plotted in Fig. 6.7. The different surface bands are marked according to their main atomic character. Solid (blue) squares indicate the Si-Au bands, open (red) circles mark those bands associated with the adatoms and restatoms, and (yellow) diamonds correspond to the bands coming from the step-edge atoms. We see that only those bands that come from the step-edge atoms are modified as we change the strength of the buckling distortion. The step-edge gap Δ_{edge} is strongly reduced as the size of the distortion diminish. The difference between the average position of the step-edge bands is 0.9 eV for configuration (3), but only 0.2 eV for the structure (1). The occupied step-edge band, associated with the up-edge atoms, is always very flat (dispersion smaller than 0.1 eV), and its position evolves from -0.8 eV (below E_F) in (3) to -0.17 eV in (1). The behavior of the “unoccupied" step-edge band, coming from the down-edge atoms, is somewhat more complex. For configurations (1) and (2) this band is pinned at E_F, whereas its average position in (3) is $\sim$0.15 eV above E_F. This is in agreement with our proposal for the metal-insulator transition. However, while the dispersion of the band is very small for configurations (1) and (2), for structure (3) it becomes $\sim$0.35 eV. As a consequence of the strong dispersion, the band presents a small partial occupation also in configuration (3). This small occupation may be an artifact of the DFT-LDA calculation as pointed out in Sec. 6.2.

As expected, when the step-edge buckling h is reduced, the down-edge atom band is shifted to lower energies and this shift is accompanied by a charge transfer from the Si-Au band to the step-edge. However, we can expect this charging to be moderate and the occupa-

tion of this band should always remain relatively small. Indeed, going from configuration (3) to (2) shifts down the center of the band $\sim$0.2 eV, while going from configuration (2) to (1) this band does not considerably move respect to the other surface bands. As a consequence, the closing of the step-edge gap implies a larger movement of the occupied step-edge band, which moves $\sim$0.6 eV to higher energies. This asymmetric closing of the step-edge gap is a distinct feature of our theoretical model of the Si(557)-Au and has been claimed to be in disagreement with the experimental evidence [33]. In fact, the observed gap closing in the dI/dV spectra on the step edge reported in Ref. [33] and presented in Fig. 6.9 is apparently symmetric. However, if we examine these data in detail we can find several features that are in qualitative agreement with the predictions of our model. For example, the differences between the low and room temperature data are more significant for the occupied part of the spectrum. In particular, a strong peak located at $\sim$0.7 eV below E_F in the low temperature spectrum disappears at room temperature. This energy coincides nicely with the position of the occupied step-edge band in our low temperature configuration (3).

6.5 Simulated STM and STS images

The ground state structure of Fig. 6.1 and the electronic bands shown in Fig. 6.2 can perfectly explain the low-temperature STM images of the surface in Fig. 6.11. The step-edge exhibits a buckling, with A atoms lying $\sim$0.7 Å below B atoms. Furthermore, a high contrast between these two types of silicon atoms is guaranteed. Empty-state STM images will preferentially show A atoms, while filled-state images will reflect the location of B atoms.

The simulated images using Tersoff-Hamann theory (see Sec. 2.4.1) can be found in Fig.6.10 (a), the upper part of the panel corresponding to the ground-state configuration and the lower part to the reversed step-edge buckling. The images are very similar. They are dominated by two chains showing a double periodicity along the step-edge direction in good agreement with low-temperature images reported for this system [19, 30]. One of the chains is the row of adatoms. The other corresponds to the step-edge, where only every other atom is visualized.

The situation changes at higher temperatures. The time necessary to flip between the different step-edge configurations gets shorter as the temperature increases. Given the size of the calculated energy barrier, at room temperature one can expect that STM images show a time average of the electronic and atomic structure of the surface. This corresponds to an order-disorder model of the transition and has been modelled in Fig. 6.10 (b) by averaging the STM images of the two structures. As a consequence, the double periodicity is lost and all the atoms in the step-edge appear with similar intensities. This explains the apparent periodicity doubling observed by Ahn *et al.* [30] upon cooling. A similar effect would be observed if the transition is of a displacive type. In such case the room temperature structure will not show a periodicity doubling. However, taken into account the small energy barrier and the behaviour of silicon surfaces, it is quite tempting to identify the transition with freezing of the dynamical fluctuations.

In Fig. 6.8 we show the projected density of state (PDOS) onto the step-edge atoms as a function of the energy. This can be directly compared with the dI/dV spectra measured on the step edge and presented in Fig. 6.9 The solid (blue) curve presents the PDOS for the our low temperature configuration (3). Below E_F we find the main peak at -0.71 eV in good

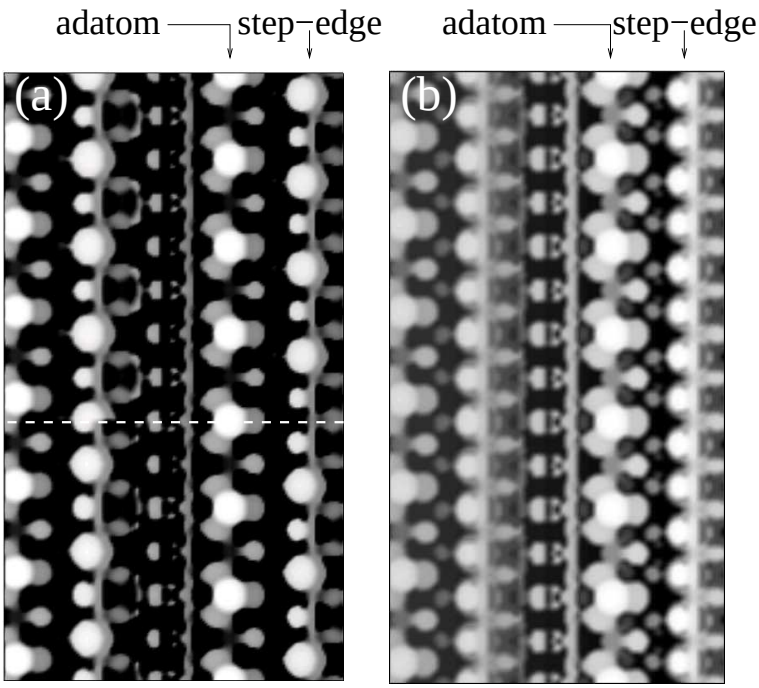

Figure 6.10: Simulated STM images at low (a) and high temperature (b) for a +0.7 V bias voltage (empty states). The upper part of panel (a) corresponds to the ground state structure, while the lower part is obtained with the reversed step-edge configuration. Panel (b) combines both images.

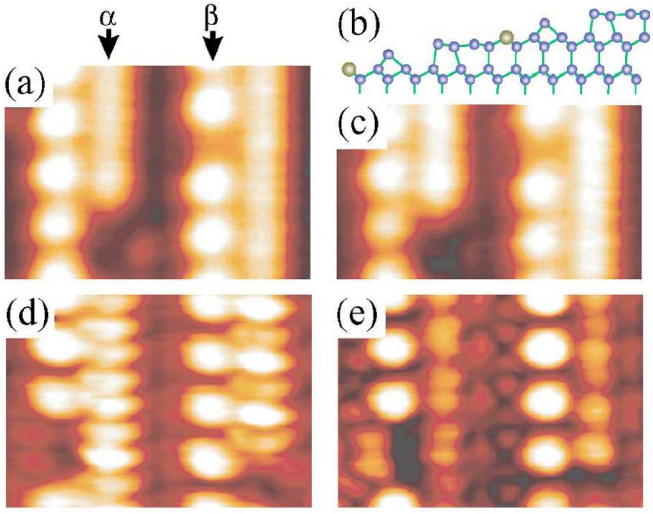

Figure 6.11: Experimental Empty-state STM images at (a),(c) 300 and (d),(e) 78 K with a sample bias of (a),(d) V_s=1.0 and (c),(e) 0.7 V. The structural model of Si(557/Au is shown in (b) schematically, where the large and small circles denote Au and Si atoms, respectively. Picture taken from Ref. [30].

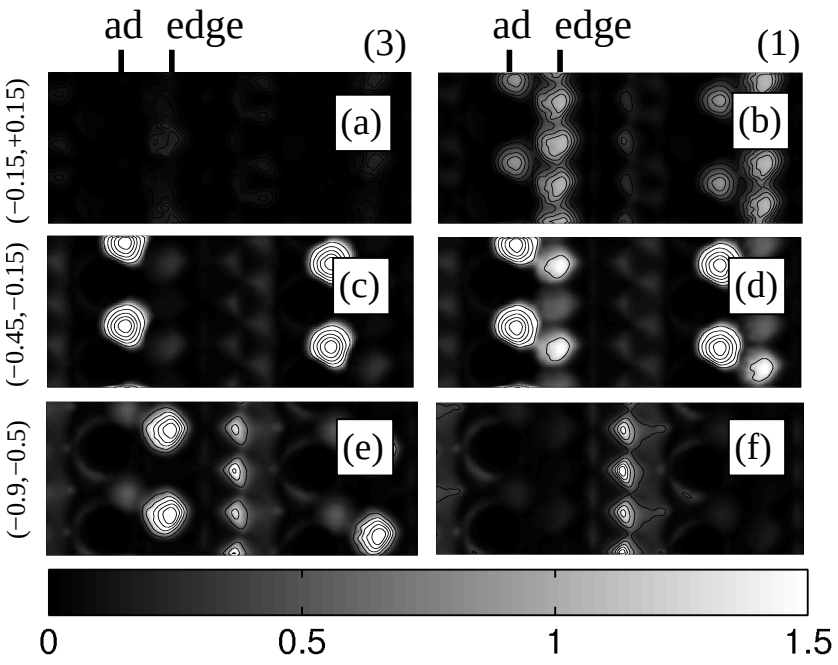

Figure 6.12: Calculated maps of the density of states as a function of the energy for the Si(557)-Au surface. Panels (a), (c) and (e) show the result for a buckled step-edge (corresponding to configuration (3) in Fig. 6.6). Panels (b), (d) and (f) correspond to a negligible step-edge buckling (using configuration (1) in Fig. 6.6) The density of states is integrated in various energy ranges: from -0.9 to -0.5 eV (panels e and f), from -0.45 to -0.15 eV (panels c and d) and from -0.15 to 0.15 eV (panels a and b), with zero corresponding to the Fermi energy. The locations of one adatom row and one step edge are indicated by “ad" and “edge", respectively. The dimension of each image is $\sim$ 3.3 nm $\times$ 1.5 nm. The used gray scale (arbitrary units) is indicated.

agreement with the experiment. We also find the contribution coming from the bulk states up to $\sim$0.2 eV below E_F. At higher energies we find a gap in the PDOS. Two peaks, at E_F and 0.24 eV above E_F, appear due to the dispersion of the down-edge atom band. Besides the small occupation of the down-edge atom band, which is not observed in the experiment and gives rise to a peak at E_F, the main peak at -0.71 eV and the gap extending down to -0.2 eV agree with the observed low temperature dI/dV spectra. For configurations (2) and (1) the main occupied peak shifts to higher energies and, as a consequence, the gap in the PDOS is considerably reduced. Although the changes are more modest above E_F than below E_F, we also observe a shift to lower energies of the main unoccupied peak that becomes pinned at E_F. Configurations like (1) and (2) are only available at high temperature. If the structural transition is purely displacive, then the high temperature spectra can be identified with the curve for structure (1). However, in an order-disorder transition the high temperature dI/dV corresponds to an average of the curves obtained for different structures. Since STM is a local probe, such an average has to reflect the dynamics of the fluctuation process, not just a thermal average. Thus, we can expect structures similar to configuration (1) to have a strong weight in this average.

Thus we have seen that our model can explain some features of the dI/dV obtained on the step edge of the Si(557)-Au surface. It is also interesting to note that these experiments mainly reflect the changes in the atomic and electronic structure of the step edge. The curves in Fig. 6.8 do not contain features directly related with the Si-Au bands that dominate the pho-

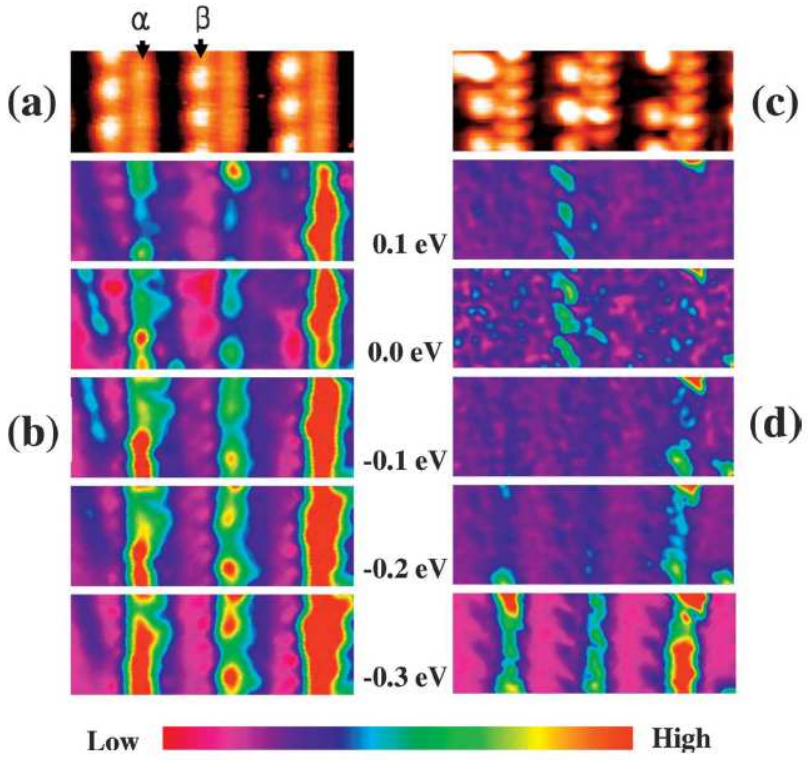

Figure 6.13: Experimental color STM topographic images of Si(557)-Au at (a) 300 and (c) 78 K V_s= +1.5 V. dI/dV maps at (b) 300 and (d) 78 K, which were acquired by CITS measurements at the given bias voltages, simultaneously with the constant current topography. Here, the intensity scale of the dI /dV maps, which represents local density of states (LDOS), is given at the bottom. Picture taken from Ref. [33].

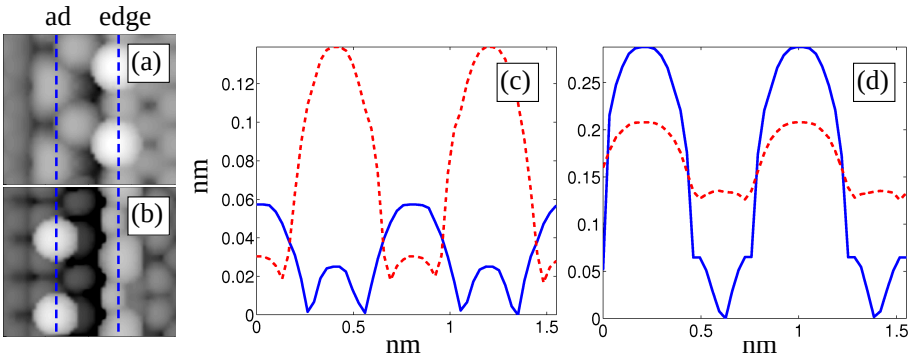

Figure 6.14: Simulated STM images with bias of (a) -1.0 V and (b) +0.6 V. Plots in (c) and (d) show the calculated topography along the step edge (“edge") and the row of adatoms (“ad") respectively. Solid lines are for empty states (positive bias) and dashed lines for occupied states (negative bias). The used scan lines are indicated by dotted lines in (a) and (b).

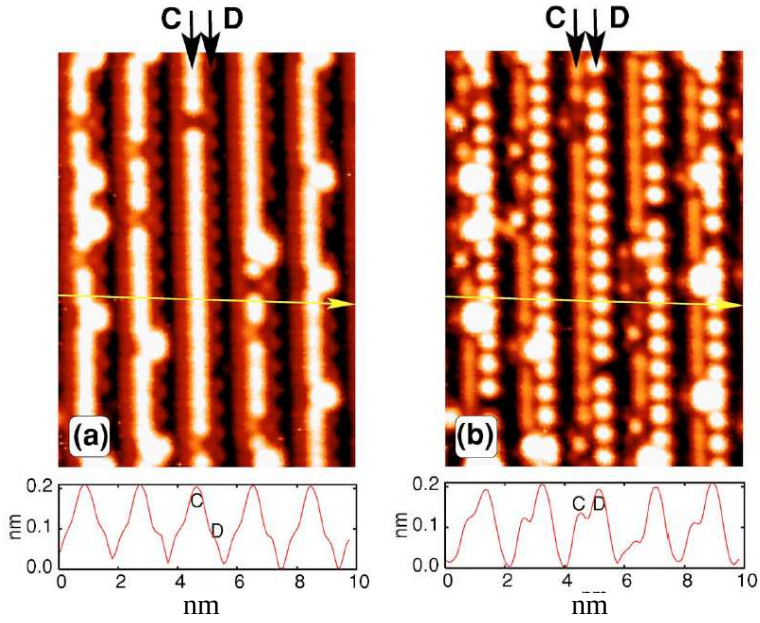

Figure 6.15: The 9.75×13.5 nm^2 Experimental STM topography images of the same area of the Si(557)/Au surface recorded at two different sample biases U=-1.0 V (a) and U=1.0 V (b) with the tunneling current I=0.05 nA. The bottom panels show profile lines perpendicular to the chains, indicated by long arrows in the main panels. Picture taken from Ref. [34].

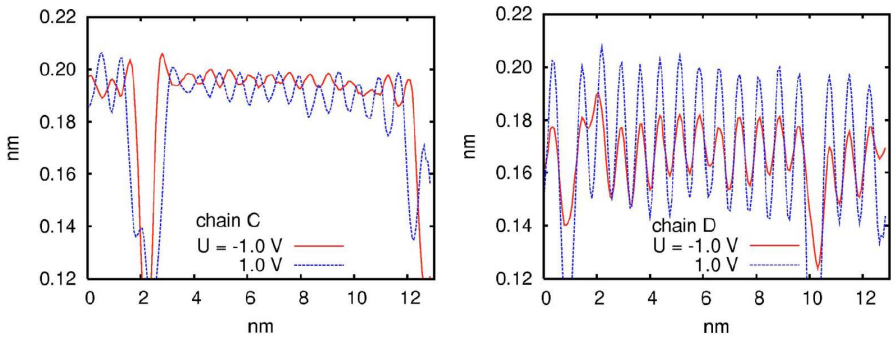

Figure 6.16: Experimental STM cross sections along two different chain structures in the Si(557)/Au surface (see Fig. 6.15). Along chain C for bias voltage U=-1.0 V (solid line) and +1.0 V (dashed line), the bottom panel, along chain D. Picture taken from Ref. [34].

toemission. In our model the metal-insulator transition of the Si-Au bands is a consequence of the change in position of the down-edge atom band, from above E_F to be pinned at E_F.

Fig. 6.12 shows the calculated maps of the local density of states (LDOS). These maps can be compared with the dI/dV maps of Fig. 6.13. The LDOS maps of the surface were produced mimicking the experimental procedure: first we find the "tip height" $Z_{tip}(x, y)$ corresponding to a constant current image at a positive bias of +2.0 V (the results of the LDOS maps do not significantly depend on this voltage),

$$I = \int_{E_F}^{E_F+V} d\epsilon \; \rho(x, y, Z_{tip}(x, y), \epsilon) = constant, \tag{6.1}$$

where $\rho(\mathbf{r}, \epsilon)$ is the local density of states calculated for the energy ϵ at point $\mathbf{r}$. We then plot

the local density of states on the surface $Z_{tip}(x, y)$ integrated in small energy intervals ΔV as an approximation to the measured dI/dV maps

$$LDOS(x, y, V) = \int_{E_F+V-\Delta V/2}^{E_F+V+\Delta V/2} d\epsilon\ \rho(x, y, Z_{tip}(x, y), \epsilon). \tag{6.2}$$

The size of the intervals ΔV depends on the fineness of the k-sampling and the dispersion of the bands. For typical calculational parameters ΔV cannot be too small. In our case we have divided the range between +0.15 eV and -0.9 eV in two intervals of 0.3 eV and one of 0.4 eV, which correspond to the main position of the different surface bands in the low temperature structure.

In agreement with the experimental results, the data in Fig. 6.12 are dominated by features coming from the step edge and the adatom-restatom row, that correspond respectively to the α and β chains of Fig. 6.13. At low temperatures and small voltage (panels (a) and (c)) the LDOS maps are dominated by the signal coming from the restatoms at $\sim$0.3 eV below E_F. We can only see extremely faint features associated with the step edge and the Si-Au chain in the middle of the terrace. We need to go to lower energies, around -0.8 eV, to observe a strong feature associated with the step edge (panel (e)). We can also see an increase in the intensity of the signal coming from the middle of the terrace. This corresponds to a relatively flat band associated with one of the three silicon atoms bonded to each gold atom. This surface resonance is not clearly marked in Fig. 6.7 but is marked with open circles in the band structure of Fig. 6.2. The bonds between gold and the other two silicon atoms generate the dispersive Si-Au band seen in photoemission that, however, only produces a very weak signal in the STM and STS images. At high temperature (panels (b), (d) and (f)) the situation changes as seen in the experiment: the step-edge becomes clearly visible at low voltages.

Recently, Krawiec *et al.* [34] have reported an interesting experimental result. While the topography of one of the two atomic rows that characterize the STM images of the Si(557)-Au depends on the sign of the applied bias voltage, it remains unchanged for the other wire. They suggest that the different behavior is an indication that both wires are made of different materials, gold and silicon (see Fig. 6.15 and Fig. 6.16). However, we claim that this experimental observation can be perfectly understood using the present structural model where the two prominent chains are assigned to the step edge and the adatom row respectively. The step edge shows a reverse corrugation as function of the bias polarity, whereas this does not happen for the adatom row. The silicon adatoms are $\sim$1.3 Å higher than the other atoms in the surface layer, except for the restatoms that only lie $\sim$0.8 Å below. Although the adatoms produce more pronounced features at positive bias and the restatoms at negative bias, for scan lines taken along the rows of adatoms the atomic topography dominates over the electronic effects. Therefore, the STM images show maxima at the adatom positions irrespective of the sign of the applied voltage. This can be seen in Fig. 6.14 (d). The corrugation is larger for empty states and the data are in good qualitatively agreement with the images of Krawiec *et al.* in Fig. 6.16. In contrast, the electronic effects dominate for the scans taken along the buckled step-edge, and the topography can show a pronounced bias dependence. This is shown in Fig. 6.14 (c), again in good qualitative agreement with the data for chain C in Fig. 6.16. Notice that we use our low temperature structure (with fully developed step-edge buckling) to generate the images in Fig. 6.14. Although the experiments of Krawiec *et al.* are made at room temperature, the use of this geometry is justified by the fact that these authors concentrate in structure of the step edge of a few nanometers bounded by defects. The presence of defects

stabilizes the step-edge distortion up to room temperature for this relatively short chains, as was mentioned above.

It is interesting to note that one of the criticisms of Yeom *et al.* [33] towards the low temperature structure proposed by Robinson *et al.* [29] and Sánchez-Portal *et al.* [70, 71] was based on the predictions, using such structural model, of the appearance of a step-edge modulation for both, empty and occupied states [71]. According to Yeom *et al.*, such modulation could only be observed for empty states. However, this is disagreement with the results presented in Ref. [34] that we just have discussed above. Of course, one could argue that the step-edge modulation observed in the presence of defects is different from the modulation stabilized at low temperature. However, most experiments to date have been performed on samples with a considerable concentration of defects and the observations of Krawiec *et al.* seem to agree with the predictions from theory. Thus, it is quite tempting to identify the distortions observed at low temperature and in the presence of defects. Furthermore, the simulated STM images seem to reproduce the change in the relative intensity of the step edge and the adatom row as a function of voltage. In Fig. 6.14 (a) and (b) we can see that for a voltage of -1.0 V the step edge is more intense that the adatoms, whereas for +0.6 V the situation is reversed. This is in agreement with the STM images shown in Fig. 6.15, although might be strongly dependent on the tunneling conditions (e.g. this change is not so clear in the data in Fig. 2 of Ref. [33]).

The agreement of the simulations in Fig. 6.14 with experiment is qualitative. From a more quantitative point of view there are some discrepancies: *i*) the calculated corrugations are too large, and *ii*) the step edge shows a larger corrugation for occupied states than for empty states, which is not observed in the experiment [34]. We should point here that we are using the simple Tersoff-Hamann [99] theory for our simulations. In this theory the STM images are obtained from the local density of states of the surface according to Eq. 6.1 and all the effects induced by the tip are neglected. The observed discrepancies are probably related to the simple theoretical treatment and the use of a basis set of confined atomic orbitals in our calculations [84, 120]. This basis set is numerically very efficient. However, due to the short cut-off radii of the orbitals, it is not adequate to simulate the smooth decay of the wavefunctions towards the vacuum and tends to emphasize the structural corrugation over the electronic effects and, in general, leads to an overestimation the surface corrugation. This also explains, at least partially, the second discrepancy. The empty states images might be also influenced by the difficulties of the DFT calculations to properly describe the excited states.

6.6 Molecular Dynamics Simulations

Our MD simulations have been performed using a DZ basis set, similar to that used in the initial studies of the structural properties of the Si(557)-Au surface. [69–71] With this basis set we can perform simulations of several picoseconds. Although less complete than the DZP basis set the structural and electronic properties obtained with the DZ basis set are very similar to those described above. Fig. 6.17 shows the behavior of several degrees of freedom during the last 4 ps of one of our MD simulations. The total simulation time is 8 ps (8000 time steps). The temperature of the system oscillates around 300 K after a thermalization time of $\sim$1 ps. Our simulation cell contains one unit cell of the Si(557)-Au surface. With this “small" cell we cannot obtain a realistic picture of the structural transition in the surface. Furthermore, we have seen that the use of a DZ basis set causes a severe underestimation of the energy

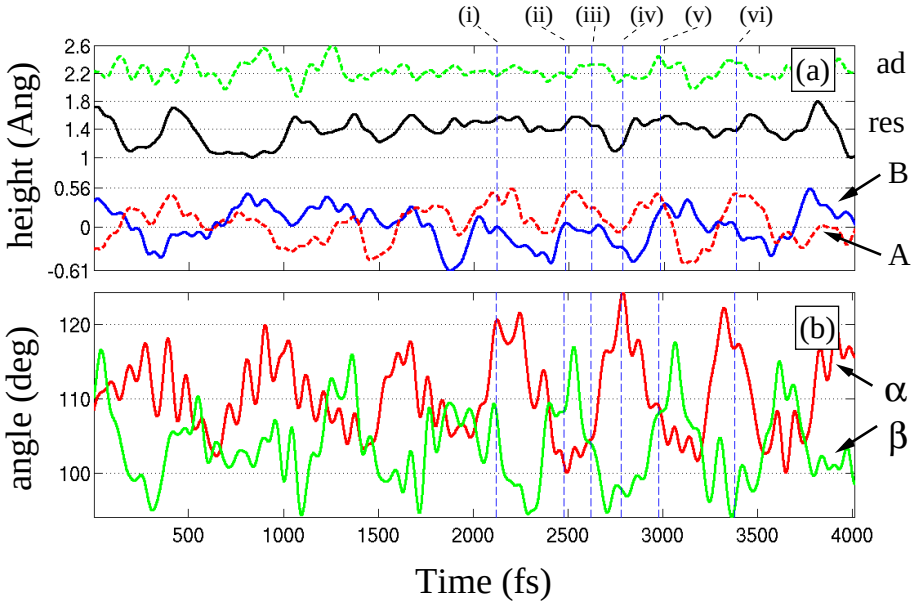

Figure 6.17: Last 4 ps of a molecular dynamics simulation of the Si(557)-Au reconstruction performed at a temperature of ∼300 K. A DZ basis set was used for this calculation and the total simulation time is 8 ps. Panel (a) displays the height of different atoms as a function of time (see also Fig. 6.1): adatom (*ad*, greed dashed), restatom (*res*, solid black) and the step-edge atoms (B, solid blue and A, dashed red). The two inequivalent Si-Au-Si bond angles (α and β) are presented in panel (b). The vertical lines mark the instantaneous configurations for which the band structures are shown in Fig. 6.18

barrier between the two step-edge equilibrium configurations (the barrier is ∼30 meV and the equilibrium step-edge distortion h_{eq} ∼0.4 Å). However, the MD simulations are a very important tool to understand the coupling between different vibrational modes and between the atomic and electronic degrees of freedom. In particular, we want to check if a well-defined fluctuation of the step edge exists at high temperatures and how this movement is coupled with other vibrational modes. We also study the effect in the electronic structure of atomic movements that can be excited at reasonable temperatures and are different from the step-edge fluctuation studied in detail above.

Fig. 6.17 shows a clear oscillation of the step-edge, the atoms changing their relative positions and residing for intervals of less than 1 ps in a given up-down configuration. We can also observe that the system spends a considerable amount of time in configurations where the step-edge distortion h is small (corresponding to a small step-edge gap Δ_{edge}). Besides the step edge, other degrees of freedom show strong fluctuations in spite of the moderate temperature. Particularly remarkable are the cases of the restatom (marked with *res* in Fig. 6.17, see also Fig. 6.1), the Si-Au-Si bond angles (α and β) and, to less extent, the adatom (*ad*). As a consequence, the corresponding energy levels also exhibit a considerable movement during the simulation. The case of the step-edge bands has been studied in detail in Sec. 6.2. The bands associated with the restatom and the adatom oscillate with an amplitude of up to ∼0.2 eV. This can be easily appreciated for the adatom band (flat band ∼0.5 eV above E_F) in the band structures shown in Fig. 6.18 corresponding to different snapshots of the simulation. This movement might be one of the reasons why a well-defined restatom state has not been detected in photoemission experiments [19] on this surface and why the adatom band appears as a relatively broad structure between 0.5 and 1 V (with its maxima at ∼0.7 V) in recent STS

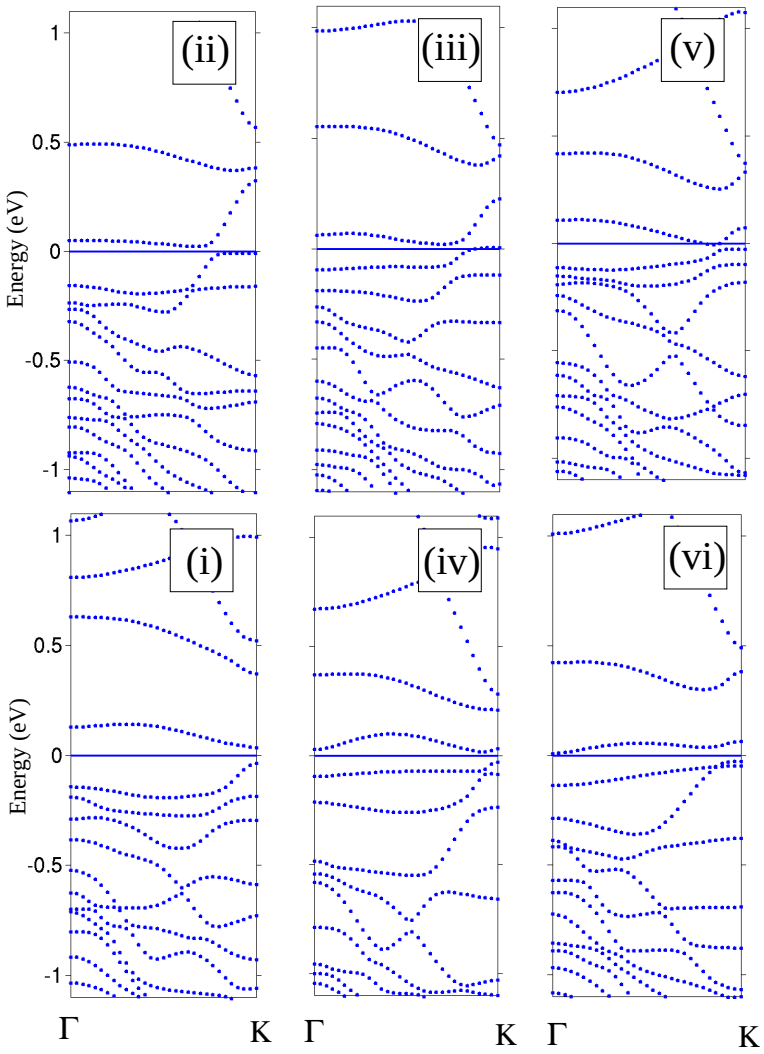

Figure 6.18: Band structures (calculated with a DZ basis set) corresponding to the snapshots selected in Fig. 6.17. For configurations (ii), (iii) and (v) (upper panels) the dispersive Si-Au band clearly crosses E_F and the down-edge atom band is pinned at E_F whereas, for configurations (i), (iv) and (vi) (lower panels), the lower branch of the Si-Au band lies below E_F and a tiny gap is developed between this band and the down-edge atom band, i.e. E_F lies within the Si-Au band gap Δ_{Au}.

spectra obtained at room temperature [37]. The Si-Au-Si bond angle has an important influence on the Si-Au band that dominates the photoemission of the surface. The presence of a row of adatoms induces a periodicity doubling in the terraces of the surface that is reflected in an alternating Si-Au-Si bond angle and the opening of a gap Δ_{Au} in the dispersive Si-Au band. In the equilibrium configuration the values of these two angles are 111.6 and 103.7 degrees respectively for β and α. In Fig 6.17 we see that these values change by $\sim \pm 10$ degrees along the simulation. Changing the Si-Au-Si bond angles changes the size of the Δ_{Au} gap and thus influences the metallic or insulating character of the instantaneous configurations.

The influence of the coupling between the electronic and atomic degrees of freedom in the band structure is clearly shown in Fig 6.18 and Fig. 6.19. We stress that these band structures are calculated with a DZ basis set and, therefore, differ slightly from those shown in Fig. 6.7, calculated with a more complete DZP basis. Fig 6.18 shows the band structure for a few

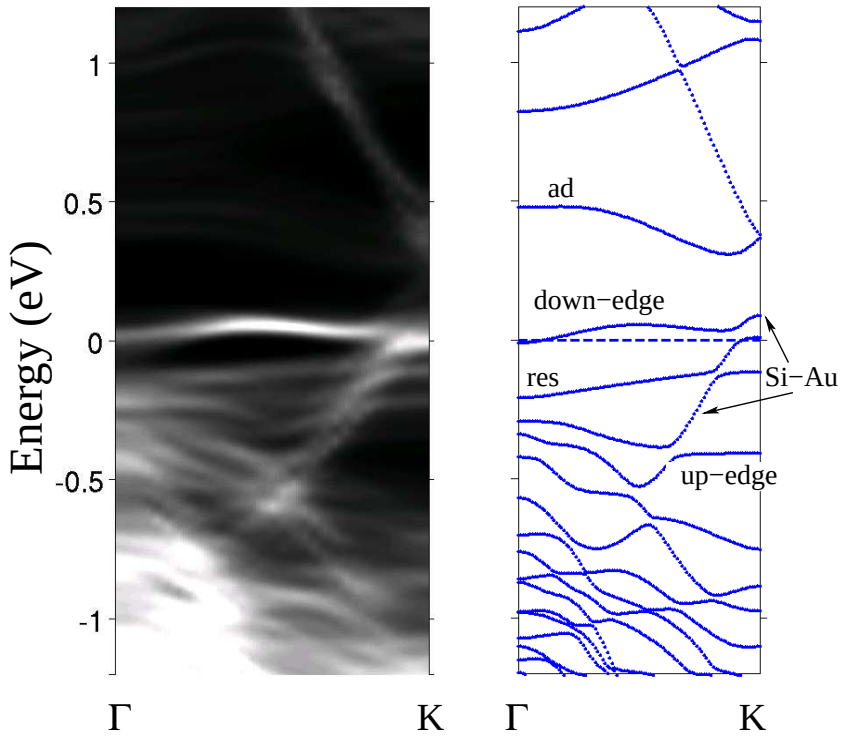

Figure 6.19: Average band structure (calculated with a DZ basis set) during the last 3 ps of the molecular dynamics simulation of the surface at room temperature shown in Fig 6.17. The average is done over 151 configurations (i.e., the band structures are calculated at intervals of 20 fs). The time average is compared with the band structure for the equilibrium configuration.

selected structures (indicated in Fig. 6.17). Fig 6.19 shows the band structure averaged over the last 3 ps of the simulation (using 151 different configurations, each one taken every 20 fs) and compares it with the band structure for the equilibrium structure. The three band structures in the upper panels of Fig 6.18 are clearly metallic: the dispersive Si-Au band crosses E_F and the down-edge atom band is pinned at the Fermi level. For configurations (ii) and (iii) there is an evident reduction of the Si-Au gap Δ_{Au} and a shift in the position of the Si-Au band. This is due to the change of the α and β angles that become quite close or, like in structure (ii), even appear reversed respect to the equilibrium configuration. For configuration (v) we can also see that the step-edge gap Δ_{edge} is almost closed due to the very similar height of both step-edge atoms. The three lower panels of Fig. 6.18 show semiconducting band structures where the lower branch of the Si-Au band is fully occupied and a small gap is developed between the down-edge atom band and the Si-Au band. As a consequence, the Fermi level lies inside Δ_{Au}. This is particularly clear in the case of configuration (i). In the three configurations, angles α and β differ by a similar or larger amount than in the equilibrium structure and the step edge shows a considerable buckling. This guarantees large values of Δ_{Au} and Δ_{step} and thus insulating configurations of the surface.

The results of the MD simulation indicate that at room temperature we find large fluctuations of Δ_{edge} and Δ_{Au}. According to our model of the electronic structure of the Si(557)-Au surface (schematically summarized in Fig. 6.5) this implies that at room temperature the system alternates between metallic and insulating configurations. This phenomenon does not depend on the character of the ground state, which will be insulating if the values of Δ_{Au} and Δ_{step} are large enough in the equilibrium configuration.

Interestingly, many bands that can be found in the equilibrium band structure produce very faint signals in the MD average shown in Fig. 6.19. This is the case, for example, of the adatom band and the occupied (up-edge atom) step-edge band which almost disappear from the average. The restatom band also produces a quite weak and broad structure around -0.2 eV. The most visible features in the MD averaged band structure are: *i*) the occupied part of the Si-Au band which extends from E_F at the zone boundary down to -0.6 eV where it merges with the bulk bands and the unoccupied branch of the Si-Au band from $\sim$0.4 eV above E_F to higher energies, *ii*) a quite flat feature coming from the unoccupied step-edge band right above E_F (and thus not visible by photoemission) and, *iii*) the silicon bulk bands extending around Γ from $\sim$0.5 eV below E_F towards lower energies.

6.7 Conclusions

We have presented a detailed discussion of the electronic structure of the Si(557)-Au surface and its coupling to the structural degrees of freedom. Our calculations are based on the structural model for the low temperature phase of the surface obtained from X-ray diffraction [29] and density functional calculations [70]. The results are compared with recent experimental information obtained by ARP [28, 30], STM and STS [33, 34, 37]. Our main observations are:

i) The band splitting observed in the experimental electronic band structure is successfully reproduced, pointing out the important role played by the spin-orbit coupling in this system. The spin-orbit splitting in this class of systems has also been reported experimentally very recently [32, 62]. From a general perspective, this raises the question of whether systems composed by atomic-scale wires of heavy atoms on semiconducting substrates can be used to create or transport spin-polarized currents, and thus be useful for future electronic devices.

ii) Contrary to the claims of Yeom *et al.*, we have seen that the calculations using the theoretical structural model in Fig. 6.1 provide nice qualitative agreement with the STM and STS images obtained at low temperatures [33] and around structural defects that stabilize the step-edge distortion up to room temperature [34]. Together with the successful description of the experimental band structure, these results give further support to the current structural model of the Si(557)-Au surface.

iii) We have shown that the theoretical band structure is close to a metal-insulator transition. The transition is controlled by the relative positions of the dispersive gold-derived and the flat step-edge bands. The later splits into an occupied and an unoccupied band separated by a gap Δ_{edge} whose size depends on the degree of step-edge buckling, while the former shows a gap Δ_{Au} associated with the presence of a row of adatoms doubling the periodicity along the $[\bar{1}10]$ direction. If Δ_{Au} and Δ_{edge} are large enough the surface becomes insulating at low temperature (see Fig 6.5).

iv) At low temperature the step-edge distortion is large and so is Δ_{edge}. As the temperature increases, configurations with a smaller step-edge buckling, and thus with a smaller Δ_{edge},

are available. For sufficiently small values of Δ_{edge} the system becomes metallic. We argue that this is consistent with the observation of a metal-insulator transition in the Si(557)-Au transition [30].

v) In the present model the metal-insulator transition is accompanied by an asymmetric (respect to E_F) closing of the gap. Yeom *et al.* claimed that this is in disagreement with their experimental results. However, we argue that our data provide a simple explanation to the strong changes observed for the occupied states in the dI/dV spectra taken over the step-edge by these authors [33] (a strong peak at -0.71 eV in the low temperature spectra disappears at higher temperatures).

vi) Our simulated dI/dV maps are in good qualitative agreement with the experimental results at both low and high temperatures. We assume that at room temperature the system spends a considerable amount of time in structures with a small step-edge distortion. The step edge produces a strong signal that dominates the dI/dV maps of these structures at low voltages, however, in the low temperature structure the step edge does not produce any distinct feature at small voltages.

vii) Molecular dynamics simulations of the system show that, besides the fluctuation of the step edge, other vibrational modes are present at room temperature and also have an influence on the electronic structure. In particular, the oscillation of the Si-Au-Si bond angles changes considerably the Δ_{Au} gap. Most configurations with small Δ_{Au} are metallic and contribute efficiently to the metallic character of the surface at room temperature.

viii) Below E_F the MD averaged band structure is dominated by a gold derived band that extends from E_F down to -0.6 eV where it merges with the bulk silicon bands. Other surface bands in the occupied part of the spectrum produce weaker features due to the thermal fluctuations of the structure. This seems in agreement with the observed photoemission.

The results presented in this chapter seem to correctly explain many of the experimental observations on the Si(557)-Au surface. However, further theoretical and experimental work is still necessary to understand this surface. In particular, it is necessary to characterize the dynamics of the structural transition [133] and its relation with the observed metal-insulator transition. Furthermore, the photoemission data of Ahn *et al.* [30] suggest that only one of the dispersive bands that dominate the spectrum of the Si(557)-Au suffers the metal-insulator transition. This is difficult to explain within the current theoretical model, where the appearance of two bands is due to the spin-orbit splitting. The disorder associated with the presence of defects and the different photoemission matrix elements of the two bands can be behind this observation and have to be analyzed before driving further conclusions from this observation. Finally, we have seen that the calculated LDA ground state of the Si(557)-Au is metallic. This is due to the small overlap between the down-edge atom band and the dispersive Si-Au band. We have argued that this failure could be corrected with an improved treatment of the electron exchange and correlation that would provide a better description of the excited electronic states. This is challenging due to the large cell necessary to study the Si(557)-Au surface. However, it would be very interesting to direct future efforts along this direction.

Chapter 7

Si(553)/Au

7.1 Introduction

The existence of the Si(553)/Au reconstruction - exhibiting clear one-dimensional properties both in STM images and in the band structure - was recently demonstrated by Crain et. al. [58]. The physical properties of the Si(553)/Au have many similarities with the Si(557)/Au reconstruction studied in the previous chapter, but it bears two very important structural differences: (i) the terraces are cut into opposite direction than in the Si(557)/Au and (ii) the terrace-width is narrower, consisting only of nine silicon atoms (in the case of Si(557)/Au they are twelve). In the electronic structure, the existence of a metallic one-dimensional band with a peculiar $\sim \frac{1}{4}$ filling has been reported for the Si(553)-Au surface [1, 58] (see also Fig. 7.1). This quarter-filled band could create an opportunity for observing large spin-charge separation if electron-electron interactions (U) could be increased, for example, using a somewhat different substrate. This is in contrast with half-filled bands, which are unstable against a Mott-Hubbard transition for large values of U, preventing the observation of a Luttinger metal [1].

In the STM images, some interesting effects are seen in the terrace step-edge (that is the most brightest feature in STM). Snijders, et. al. [64] find a lowering of the symmetry in the step-edge to $\times 2$, as the temperature is lowered from room temperature down to $\sim$ 100 K and a $\times 3$ periodicity below $\sim$ 40 K, accompanied with a $\times 2$ periodicity at the middle of the terrace [64]. Ahn. et. al., [59] find a similar behaviour and both authors observe a gap-opening in the electronic structure corresponding to the different periodicities (see also Figs. 7.2 and 7.14).

Althought there is lot of experimental data available on the Si(553)/Au reconstruction [1, 58, 59, 61, 63, 64], its geometry on the atomic level is still not completely established. As a starting point, it would be interesting to obtain the high-temperature ($\times 1$ periodic) structure in order to understand the peculiar electronic structure seen in the experiments. With this objective, in Sec. 7.2, we first propose five models based on our earlier experience with the closely related Si(557)/Au surface of Chap. 6. Then, in Secs. 7.3-7.7 we go even further and develop a labelling scheme for finding all physically sound surface geometries. This method can be applied in general to all similar surface reconstructions and it allows us to enumerate the amount of different geometries and generate them automatically. We use it to check a large group (210 in total) of trial geometries for the Si(553)/Au reconstruction and find various energetically very stable models. We also test some surface geometries featuring π-bonding

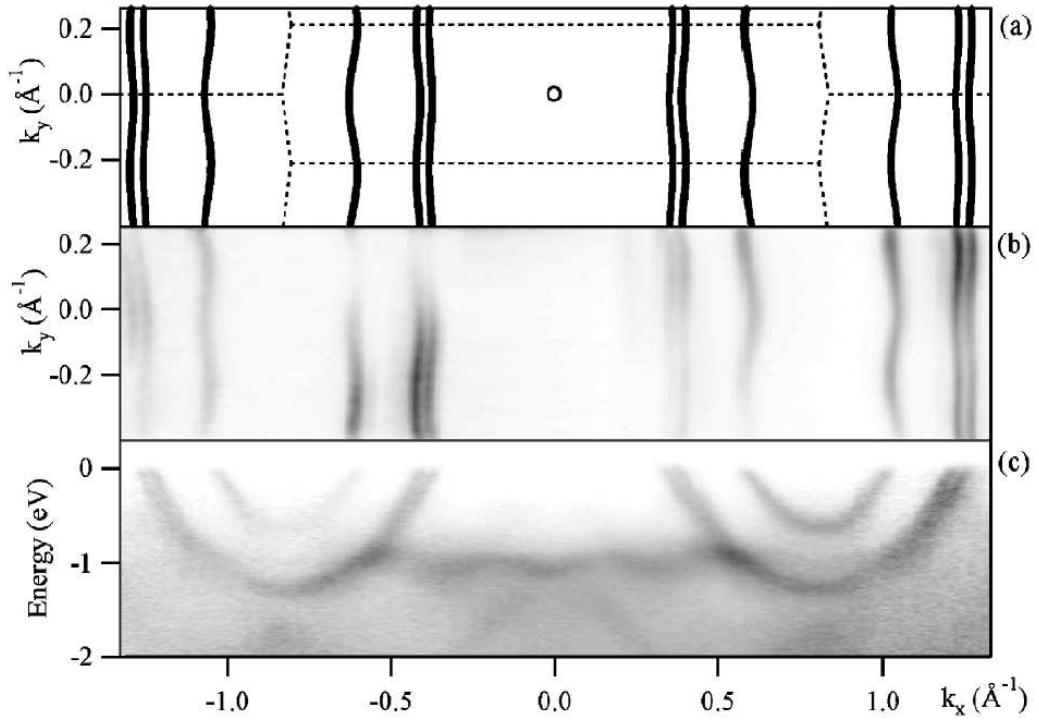

Figure 7.1: Experimental angle-resolved photoemission data of the band dispersion (c) and Fermi surface (b) of the Si(553)-Au chain structure. The Brillouin zone is given in (a), together with a tight binding fit to the Fermi surface. Three metallic bands disperse through the Fermi level (E_F=0), two of them about $\frac{1}{2}$ filled and one $\sim \frac{1}{4}$ filled. High photoemission intensity is shown dark. k_x is along the $[1\bar{1}0]$ chain direction and k_y along $[11\bar{2}]$. Picture taken from Ref. [58].

chains.

At least within our computational scheme, the new models are energetically comparable or even more favourable than the sole structure proposed to date for the Si(553)-Au surface [1]. Band structures are analyzed and the possible origin of the dispersive one-dimensional bands in this reconstruction is discussed.

In the final section 7.8, we test, using *ab-initio* calculations the proposition made by Ghose, et. al. [61] for the Si(553)/Au structure. This model, based on the x-ray diffraction experiment is quite a peculiar one, involving twice the amount of gold than other proposals [58–60,63,64]. The stability, geometric- and electronic-structure of this model are analyzed.

Parameters according to Tab. 2.2 and corresponding to the LDA approximation (`Si.psf`, `H.psf` and `Au.vps`) are used throughout this chapter. Some calculations using the VASP code are performed in Sec. 7.7.

Some of the results of this chapter have been published in Ref. [102].

7.2 Structures based on analogies

In this section, we base our investigation of the Si(553)-Au reconstruction on a plausible analogy with the closely related and better known Si(557)-Au surface of Chap. 6. Both surfaces contain steps along the $[1\bar{1}0]$ direction. In fact, the orientation of the chains along

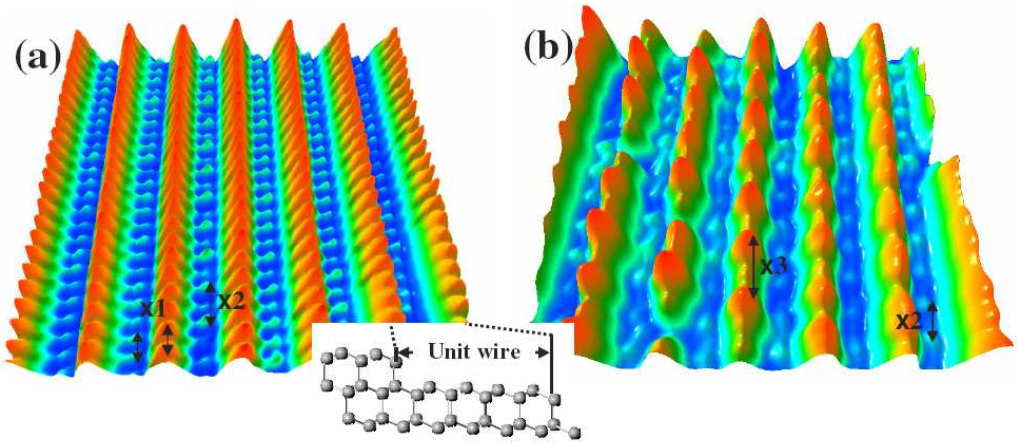

Figure 7.2: Experimental STM topographs of Si(553)-Au at (a) 300 and (b) 45 K for an area of 10x10 nm^2 at 0.2 and 0.5 V biases (empty states), respectively. The ball and stick model in (a) shows the cross-sectional view of the unreconstructed Si(553) surface with steps and a narrow terrace. Picture taken from Ref. [59].

the $[1\bar{1}0]$ directions seems to be common to all the silicon reconstructions forming monatomic gold chains [1]. We recall some properties of the Si(557)-Au reconstruction from Chap. 6: *i*) Gold atoms occupy substitutional positions in the top Si layer in the middle of the terraces; *ii*) the atoms close to the step-edge are strongly rebonded, forming a structure reminiscent of the so-called honeycomb chain (HC) [66]; *iii*) the structure doubles its periodicity along the direction of the steps due to a buckling of the atoms in the step-edge; *iv*) there is also a row of adatoms on each terrace. The miscut direction is opposite for the Si(553)-Au and the Si(557)-Au surfaces. This would open the possibility of a different rearrangement of the step-edge in both cases. However, we do not consider this possibility here, and our models for the Si(553)-Au are fabricated using the building blocks listed above.

We recall from Sec. 3.4 and from Chap. 4 and Chap. 6 the importance of the HC structure for the gold induced reconstructions; the HC is known to occur in the Si(557)-Au surface [29, 69, 70]. We saw in Chap. 4 that it is also the key ingredient of a recent proposal for the structure of the Si(111)-(5×2)-Au reconstruction. The HC structure is illustrated again in figure 7.3. We see that the HC structure involves two unit cells of the unreconstructed Si(111) surface, with one atom removed from the top Si layer. This flattens the surface and removes surface stress as was discussed in Sec. 3.4. The inset of figure 7.3 shows a side view of the HC. The unsaturated bonds are illustrated, and the mechanism behind this reconstruction was explained in Sec. 3.4. We recall from Sec. 3.4 that the electron count in the HC is odd, so one additional electron is needed to yield an electronic closed-shell structure. If there is a neighbouring alkali-metal atom, it donates one electron to the HC, thus contributing to the stabilization of the structure. In the case of gold, which has a stronger electron affinity, the situation is different. Gold is likely to take electrons away from the silicon structure. In principle, this does not prevent an electronic stabilization mechanism: one electron may be transferred to the 6s Au state, leading again to a closed-shell structure. However, in reality we are far from this *ionic* situation. As we saw in the case of the Si(111)/Au-5x2 and Si(557) in Chaps. 4,6, the states of gold are strongly hybridised with those of the neighbouring silicon atoms creating several dispersive bands that are, in principle, metallic.

The structural elements presented above can be used to build many models for the gold induced reconstructions on stepped silicon surfaces. The length of the terraces and the registry with the underlying silicon layers (assumed to be unreconstructed) impose some geometrical restrictions. Some of these were explained in Sec. 3.5. The effect of the introduction of the HC in the Si(111) is schematically illustrated in figure 7.3. While flattening the surface, the HC creates a stacking fault towards the $[\bar{1}\bar{1}2]$ direction (at the right of the HC in the figure) that can be avoided by introducing a surface dislocation (SD). In the upper part of figure 7.3 the SD is introduced immediately after the HC, thus recovering the perfect stacking of silicon. On the lower part of the figure the stacking fault remains until the SD is introduced.

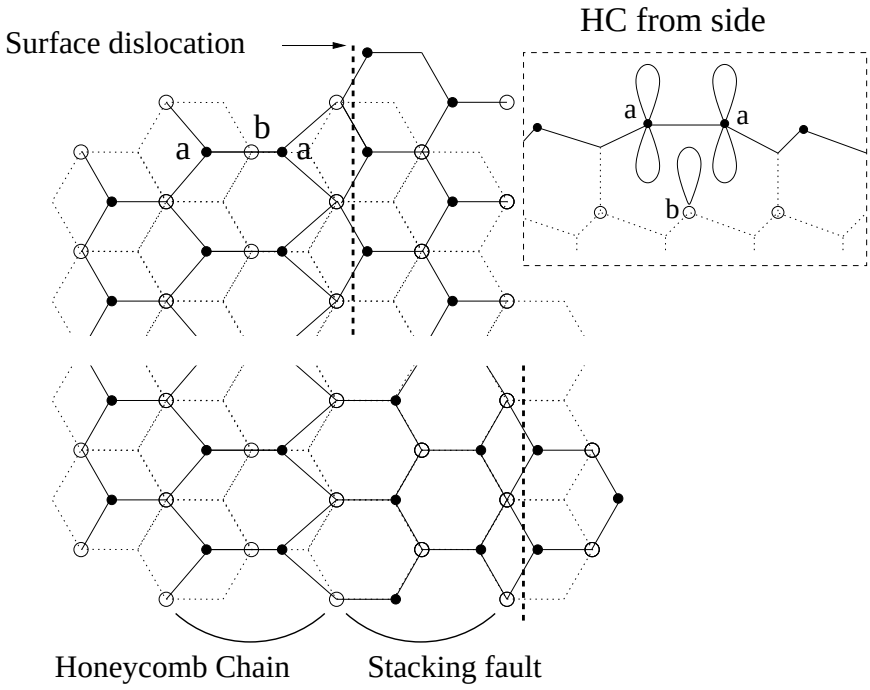

Figure 7.3: Some structural patterns appearing in the metal induced reconstructions of the Si(111) surface. The bonds within the surface bilayer are indicated by solid lines while dotted lines are used for the underlying bilayer. The atoms occupying the highest positions in the surface bilayer are represented by solid circles. Open circles are used for those in the lower bilayer. A side view of the HC structure is shown in the inset.

To name our structural models of the Si(553)-Au surface we have developed a notation which we believe may be useful for other similar systems (this notation will be further developed in Sec. 7.4). The first double-layer in the unreconstructed Si(111) can be expressed using a 1×1 unit cell with a two atoms basis. This entity is named "S". If this block contains a stacking fault (i.e. its bonds coincide with those of the second double-layer) it is called "S_f", f standing for faulted. HC has a 2×1 unit cell and is indicated by "H". The SD is indicated with "D". It is basically equal to "S", but one of its atoms is over coordinated. Using this notation, the upper part of figure 7.3 can be abbreviated as (starting from the HC) HDS and the lower part as HS_fD. The substitution of a silicon atom by gold is indicated using a $+$ superscript.

Our models for the Si(553)-Au surface can be seen in figure 7.4. Models I to V are generated by placing the HC structure with the accompanying dislocation, and the chain of gold

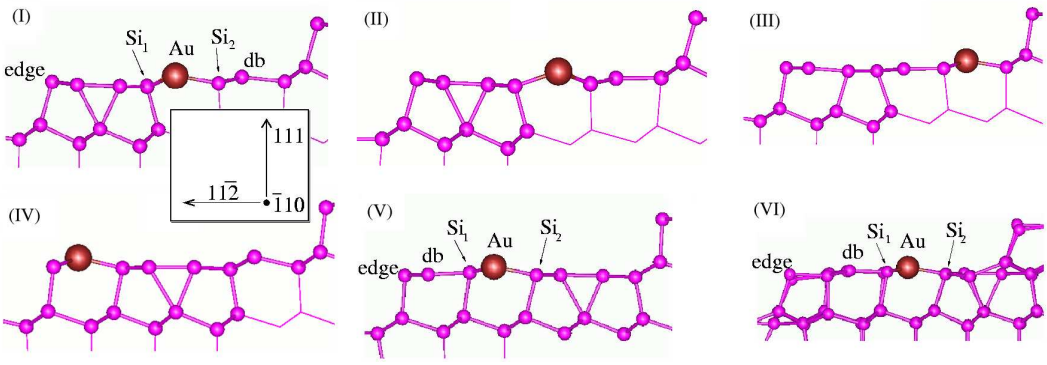

Figure 7.4: Relaxed structures of the different models for the Si(553)-Au surface studied here. Models I to V are proposed from an analogy with the structure of the Si(557)-Au surface. Structure VI has been proposed recently by Crain *et. al.* [1]. Large circles indicate gold atoms. Some of the atoms are labelled (see figure 7.5). The inset clarifies the orientation of the steps.

Table 7.1: Relative surface energies (in meV/Å^2) of different structures of the Si(553)-Au surface. The numbers in the first column refer to figure 7.4, while the names of the models are assigned according to the nomenclature explained in the text. Column labelled $\times 1$ presents the results for the smaller unit cell (with a single Au atom). The systems in columns $\times 2$ and $\times 3$ included, respectively, two and three unit cells along the step direction. This was done in order to study the stability of the step-edge respect to several structural distortions. However, the relaxed structures always returned to an almost perfect undistorted $\times 1$ periodicity. The $\times 1$ and $\times 2$ slabs contained four silicon double-layers, while the $\times 3$ slabs only had three silicon double-layers. The number in parenthesis was obtained using a DZP basis.

	Model	$\times 1$	$\times 2$	$\times 3$
I	HD^+S	0	0	0
II	HS^+_fD	1.4	-	-
III	HDS^+	7.0	7.3	-
IV	S^+HD	11.3	-	-
V	SS^+H	5.3 (5.6)	6.0	5.8
VI	Crain *et. al.*	-	-	5.7

atoms in different positions of the terrace. Model VI has been previously proposed by Crain *et al.* [1]. The unit cell of the structure VI is three times larger along the step direction than that of the other models. This is due to the extra Si atoms attached to the step-edge: there are two atoms every three possible sites. This was proposed as an explanation for the 1×3 superlattices (see Fig. 7.2) frequently observed in the STM images [1, 58]. We have decided not to impose the appearance of superlattices in our models. Instead we studied the stability of the step-edge against structural distortions that might be responsible of the periodic modulation in the STM images, analogical to the case of the Si(557)-Au surface and Sec. 6.3.

The main results of this section can be found in figure 7.4 and table 7.1, where the relaxed structures and the relative surface energies of the different models of the Si(553)-Au reconstruction are presented. Model I is the most stable structure. It presents a strong similarity with the Si(557)-Au reconstruction (see Fig. 6.2). The HC is placed at the step-edge and the gold atoms reside in the middle of the terrace. The main differences in the present case are the presence of a SD, associated with the HC and the different orientation of the steps, and

the absence of adatoms due to the smaller terrace. Models I and II only differ in the position of the SD and have almost degenerate energies. Changes in the location of the gold chain have stronger impact in the energy. This becomes clear by comparing models I and III, which solely differ in the site occupied by the gold atoms. This suggests that the ideal location of the gold chain is in the middle of the terrace, as was previously found for the Si(557)-Au reconstruction [69, 70].

We also tried structures where the HC has been moved away from the step-edge. In both cases, model IV and V, this yields to an increase of the surface energy. This seems to indicate that the HC is an especially stable rearrangement of the step-edge in vicinal Si(111) surfaces. In fact, in the case of Si(557)-Au surface, the HC structure formed spontaneously at the step-edge during the geometrical optimisations using density-functional calculation [69]. The model IV, with the gold chain in a position neighbouring to the step-edge, is the most unstable configuration. This points again to the larger stability of the gold substitution in the middle of the terraces.

The model by Crain *et al.* [1] (model VI) is indeed a simple variant of model V. A silicon dimer is attached to two of the step-edge atoms and another two silicon atoms in the terrace. This creates a $\times 3$ modulation along the step-edge direction similar to what has been observed in some STM images [1, 58] (see also Fig. 7.2). Interestingly, the addition of these silicon dimers leaves the surface energy almost unchanged (see table 7.1). This is consistent with the observation of large variations in the concentration of the extra silicon atoms attached to the step edge and, probably, a high mobility of these atoms. Again this seems to be consistent with the STM observations.

As was explained in Secs. 6.3-6.5, in the case of the Si(557)-Au surface the doubling of the periodicity observed with the STM can be explained as a result of a buckling of the step edge. Since this could also provide an explanation for the modulations observed in the Si(553)-Au surface, we have explored the stability of two of our models (I and V) respect to similar distortions. We have used supercells containing two or three unit cells along the step. Our relaxations started from structures where one of the atoms of the step edge was moved either upwards or downwards by $\sim$0.3 Å. In some cases, the atoms with unsaturated dangling-bonds in the terrace (see figure 7.4) were also moved upwards in an attempt to force their charging with electrons transferred from the step edge. In the case of model I this would leave a metallic step-edge band, susceptible to favour structural distortions. In other cases, the whole structure was relaxed under the constriction of a particular step-edge configuration. However, in all cases we were unable to stabilize the step-edge buckling. Once all the degrees of freedom were optimized the structures always returned to an almost perfect $\times 1$ periodicity.

We now turn our attention to the electronic band structures of our most stable models. Based on earlier studies of the Si(557)-Au surface we expect to find two surface bands with different dispersions near the Fermi level associated with the Si-Au bonds [69, 70], similar to those depicted in Fig. 6.2. In the present case, these should be a flat band originating from the Si_2-Au bonds, and a dispersive band coming from the more overlapping Si_1-Au bonds (see figure 7.4 for the labelling of the atoms). In the present calculations we have only included scalar-relativistic effects for gold. In fact, the effect of the spin-orbit interaction is expected to be negligible for the total energy of these surfaces (we have zero spin polarization). However, as we demonstrated in Sec. 6.2, the dispersive Si_1-Au band shows a considerable spin-orbit splitting (up to $\sim$200 meV near the Fermi level). As depicted in Fig. 7.1, the photoemission of the Si(553)-Au surface shows a half-occupied band featuring a clear splitting, almost identical

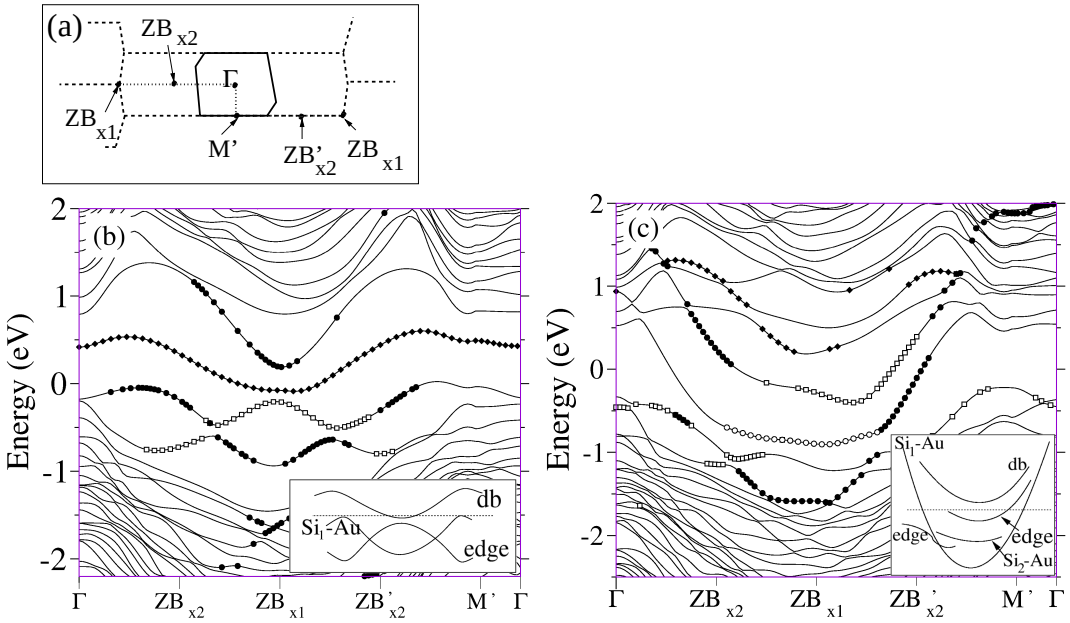

Figure 7.5: Panel (a) illustrates the Brillouin zones for the ($\times 1$) and ($\times 3$) periodicities along the step-edge. The path Γ-$ZB_{\times 2}$-$ZB_{\times 1}$-$ZB'_{\times 2}$-M$'$ is parallel to the steps, while M$'$-Γ is perpendicular. The band structure of the systems $HD^{+}S$ and $SS^{+}H$ are plotted in panels (b) and (c), respectively. Bands pertaining to the Si_1-Au and Si_2-Au *bonds* (solid and open circles, respectively), to the step edge (squares), and to the dangling bonds in the terraces (diamonds) are indicated. The atomic labels are consistent with those in figure 7.4. The insets show a schematic representation of the most prominent surface bands.

to that observed for the Si(557)-Au, and a dispersive quarter-filled band at lower binding energies. We think that the surface bands showing splitting in the experiment have to be identified with those coming from the Si_1-Au bonds.

Figure 7.5 (b) and (c) show the band structures of the models I and V, respectively. The different symbols reflect the main atomic character of the surface bands, as obtained from a Mulliken population analysis (see Sec. 2.4.2). In figure 7.5 (b) we can find an almost fully occupied band pertaining to the Si_1-Au bonds very close to the Fermi level. A dispersive band, coming from the dangling bonds in the terraces, appears practically empty. The agreement with the experimental spectra of Fig. 7.1 could be improved if the population of this band would increase. Such electron can occur associated with the presence of extra silicon atoms attached to the step-edge [1], or to the terraces (see Sec. 4.4). A surface band associated with the step-edge crosses the Si_1-Au band and almost reaches the Fermi level. There is no evidence of this band in the experiment. The band structure of model II is almost identical to the band structure of model I. A more thorough analysis on model (II) is done during the systematic search of structures in Sec. 7.5.

The band structure of model V (figure 7.5 (c)) features both a dispersive and a flat bands associated with the Si-Au bonds. The step-edge gives rise to a metallic band with a small filling. The presence of this band implies that structural distortion of the step-edge with an electronic driving force are possible. However, as described above, we have failed to stabilize such distortion in our calculations up to now.

The band structure of the model VI is presented in figure 7.6. The larger unit cell makes the comparison with the band structures in figure 7.5 somewhat complicated due to the back-folding of the bands. There is a clear gap in the Si_1-Au band associated with the symmetry

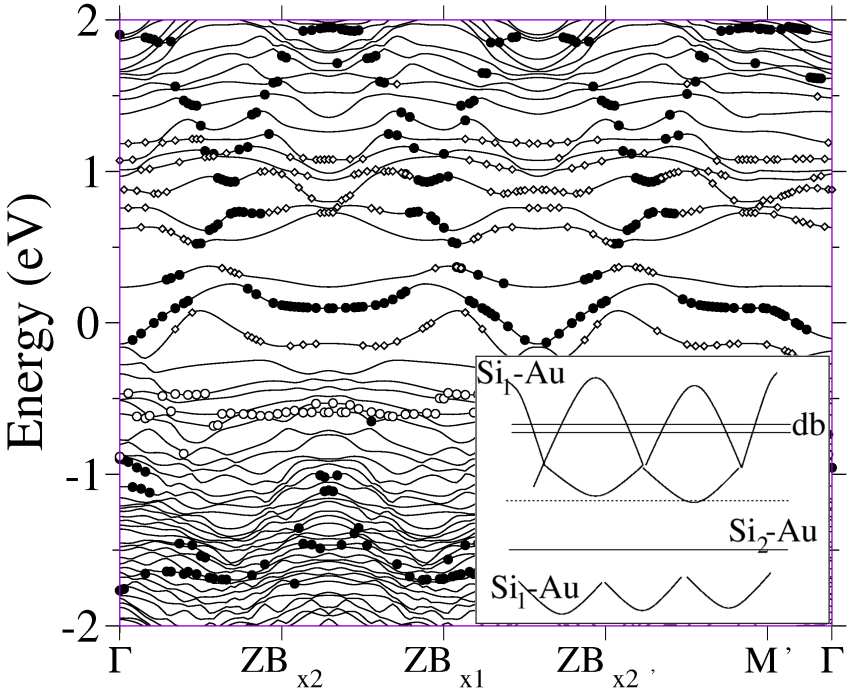

Figure 7.6: As in figure 7.5 (b) and (c), but for model VI.

breaking induced by the silicon dimers attached to the step-edges and to some of the atoms in the terraces. The changes in the three Au-Au distances in the unit cell are -0.12, -0.16 and +0.28 Å, while the corresponding Si_1-Au-Si_1 bond angles are 103°, 100° and 115°. Notice that the possible mirror symmetry of the structure is also broken in our final relaxed configuration. This can also be noticed in the slight buckling of the silicon dimers, visible in figure 7.3.

None of the band structures of the models provided in this section are able to explain the photoemission data of Fig. 7.1 for the Si(553)-Au surface. However, some of the main qualitative features are reasonably described by the band structure of model V, shown in figure 7.5 (c). There are two metallic bands with quite similar dispersions. One of them is close to half-filled and comes from Si_1-Au bonds (and, therefore, likely to exhibit an observable spin-orbit splitting). The other one comes from the step-edge and presents a small fractional filling. However, the band originating from the Si_2-Au bonds is not seen in the experiment and the details of the band structure are far from those observed experimentally.

7.3 Strategy of the structural search

In the previous section we generated "manually" configurations for the Si(553)/Au reconstructions using different physical (electron-counting, coordination, etc.) arguments. This way we were able to search only through a relatively small amount of structures, five in total. We would now like to search through a larger set of reconstructions and, somehow, calculate or at least enumerate all "reasonable" surface coordinations.

According to our experience with the silicon reconstructions, almost any trial geometry

that is not completely absurd relaxes to a nearby local minimum. However, the number of local minima scales roughly exponentially with the number of atoms involved in the reconstruction and the problem becomes intractable for large cells. Apart from this heuristic approach one can use more sophisticated algorithms that can automatically find optimum geometries. Some examples are simulated annealing [136, 137] and Monte Carlo simulations of different types, including genetic algorithms [138–140]. Monte Carlo techniques have been traditionally used to find cluster geometries [141], and have been recently extended to find surface reconstructions [142, 143]. Unfortunately these methods are computationally very expensive requiring long simulations with thousands of evaluations of the system energy (and interatomic forces in some cases). Particularly, genetic algorithms are very powerful but typically need hundrends of generations, each one containing tens of trial geometries [141]. Therefore, they are mostly restricted to the use of empirical interatomic potentials which, however, might not be sufficiently accurate to reproduce the energetics of the different geometries explored.

In the present work we adopt a compromise between these two ideas. Due to the lack of reliable empirical potentials to represent the interaction between the gold and silicon atoms in the surface, we need to explore the energetics of the different models of the Si(553)-Au reconstruction at the density functional or similar level of theory. This precludes the use of Monte Carlo algorithms to perform a global search of the reconstruction structure. However, we do not want to restrict our search to explore a “few" structural models. Thus, we will rather make a *systematic* search of the optimum surface model within a large family of physically motivated structures. Our approach is the following:

i) a family of likely structural models for the Si(553)-Au surface reconstruction is defined using a heuristic procedure based on the analogy with other related and better known surfaces;

ii) a compact notation is designed to label unambigously each of the possible structures within this family;

iii) from each of these labels, a trial geometry is generated automatically and an initial constrained relaxation is performed to avoid the appearance of unphysical bond distances;

iv) “fast" density functional calculations using SIESTA are used to relax each of the structures to its closest local energy minimum;

v) the most stable configurations from step *iv*) are studied using more time consuming “accurate" SIESTA calculations;

vi) finally, since the energy differences between different structural models are quite small, we check the energy ordering of our most stable configurations using a different methodology: plane-wave calculations using the VASP code.

By “fast" SIESTA calculations we mean here calculations performed using small basis sets (i.e, with a small number of basis orbitals per atom, like SZ or DZ basis sets [84, 86]), limiting the number of k-points and optimized degrees of freedom and/or using less stringent criteria than usual for the convergence of the self-consistency cycles. These approximations substatially reduce the computational cost. Therefore, it becomes possible to relax the hundreds of different configurations within our family of structures. We will see below that the energies obtained in this first step are reliable enough to select a set of a few tens of structures containing the most promising structural candidates. “Accurate" SIESTA calculations are performed for these configurations using DZP basis sets, a larger k-sampling and well converged self-consistency. We can see that the use of a code that utilizes basis sets of atomic orbitals is instrumental for this gradual increment of the accuracy of the calculations: while the pseudopotentials, density functional, and basic numerical scheme remains unchanged, the size of

the basis set (the main factor limiting the size of the studied systems and the computational time) can be varied. This provides a very convenient way to deal with the trade-off between computational speed and accuracy of the calculation.

In the following we present in detail the hierarchy of approximations used to perform our simulations. As a starting point we automatically generate approximate coordinates for all possible structures fulfilling certain conditions. These conditions will be explained in detail in the next section. Our family of structural models is based on plausible analogies with the structure of other related surface reconstructions like the Si(557)-Au or Si(111)-(5×2)-Au. While reasonable atomic coordinates within the plane of the terrace (that we take as the xy-plane) are relatively easy to guess due to the registry with the sub-surface bilayer, the height of the different atoms in the surface bilayer is more problematic. For this reason, in the first relaxation (named Sz hereafter) only the atoms in the topmost bilayer are allowed to relax in the z-direction (normal to the terrace). This relaxation step ensures the interatomic distances to be reasonable without changing the topology of the surface bilayer and its registry with the underlying atoms. For the Sz relaxations we use a SZ basis set and a 2×1 k-sampling. To further accelarate the simulations the parameter determining the convergence of the density matrix in each relaxation step (DM.Tolerance [144]) is set to 10^{-3}. The typical value given to this parameter to ensure a very good convergence of the self-consistent solution is 10^{-4}. However, we have checked that increasing this value to 10^{-3} only introduces small errors in the calculation of energy and forces: for example, the maximum force difference during the relaxation of a few representative structures of those studied here was less than 0.01 eV/Å when the two different convergence criteria were used. In spite of this moderate effect on the results, in some cases increasing the value of DM.Tolerance to 10^{-3} reduces considerably the number of steps per self-consistency cycle. In the next step (named Sy hereafter) all atoms are allowed to move (except the silicion atoms in the bottom of the slab and the hydrogen atoms directly bonded to them). However, in order to preserve the topology of the selected configuration, the positions of the atoms along the direction parallel to the step edges (y-axis) is fixed. Other parameters have the same value as in the relaxation Sz. The purpose of the relaxations Sz and Sy is to provide a sound initial configuration from the coordinates generated automatically. Using this corrected guess we can proceed further allowing all degrees of freedom in the slab to relax and using a more complete DZ basis set and accurate 8×4 k-sampling. We call this the $D^{\star}$ relaxation. Finally, in the D relaxations we further decrease the tolerance for the covergence of the elements of the density matrix to its usual default value in SIESTA [144] of 10^{-4}. We use a DZP basis set for our most accurate relaxations (DP hereafter). Adding a polarization shell with d symmetry can be especially important to accurately describe “unusual" coordinations of the silicon atoms which cannot be described with simple sp hybridizations.

The use of this series of optimization schemes with ever-increasing accuracy ($Sz \rightarrow Sy \rightarrow D^{\star} \rightarrow D \rightarrow DP$) is much more efficient than starting directly with a relaxation at the DP or similar level. The reason for this efficiency gain is twofold: *i*) the initial coordinates used to start each relaxation have been optimized at the previous level and, therefore, they are an initial guess of increasing quality; *ii*) the energy estimates obtained with the less accurate relaxations, already at the Sy level, are accurate enough to allow discarding many of the possible configurations in favor of the most favorable models. This is the case even if at the Sy level we use a minimal basis set, a thin slab of two bilayers and we fix the atomic coordinate parallel to the step edge in order to preserve the selected bonding topology. One has to take into account that a minimal basis for Si contains only four orbitals, a DZ basis eight orbitals, and a DZP basis thirteen

orbitals. Thus the computational cost changes dramatically when changing the basis set size. Additional gains are obtained by using smaller k-samplings and reducing the number of step in each self-consistent cycle.

7.4 Structural models: a labelling scheme

The structural models that we are considering for the Si(553)-Au reconstruction are based on the analogy with the Si(557)/Au and the Si(111)/Au-5x2 reconstructions of Chaps. 4 and 6. The most important features of the most stable structural models of these surfaces are:

i) the reconstruction only involves the atoms in the topmost bilayer;

ii) the gold atoms occupy substitutional positions in the surface layer, which are much more favorable than adatom-like sites;

iii) positions of gold in the middle of terraces are favored over step-edge decoration;

iv) frequent appearance of the honeycomb chain (HC) structure.

Fig 7.7 (a) shows a schematic view of an unreconstructed Si(553) surface. Taking into account the points *i*) and *ii*) we only explore here reconstructions generated adding an additional bilayer ontop of this unreconstructed substrate. One of the silicon positions is replaced by a gold atom. Different registries with underlying bilayer are allowed, as well as, the presence of HC structures. Fig 7.7 (b), (c) and (d) show a few possible structures. Structure (b) recovers the unreconstructed surface. Structure (c) presents stacking fault in the middle of the terrace with the accompanying surface dislocations with under- and over-coordinated atoms (indicated by arrows in Fig. 7.7). In panel (c) the surface bilayer contains a HC structure in the middle of the terrace. Notice that the HC reconstruction also creates a stacking fault towards the $[\bar{1}\bar{1}2]$ direction (i.e., towards the inner part of the terrace). This stacking fault has to be corrected in order to connect with the bulk structure. Therefore, it is necessary to introduce a surface dislocation with over-coordinated atoms (marked with an arrow).

In Sec. 7.2 we explored a few structural models for the Si(553)-Au reconstruction based on an analogy with the Si(557)-Au surface. Here we want to move a step further and to make a comprehensive search among the structural models that can be built following the rules (*i*)-(*iv*) presented above. We consider *all* possible structures where the atoms of the topmost bilayer present coordinations between 2 and 4 with other atoms in the same bilayer. The final coordination depends on the registry with the underlying silicon structure. One of the silicon atoms in the unit cell is replaced by a gold atom. The Si(553)-Au reconstruction is known to suffer several distortions that increase the size of the unit cell along the step direction as the temperature is decreased. [59, 64] However, here we only consider models that preserve the $\times 1$ periodicity of the silicon substrate along the steps and, therefore, are relevant to model the high temperature structure.

We have developed a simple labelling scheme for the family of structural models that fulfill the criteria presented above. We can label each structure and thus count the total number of different trial structures within this family. Furthermore, this scheme can be easily translated into a procedure to automatically generate the trial geometries. The basis of our labelling procedure can be found in Fig. 7.8. First, the possible positions within the *xy* plane of the surface atoms are discritized and approximated by the points of a grid. The grid is formed by nine columns and two rows. The nine columns correspond to the positions of the atoms along the $[11\bar{2}]$ direction in the terrace of an unreconstructed Si(553) surface (see the Fig. 7.7 (b)).

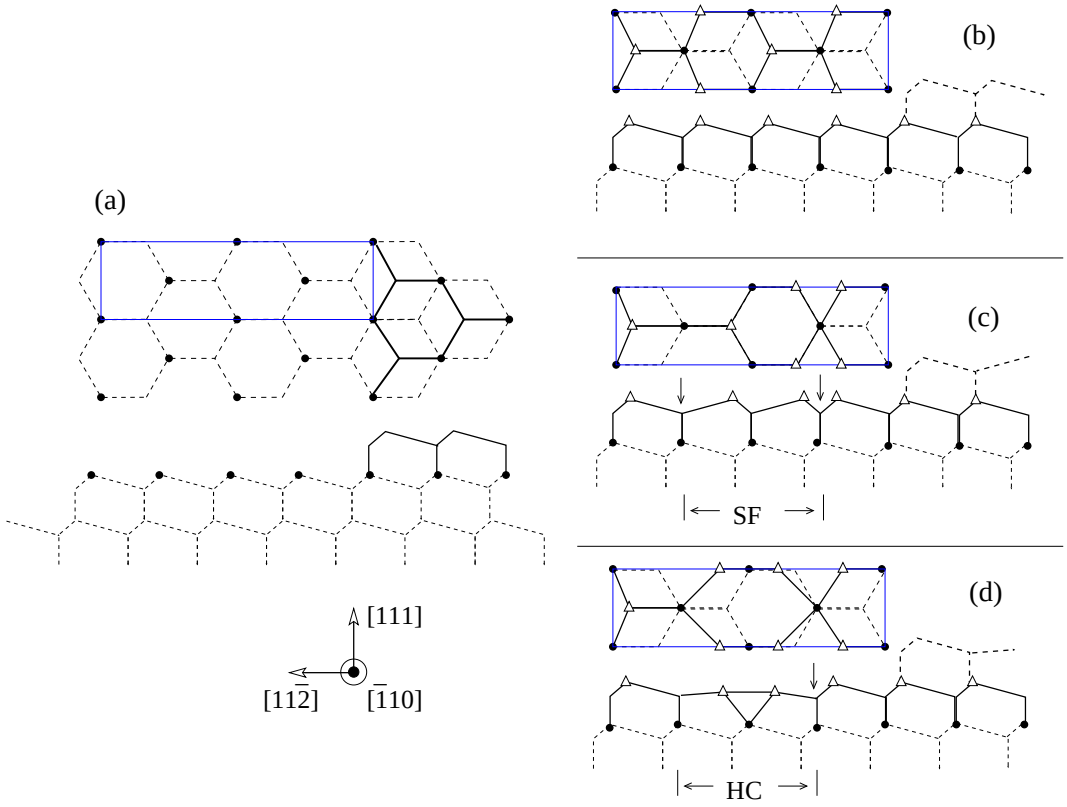

Figure 7.7: (a) Schematic view of the unreconstructed Si(553) surface. The steps run parallel to the $[\bar{1}10]$ direction and are oriented towards the $[11\bar{2}]$ direction. The rectangle indicates the "unit cell" *within* the terrace, containing nine inequivalente silicon sites (with four unsaturated dangling-bonds). Panels (b), (c) and (d) show configurations generated by adding a silicon bilayer on top of the structure in panel (a). The different reconstructions explored in this paper are obtained by changing the structure of this surface bilayer and/or its registry with the underlying atoms. Open triangles represent atoms in the topmost atoms and solid circles the higher atoms in the second bilayer. These structures (and all the structures considered in the present work) preserve a $\times 1$ periodicity along the step. Structure (b) recovers an unreconstructed silicon structure. Structure (c) presents a surface dislocation close to the step egde that generates a stacking fault (SF) that is later corrected creating another surface dislocation in order to connect with the bulk structure. Surface dislocations create under- and over-coordinated atoms which appear indicated by arrows. Model (d) presents a honeycomb-chain (HC) structure and the accompanying surface dislocation.

Second, all possible structures created by distributing the atoms among the grid points can be translated into a sequence of nine numbers. The position along the horizontal coordinate (column) is indicated by the order in the numerical sequence. The first number corresponds to the atoms at the step edge. For a given column, a "2" ("4") indicates that a silicon (gold) atom is located in the higher row, i.e., in the middle of the rectangular terrace unit cell, whereas a"1" ("3") indicates that a silicon (gold) atom sits over a grid point in the lower row. A "0" indicates that there are no atoms in that column. Using this scheme, the unreconstructed Si(553) surface in Fig. 7.7 (b) can be label as (1,2,2,1,1,2,2,1,1), while structures in panels (c) and (d) would receive the label (1,2,2,2,1,1,2,1,1) and (1,2,2,1,0,1,2,1,1), respectively. Other examples, corresponding to models already studied in Sec. 7.2 can be found in Fig. 7.8.

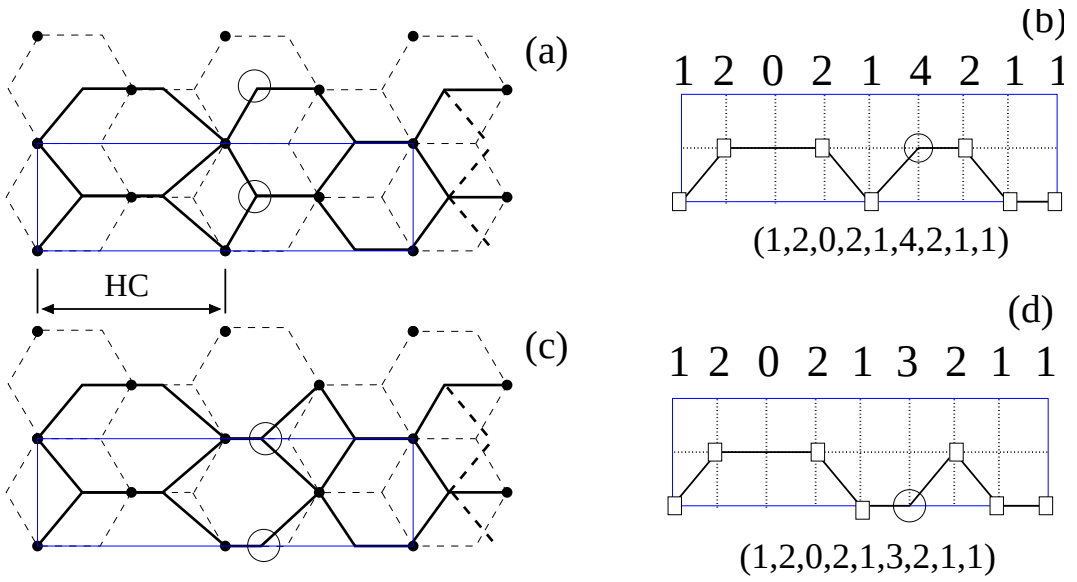

Figure 7.8: (a) and (c) show two possible structures for the Si(553)-Au surface already explored in Sec. 7.2. These structures are characterized by the presence of a HC structure close to the step-edge. Solid lines indicate the bonds between atoms in the topmost bilayer of a given terrace, thin dashed lines correspond to the underlying silicon bilayer, and thick dashed lines indicate a few bonds of the upper terrace. The small solid circles mark the positions of the higher silicon atoms in the underlying bilayer The large open circles mark the substitutional sites occupied by the gold atoms. The rectangle corresponds to the terrace "unit cell". Panels (b) and (d) schematically explain how the structure of the surface bilayer can be translated into a sequence of nine numbers. First the possible positions of the atoms are approximated by the points of a grid. The grid is formed by nine columns and two rows. The position along the horizontal coordinate is indicated by the order in the numerical sequence. The first number corresponds to the atoms at the step edge. A "2" ("4") indicates that a silicon (gold) atom is located in the higher row, i.e., in the middle of the rectangular cell. A "1" ("3") indicates that a silicon (gold) atom sits over a grid point in the lower row. A "0" indicates that there are no atoms in that column.

In principle, using our notation we can generate M different models, with

$$M = 2^{(N_{Si}+1)} \frac{9!}{(8-N_{Si})!\, N_{Si}!} \tag{7.1}$$

and N_{Si} being the number of silicon atoms in the surface bilayer. Since we always have one gold atom, the total number of atoms in the terrace unit cell is N_{atm}=N_{Si}+1. We consider here structures with N_{Si}=7. In this way, the family of structures studied here includes the five models already discussed in Sec. 7.2. Furthermore, having N_{atm}=8 is a necessary condition to allow for the formation of the HC structure, which is one of the common building blocks to several gold induced reconstructions in Si(111) and vicinal Si(111) surfaces (see above). With N_{Si}=7 we have M=18432 different models. This large number can be considerably reduced imposing a few constraints to ensure that the models represent physically sound structures. These constraints are: *a*) in order to connect with the bulk structure the last number of the series must be either 1 or 3; *b*) the dangling-bonds of the underlying silicon bilayer must be saturated either by an atom or by a dimer as in the HC structure, therefore the first number of the labelling sequence must be always 1 or 3, *c*) the fifth number must be 0, 1 or 3 (if 0, then the neighboring numbers must be either 1 or 3), and *d*) the third and seventh number must be 0, 2 or 4 (if 0, then the neighboring numbers in the sequence must be 2 or 4); *e*) to

ensure the connectivity within the surface bilayer, a non-zero number in the sequence cannot be surrounded by zeros and *f*) two or more zeros cannot appear together. Taken into account conditions (*a*)-(*f*), the number of possible configurations with N_{atm}=8 and N_{Si}=7 is reduced to M=210. In the following section we will explore these 210 configurations using "fast" SIESTA calculations, as decribed in the previous section, and a few tens of the most stable configurations will be selected to perform more accurate SIESTA and VASP calculations.

Our notation provides information about the connectivity within the surface bilayer and the registry with the substrate. From a given sequence of nine numbers we can generate a trial geometry. However, we lack information about the heights of the different atoms. Due to this and to the discretization of positions in the *xy*-plane, the bond lenghts and angles in the automatically generated structures can considerably depart from the correct values. For this reason, as a first step to get sound initial configurations we need to perform constraint relaxations that, while preserving the bonding topology of the selected configuration avoid unphysical bond distances and angles. We use the Sz and Sy relaxations described in the previous section for this.

Besides the family of structures described above, we have explored a few structural models based on the π-bonded chain reconstruction of the Si(111) surface. [114,145,146] In principle, our notation cannot describe these bonding pattern: it can only describe structures which are based on a "flat" surface bilayer. This is partially due to the lack of information about the atomic heights. However, we can modify our notation to describe the π-bonded chain structures. This is done allowing for a double occupation of the columns and is schematically illustrated in Fig. 7.9. These double occupation indicates the position of the π-bonded chain in the structure. We still have the ambiguity about the relative height of atoms in the π-bonded chain, which is known to be tilted. There are two possibilities which are usually referred as negative or positive tilt. [147] In our notation these two different tilts of the π-chain are indicated by the order of the pair of indices, the second index corresponding to the higher atom. In Fig. 7.9 we present a Si(553) surface reconstructed with the negative tilt chain. This negative tilt π-chain block corresponds to the label (...,1,0,2,21,1,...), while the label (...,1,0,2,12,1,...) denotes the positive tilt structure. Both configurations are quite similar and first-principles calculations predict them to be almost degenerate in energy and separated by a very small energy barrier. [148, 149] Experimentally the positive tilt structure has been traditionally favored. [145–147] In the case of the Si(553) stepped surface, our calculations predict the negative tilt structure to be slightly more stable.

This notation opens the possibility of generating and studying all possible structures containing the π-bonded chain. However, we have not pursued this approach here and we limit to consider nine different structural models that are obtained after the substitution of one silicon atom by a gold atom in different positions of a π-bonded chain reconstruction similar to that shown in Fig 7.9.

Next we take advantage of the methodology described in sections 7.3 and 7.4 to make an extensive search of the structure of the Si(553)-Au reconstructions. We make a systematic search within the 210 structures that can be generated with the notation presented in Sec. 7.4 (models based on "flat" bilayers with different coordinations and registries with the susbtrate) with seven silicon atoms and one gold atom in the terrace unit cell. We also present results from a much more restricted search for structures based on the π-bonded chain reconstruction (see Sec. 3.3.2). Finally the most stable structures from these two searches are studied using accurate SIESTA and VASP calculations. We present results for the band structure and the

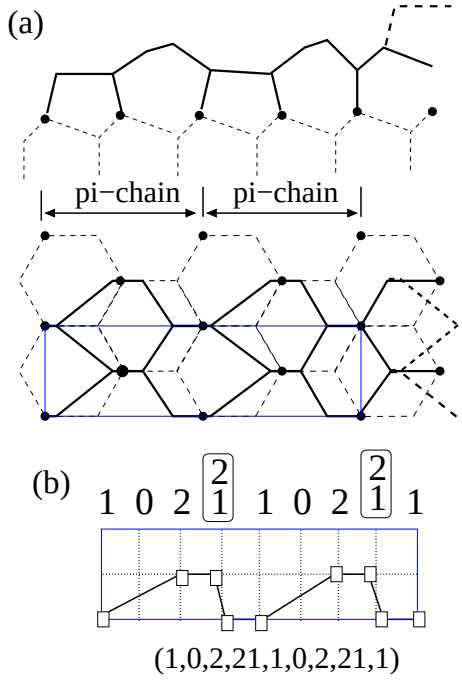

Figure 7.9: (a) Scheme of a π-bonded chain reconstruction of the Si(553) surface, and (b) the proposed notation for such structure. The presence of the π-bonded chain at a certain location is indicated by the double occupation of the corresponding column, the second atom of this pair occupies the higher position along the π-chain.

simulated STM structures of some of the final models.

7.5 Systematic search: “flat” bilayers with N_{atm}=8

We first explore the energy of the 210 possible configurations using our fastest relaxation schemes, Sz and Sy, described in Sec. 7.3. These calculations transform an initial structure automatically generated from a given label into a physically sound structure. In spite of the thin slab and minimal basis utilized, the relative energies obtained at the Sy level (ΔE_1) already provide a good guide to eliminate the most unstable structures. In Table 7.2 we can find a list with the 80 most stable configurations ($\Delta E_1 \leq \sim$33 meV/Å^2) obtained after Sy relaxations. Several of the initial structures converge to the same configuration, so these 80 trial structures give rise only to $\sim$40 different models. This is clearly seen in Fig.(7.11), where the plateaus in the energy curve correspond to this “lumping” of several initial geometries into a single geometry. These transformations typically take place by a displacement of the surface bilayer as a whole, thus changing its registry with underlying substrate, or by the movement of a vacancy to a neighboring position (using our notation this corresponds to a transformation (..,0,1,2,..) $\rightarrow$ (..,1,0,2,..)). This happens for example in the case of the (1,2,2,1,1,0,4,1,1) initial structure, that transforms into a configuration that is better described with the label (1,2,0,2,1,1,4,1,1) and is one of the most stable structures. This can be seen in Fig. 7.10

The 68 most stable structures, as predicted by ΔE_1, are then calculated again, this time with more accurate relaxation schemes up to the DP level (for details, see Tab. 7.2). Hereafter, we will refer these final relative energies with ΔE_2. A comparison between ΔE_1 and ΔE_2 can

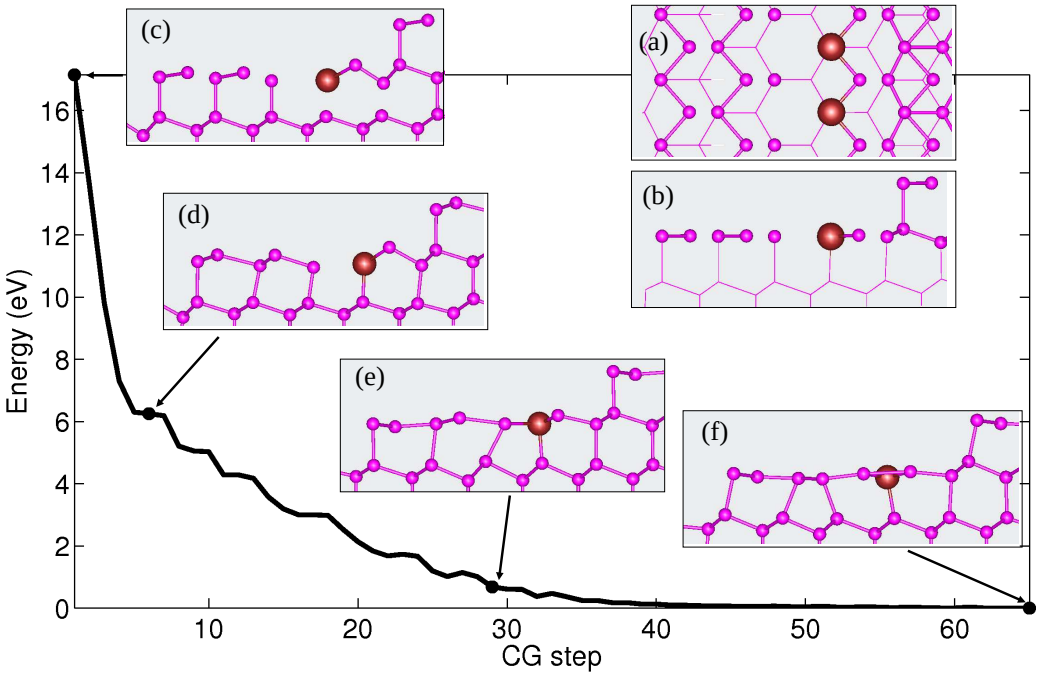

Figure 7.10: Relaxation of the structure generated from the label (1,2,2,1,1,0,4,1,1) at the Sy level. Insets (a) and (b) present a top and a lateral view of the automatically generated structure. Inset (c) presents the structure after the relative heights of the atoms have been corrected by the Sz relaxation. In point (d) we have already reached a structure similar to the configuration that we want to explore. However, this configuration is not stable and transforms by the displacement of the surface bilayer (inset (e)) into a different structure. The final structure, shown in inset (f), is better described by the (1,2,0,2,1,1,4,1,1) label.

be found in Tab. 7.2 and Fig. 7.11. From Fig. 7.11 we observe that again, several initial configurations end up in only few final geometries, but in a slightly different way than in the case of ΔE_1. Some of these final geometries are marked with labels f1-f10 both in Fig. 7.11 and Tab. 7.2.

The labelled final structures are shown in Fig. 7.12. The fast Sy relaxations (ΔE_1) predicted f1 to be most stable configuration. It exhibits a HC structure at the step-edge, while the gold atom is located at a surface dislocation in the middle of the terrace. The presence of a surface dislocation is necessary to recover the bulk stacking disrupted by the HC. The position of the gold atom seems reasonable, gold should be a better option than silicon to sit at the dislocation since gold does not exhibit strong directional bonding. However, using a more complete basis set (already a DZ basis gives the correct result) and a thicker slab the f2, f3 and f4 geometries become the most favorable structures (they are almost degenerate and $\sim$4 meV/Å^2 more stable than f1). This points to the importance of using more complete (and thus flexible) basis sets when the coordination of the surface atoms departs from simple sp hybridization (like in the case of the HC structure or at the surface dislocations).

Our results indicate that the configurations featuring a HC structure at the step edge (similar to the Si(557)-Au structure) are the most stable, at least within the family of reconstruction considered here. This confirms the results obtained in Sec. 7.2, where we only studied six different models. The configurations f4 and f2 in the present study correspond with the most stable structures obtained in Sec. 7.2 (named respectively I and II in that reference). Also configuration f8, f9 and f10 correspond to structures III, IV and V in Sec. 7.2. Configuration

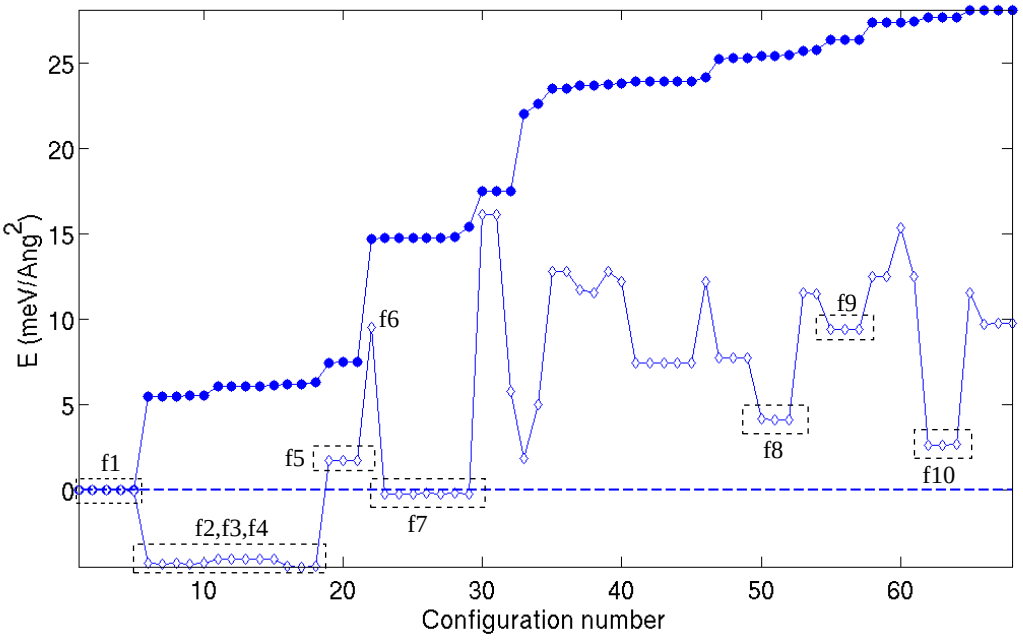

Figure 7.11: Relative energies after fast Sy (ΔE_1, solid circles) and accurate DP (ΔE_2, open diamonds) relaxations for the systems listed in Tab. 7.2. The system labels f1-f10 correspond to those of Tab. 7.2 and Fig. 7.12.

f3, however, is a new configuration exhibiting a double honeycomb structure similar to that found in some models of the Si(111)-(5×2)-Au reconstruction (see Chap. 4).

In Sec. 7.4 we pointed out that our labelling scheme excludes, in principle, structures based on the π-bonded chain reconstruction. However, in Fig. 7.12 we can find one structure where the π-bonded chain reconstruction has emerged spontaneously. In configuration f6 the gold atom is located very close to the step edge. The initial structure corresponds to a largely unreconstructed terrace. It is well known [115] that the energy barrier for the transformation from the unreconstructed Si(111) to the π-bonded chain Si(111)-(2×1) reconstruction is very small. Therefore, the appearance of the π-bonded chain in this case is not very surprising.

The experimental electronic band structure, as determined by photoemission experiments [1, 1, 59], presents three bands with parabolic dispersion and strong one-dimensional character. Two of them are similar to those found for the Si(557)-Au surface and, therefore, can be assigned to the spin-split bands formed from the hybridization of Au 6p states with the sp lobes of the neighboring Si atoms, as proposed in Chap. 6. The third band appears centered around the same point in reciprocal space, but at higher energies and thus with a lower occupation around $\frac{1}{3}$.

In Fig. 7.13 we can find the band structures of the models f2 and f3. The band structure of the model f4 can be found in Fig. 7.5b. The geometries of f2 and f4 are very similar (see Fig. 7.12) but their band structures present some small but essential differences. Both models present one dispersive one-dimensional band coming from the hybridization of gold with its silicon neighbors. This band can be identified with the spin-split bands observed in the Si(553)-Au surfaces [1, 62] and Si(557)-Au [28]. Two other surface bands appear close to the Fermi level: a dispersive band coming from a silicon dangling-bond in the surface and a

No.	Initial configuration	ΔE$_1$ (meV/Å^2)	ΔE$_2$ (meV/Å^2)	No.	Initial configuration	ΔE$_1$ (meV/Å^2)	ΔE$_2$ (meV/Å^2)
1	1,2,2,0,1,1,4,1,1	0.00	0.00	41	1,2,2,0,3,1,2,1,1	23.88	7.47
2	1,2,2,1,0,1,4,1,1	0.00	0.00	42	1,2,2,3,0,1,2,1,1	23.90	7.48
3	1,2,2,1,1,0,4,1,1	0.00	0.00	43	1,2,2,3,1,0,2,1,1	23.91	7.47
4	1,2,0,2,1,1,4,1,1	0.00	0.00 (f1)	44	1,2,0,2,3,1,2,1,1	23.91	7.47
5	1,0,2,2,1,1,4,1,1	0.01	-0.01	45	1,0,2,2,3,1,2,1,1	23.91	7.47
6	1,2,2,0,1,3,2,1,1	5.51	-4.27	46	1,2,0,2,1,1,2,2,3	24.13	12.18
7	1,2,2,1,0,3,2,1,1	5.51	-4.29	47	1,2,0,2,1,2,4,1,1	25.23	7.76
8	1,0,2,2,1,3,2,1,1	5.51	-4.26	48	1,0,2,2,1,2,4,1,1	25.24	7.77
9	1,2,2,1,3,0,2,1,1	5.53	-4.30	49	1,2,2,0,1,2,4,1,1	25.24	7.77
10	1,2,0,2,1,3,2,1,1	5.54	-4.28 (f2)	50	1,2,0,2,1,2,2,3,1	25.41	4.17 (f8)
11	1,2,2,1,1,0,2,3,1	6.08	-4.02	51	1,2,2,0,1,2,2,3,1	25.41	4.13
12	1,2,0,2,1,1,2,3,1	6.09	-4.01 (f3)	52	1,0,2,2,1,2,2,3,1	25.42	4.13
13	1,2,2,0,1,1,2,3,1	6.09	-4.02	53	1,2,0,4,1,2,2,1,1	25.67	11.56
14	1,2,2,1,0,1,2,3,1	6.09	-4.01	54	1,2,4,0,1,2,2,1,1	25.72	11.50
15	1,0,2,2,1,1,2,3,1	6.12	-4.02	55	1,4,2,0,1,1,2,1,1	26.31	9.40
16	1,0,2,2,1,4,2,1,1	6.21	-4.42	56	1,4,2,1,0,1,2,1,1	26.34	9.40
17	1,2,0,2,1,4,2,1,1	6.23	-4.46 (f4)	57	1,4,2,1,1,0,2,1,1	26.36	9.40 (f9)
18	1,2,2,0,1,4,2,1,1	6.29	-4.45	58	1,4,0,2,1,2,2,1,1	27.35	12.50
19	1,2,0,2,3,2,2,1,1	7.47	1.75 (f5)	59	1,0,4,2,1,2,2,1,1	27.35	12.49
20	1,2,2,0,3,2,2,1,1	7.49	1.73	60	1,2,4,0,1,1,2,1,1	27.37	15.34
21	1,0,2,2,3,2,2,1,1	7.49	1.74	61	1,4,2,0,1,2,2,1,1	27.40	12.50
22	1,0,4,1,1,2,2,1,1	14.69	9.55 (f6)	62	1,2,2,3,1,2,2,0,1	27.62	2.66
23	1,2,2,1,1,0,2,4,1	14.76	-0.20	63	1,2,2,3,1,2,0,2,1	27.63	2.66 (f10)
24	1,2,2,1,0,1,2,4,1	14.76	-0.20	64	1,2,2,3,0,1,2,2,1	27.63	2.68
25	1,2,2,1,1,2,0,4,1	14.77	-0.21	65	1,4,2,1,1,0,2,2,1	28.08	11.52
26	1,2,0,2,1,1,2,4,1	14.77	-0.17 (f7)	66	1,0,4,2,1,1,2,2,1	28.09	9.70
27	1,2,2,0,1,1,2,4,1	14.78	-0.20	67	1,4,2,1,0,1,2,2,1	28.09	9.75
28	1,2,2,1,1,2,4,0,1	14.82	-0.18	68	1,4,2,0,1,1,2,2,1	28.09	9.75
29	1,0,2,2,1,1,2,4,1	15.41	-0.20	69	1,2,2,1,0,3,2,2,1	28.91	
30	1,0,2,2,1,3,2,2,1	17.49	16.12	70	1,2,0,4,1,1,2,1,1	29.48	
31	1,2,0,2,1,3,2,2,1	17.49	16.13	71	1,2,4,1,0,1,2,1,1	29.48	
32	1,2,2,0,1,3,2,2,1	17.50	5.77	72	1,2,4,1,1,0,2,1,1	29.51	
33	1,0,2,3,1,2,2,1,1	21.98	1.89	73	1,0,2,1,1,4,2,1,1	32.35	
34	1,0,2,4,1,2,2,1,1	22.57	5.00	74	1,1,2,4,1,0,2,2,1	33.05	
35	1,2,2,1,1,2,0,2,3	23.49	12.80	75	1,1,2,4,1,2,2,0,1	33.05	
36	1,2,2,1,1,2,2,0,3	23.49	12.79	76	1,1,2,4,1,2,0,2,1	33.06	
37	1,2,2,1,0,1,2,2,3	23.64	11.70	77	1,2,0,2,3,1,2,2,1	33.43	
38	1,2,2,0,1,1,2,2,3	23.68	11.55	78	1,2,2,0,3,1,2,2,1	33.43	
39	1,2,2,1,1,0,2,2,3	23.72	12.78	79	1,0,2,2,3,1,2,2,1	33.43	
40	1,0,2,2,1,1,2,2,3	23.79	12.20	80	1,2,0,2,1,2,2,1,3	33.48	

Table 7.2: Results from the automatic structural search. Total energies ΔE_1 are obtained using a thin slab of only two silicon bilayers and the fastest (and less accurate) relaxations (Sz and Sy). Only the 80 most stable configurations (out of the total 210 studied structures) are included in this table, with a maximum energy difference of $\Delta E_1 \sim 33$ meV/Å^2. The configurations are numbered according to their predicted stability. The initial configurations are labelled using the notation developed in Sec. 7.4. The 68 most stable structures, according to ΔE_1 are also calculated using a thicker slab of four bilayers and our accurate SIESTA calculations ($D^\star \rightarrow D \rightarrow DP$), resulting in the energy ΔE$_2$. Many of the initial configurations converge to a single configuration, this degeneracy being slightly different in the case of ΔE_1 and ΔE_2 (see also Figs.(7.11) and (7.12)). Some of these single configurations have been indicated by (f1)-(f10).

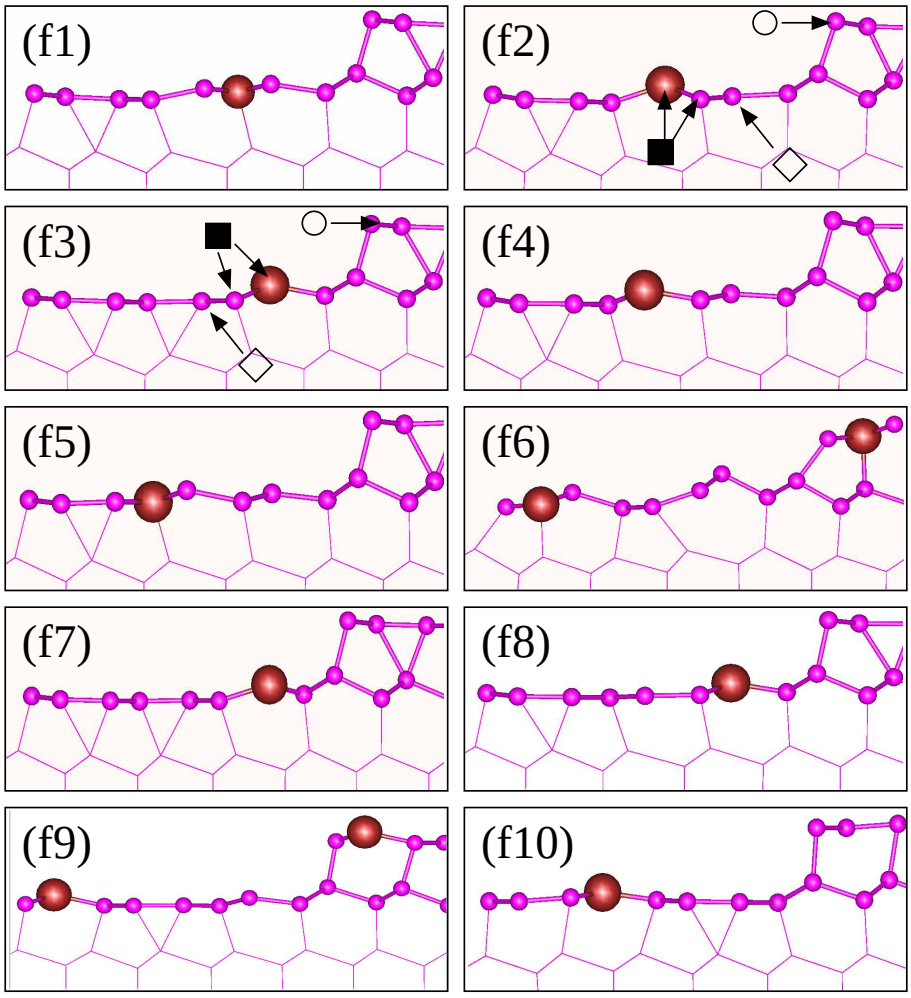

Figure 7.12: Final geometries (at the DP level) for a few selected configurations from those listed in Tab. 7.2 and Fig. 7.11. For (f2) and (f3) some symbols for the population analysis of the band structure have been added (see Fig. 7.13).

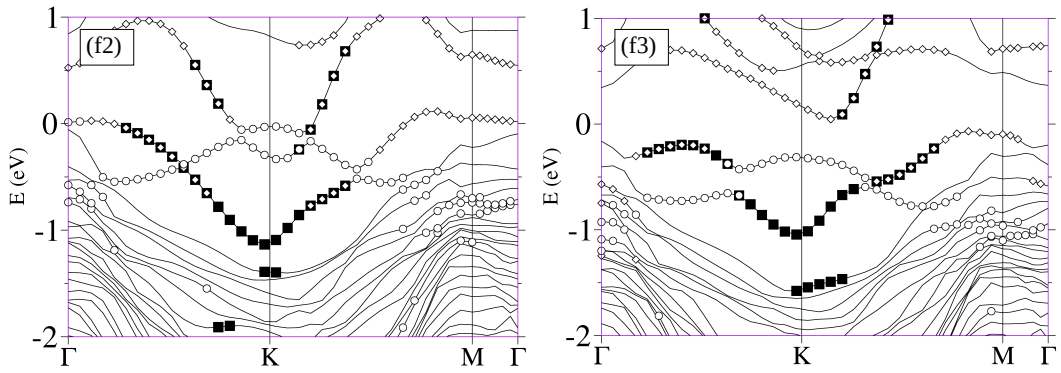

Figure 7.13: Band structures for models f2 and f3, calculated using SIESTA. The atomic character of different bands is indicated with the same symbols as in Fig. 7.12. Filled squares indicate the contribution coming from the gold atoms and their silicon neighbors, open circles that coming from the atoms at the step edge, and open diamonds that of some silicon atoms in the surface presenting some unsaturated bonds.

band derived from the atoms at the step edge (that has a HC structure). These bands are also present for both models. However, while in the case of the f4 structure the step-edge band is completely filled and the dangling-bond band is empty (Fig. 7.5b) in the case of the f2 model these two bands cross and the dangling-bond band has a small occupation of $\sim \frac{1}{5}$ electrons closer to the experimental observation.

The population of the different bands can be roughly understood taking into account the larger electron affinity of gold and the HC structure [66] as compared to other atoms in the surface. The population of the dangling-bond band is thus depleted in favor of the other surface bands. The differences between the f2 and f4 structures are more subtle. These two models only differ in the position of the surface dislocation. Energetically this structural change has small consequences and both structures are almost degenerate. However, it changes the occupation of the dangling-bond band. In the case of the f2 model the dislocation involves the gold atoms and some of the silicon atoms of the HC structure. This increases slightly the energy of the bands associated with the HC and, as a consequence, the step-edge band transfers some of its population to the dangling-bond band.

Fig. 7.13 also shows the band structure of the f3 model. The dangling-bond band is missing in this case. This spoils the comparison with experiment. The other two bands (gold and step-edge derived) are very similar to those found for the f2 and f4 models. This is reasonable taking into account the similar gold site and structure of the step-egde.

Fig. 7.23 (b) shows the band structure of the f2 model calculated including the spin-orbit interaction with the VASP code. The band structure is in excellent agreement with that calculated using SIESTA. It also confirms that all the bands close to E_F with a significant weight in the gold atoms exhibit a splitting that has its origin in the spin-orbit interaction.

Although the band structure of the model f2 does not exactly reproduce the photoemission results [1, 1, 59], particularly the characteristic band fillings mentioned above, it has some clear qualitative similaritires with them. We find two bands with similar dispersions, with their minima $\sim$1 eV and $\sim$0.5 eV below the Fermi energy at the Brillouin-zone boundary. This corresponds very well to the photoemission data. Furthermore, the band with its minima at lower energy shows a notable band splitting near the Fermi energy due to the spin-orbit interaction. The is in good agreement with the experiments. However, the band structure of Fig. 7.23 (b) has two important differences compared to the photoemission data. Firstly, the dangling-bond band presents an important spin-orbit splitting associated with its appreciable hybridization with gold (see Fig. 7.13). This splitting is not observed in the experiments. Secondly, the theoretical band structure has one extra band not seen in photoemission. This band is associated with the HC structure at the step-edge edge and has its minimum at Γ, contrary to the case of the other two bands.

We can also compare the predictions for our models with the experimental STM images. In Fig. 7.15 and Fig. 7.16 we show the simulated STM images at different voltages for the f2 and f4 models. In agreement with the experimental images [59, 63, 64] the most prominent feature is the step edge. Within the terrace we find signals coming from the row of gold atoms and its neighboring HC structure. The gold chain is seen as a continuous line for occupied states and presents more structure for empty states. For both positive and negative voltages we can also distinguish a signal coming from the unsaturated silicon dangling bond in the terrace close to the step edge. The step edge and the gold chain could be identified with the two parallel chains reported by Snijders *et al.* [64] In their recent experiment, they observe a strong polarity despendence in the STM images, and in particular, find zigzag structures for empty states and

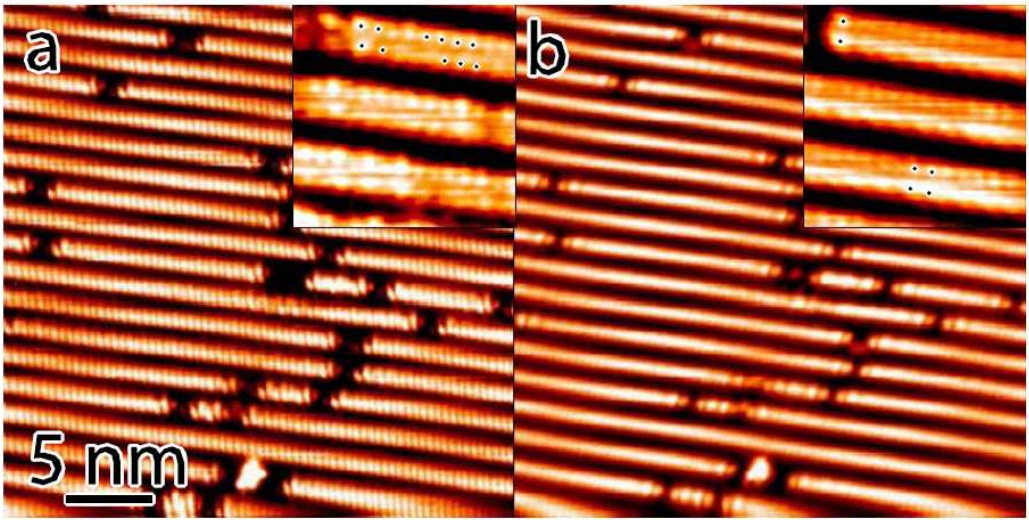

Figure 7.14: Experimental (a) empty state and (b) filled state (±0.5 V, 50 pA) STM images taken simultaneously at RT. Insets show magnifications. The structure in the chains is indicated with dots. Picture taken from Ref. [64].

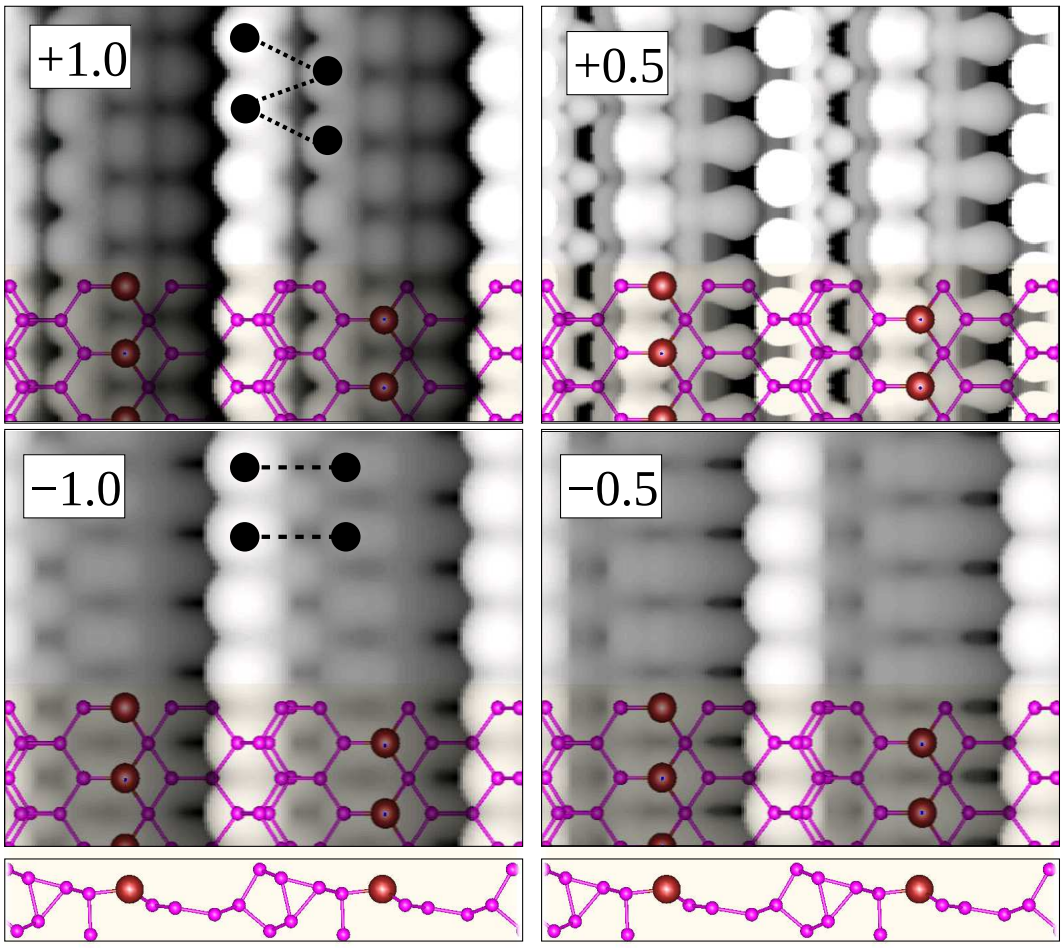

Figure 7.15: Simulated STM images, calculated using SIESTA, for model f2. The insets of the panels indicate the bias voltage in Volts. Some features having a strong polarization with respect to the voltage are indicated by filled circles.

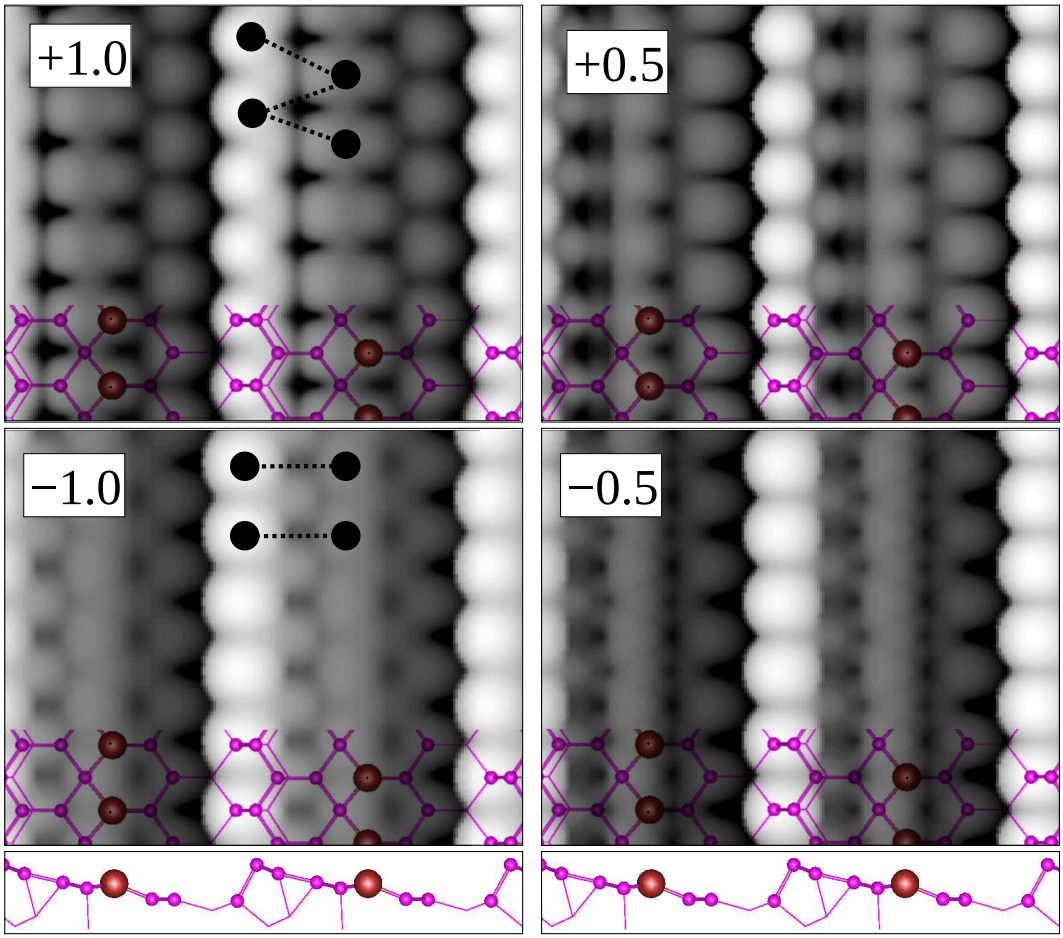

Figure 7.16: Simulated STM images, calculated using SIESTA, for model f4. The insets of the panels indicate the bias voltage in Volts. Some features having a strong polarization with respect to the voltage are indicated by filled circles.

ladder configurations for filled states. In figures 7.15 and 7.16 we have sketched some possible candidates for this kind of behaviour. For f2 (Fig. 7.15), the ladder structure in filled states could result from the registry of the step-edge with respect to the gold atoms. For empty-states images the step-edge becomes slightly more visible and the zigzag geometry could result from the atoms inside the honeycomb-chain. In the case of model f4 (Fig. 7.16), we can identify two entities that change their registries when going from filled to empty states. They are the step-edge and the complex formed by Au and the surface dislocation. They show, similar to the experiment, ladder and zigzag configurations respectively for filled and empty states.

7.6 Restricted search: structures based on the π-bonded chain

We first explore two models of the Si(553) stepped silicon surface where the terraces are fully covered by a (2×1) π-bonded chain reconstruction. They correspond to two slightly different arrangements of the π-bonded chain (Fig 7.17). Our most stable geometry (model p0) correspond to the so-called negatively tilted π-bonded chain. [147] In low energy electron diffraction experiments of the flat Si(111) surface the positive-tilt π-bonded chain is usually

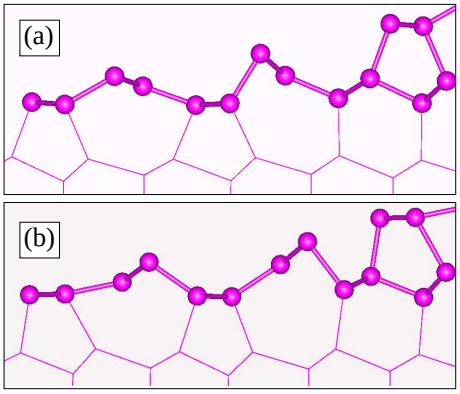

Figure 7.17: Two possible models of the Si(553) surface based on a π-bonded chain reconstruction of the terraces. Model p in panel (a) and model p0 in panel (b).

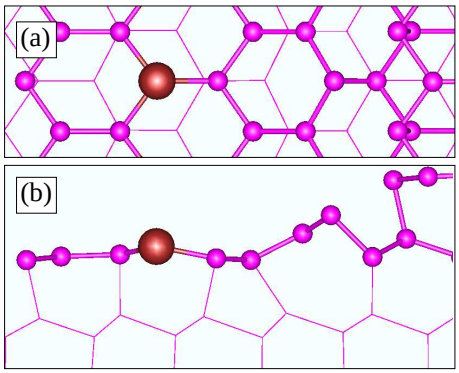

Figure 7.18: Top (a) and side (b) view of the relaxed structure of the p4 model.

favored over the negative tilt. [145–147] However, first-principles DFT calculations predict both structure to be very close in energy and there are conflicting claims about which of them is more stable. [148, 149]

We now proceed to make all possible substitutions of silicon by gold in the surface bilayer. This gives rise to nine different models for the Si(553)-Au reconstructions that we name pX, with X=1 corresponding to a substitution at the step edge and X>1 to a substitution in the terrace. The final energies after accurate SIESTA relaxations (DP level) are listed in Tab. 7.3. In several cases the initial structure was not stable and suffers strong modifications during the relaxation. These changes are also summarized in Tab. 7.3. Model p4, illustrated in Fig. 7.18, is the most stable structure. The π-bonded chain where the gold substitution takes place transforms into a structure similar to the unreconstructed Si(111) surface. This is reasonable taking into account the atomic configuration of gold and confirms the tendency of gold to occupy substitutional positions in the middle of the terraces. [1, 69, 70]

The next most favorable model, p2, is illustrated in Fig. 7.19. Again the π-bonded chain where the substitution took place has disappeared. However, this time a configuration reminiscent of the HC structure has formed in the middle of the terrace. This transformation is accompanied by an expansion of the surface bilayer (see the forward movement of the step-edge atoms in Fig. 7.19).

The band structure calculated for the p2 model, shown in Fig. 7.19 (c), presents similar

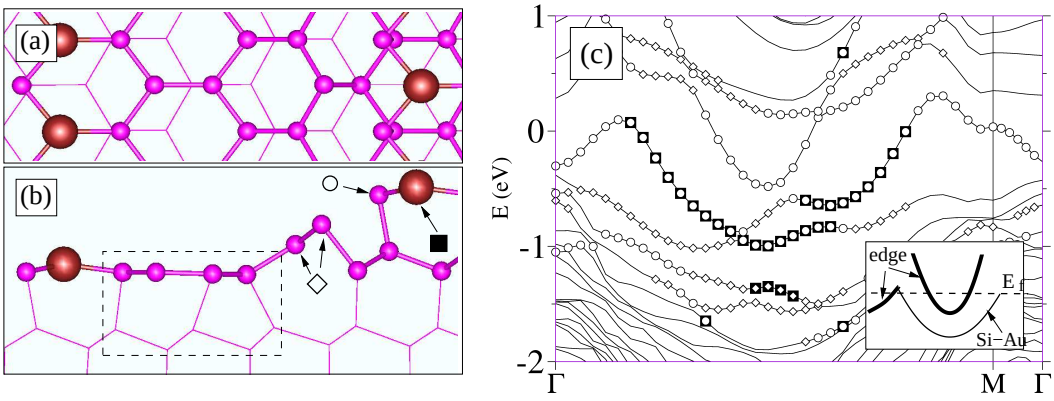

Figure 7.19: Top (a) and side (b) view of the relaxed structure of the p2 model. (c) Electronic band structure. The symbols highlight those surface bands with an appreciable weight from the surface atoms marked with the same symbols in panel (b). The inset shows a schematic representation of the most prominent surface bands. The HC structure in the middle of the terrace is indicated by a box.

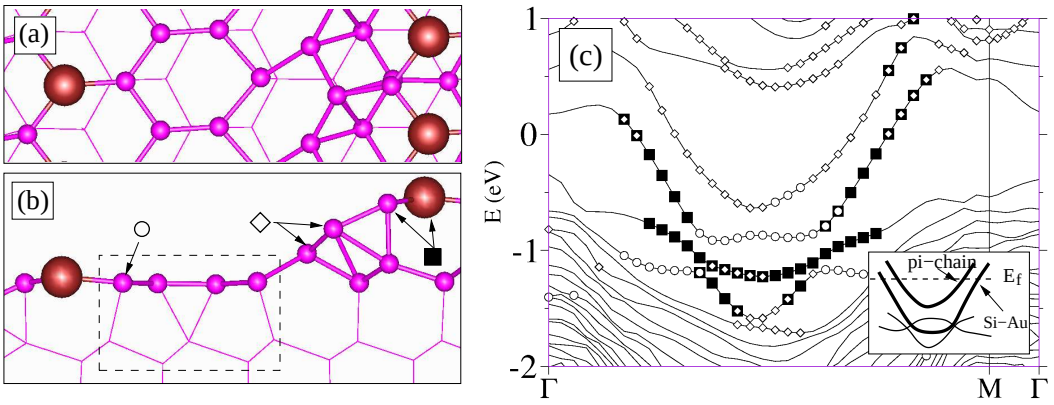

Figure 7.20: Top (a) and side (b) view of the relaxed structure of the p2* model, obtained after the reconstruction of the step edge. (c) Electronic band structure. The symbols indicate those surface bands with an appreciable weight from the surface atoms marked with the same symbols in panel (b). The inset shows a schematic representation of the most prominent surface bands. The HC structure is highlighted by a box.

characteristics to the experimental band structure (see the previous section). We can see in Fig. 7.19 (c) that the p2 model presents two metallic dispersive bands centered at point K in the zone boundary. One of theses bands is associated with the Si-Au bonds between gold and the neighboring silicon atoms in the step edge. It has a considerable gold weight and, therefore, is expected to exhibit a splitting if the spin-orbit coupling is taken into account. The other band, however, is mainly derived from the unsaturated dangling bonds of the silicon atoms at the step edge and presents a smaller filling. As expected, the π-bonded chain structure that remains in the terrace does not give rise to any metallic band.

The electron pocket of the step-edge band around K has an occupation of $\sim$1/4, quite close to that found in the experiment. There is another small electron pocket associated with the step-edge around Γ which is not observed in the experiment. Thus we can assign a population of $\sim$0.4 to the surface bands with a larger weight in the step-edge atoms. The dispersive band with a mixed silicon-gold character has an occupation of $\sim$0.6 electrons. Therefore, the total population associated with the step-edge derived surface bands is one. This is somewhat

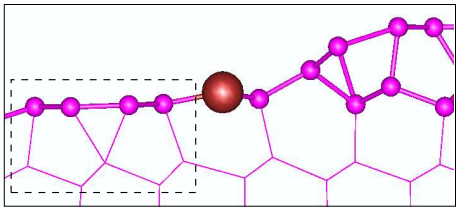

Figure 7.21: Side view of the p5* model. The HC structure emerges and is highlighted by a box.

Name	Configuration	ΔE (meV/Å^2)
p	(1,0,2,12,1,0,2,12,1)	1.82
p0	(1,0,2,21,1,0,2,21,1)	0.00
p1	(3,0,2,21,1,0,2,21,1)	14.92
p2	(1,0,4,21,1,0,2,21,1)→(1,4,2,1,1,0,2,21,1)	4.13
p3	(1,0,2,41,1,0,2,21,1)→(1,2,4,1,1,0,2,21,1)	8.15
p4	(1,0,2,23,1,0,2,21,1)→(1,2,2,3,1,0,2,21,1)	0.00
p5	(1,0,2,21,3,0,2,21,1)→(1,2,0,2,1,3,2,21,1)	7.07
p6	(1,0,2,21,1,0,4,21,1)→(1,2,2,1,1,4,2,1,1)	9.13
p7	(1,0,2,21,1,0,2,41,1)	8.30
p8	(1,0,2,21,1,0,2,23,1)	11.98
p9	(1,0,2,21,1,0,2,21,3)	15.90
p2*		-4.28
p4*		-2.69
p5*		0.38

Table 7.3: Relative surface energies of different structures based on a π-bonded chain reconstruction of the terraces of the Si(553) and Si(553)-Au surfaces. Models p and p0 correspond to the clean silicon surface. pX corresponds to the substitution of a gold atom in position "X" of structure p0. During the relaxation process several of these structures transform into configurations with a different bonding topology. This change is also indicated. pX* refers to pX configurations after the formation of bonds between the step edge and the neighboring π-chain structure. All energies correspond to our most accurate SIESTA calculations.

surprising if we take into account that the Si atoms at the step-edge have, in principle, three electrons to populate these surface bands. However, one of these electrons is transferred to the Au 6s states (which appear several eV below E$_F$) and the other electron populates states with large contribution from the HC structure (which does not exhibit any metallic band).

Further investigation of the p2 model reveals that it is a metastable configuration. Performing the relaxations with a more stringent force tolerance of 0.01 eV/Å results in a more stable structure. This structure, labelled p2* and illustrated in Fig. 7.20, exhibits a strong rebonding of the step edge. The π-bonded chain suffers a small translation along the $[\bar{1}10]$ direction in order to saturate the dangling bonds at the step edge. The new position of the atoms of the π-bonded chain seems to be a compromise between creating a surface dislocation and saturating the dangling bonds at the step edge. The band structure, shown in Fig. 7.20 (c), is quite similar to that of the p2 model. The role of the step-edge atoms is now played by the silicon atoms that formed the π-bonded chain. A quite dispersive surface band, coming from these atoms, appears centered at K. Another dispersive band with a strong gold weight appears at lower energies. Although the topology of the band structure resembles that observed in the

experiment, the filling of the parabolic silicon band is in this case close 0.4, i.e. larger than that observed experimentally. Fig. 7.20 (c) also highlights one of the bands associated with the HC structure, showing a characteristic dispersion. [66]

The band structure of model p2*, calculated using VASP and including the spin-orbit interaction (Fig. 7.23 (a)) shows quite good, although not perfect agreement, with the experiments. As in the case of the f2 model (see above), due to the spin-orbit interaction the dispersive bands suffer a splitting proportional to their weight in the gold atoms in the surface. Thus, the splitting is much larger for the dispersive band starting at lower energies. Again, in contradiction with the experimental observations we find some degree of splitting also for the parabolic band appearing at higher energies, although this splitting is smaller. The overall conclusion from Fig. 7.23 (a) is that the p2* outperforms the f2 model in terms of reproducing the photoemission results.

The simulated STM images for this structural model are shown in Fig. 7.22. The dependence on the polarity seems to be much larger than for models f2 and f4. The structure of the STM images becomes more complex when going from filled to empty states as several "spots" appear and the identification of zigzag or ladder-like structures becomes quite arbitrary.

Models p4 and p5 exhibit a similar rebonding of the step edge as explained above in the case of p2 and p2*. However, these new geometries, p4* and p5*, are not as stable as p2* (see Tab. 7.3). Geometry p5* also develops the HC structure in the terrace as can be seen in Fig. 7.21.

7.7 Most stable structures: combined SIESTA and VASP results

In Tab. 7.4 we compare the converged energies of the most stable models found in the previous sections for the Si(553)-Au reconstruction. As discussed in the previous sections, these models have been found *i*) using a systematic search among all possible model based on a flat surface bilayer and eight atoms in the terrace unit-cell and, *ii*) the substitution of gold in different positions of a π-bonded reconstruction of the Si(553) terraces. These two classes of models have different number of atoms. In order to compare the relative surface energies we need to define the chemical potential of silicon. Since the surface should be in equilibrium with bulk, we have chosen the chemical potential equal to the total energy of a silicon atom in bulk. Since the energy differences are quite small we have decided to perform the calculations of the most stable structure with a different methodology in order to cross-check our results. We have used the plane-wave code VASP for this purpose. [118, 119] We can see that there is an excellent agreement between SIESTA and VASP results. Geometries f4 and f2 (see Fig. 7.12) are the most stable structural models of those found in this extensive structural search. These two models can be considered degenerate within the precision of the calculations.

Models f2 and f4 were already obtained as the most stable ones in the much more restricted structural search of Sec. 7.2. The present calculations confirm that they are certainly among the most stable reconstructions of Si(553)-Au surface that only involve the topmost bilayer.

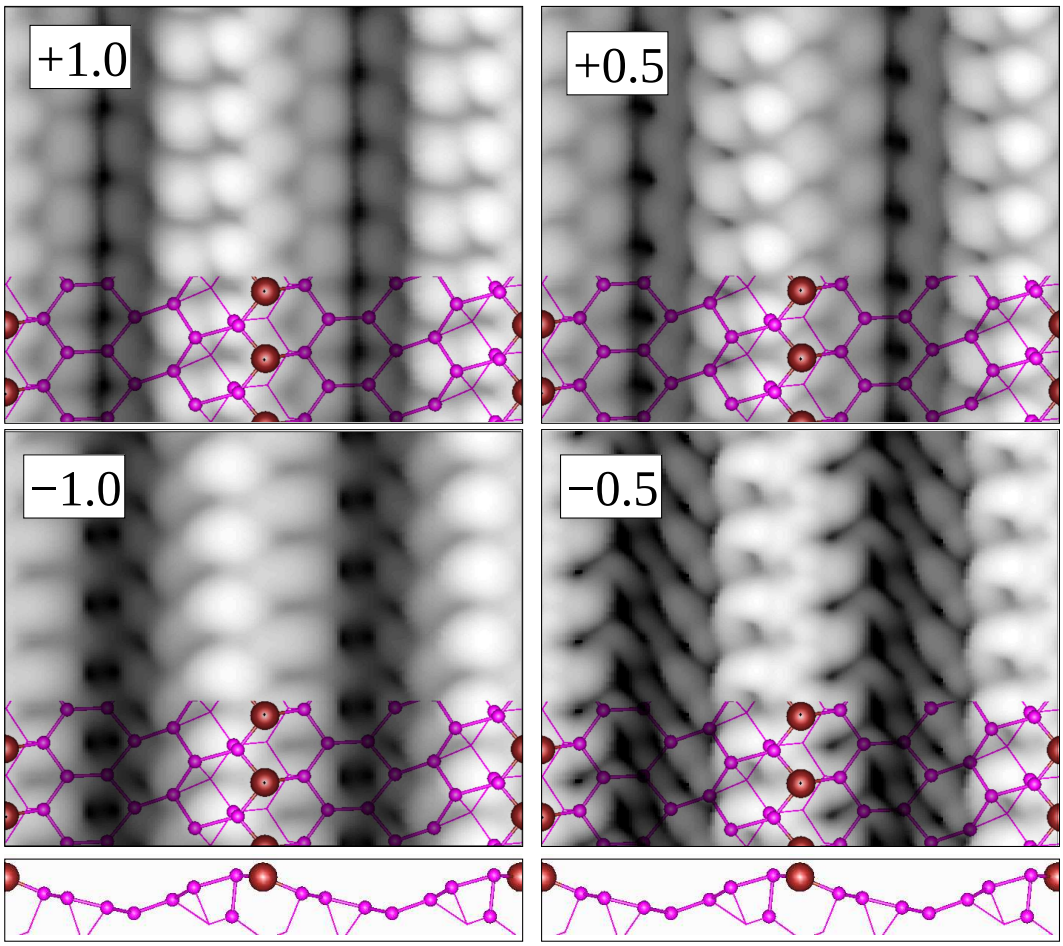

Figure 7.22: Simulated STM images, calculated using SIESTA, for model p2*. The insets of the panels indicate the bias voltage in Volts.

Name	ΔE (meV/Å^2)	
	SIESTA	VASP
p2*	4.85	4.93
p4*	6.44	6.54
p5*	9.51	9.13
f1	4.63	4.27
f2	0.17	-0.08
f3	0.42	0.51
f4	0.00	0.00

Table 7.4: Relative surface energies of our most stable models calculated using both SIESTA and VASP.

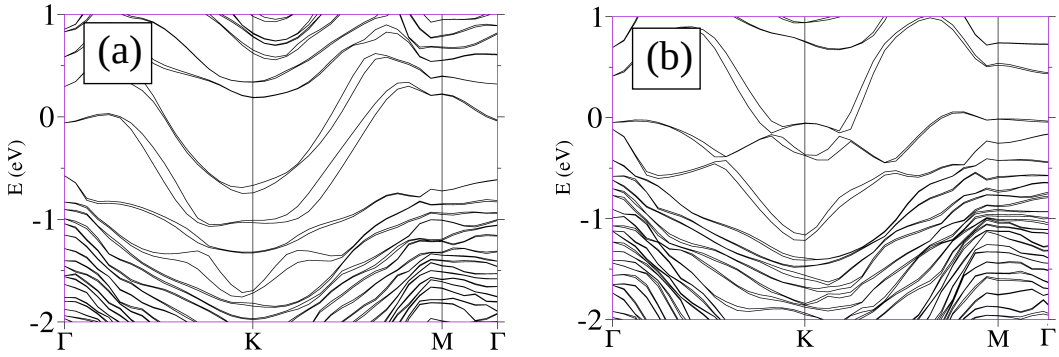

Figure 7.23: Band structures calculated using VASP and including the spin-orbit coupling for (a) model p2* and (b) model f4.

7.8 The double-row model

The proposal for the structure of the Si(553)-Au reconstruction by Ghose *et. al.* [61] can be seen in Fig.7.24 (a) and (b). The main features are the double row of gold atoms located at the step edge of the Si(553) surface and the silicon adatoms residing right below some of these gold atoms. This reconstruction is quite different from the other and better known structures induced by the deposition of gold on vicinal Si(111) surfaces like the Si(557)/Au of Chap. 6 and the models for the Si(553)/Au of the previous sections. Particularly surprising is the position of the gold atoms at the step edge. It has been shown by density functional calculations in several similar surfaces that the silicon subsitutional sites in the middle of the terraces are typically more favorable for gold [69, 70, 102]. Another striking fact is the very large distance between the gold atoms along the step edge (see Fig. 7.24 (a)). This distance ($\sim$3.8 Å) has to be compared, for example, to the nearest neighbor distance in bulk gold (2.9 Å). In the direction perpendicular to the step edge we find two slightly different Au-Au distances, $\sim$2.7 Å and $\sim$2.8 Å. These distances are intermediate between the bond length of the gold dimer (2.5 Å) and that of bulk. Another peculiarity of this structure is that the silicon terrace remains basically unreconstructed. This is in clear contrast with other systems like the Si(557)-Au and the Si(111)-(5$\times$2)-Au studied in previous chapters. For example, the HC structure is absent in the model studied here. Thus, the gold double-row model proposed by Ghose *et. al.* can be pictured as a collection of gold dimers attached to the edges of the terraces of a largely unreconstructured Si(553) surface. The gold dimers are oriented along the normal to the step edge. There are two types of gold dimers. This configuration can be justified for one of these dimers, which bonds to a silicon adatom in the terrace below with a reasonable Si-Au distance of $\sim$2.4 Å. However, this arrangement seems rather artificial and unstable for the other dimer. We performed structural relaxations to study the stability of this structural model. As we will see below the model turns out to be unstable and its structure is greatly modified during the relaxation. One could always argue that this result is a pathology of the local density approximation or other approximations used in this work. For this reason we have perfomed constrained relaxations that, while optimizing some of the bond lengths and bond angles, preserve the main characteristics of the structure in Ref. [61]. The electronic band structure and the simulated STM images are then calculated for this optimized structure and compared to the available experimental information.

Fig. 7.24 (c) and (d) shows the result of a constrained relaxation in which the relative positions of the gold atoms are not allowed to change (i.e. the gold atoms cannot move respect to each other). All other degrees of freedom are optimized: *i*) the position of the center of mass of the gold atoms and, *ii*) the positions of all the silicon atoms in the slab, except those in the lowest layer which remain in perfect bulk positions. As a stronger scatterer, the gold positions should be the most reliable in the experiment [29, 61]. This justifies the approach followed here. After this constrained relaxation, the silicon atoms of the first layer reconstruct to some extent. The atoms labeled “up” and “b” (see Fig. 7.24 (c) and (d)) give rise to a buckling of the surface, discussed in Sec. 3.3, in which there is a charge transfer from the lower atom to the the elevated one. This is clearly reflected in the electronic band structure shown in Fig. 7.24 (e). The “up” atom creates a fully occupied band with small dispersion (solid circles), while a more dispersive unoccupied band (open squares) is associated with the “b” atom. Atom labeled “db” has a partially occupied dangling-bond. The corresponding dispersive metallic band (solid squares) can be found close to the Fermi level in Fig. 7.24 (e).

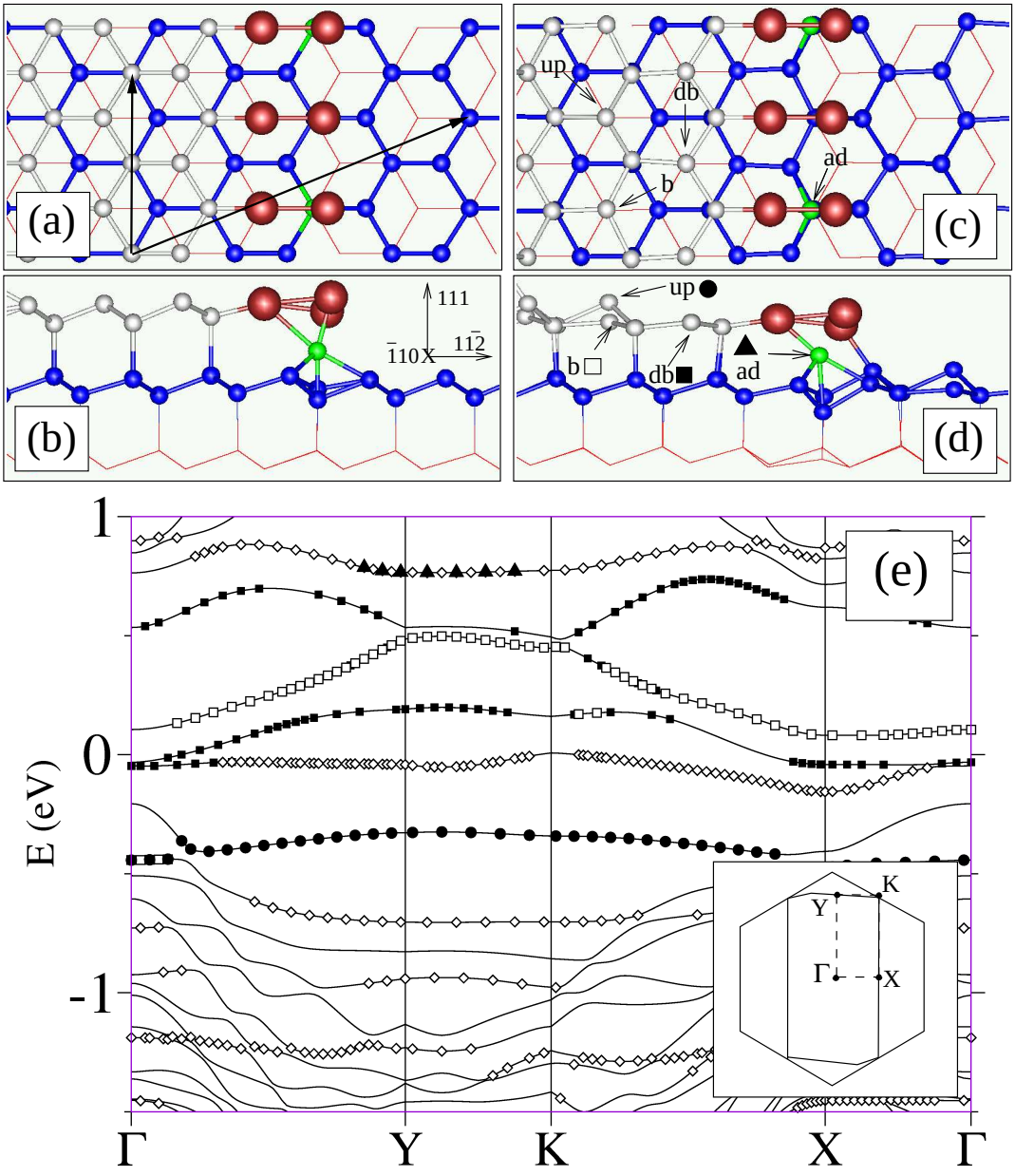

Figure 7.24: The model of Ghose *et. al.* [61] for the Si(553)-Au reconstruction (a and b, panel (a) also shows the unit cell vectors). The same structure after constrained relaxation (c and d) and the corresponding band structure (see text). The main atomic character of the surface bands is indicated with different symbols in panel (e) which correspond to those used to label different atoms in panels (c) and (d). The diamonds correspond to the gold atoms in the step edge and their neighboring silicon atoms. The inset of panel (e) illustrates the Brillouin-zone of the Si(553)-Au reconstruction. The Brillouin-zone of a 2×2 supercell of the unreconstructed Si(111) surface is also shown for comparison. The Γ-Y and K-X directions are parallel to the gold wires.

Several surface bands appear associated with the gold atoms and their neighboring silicon atoms in the step edge (open diamonds). However, all these bands are quite flat. This is in contrast with the band structures of other reconstructions of gold in vicinal Si(111). In those cases the gold atoms occupy silicon substitutional positions in the middle of the terraces and produce quite dispersive one-dimensional bands that dominate the photoemission spectra (see previous sections and Chaps. 4-6). Furthermore, in Chap. 6 it was shown that the presence of gold induces a spin-orbit splitting of the hybrid silicon-gold bands that explains the observation of two proximal one-dimensional bands in the Si(557)-Au surface [28, 30]. The photoemission of the Si(553)-Au surface also shows two proximal half-filled bands similar to those of the Si(557)-Au [1, 58, 59]. Therefore, it is tempting to associate these bands with the gold wires and their silicon neighbors in analogy to the case of Si(557)-Au. Since in the present calculations we are not including the spin-orbit interaction, these two proximal bands should appear as a single dispersive band. Unfortunately, a dispersive band associated with the gold atoms is completely absent in Fig. 7.24 (e). The band coming from the partially occupied dangling-bonds in the "db" atoms could be identified with the $\sim$1/4 filled band (see Fig. 7.1) of the Si(553)-Au [1, 58, 59]. However, this identification is also not very clear since in the experiment this band goes down to much lower energies. We can thus conclude that the band structure calculated for the model proposed by Ghose *et al.* fails to reproduce the photoemission data. Of course, given the discrepancy in the gold coverage reported in the photoemission work [1, 58] and the x-ray diffraction work of Ghose *et al.* [61], it is perfectly plausible that we are dealing with different reconstructions of the surface. In such case, the data reported in Fig. 7.24 (e) can be considered as the predicted electronic band structure for the double row model proposed by Ghose *et al.* using the local density approximation.

Simulated STM images for filled and empty states are presented in Fig. 7.25. The gold atoms show as alternating bright spots along the $[\bar{1}10]$ direction with a $\times 2$ periodicity. This periodicity reflects the alternating heights of the gold atoms induced by the presence of a row of silicon adatoms below them. Another feature with $\times 2$ periodicity is seen in the middle of the terrace as a result of the buckling of the silicon surface layer. In spite of the difference in the reported gold coverages we can insist in comparing with the available experimental images [1, 58–60]. At room temperature the step edge is observed in the experiment as a continous bright line. Another less pronounced feature is found in the middle of the terrace with a $\times 2$ modulation already at room temperature. At low temperature the terrace chain shows a more clear $\times 2$ periodicity, while the line at the step edge develops a $\times 3$ modulation. While the doubling of the periodicity in the middle of the terrace is reproduced by the model studied here, the image produced by the step edge is quite different. The appearance of bright spots in the step edge is linked to the presence of the silicon adatom in the terrace below. One could then speculate on creating a better agreement with the STM images by introducing an adatom only every three unit cells. However, this could hardly produce the observed temperature variation. We can thus conclude that the STM images predicted for the double row model of the Si(553)-Au reconstruction differ considerably from the reported STM images.

So far we have analyzed the results obtained for a structure optimized under the restriction that the gold atoms remain at the experimentally determined positions. We can now release this constraint and, starting from this partially relaxed structure, fully optimized the geometry of the surface. By doing this we discover that the proposal of Ghose *et al.* is not stable, at least within our computational approach. Although we do not find strong changes in the silicon terrace, the structure of the gold double-row is completely modified. This is clearly

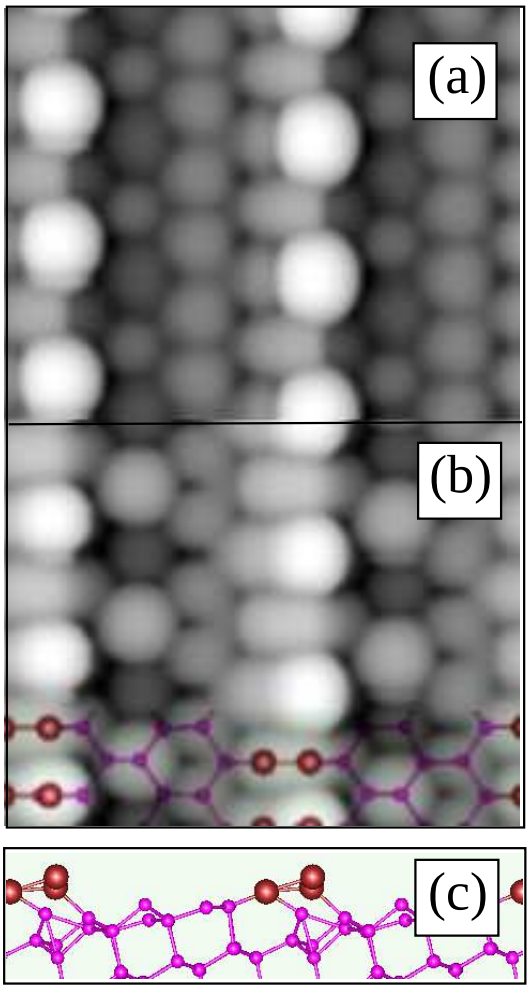

Figure 7.25: Simulated STM images of the double row model [61] of the Si(553)-Au reconstruction after constrained relaxation: panel (a) for a +1.0 V bias voltage (empty states), and (b) for -1.0 V bias voltage (filled states). Panel (c) shows the corresponding atomic configuration viewed from the side.

seen in Fig. 7.26, where we show the structure of the surface after 300 steps of unconstrained structural relaxation. The gold atom that was initially sited on top of the silicon adatom has moved to a new position on top of the neighboring rest-atom. The configuration of the silicon adatom has also changed considerably. The adatom moves to a higher position, its height over the terrace being now comparable to that of the gold atoms. This movement is possible because the adatom breaks a bond with one of the silicon surface atoms and adopts a bridge-like configuration. This broken bond is replaced by a new Si-Au bond. Although the structure shown in Fig. 7.26 is not completely relaxed, it becomes clear that the model of the surface proposed in Ref. [61], based on a silicon step edge decorated with gold dimers, is not stable. In particular, the adsorption of one of the gold atoms on top of a silicon adatom is avoided. This is consistent with previous density functional calculations [67,70]. In these calculations it was shown that the adsorption of gold as an adatom over the silicon surface is quite unfavorable compared to the substitution of the gold atoms in the surface layer.

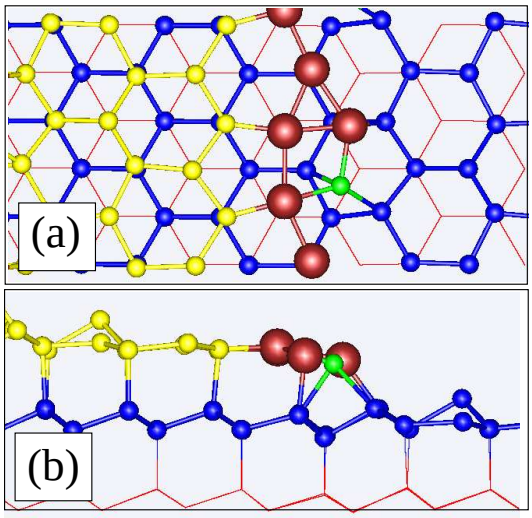

Figure 7.26: Top (a) and lateral (b) view of the double row model [61] of the Si(553)-Au after 300 steps of unconstrained structural relaxation.

7.9 Conclusions

Our study of the Si(553)/Au surface reconstruction has covered three different subjects: (i) In Sec. 7.2 we presented five new models for the Si(553)-Au surface constructed using the silicon honeycomb structure of Sec. 3.4 and the substitution of the gold atoms in the surface layer. These models were compared to an earlier proposal [1], which corresponds to one of our models (model V) with the addition of silicon dimers at the step edge. Although the energy differences between different structures are relatively small, one of our models (model I) was clearly the most favourable. Unexpectedly, the attachment of extra silicon atoms to the step edge in model V has little effect on the surface energy. This might open a route for the modification of the structures. We also investigated the possibility to induce periodic modulations in the structures that might lower the energy and reproduce some of the patterns seen in the STM images (Fig. 7.2) [58, 59]. However, although further investigation is necessary, the few structures considered in Sec. 7.2 proved to be quite stable against distortions that would double or triple the unit cell. Neither the band structures of our models nor that of the model proposed by Crain *et al.* [58], seem to provide a complete description of the photoemission spectra. However, the band structure of the models I and V present some of the main features of the experimental data.

(ii) We continued the investigation in Sec. 7.4 by presenting a labelling scheme for generating geometries with different coordinations of the surface atoms. We used this idea to make an exhaustive study of the Si(553)-Au reconstruction when the number of atoms in the first double-layer is N-1, where N is the number of atoms of the unreconstructed surface. The removal of one atom is crucial if one wishes to introduce honeycomb-chains on the surface (with analogy to the Si(557)-Au surface of Chap. 6) and eliminate dangling bonds. On the other hand it creates surface-dislocations and/or stacking-faults that cost extra energy. We considered all possible combinations of these elements with all possible gold-substitutional sites, for all systems in which the coordination between the atoms in the first double-layer can vary from 2 to 4. Imposing some physically meaningfull constraints (not allowing isolated atoms,

etc.), we found out that the number of different reconstructions is 210. We then proceeded in calculating the total energy of all these structures taking an advantage of a scheme, where we gradually made finer and finer calculations by changing the basis set, k-point sampling and the accuracy of self-consistency. The results confirmed that we had already found the most optimal structures in Sec. 7.2; in general, systems featuring the honeycomb-chain at the step-edge were observed to be the most stable ones. The notation was also used to make the generation of other trial geometries easier; in particular, we used it to generate π-bonding structures (having the same number of atoms N, as the unreconstructed surface) and then substituted silicon atoms by gold.

The most stable ones among all the studied structures where those having a honeycomb-chain in the step-edge and a gold-atom in the middle of the terrace. These structures were observed to have similar polarization with respect to the tunneling voltage as seen in the experimental STM images [64]. The most stable one of these structures has also a band structure reminiscent to that of the photoemission experiment of Fig. 7.1, althought instead of a single band and a doublet band, as seen in the photoemission, two doublet bands appear due to the spin-orbit interaction. On the other hand, the most stable structure among the π-bonding models reproduces the photoemission results [58, 59] extremely well, including a single and a doublet parabolic bands. Unfortunately it is less stable than the most stable model featuring a HC on the step-edge. We suggested that the correct Si(553)/Au geometry might then be some combination of the π-bonding structure and the honeycomb-chain at the step-edge.

(iii) In Sec. 7.8 we tested the double row model proposed by Ghose *et al.* [61] for the Si(553)-Au reconstruction. We address the stability of the model, as well as its electronic band structure and STM images. Using the geometry obtained in a constrained structural relaxation, which preserves the main characteristic of the proposal of Ref. [61], we calculate the band structure and STM images. We only find a dispersive band with fractional filling close to the Fermi level. This band comes from the silicon dangling-bonds in the surface and its energy position and filling seems quite different from the bands observed in the photoemission experiments [58, 59]. Dispersive bands associated with the gold atoms and their silicon neighbors are completely absent, which also seems to be in disagreement with the experimental evidence [58, 59, 71]. At variance with the room temperature experimental STM images [58, 59], our simulated STM images do not show the step edge as a continuous bright line, but exhibit a $\times 2$ modulation associated with the presence of the adatoms in the neighboring terrace. In the low temperature experimental images the step edge develops a $\times 3$ periodicity [59]. It might be possible to induce this $\times 3$ periodicity in our calculated STM images by modifying the adatom content. However, it is not clear how this could reproduce the temperature dependence. In summary, the calculated band structure and STM images for the model proposed in Ref. [61] do not provide a good agreement with the available experimental information for this surface. Of course, it might be argued that this is a consequence of the different gold coverage in the different experimental approaches [58, 61]. In fact, it is possible that the surface reconstructions studied by x-ray diffraction in Ref. [61] and by photoemission and STM in references [58], [59], and [60] are different. Unfortunately, the structure provided by Ghose *et al.* [61] is unstable, at least at the level of the local density approximation. When the geometry is relaxed without any constraints the structure of the gold double-row attached to the step edge severely modifies from the proposal of Ref. [61]. Therefore, we propose that the data of Ghose *et al.* should be reanalyzed in the light of the present results and new proposal for the structure of the Si(553)-Au surface obtained.

Chapter 8

Implementation of the LDA+U method

8.1 Introduction

The LDA+U method was developed by Anisimov and co-workers [150–153] with the objective to improve the treatment of the electron-electron interaction for localized electrons within the LDA description.

It can be shown that LDA implicitly assumes the electron-electron interactions, that for localized electrons can be described with Hubbard parameter U, to be small compared to the band width W [150]. However, for very localized electrons, while the band width may be small, the electron-electron interactions can be quite big. A classical example are the transition-metal oxides, were a strong localization of the metallic d-electrons take place.

This limitation of LDA manifests in several deficiencies, including the self-interaction of the electrons. The exhange interaction in LDA is obtained from a free electron gas of similar density. However, for localized electrons this approximate treatment of the exchange gives rise to the interaction of a given electron with itself. As electrons get more localized (and as W gets smaller), the self-interaction becomes more and more significant.

The LDA+U method has proven very succesfull with materials featuring partially filled d or f shells [153]. The computational cost is comparable to an LDA calculation and the few parameters needed by this method, can be calculated from first principles (this will be discussed in Sec. 8.4). For this reason we came forward to implement it into the SIESTA code.

8.2 Theory and methods

We proceed to obtain the standard, rotationally invariant LDA+U implementation by Anisimov, et. al. [153]. On the way we learn how the self-interaction and exchange energy terms are obtained.

By minimizing the total energy of Eq. (2.1) using the Slater determinant of Eq. (2.2) as a trial wavefunction, one obtains the expression for the Hartree-Fock (HF) energy:

$$\langle \Psi | H | \Psi \rangle = \sum_i \int d\mathbf{r} \psi_i^*(\mathbf{r}) (\hat{T} + V_{ext}) \psi_i(\mathbf{r}) + E_{ee}, \tag{8.1}$$

where E_{ee} is the electron-electron interaction:

$$E_{ee} = \sum_{(i,\sigma)\neq(j,\sigma')} \int d\mathbf{r}d\mathbf{r}' \frac{e^2}{|\mathbf{r}-\mathbf{r}'|} |\psi_i^\sigma(\mathbf{r})|^2 |\psi_j^{\sigma'}(\mathbf{r}')|^2$$
$$- \sum_{i\neq j,\sigma} \int d\mathbf{r}d\mathbf{r}' \frac{e^2}{|\mathbf{r}-\mathbf{r}'|} \psi_i^{\sigma*}(\mathbf{r})\psi_i^\sigma(\mathbf{r}')\psi_j^{\sigma*}(\mathbf{r}')\psi_j^\sigma(\mathbf{r}). \quad (8.2)$$

We rewrite this:

$$E_{ee} = \frac{1}{2} \sum_{i,j,\sigma,\sigma'} \int d\mathbf{r}d\mathbf{r}' \frac{e^2}{|\mathbf{r}-\mathbf{r}'|} |\psi_i^\sigma(\mathbf{r})|^2 ||\psi_j^{\sigma'}(\mathbf{r}')|^2$$
$$-\frac{1}{2} \sum_{i,j,\sigma} \int d\mathbf{r}d\mathbf{r}' \frac{e^2}{|\mathbf{r}-\mathbf{r}'|} \psi_i^{\sigma*}(\mathbf{r})\psi_i^\sigma(\mathbf{r}')\psi_j^{\sigma*}(\mathbf{r}')\psi_j^\sigma(\mathbf{r})$$
$$= E_H + E_{exc}, \quad (8.3)$$

where the first term (E_H) is known as the Hartree energy and the last term (E_{exc}) is the so-called *exchange* term. One observes that now the indices run over all i, σ and j, σ'. This has been achieved by adding and subtracting the term i=j of the electron-electron interaction of Eq. (8.2). The positive term is included into the E_H and the negative one into the E_{exc} term, this way obtaining a more symmetric form at Eq. (8.3). Hartree energy can also be written using the electron-density only:

$$E_H = \frac{1}{2} \int d\mathbf{r}d\mathbf{r}' \frac{e^2}{|\mathbf{r}-\mathbf{r}'|} \rho(\mathbf{r})\rho(\mathbf{r}'), \quad (8.4)$$

where $\rho(\mathbf{r})$ is the total electron density (including both spins).

We recall that the electron-electron interaction in LDA is approximated by E_{ee}=E_H+E_{xc}, where E_H is the Hartree term and E_{xc} is the exchange-correlation energy which is parametrized from the results of a homogeneous electron gas.

The self-interaction problem is now easy to understand: in the LDA approximation the electron self-interaction, i.e. the terms of the Hartree energy with (i, σ)=(j, σ') are supposed to cancel with E_{xc} (that is including the exchange energy). However, since the exact E_{xc} is not known and is parametrized from simple model systems like the homogeneous electron gas, this cancellation is incomplete.

We now consider the possibility to go beyond the LDA, and in some approximate way, include the electron-electron and exchange terms of Eq. (8.3) for electrons tightly localized around the atomic center. For very delocalized electrons we do not need to worry since the LDA description is quite appropriate. We start by considering a set of orthonormal atomical orbitals $|\phi_i\rangle$ at the same site. Our objective is to calculate exactly the E_H+E_{exc} total energy of Eq. (8.3) for an isolated system consisting of these orbitals. The eigenstates of this system are then $|\psi_\alpha^\sigma\rangle$ (σ and k are the spin and eigenvalue indexes, respectively) that are linear combinations of $|\phi_i\rangle$, i.e.

$$|\psi_\alpha^\sigma\rangle = \sum_n a_{\alpha\sigma}^n |\phi_n\rangle. \quad (8.5)$$

For later use, we introduce the following occupation number operator:

$$\hat{n}_{kl}^\sigma = \sum_i |\phi_k(\mathbf{r}_i)\rangle \hat{s}_\sigma \langle\phi_l(\mathbf{r}_i)| \quad (8.6)$$

where $\hat{s}_\sigma$ operates on spin σ only. Using a Slater determinant, constructed with the eigenstates of Eq. (8.5), as the wavefunction, leads to the following expectation value for the operator $\hat{n}^\sigma_{kl}$

$$n^\sigma_{kl} = \langle\Psi|\hat{n}^\sigma_{kl}|\Psi\rangle = \sum_\alpha a^{k*}_{\alpha\sigma} a^l_{\alpha\sigma}. \tag{8.7}$$

Using Eq. (8.5) with the Hartree term in Eq. (8.3) results in:

$$\begin{aligned} E_H = \\ \frac{1}{2}\sum_{ij\sigma\sigma'}\Big(\int d\mathbf{r}d\mathbf{r}'\frac{e^2}{|\mathbf{r}-\mathbf{r}'|}\phi^*_{i'}(\mathbf{r})\phi_{j'}(\mathbf{r})\phi^*_{i''}(\mathbf{r}')\phi_{j''}(\mathbf{r}')\Big)\sum_{i'j'i''j''} a^{i'*}_{i\sigma}a^{j'}_{j\sigma}a^{i''*}_{j'\sigma'}a^{j''}_{j\sigma'} \\ = \frac{1}{2}\sum_{i'j'i''j''}\sum_{\sigma\sigma'}\Big(\int d\mathbf{r}d\mathbf{r}'\frac{e^2}{|\mathbf{r}-\mathbf{r}'|}\phi^*_{i'}(\mathbf{r})\phi_{j'}(\mathbf{r})\phi^*_{i''}(\mathbf{r}')\phi_{j''}(\mathbf{r}')\Big) \\ \times(\sum_i a^{i'*}_{i\sigma}a^{j'}_{i\sigma})(\sum_j a^{i''*}_{j\sigma'}a^{j''}_{j\sigma'}) \end{aligned} \tag{8.8}$$

Using Eq. (8.7) and changing the names of the indices (namely m→i',m'→j', m"→i",m"'→j"), gives

$$\begin{aligned} E_H = \\ = \frac{1}{2}\sum_{\{m\}\sigma\sigma'} U_{mm''m'm'''}n^\sigma_{mm'}n^{\sigma'}_{m''m'''} \\ = \frac{1}{2}\Big(\sum_{\{m\}\sigma} U_{mm''m'm'''}n^\sigma_{mm'}n^\sigma_{m''m'''} + \sum_{\{m\}\sigma} U_{mm''m'm'''}n^\sigma_{mm'}n^{-\sigma}_{m''m'''}\Big), \end{aligned} \tag{8.9}$$

where

$$U_{mm''m'm'''} = \int d\mathbf{r}d\mathbf{r}'\frac{e^2}{|\mathbf{r}-\mathbf{r}'|}\phi^*_m(\mathbf{r})\phi_{m'}(\mathbf{r})\phi^*_{m''}(\mathbf{r}')\phi_{m'''}(\mathbf{r}'). \tag{8.10}$$

In a similar fashion, for the exchange term we obtain:

$$E_{exc} = -\frac{1}{2}\Big(\sum_{\{m\}\sigma} U_{mm''m'''m'}n^\sigma_{mm'}n^\sigma_{m''m'''}\Big). \tag{8.11}$$

By combining Eq. (8.9) and Eq. (8.11) we get finally:

$$\begin{aligned} E_H + E_{exc} = \frac{1}{2}\sum_{\{m\}\sigma}\Big(U_{mm''m'm'''}n^\sigma_{mm'}n^{-\sigma}_{m''m'''} \\ +(U_{mm''m'm'''} - U_{mm''m'''m'})n^\sigma_{mm'}n^\sigma_{m''m'''}\Big). \end{aligned} \tag{8.12}$$

We have now expressed correctly the electron-electron interaction for an isolated system (consisting of orbitals ϕ_i). The energy in Eq. (8.12) depends through the occupation numbers $n^\sigma_{mm'}$ on the wavefunction Ψ. We now wish to use this expression for an isolated system to correct the LDA energy of localized electrons. This connection is established by calculating the occupation numbers using the LDA wavefunction.

Due to the fact that we are considering two "disconnected" systems (the isolated orbitals and the LDA system), the Coulombic interactions in Eq. (8.10) are effective interactions (in

the Anderson model language, they are "renormalized") and they must be screened by the surrounding electronic density. These effective interactions are the only parameter needed in the LDA+U method. If we define two effective (empirical for the time being) parameters, U and J as

$$U = \frac{1}{(2l+1)^2} \sum_{mm'} U_{mm'mm'} = F^0 \tag{8.13}$$

$$J = \frac{1}{2l(2l+1)} \sum_{m \neq m'} U_{mm'm'm} = \frac{F^2 + F^4}{14} \tag{8.14}$$

then any of the integrals in Eq. (8.12) can be expressed by:

$$U_{m,m'',m',m'''} = \sum_k a_k(m, m', m'', m''') F^k, \tag{8.15}$$

the terms F^k being the slater integrals and

$$a_k(m, m', m'', m''') = \frac{4\pi}{2k+1} \sum_{q=-k}^{k} \langle lm|Y_k^q|lm'\rangle \langle lm''|Y_k^{q*}|lm'''\rangle, \tag{8.16}$$

where F-values can be determined from the U and J values given as an input to the LDA+U scheme (see Eq. (8.13) and Eq. (8.14)). The terms in Eq. (8.16) include integrations over three spherical harmonics, and can be calculated using the Wigner-$3j$ symbols [154].

It is necessary to add some terms to Eq. (8.12) in order to properly define a correcting energy functional,

$$\begin{aligned} E_U[\{n\}] = \frac{1}{2} \sum_{\{m\},\sigma} \Big\{ & U_{m,m'',m',m'''} n^{\sigma}_{m,m'} n^{-\sigma}_{m'',m'''} + \\ & \Big(U_{m,m'',m',m'''} - U_{m,m'',m''',m'} \Big) n^{\sigma}_{m,m'} n^{\sigma}_{m'',m'''} \Big\} \\ - \frac{1}{2} \Big(& UN(N-1) - J[N^{\uparrow}(N^{\uparrow}-1) + N^{\downarrow}(N^{\downarrow}-1)] \Big). \end{aligned} \tag{8.17}$$

The last line in Eq. (8.17) is a correction-term to cancel out the electron-electron interaction already taken into account by the original LDA total energy. This way, the average electron-electron interaction energy included in the LDA calculation is removed by the term $\frac{1}{2}UN(N-1)$ and the correct energy is put explicitly by the sum in Eq. (8.17). The final, corrected LDA+U energy functional is then:

$$E_{LDA+U} = E_{LDA} + E_U, \tag{8.18}$$

where E_{LDA} is the LDA functional of Eq. (2.5). The functional of Eq. (8.17) is originally due to Anisimov, et. al. [153]. There exists also simplified versions (see, for example [155]).

In order to get the potential resulting from Eq. (8.17) to include it into the LDA calculations, we apply the variational principle with each $n^{\sigma}_{m,m'}$ and obtain:

$$V_U = \sum_{m,m'} |m, \sigma\rangle V^{\sigma}_{m,m'} \langle m', \sigma|, \tag{8.19}$$

where the elements $V_{m,m'}$ are as follows:

$$V_{m,m'} = U_{m,m'',m',m'''} n^{-\sigma}_{m'',m'''} + \Big(U_{m,m'',m',m'''} - U_{m,m'',m''',m'}\Big) n^{\sigma}_{m'',m'''}. \tag{8.20}$$

Here we have also adopted the notation:

$$\langle m, \sigma| = \hat{s}_\sigma \langle \phi(\mathbf{r})|, \tag{8.21}$$

where the orbital $\phi(\mathbf{r})$ has the magnetic quantum number m and $\hat{s}_\sigma$ is operating on spin σ only.

In a practical LDA+U calculation, the occupation numbers $n^{\sigma}_{m,m'}$ are calculated as in Eqs. (2.38)-(2.39) (when calculating occupation numbers, one must set $V_{\eta\kappa}$=1). Then the potential term Eq. (8.19) is evaluated (again using Eqs. (2.38)-(2.39)) and the SCF cycle of the KS scheme is let to converge the system. After this initial SCF cycle, charge transfer has occurred and the occupation numbers have changed, so one has to calculate the occupations again. This changes the potentials so a new SCF cycle must be performed. Therefore, we have two nested self-consistency loops. One in the density for fixed occupations and one in the occupations themselves. The details for controlling this extra SCF cycle are described in Sec. 8.5.

8.3 Hubbard U and orbital occupations

The U parameter in Eq. (8.13) is frequently regarded as an effective parameter U_{eff}=U-J. This equals in setting J=0 in Eq. (8.13). Then the energy of the "+U" correction in Eq. (8.17) can also be expressed in terms of the eigenvalues λ^{σ}_i of the occupation matrix $n^{\sigma}_{m,m'}$ [155]:

$$E_U = \frac{U}{2} \sum_\sigma \sum_i \lambda^\sigma_i (1 - \lambda^\sigma_i). \tag{8.22}$$

This expression clearly shows that the correction term in LDA+U favors integer occupations. It also provides a simple way to check our numerical implementation that uses equation (8.17) to calculate the total energy and the Hamiltonian. In fact, in the limit J=0 the energies calculated directly from Eq. (8.22) perfectly reproduce those given by SIESTA.

8.4 Calculating the effective Hubbard parameter U

In Eq. (8.17), the average electron-electron interaction in LDA is approximated by the term:

$$E^{ee}_{LDA} = \frac{1}{2} UN(N-1), \tag{8.23}$$

where N is the total occupation of the shell we wish to treat with the LDA+U. One could then, in principle, change the occupation number N, see how the LDA energy of the system changes and from this variation get the value of U (assuming that other energy terms show vanishing variation with respect to N), by simply fitting the {E_{LDA},N} values to Eq. (8.23). One could also use the second derivative of the total energy and Eq. (8.23):

$$\frac{\partial^2 E_{LDA}}{\partial N^2} \approx \frac{\partial^2 E^{ee}_{LDA}}{\partial N^2} = U \tag{8.24}$$

These techniques can be employed if one has a good control over the occupation number N. This is the case, for example, in the Linear Muffin Tin Orbital (LMTO) method. In the LMTO method one can isolate an atom, by neglecting the hybridization of its orbitals with the rest of the system and this way forcing the desired occupation [151, 156, 157]. One can also exploit the Janak theorem:

$$\epsilon_i = \frac{\partial E(N)}{\partial n_i}, \tag{8.25}$$

where E is the total energy, n_i the occupation of the state i and ϵ_i its eigenvalue, in order to determine the U from the eigenvalue shifts. For example, Anisimov and Gunnarsson [151] use the following formula with the iron d-orbitals:

$$U = \epsilon\Big(\frac{n}{2}+\frac{1}{2},\frac{n}{2}\Big) - \epsilon\Big(\frac{n}{2}+\frac{1}{2},\frac{n}{2}-1\Big), \tag{8.26}$$

where $\epsilon(n\uparrow, n\downarrow)$ is the spin-up 3d eigenvalue, depending on the spin-up ($n\uparrow$) and spin-down ($n\downarrow$) 3d occupations. U can thus be determined from the shift in the d eigenstates.

Pickett et. al [158] use a variation of the constrained charge scheme [159] for the determination of U. Their idea consists of applying small potential shifts to a given atom (orbitals of Eq. (8.5)) and see how the system responds to this small perturbation. Potential shifts are projector-like potential terms:

$$V_i = |\phi_i\rangle w \langle\phi_i|, \tag{8.27}$$

where w is the potential shift and ϕ_i is an atomic orbital. One can then show (see below), that

$$U \approx \frac{\partial w}{\partial N}, \tag{8.28}$$

where the potential shift w has been applied to all of the orbitals of the shell and N is again the total occupation of the shell.

In the following, we use similar notation to that of Gironcoli and Cococcioni [155]. We start by introducing the constrained-LDA functional:

$$E[\{q_I\}] = \min_{n(\mathbf{r}),\,\alpha_I} \Big\{E_{LDA}[n(\mathbf{r})] + \sum_I \alpha_I (n_I - q_I)\Big\}, \tag{8.29}$$

where n_I, q_I and α_I are the occupation numbers, the constrained occupation numbers and the Lagrance multipliers, respectively. Here the index I goes over the atoms in the unit cell and n_I is the total occupation of the desired shell. The constrained occupation numbers q_I represent the desired occupation for atom I. Lagrance multipliers maintain the number of electrons constant. One can, via a Legendre transformation [158], pass to a functional where the independent variable are the α_I's:

$$E[\{\alpha_I\}] = \min_{n(\mathbf{r})} \Big\{E_{LDA}[n(\mathbf{r})] + \sum_I \alpha_I n_I\Big\}. \tag{8.30}$$

In this case, one chooses a set of α_I's (usually only one of them is different from zero), and then performs the self-consistent LDA calculation to minimize the $E[\{\alpha_I\}]$.

Because $E[\{\alpha_I\}]$ is the minimum according to the variational principle, it also satisfies:

$$\frac{\partial E[\{\alpha_I\}]}{\partial n_J} = 0. \tag{8.31}$$

This way we get, using Eq. (8.30) and remembering that α_I's are kept constant (the variational minimization was done for a chosen set of α_I's):

$$\frac{\partial E_{LDA}[n(\mathbf{r})]}{\partial n_J} + \alpha_J = 0 \Leftrightarrow \frac{\partial E_{LDA}[n(\mathbf{r})]}{\partial n_J} = -\alpha_J. \tag{8.32}$$

In the next derivative, the α_I's are allowed to vary. We thus take a derivative over all self-consistent electron-densities (there is a self-consistent electron density for each set of α_I's):

$$U = \frac{\partial^2 E[n(\mathbf{r})]}{\partial n_J^2} = -\frac{\partial \alpha_J}{\partial n_J}. \tag{8.33}$$

Here we have used the Eq. (8.24).

In Eq. (8.33) we have assumed:

$$\bar{\alpha} = F(\bar{n}), \tag{8.34}$$

where $\bar{\alpha} = (\alpha_1, \alpha_2, ..., \alpha_N)$ and $\bar{n} = (n_1, n_2, ..., n_N)$, but in the calculations we impose the potential shifts $\bar{\alpha}$ and get the occupations, so

$$\bar{n} = F^{-1}(\bar{\alpha}). \tag{8.35}$$

In the calculations, we thus first create the matrix:

$$U_{IJ}^{-1} = \frac{\partial n_I}{\partial \alpha_J} \tag{8.36}$$

and then invert it to get the U=U_{11}.

8.5 Details of the implementation

In our implementation of the LDA+U we use the same routines to create the atomic orbitals and the projectors $\langle m, \sigma|$. The projectors created for one atom species are then identical to a SZ basis. From this basis one can choose which projectors $\langle m, \sigma|$ are used. (for example, in the case of iron, one would choose the d-orbitals).

The projectors in one atomic center should not overlap with the ones in the neighboring atoms (otherwise, the occupation numbers are not well defined). For this reason, one should use highly localized projectors (setting the `PAO.proj_U_energyshift` to a high value, see below), or alternatively, cut the interaction range of the projector, using `PAO.proj_U_radii` and `PAO.proj_U_alpha` switches (see below). We recommend the latter approach; this way the orbital shape is more similar to the orbital of an isolated atom. This method is also consistent with earlier LDA+U studies in the literature.

In the following subsections, we explain the new program switches needed to control the LDA+U calculation. We have chosen the same format as in the SIESTA manual. The new output files produced by the LDA+U are also described.

8.5.1 New program switches

PAO.proj_U_energyshift *(real energy)*: The cutoff radius of projectors $\langle m, \sigma|$, defined with an energy cutoff exactly the same way as in `PAO.energyshift`.

Default value: `50 meV`

Note: User should take care that the projectors from different atomic sites do not overlap, either by setting this parameter to a high value, or using the `PAO.proj_U_radii` parameter instead.

PAO.proj_U_radii *(real length)*: The cutoff radius of projectors $\langle m, \sigma|$. Near this cutoff value, the projector goes smoothly to zero
(see `PAO.proj_U_alpha`).

Default value: `1000.0` a_0

Note: Must be used together with the `PAO.proj_U_alpha` parameter.

PAO.proj_U_alpha *(real)*: The projector is set to zero, by multiplying its radial part with $(\frac{1}{1+e^{(\alpha r - r_{cut})}})$, where r_{cut} is the parameter `PAO.proj_U_radii` and α the `PAO.proj_U_alpha`. This way the projector goes smoothly to zero.

Default value: `1.0`

Note: For example, with the iron d-orbitals and `PAO.proj_U_energyshift`=50 meV, a nice value for this parameter is 50. One should always check the behaviour of the projector in the file `LDAU`.

proj_U *(data block)*: Defines the atoms and orbitals that are assigned with a LDA+U projector. Each line gives the type label and the l and m quantum numbers. Here an example for the iron d-orbitals:

```
%block proj_U
Fe          2          -2
Fe          2          -1
Fe          2          0
Fe          2          1
Fe          2          2
%endblock proj_U
```

ldaU_U *(real energy)*: The value of U. The parameters F^k are calculated using the values of U and J as described in the previous section. Currently, the Slater integrals and the parameters are calculated only for d- and f-electrons.

Default value: `0.0 eV`

ldaU_J *(real energy)*: The value of J.

Default value: `0.0 eV`

ldaU_maxiters *(integer)*: This number controls the occupation number self- consistency cycle. When value of this parameter is >1, then the LDA+U occupation numbers $n_{m,m'}$ are converged. This means that in the end of every SCF cycle, the occupation numbers are recalculated, and then a new SCF cycle with the new LDA+U potentials (that depend on

the $n_{m,m'}$) is started. This procedure is repeated until the convergence of $n_{m,m'}$, as defined in `ldaU_stop`, is reached or until the occupation numbers have been calculated `ldaU_maxiters` times.

When `ldaU_maxiters`=1, the LDA+U potential is included into the Hamiltonian after the single SCF cycle has converged. The wavefunctions are calculated using this modified Hamiltonian and then the program stops. This is usefull for preliminary calculations and testing the quantitative effects of U and J.

Default value: `2`

Note: When this switch is >1, the user should increase considerably the amount of `MaxScfIterations` which in this case means the *total* amount of SCF iterations to converge the occupation numbers.

ldaU_stop *(real)*: The error in the occupation numbers at step k is defined as follows:

$$\Delta N = max\{|n^k_{m,m'} - n^{k+1}_{m,m'}|\}, \tag{8.37}$$

where $n^k_{m,m'}$ is the cross-occupation number m, m' at step k of the iteration.

Default value: `0.001`

Note: Since the error ΔN consists of summations over the density matrix elements, it should be one order of magnitude greater than `DM.Tolerance`.

ldaU_scfmaxiters *(integer)*: Maximum value of SCF iterations for one step of the occupation number iteration.

Default value: `1000`

ldaU_init *(logical)*: When the $n_{m,m'}$ converged density matrix is stored into the disk, it contains the information to calculate $n_{m,m'}$ and continue the iteration. When this switch is set to `.true.`, the occupation numbers are calculated from the `.DM` file before the SCF cycle starts and the LDA+U projectors are applied from the very start of the cycle.

Default value: `.false.`

Note: Works better when used together with `MixSCF1` set to `.true.`

ldaU_tm *(logical)*: If this switch is `.true.` then the transformation of the U-matrix is done. The review paper of Anisimov, et. al. [153], considered spherical harmonics Y^m_l. However, we are using real spherical harmonics S^m_l which are related to the spherical harmonics by:

$$S^m_l = \begin{cases} \frac{(-1)^m}{i\sqrt{2}}(Y^{|m|}_l - Y^{|m|^*}_l) & m < 0, \\ Y^0_l & m = 0, \\ \frac{(-1)^m}{\sqrt{2}}(Y^m_l + Y^{m*}_l) & m > 0. \end{cases} \tag{8.38}$$

This transformation can be expressed in matrix form for real spherical harmonics with quantum number l as $\vec{S}_l = C^l \vec{Y}_l$. The matrix C^l has the following form:

$$\mathbf{C^l} = \frac{1}{\sqrt{2}} \begin{pmatrix} i(-1)^l & 0 & \cdots & 0 & \dots & 0 & -i \\ 0 & i(-1)^{l-1} & \dots & 0 & \dots & -i & 0 \\ \vdots & \vdots & \ddots & \vdots & \iddots & \vdots & \vdots \\ 0 & 0 & \dots & \sqrt{(2)} & \dots & 0 & 0 \\ \vdots & \vdots & \iddots & \vdots & \ddots & \vdots & \vdots \\ 0 & (-1)^{l-1} & \dots & 0 & \dots & 1 & 0 \\ (-1)^l & 0 & \dots & 0 & \dots & 0 & 1 \end{pmatrix} \tag{8.39}$$

The matrices of the type $\mathrm{U}_{m,m',m'',m'''} = \langle m, m''|V_{ee}|m', m'''\rangle$ in Eq.(8.10) must then be transformed by:

$$U_{m,m'',m',m'''} = \sum_{\{M\}} U_{M,M'',M',M'''} C^{l*}_{m,M} C^{l*}_{m'',M''} C^{l}_{m',M'} C^{l}_{m''',M'''} \tag{8.40}$$

Default value: `.true.`

Note: This is basically a switch for debugging and should not be changed by the user.

ldaU_constrained *(logical)*: By using this switch, one can calculate charge-constrained calculations. These calculations can be used in determining the value of the parameters U and J as described in the previous section. When this switch is set to `.true.`, the LDA+U potential term in Eq. (8.19) is substituted by:

$$V_{constr} = \sum_{m,\sigma} |m,\sigma\rangle \alpha^{\sigma}_{m} \langle m,\sigma|, \tag{8.41}$$

where α_m is the potential shift, for orbital m (see Eq. (8.27))

Default value: `.false.`

Note: See also `potential_shift_orb_eV` and `potential_shift_eV`

potential_shift_orb_eV *(data block)*: Defines the energy shifts α_m in the units of eV as follows:

```
%block potential_shift_orb_eV
1 2 -0.1
2 3 0.1
%endblock potential_shift_orb_eV
```

In the case of iron, this would set a potential shift of $\alpha_{m=-2} = -0.1$ eV to the atom number 1 and a potential shift of $\alpha_{m=-1} = 0.1$ eV to the atom number 2 (the enumeration of orbitals starts from s and is ascending with respect to the quantum number m).

Note: Used only if `ldaU_constrained` is set to `.true.`

potential_shift_eV *(data block)*: Defines the energy shifts α_m in the units of eV as in `potential_shift_o` but without the orbital number; the potential shift is applied to the entire shell.

LatticeConstant	4.36 Å
DM.MixingWeight	0.025
DM.Tolerance	0.00018
DM.NumberPulay	9
PAO.proj_U_energyshift	50 meV
PAO.proj_U_radii	1.310 Å
PAO.proj_U_alpha	50
DM.ElectronicTemperature	50 meV

Table 8.1: Some SIESTA parameters used in the calculations of FeO. The lattice constant was optimized.

Note: Used only if `ldaU_constrained` is set to `.true.`

ldaU_forces *(logical)*: If this switch is set to `.true.`, then the force and stress resulting from the additional U energy term are added to the total force and stress.

Default: `.true.`

ldaU_disk *(integer)*: When this parameter is 1, the program writes the occupation numbers into the file `OCCU`. When setting this parameter to 2 the occupations are red from the file `OCCU`.

Default: `0`

8.5.2 Output files

A single file called `LDAU` is produced. It includes the projectors as function of radial distance as well as information about the occupation numbers, occupation number convergence and the forces. To see the convergence, use `cat LDAU | grep -i "max"`. The `LDAU` file also gives two different LDA+U total energies. Other one as defined Eq.(8.17), labelled as `Total LDA+U energy`. This energy is added to the total energy returned by Siesta. The expectation value of the LDA+U potential of Eq.(8.19) is also calculated and labelled as `Total LDA+U energy1`.

8.6 A test application of the LDA+U: FeO

The transition metal oxides are a classical example of Mott-insulators, where the effect of using LDA+U instead of the LDA should be important. The LDA+U prefers integer occupation numbers for the d-shells of iron (either fully occupied or unoccupied), breaking the symmetry of the system in this way and opening gaps in the electronic structure. In the case of the FeO, the standard (S)LDA predicts the system to be metallic, while the LDA+U corrects this situation and gives an insulating system instead [160].

Using the FeO as a test system, we wish to perform test calculations with various values for the parameter U and compare our results with an earlier calculation [160].

The antiferromagnetic phase of FeO (AFII) is illustrated in Fig. 8.1. It consists of iron planes, normal to the (111) direction. The spin-polarization of neighboring planes is different and the planes are separated by oxygen.

First of all, some standard SIESTA parameters to converge the FeO calculations are presented in Tab. 8.1. A band structure from a standard (S)GGA calculation is presented in Fig.

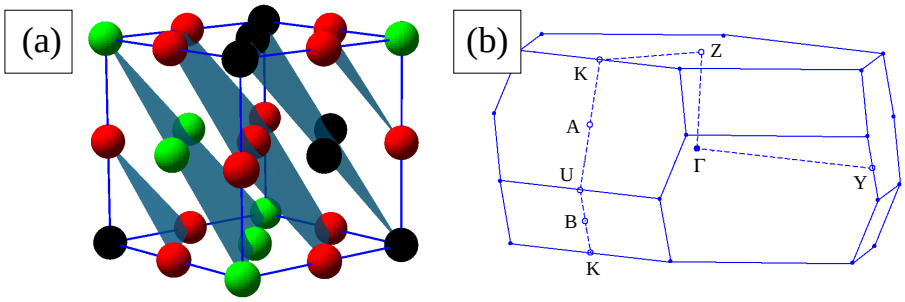

Figure 8.1: (a) The antiferromagnetic structure of FeO plotted in a box. The sides of the box have the dimension of the lattice constant. Iron atoms with spin up (down) are colored with black (green). Oxygen atoms are indicated with red color. Several (111) planes are indicated. (b) The irreducible Brillouin zone of FeO.

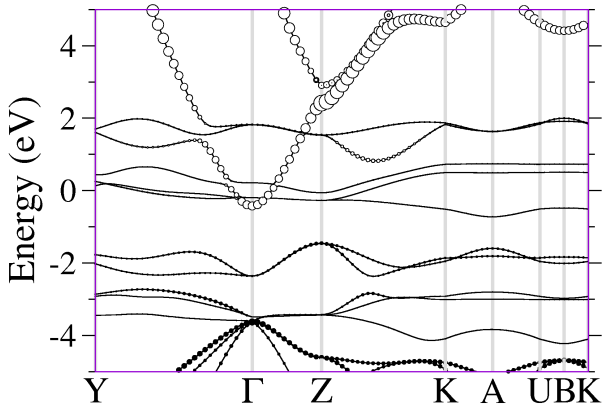

Figure 8.2: The band structure from a (S)GGA calculation of FeO. The notation corresponds to the special points in the irreducible Brillouin-zone as described in Fig. 8.1b. Bands with iron s-character and oxygen p-character are highlighted with black and white circles, respectively. Circle size is proportional to the character.

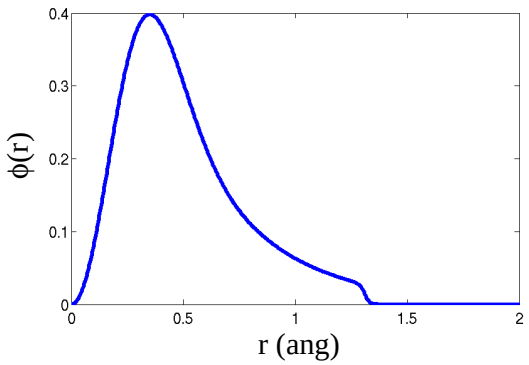

Figure 8.3: The radial part of the projectors, consisting of an iron d-orbital, created with the parameter switches `PAO.proj_U_energyshift`=50 meV, `PAO.proj_U_radii` = 1.3 Å and `PAO.proj_U_alpha` = 50.

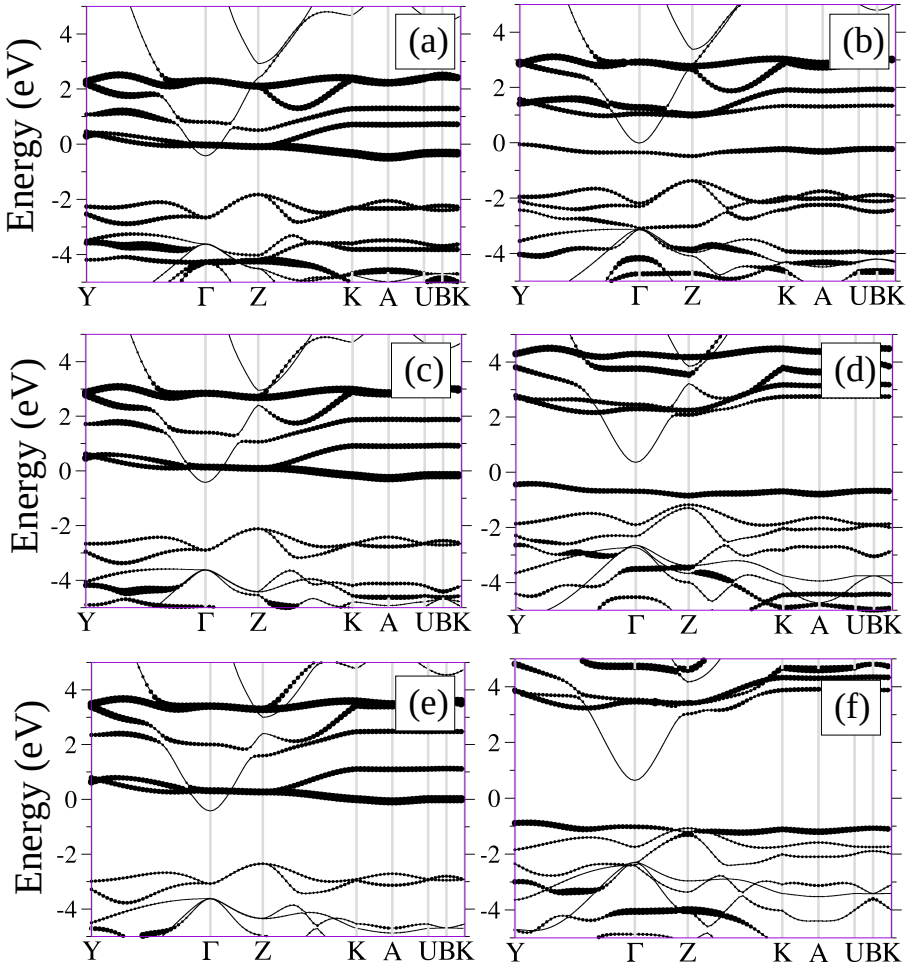

Figure 8.4: Band structure calculations with the (S)GGA+U method. With U=2 (a-b), U=4 (c-d) and U=6 (e-f). In (a),(c) and (e), the parameter `ldaU_maxiters`=1, while in (b),(d) and (f) `ldaU_maxiters`=1000 (i.e. the self-consistent cycle in the occupations was converged). States with Fe d-orbital character are marked with circles and circle size is proportional to the weight the state has in the d-orbitals.

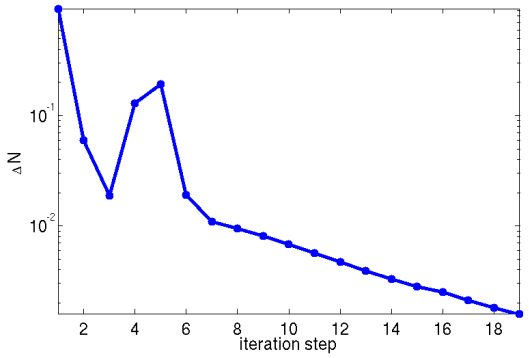

Figure 8.5: Convergence of the occupation number when U=6. Iteration step refers to the occupation number self-consistency step and ΔN is the convergence of Eq. (8.37).

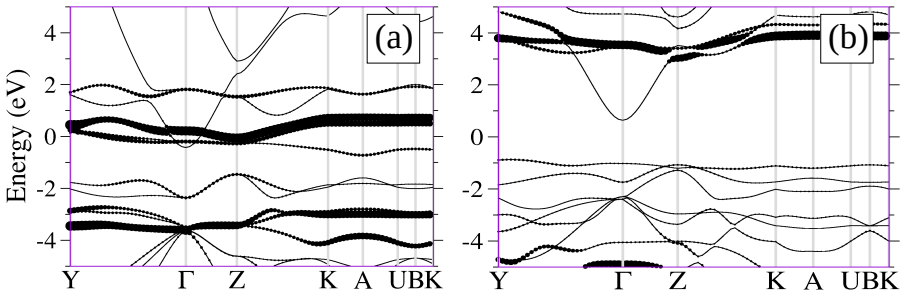

Figure 8.6: An analysis of the A_{1g} character of the bands (see text) for (a) U=0 and (b) U=6 (with occupation number self-consistency). The circle size is comparable to the A_{1g} character.

U	d_{xy}	d_{yz}	d_{z^2}	d_{xz}	$d_{x^2-y^2}$	total
0	0.93 (0.26)	0.93 (0.28)	0.93 (0.14)	0.94 (0.28)	0.93 (0.26)	4.66 (1.22)
6	0.94 (0.49)	0.95 (0.28)	0.94 (0.02)	0.95 (0.13)	0.95 (0.18)	4.71 (1.10)

Table 8.2: Orbital occupations for spin up (down) when z-axis is parallel to the (111) direction. Occupations for the atom with the majority spin up.

8.2. We see that oxygen p- and iron s-states form bands with a rather wide bandwith, while the flat bands (localized electrons) near the Fermi-level are all due to the Fe d-states.

The radial part of the projector used in the GGA+U calculations and the parameters used to create it are presented in Fig. 8.3. Calculations using different U-values were performed. The resulting band structures are plotted in Fig. 8.4.

In Fig. 8.4 the cases (a,c,e) correspond to test calculations, where the self-consistency in the occupation number was not performed. When this extra self-consistency is included in the calculation, usually 5-15 occupation number steps are needed in order to meet the requirement `ldaU_stop` = 0.002 (see Fig. 8.5). Without the self-consistency in the occupations the fully occupied d-bands are pushed downwards in energy. However, the E_f continues to be pinned by some of the d-bands. We observe that when the occupation number cycle is converged, we recover the correct behaviour and the resulting band-gap in the iron d-states is $\approx$ U. As the occupations are changing, they result in a non-symmetric orbital charges that breaks the symmetry of the system and open gaps. This is an example of Mott-insulating behaviour.

We now wish to test the rotational invariance of our LDA+U implementation and compare our band structures to those of Mazin and Anisimov [160]. We first recall from the Ligand Field Theory (LFT) that d-orbitals can be divided into bonding e_g (d_{z^2},$d_{x^2-y^2}$) and non-bonding t_{2g} (d_{xy},d_{xz},d_{yz}) orbitals (the e_g orbitals bonding with oxygen). Following Mazin and Anisimov [160], we consider the linear combination $A_{1g}=\frac{1}{\sqrt{3}}(d_{xy}+d_{xz}+d_{yz})$ and for this reason, rotate the system so that the z-axis is perpendicular to the [111] planes. After the rotation, $A_{1g}=3z^2-(x^2+y^2)$, where z is parallel to [111]. Now we can analyze the A_{1g} character of the bands, by considering their d_{z^2} and $d_{x^2-y^2}$ characters. In Fig. 8.6, we plot the band structure of the rotated system and get results similar to those of Mazin and Anisimov [160]; the flat band lowering down to the oxygen manifold as the U is increased results almost purely from the A_{1g} orbitals (although the weight is relatively small compared to some other bands). While rotating the system, we have also tested the rotational invariance of our LDA+U method; the band structures in Fig. 8.6 are identical to those of Fig. 8.4.

We took some preliminary steps in order to evaluate the value of U in FeO. In Fig. 8.7 we

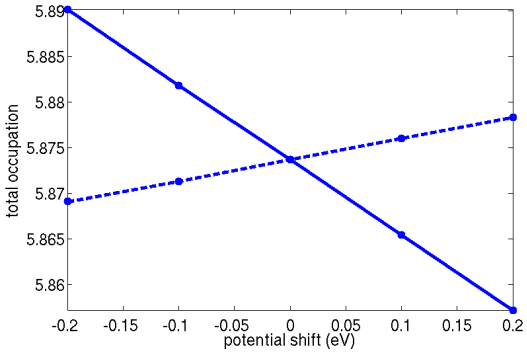

Figure 8.7: Total occupations of the iron atoms of FeO for the atom in which the potential shift is applied (solid) and the neighboring iron atom (dashed).

have plotted the total occupation of the d-shell as function of the potential shift. We used the switch `potential_shift_eV`, so the whole d-shell is subject to the potential shift. Using the simple formula Eq. (8.28), we get U≈13.0 eV. Using the formula of Eq. (8.36) yields a similar result.

Although the value of U depends on the exact shape of the projectors used, the present estimation of U seems a bit too large. We are in the process of exploring the reasons for this overestimation of U in SIESTA and how it depends on the shape and localization of the projectors.

8.7 Another test application: Sr_2VO_4

One of the first experimental studies of the $Sr_{n+1}V_nO_{3n+1}$ compounds were performed by Cyrot et. al. [80] and Nozaki et. al. [81]. The motivation for synthesizing these compounds lay in their structure: (i) they have 2-dimensional character due to the VO-planes (separated by Sr atoms) and (ii) the chemical environment for vanadium is such that a strong magnetic moment can be achieved. Both of these characteristics are thought to be the reason for the onset of superconduction in some high-T_c materials [81]. These compounds, consisting of VO-layers separated by Sr are illustrated in Fig. 8.8.

In this section we make a brief study of the Sr_2VO_4 compound using the LDA+U method. With the LDA, the system turns out to be conductor, while in the experiment it is semiconducting. This compound has already been studied using very sophisticated Path-Integral Renormalization Group method combined with DFT [82] yielding the correct semiconducting nature. We will analyze in detail the electronic properties of this system and show that with the LDA+U this problem can be solved: by studying VO_4 planes we show how the LDA+U, by favoring integer occupations, breaks the symmetry between the d-orbitals of vanadium, making the compound semiconducting in this way, in accordance with the experimental evidence.

In the calculations presented here we take U as a parameter and vary it between 2 and 6 eV, which according to our experience seem reasonable values for $3d$ transition metals. J is taken to be zero. According to Sec. 8.2 this is equivalent to having F^2=F^4=0.

In this section, we use a slightly different projector than in the case of FeO. Instead of using free-atom like orbitals with a steep cut, like those of Fig. 8.3 created using parameters `PAO.proj_U_radii` and `PAO.proj_U_alpha`, we employ the `PAO.proj_U_energyshift`

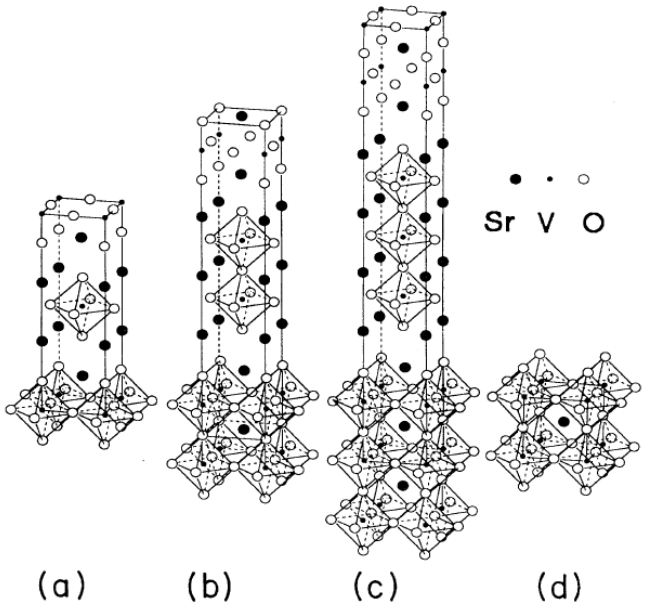

Figure 8.8: Crystal structure of $Sr_{n+1}V_nO_{3n+1}$, for (a) n=1 (b) n=2 (c) n=3 and (d) n=∞. Picture taken from Ref. [81].

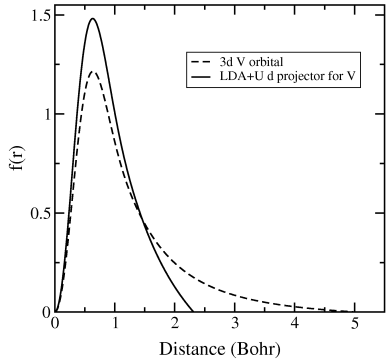

Figure 8.9: Radial dependence of the projector $|\mathrm{m}\rangle$ (r_c=2.32 a.u.) and the most extended d basis orbital (r_c=5.03 a.u.) of the V atoms.

switch to confine the projectors within some cutoff radius. This is illustrated in Fig. 8.9. The confinement radius of the LDA+U projector is 2.32 a.u., compared with the 5.03 a.u. of the d orbitals. We have checked that changing the radius of the $|\mathrm{m}\rangle$ projectors does not produce significant changes in the results as far as the projectors are quite localized. However, a direct comparison of the results obtained with different projectors is difficult since the value of U depends on the choice of projector.

8.7.1 Electronic band structure of Sr_2VO_4

The pseudopotentials and basis sets correspond to the `V.psf`, `Sr.psf` and `O.psf` in Tab. 2.2. We use a tetragonal unit cell that contains two VO_4^{4-} planes and a k-sampling of 4×4×3.

Our calculations of the Sr_2VO_4 compound show that the ferromagnetic arrangement within the VO_4 planes (perpendicular to the c axis) is ∼100 meV per V atom more stable than the

Order	ΔE(meV/atom)	μ_B	a	c
Paramagnetic	122	–	3.827	12.755
FM	0	0.88	3.837	12.732
AFM I	-2	0.88	3.837	12.731
AFM II	+78	0.02	3.839	12.690

Table 8.3: Energy differences per V atom (ΔE) in meV, local magnetic moment in each V atom (μ_B), and relaxed lattice parameters cal

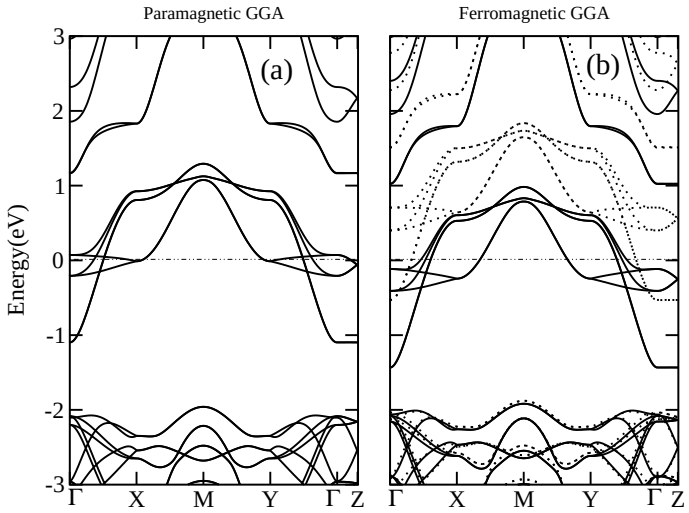

Figure 8.10: Band structure of the Sr_2VO_4 compound calculated with GGA. (a) Paramagnetic configuration, and (b) ferromagnetic configuration (full lines for majority spin and dashed lines for minority spin). Energies are referred to the Fermi level.

antiferromagnetic arrangement within the plane (AFMII) and ∼120 meV than the paramagnetic compound. Once the ferromagnetic order is set up in the plane, the ferromagnetic and antiferromagnetic (AFMI) stacking of the planes are almost degenerate. This implies that the magnetic interaction between the planes is quite small. In the ferromagnetic phase, the V atom presents a localized magnetic moment of ∼0.9 μ_B. Thus it can pictured as a V^{4+} ion.

8.7.2 VO_4^{4-} plane

We have decided to start our investigation of the effect of the U-Hubbard term using the smallest relevant unit necessary to make a reasonable description of the Sr_2VO_4 compound. We have used charged VO_4^{4-} planes. The structure of the oxygen octahedra is taken from the Sr_2VO_4 geometry and is illustrated in Fig. 8.11.

The valence configuration of vanadium is $3d^3 4s^2$ while that of oxygen $2s^2 2p^4$. The effect of the Sr^{2+} ions is supposed to be, as a first approximation, just to dope the VO_4 planes with extra-electrons. For this reason we charge the VO_4 planes with four extra electrons, this way mimicking the situation in the real compound. Now the oxygen p-orbitals still need 4 electrons to get a closed p-shell, leaving only one electron for the vanadium atom. In the LDA approximation this electron is most probably distributed between all the vanadium d-orbitals. This situation is likely to change when using the LDA+U that favors the integer occupation numbers.

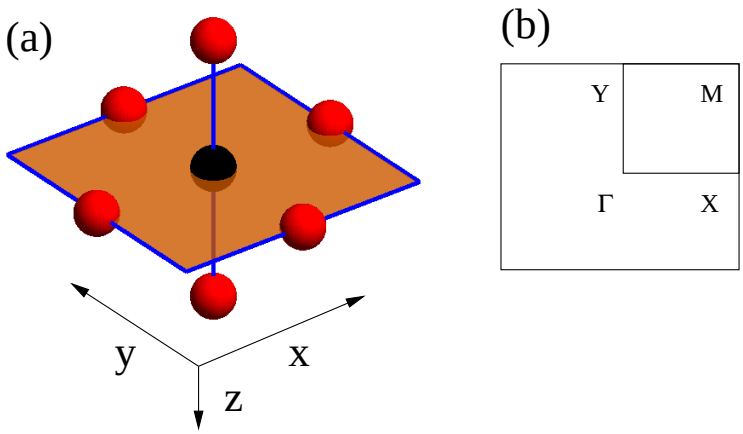

Figure 8.11: (a) VO_4 plane. The vanadium atom is marked with a black sphere and the oxygen atoms with red spheres. with filled circles. Coordinate directions used in this section are indicated by arrows. (b) The irreducible Brillouin-zone of a VO_4 plane.

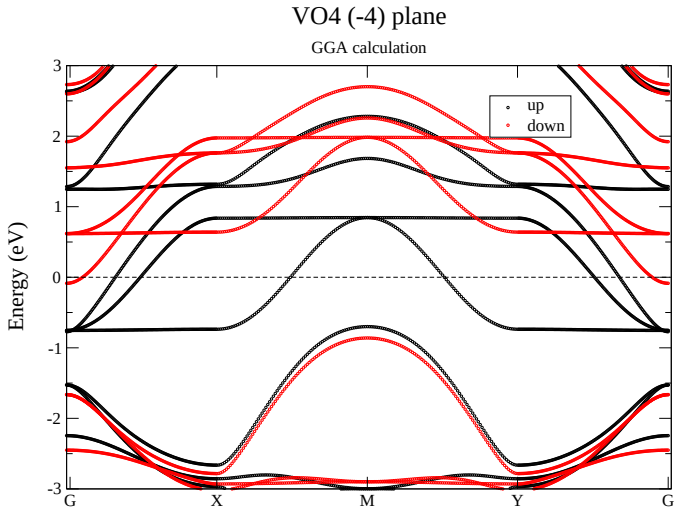

Figure 8.12: Band structure of a VO_4^{4-} plane as calculated with GGA

In Fig. 8.12 we can find the band structure around the Fermi energy of such charged plane as calculated with GGA and the same parameters used for Sr_2VO_4 (except the in-plane k-sampling which was increased to 10×10). The distance between planes is 30 Å and, therefore, the interaction between planes, if any, is purely electrostatic.

For the majority spin the Fermi level is pinned by two bands coming from the d_{xz} and d_{yz} orbitals, which are degenerate by symmetry. These bands can accommodate two electrons. However, the using simple electron counting arguments described above we would assign only one d electron to each V atom. In principle structural distortions, that make d_{xz} and d_{yz} inequivalent, could open a band gap and render a semiconducting system. In practice, our relaxations, at least at the GGA level show very small distortions (of course this is not completely conclusive since the relaxations were started from quite symmetric geometries). The GGA occupations (Eq. 8.6) of the different orbital of the d-shell are in the range 0.3-

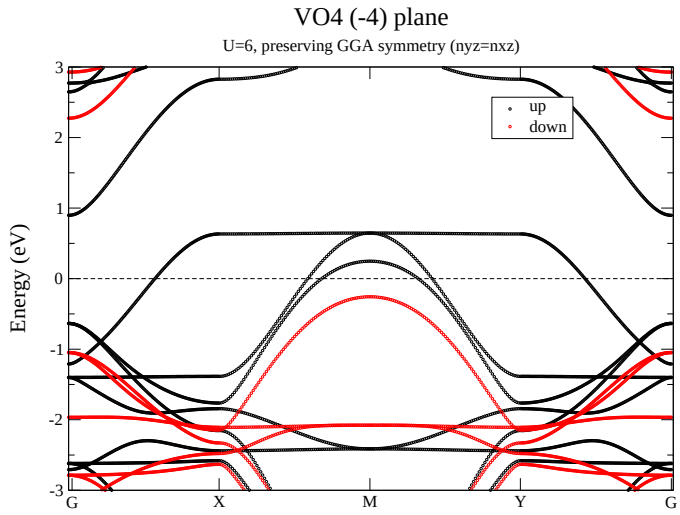

Figure 8.13: Band structure of a VO_4^{4-} plane as calculated with GGA+U scheme with U=6 eV and J=0, starting from a converged GGA density.

0.6, the larger occupations are for the d_{xz} and d_{yz} orbitals. The magnetic moment (difference between spin up and down occupation) is only significant for the d_{xz}, d_{yz} and d_{xy} orbitals: μ_{xz}=μ_{yz}=0.42, μ_{xy}=0.13. The non-diagonal terms, $n_{m,m'}$ with $m \neq m'$, of the occupation matrix restricted to the d-shell are identically zero.

We introduce now a Hubbard U. The band structures presented here are obtained using U=6 eV and J=0. Fig. 8.13 shows the calculated band structure when the GGA+U calculation is started from the GGA result. We can see that the occupied d bands are shifted to lower energies, whereas the unocuppied d bands are pushed to higher energies. However, a band gap cannot be developed because the xz-yz symmetry is preserved. In fact, the structure of the occupation matrix is almost identical to that found in the case of GGA, with all the non-diagonal elements equal to zero.

However, we know that, due to the self-interaction correction included in the Hartree-Fock-like Hubbard term that we have added to our Hamiltonian, the system will tend to select integer occupations rather than fractional occupations. In other words, the d electron should occupy only one electronic state wich, in regards of the band structure of the VO_4^{-4} plane, can be assumed to have the form $|d\rangle = \cos(\theta)|yz\rangle + \sin(\theta)|xz\rangle$ The corresponding occupation matrix takes the form $n^{\uparrow}_{xz,xz} = \sin(\theta)^2$, $n^{\uparrow}_{yz,yz} = \cos(\theta)^2$, $n^{\uparrow}_{xz,yz} = n^{\uparrow}_{yz,xz} = \sin(\theta)\cos(\theta)$, and zero otherwise. In the following, we use such occupation matrix to start our GGA+U calculations.

We observe that only θ=0° (90°), and θ=45° are stable. These means that only starting from these occupations the structure of the occupations matrices is preserve during the self-consistency. In fact θ=0° corresponds to an energy maximum and θ=45° to an energy minimum. All intermediate values of θ converge to the θ=45° solution. The corresponding band structure can be seen in figures 8.15 and 8.14, while the total energies are displayed in Table 8.4. We have also tried to stabilize solution where the electron occupies a d_{xy} orbital. However, such configuration turns out to be unstable and converges to solutions where the charge has been transferred to the d_{xz} and d_{yz} orbitals.

Table 8.4: Change in the total energy of a GGA+U calculation of a VO_4^{4-} plane as a function of the presence or absence of orbital ordering.

Calculation	ΔE(meV)	
	U=6 eV	U=4 eV
GGA symmetry	0	0
$\|yz\rangle$ occupied	+44	–
$\frac{1}{\sqrt{2}}(\|yz\rangle+\|xz\rangle)$ occupied	-63	+28

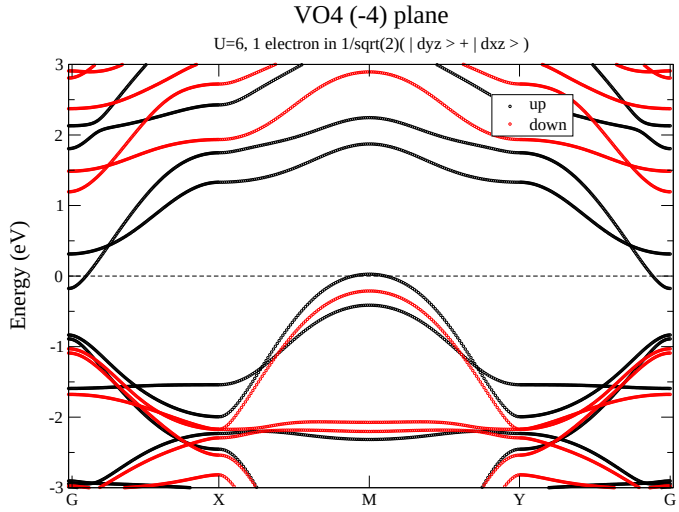

Figure 8.14: Band structure of a VO_4^{4-} plane as calculated with the GGA+U scheme. Initially, the d electron is forced to occupy a state with $\frac{1}{\sqrt{2}}(|yz\rangle+|xz\rangle)$ symmetry. U=6 eV, J=0.

We have tried to use smaller values of U. With U=4 eV, the solution where only the d_{yz} orbital is occupied turns out to we unstable and we get a solution similar to the original GGA, i.e. with half occupied d_{xz} and d_{yz} orbitals. With U=2 eV only this type of solutions, with two half occupied d orbitals, were obtained.

Notice that the energy gain due to the symmetry breaking associated with the orbital ordering is the same order of magnitude than the energy gain associated with the spin polarization (see Table 8.3). It is also clear that we can now open a gap. Indeed there is a clear gap between occupied and unocupied d states for the majority spin. However, the system does remain metallic due to the quite small overlap of two bands. These bands must have a strong oxygen character since they do not move appreciably even when the value of U applied to the d-shell of V is increased to 8 or 10 eV. As we will see below, this does not happen for the Sr_2VO_4 compound. Therefore, one has to be quite careful in order to drive conclusions from the VO_4^{4-} plane. Indeed, we will see that the results for the charge ordering are quite different for the bulk compound. Particularly the d_{xy} orbital tends to be favored over the d_{xz} and d_{yz}.

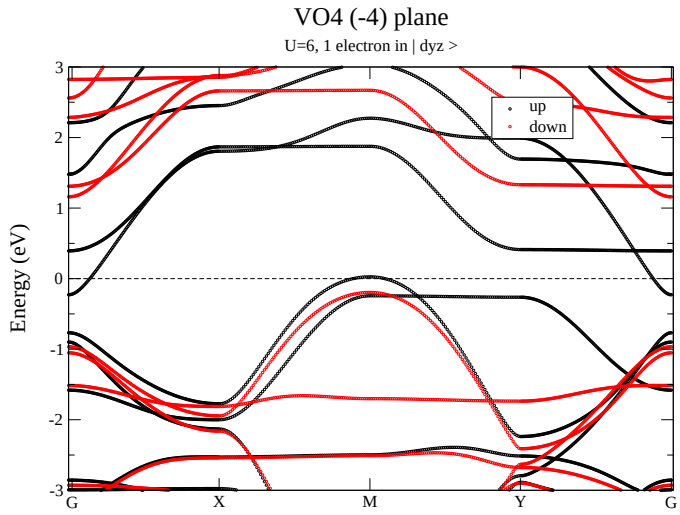

Figure 8.15: As in Fig. 8.14, but the electron occupies a state of $|yz\rangle$ symmetry.

Table 8.5: Change in the total energy (per V atom) of the FM $SrVO_4$ compound calculated with GGA+U as a function of the selected orbital ordering. In parenthesis data calculated using a finer k-point mesh of $6\times6\times3$

Symmetry	ΔE(meV/V)		
	U=6 eV	U=4 eV	U=2 eV
$\|xz\rangle$	+72	+34 (+48)	-2
$\frac{1}{\sqrt{2}}(\|yz\rangle+\|xz\rangle)$	+33	-7 (+6)	-5
$\|xy\rangle$	0	0	0

8.7.3 Band structure of Sr_2VO_4 with the LDA+U method

In Table 8.5 we can see the total energies of the different charge orderings in bulk Sr_2VO_4. Contrary to the case of the simplified model based on the VO_4^{4-} plane, for the bulk material the solution with d_{xy} fully occupied is not only stable, but the most favorable for large values of the U parameter. For U of 4 eV the solution with $|d\rangle=|yz\rangle+|xz\rangle$ occupied becomes more favorable, although the energy difference is so small that lies within the error bar of the calculation (see the change of sign in some of the small energies in Table 8.5 for the lager $6\times6\times3$ k sampling).

Figures 8.16, 8.17 and 8.18 show the band structure of Sr_2VO_4 for different charge orderings and different values of U. For most charge orders a full gap is only developed for U=6 eV. Only in the case of full occupation of $|xy\rangle$. the gap is already present for the whole Brillouin zone for a smaller value U=4 eV.

It is quite interesting to see that the results for the VO_4^{4-} plane are different from those of bulk Sr_2VO_4. This indicates that the details of the structure, not just the vanadium atoms and their nearest neighbors, are important to understand the electronic structure of this compound and, most probably, other compounds of the same family like $Sr_3V_2O_7$.

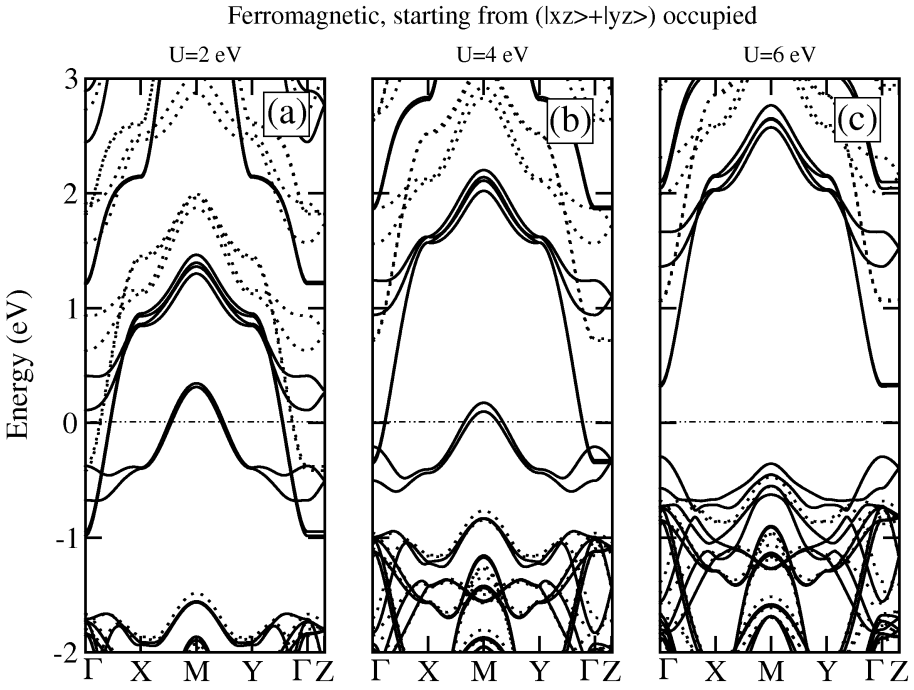

Figure 8.16: Band structure of the Sr_2VO_4 compound. Calculated Energies referred to the Fermi level.

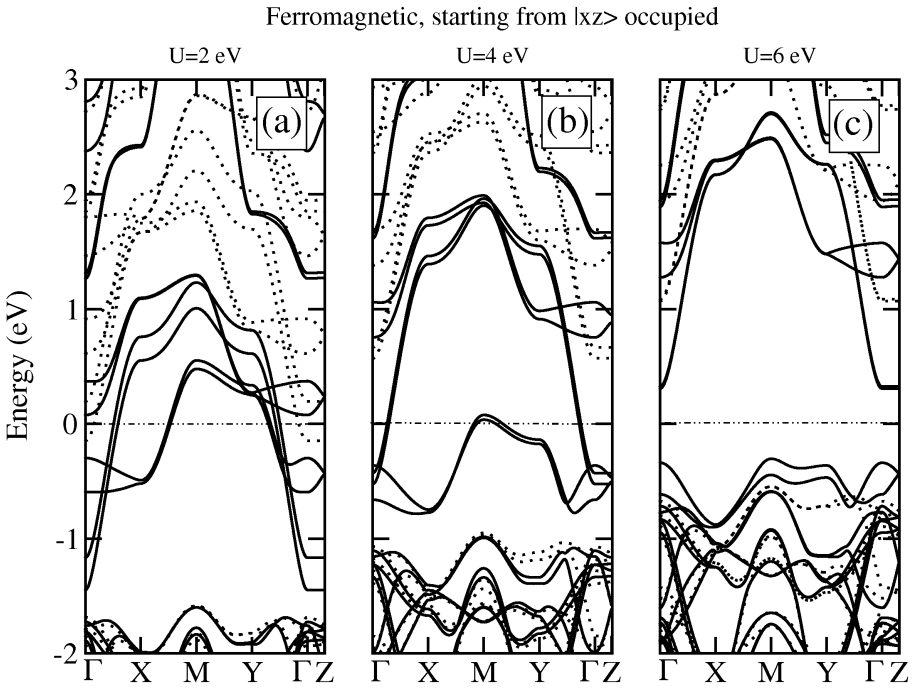

Figure 8.17: Band structure of the Sr_2VO_4 compound. Calculated Energies referred to the Fermi level.

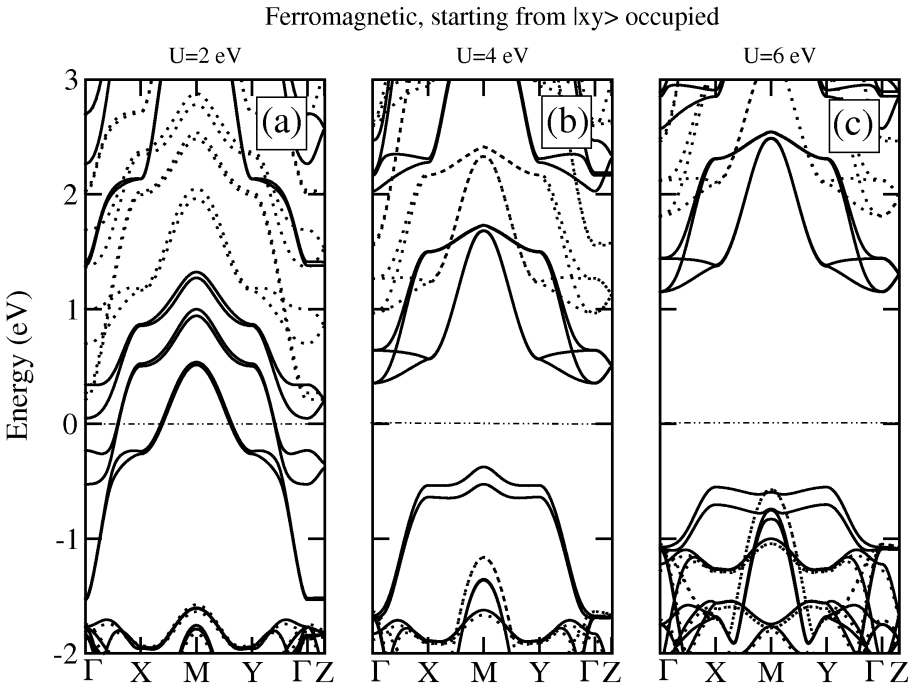

Figure 8.18: Band structure of the Sr_2VO_4 compound. Calculated Energies referred to the Fermi level.

Chapter 9

Conclusions

The main subject of this thesis is the theoretical study of the physical properties of quasi one-dimensional metal-induced surface reconstructions in Si(111) and vicinal Si(111) surfaces. In spite of the experimental interest [2–56,58–64] the geometry and detailed electronic properties of many of these reconstructions are still unknown. Therefore one of our main purposes was to propose atomic geometries for these structures and then compare the theoretical results, obtained using the SIESTA *ab-initio* method, with the available experimental data. We were able to identify plausible model geometries and, by studying the properties of such models, we could find explanations for observed physical phenomena in these surfaces. The second topic of this thesis was the implementation and testing of the LDA+U method in SIESTA that is described in Chap. 8. With the LDA+U method we can improve the description of electron-electron interactions in many systems. The application of this method for the surface reconstructions studied in this thesis and other complex systems will be the subject of future work.

In Chap. 2 we presented a summary of the methodology used throughout this work. We reviewed briefly the DFT and the local orbital formalism used by SIESTA. In Sec. 2.2.6, we also derived some formulas for the implementation of the LDA+U method as described in Chap. 8. In Sec. 2.3 we listed the pseudopotentials and basis sets used throughout this work. Some tools interesting to compare the computational data with the experiment were also briefly explained. These were the simulation of Scanning-Tunneling Microscopy images and the Mulliken population analysis to determine the atomic origin of the electronic states.

We reviewed in Chap. 3 some of the reconstructions that take place when metals are deposited on the Si(111) surface in the submonolayer regime and discussed some of the observations of photoemission and STM experiments. Some of them are, to name few, the quasi one-dimensional free-electron like bands seen in photoemission, one-dimensional row-like structures seen in STM experiments and the metal-insulator transitions that take place when the temperature is lowered, usually accompanied by band-gap opening seen by photoemission and a change of the periodicity of the STM images. Some of the bands also exhibit a splitting that was originally attributed to the Luttinger-liquid. As we pointed out in this chapter, with our models and results based on the *ab-initio* calculations, we have been able to explain very satisfactorily most of the mentioned physical phenomena. Most of these models assume that the metals form monatomic wires, situated in silicon substitutional sites.

In Sec. 3.3, in order to understand better what happens on these surface reconstructions, we looked at some of the typical structural patterns appearing in the reconstructions of clean

Si(111) surfaces, such as the buckling, π-bonding and the adatom reconstructions. We discussed how each one of these reconstructions solves the problem of the elimination of the dangling bonds while minimizing the surface strain. We also explained, in Sec. 3.4, the theory behind the so-called honeycomb-chain Si(111) reconstruction that seems to be a key ingredient when certain metals are deposited on the Si(111) surface. In Sec. 3.5 some general aspects of the silicon stacking and coordination were discussed. Finally, in Sec. 3.6 we performed test calculations on the buckling, π-bonding and the adatom reconstructions. We tested the convergence of the calculations with respect to several computational parameters, such as the basis-set, slab-thickness and the k-point sampling and compared our results to earlier published ones.

The first quasi one-dimensional surface reconstruction we studied is the Si(111)-5x2/Au [2–25, 67, 68] presented in Chap. 4. We started by making a brief review of the history of this reconstruction, pointing out that the first observation of this surface reconstruction was made some thirty years ago, and that ever since, as the experimental methods have been evolving, the different propositions for its atomic level geometry have been flourishing. We discussed the latest experimental results, involving photoemission and STM experiments and studied with *ab-initio* calculations some of the recent models proposed for this surface reconstruction. During this study, we found a totally new geometry for the Si(111)-5x2/Au, that is not only energetically more favorable than the earlier models, but also reproduces very well the results of a very recent photoemission experiment and, to some extent the experimental STM images. We also studied the energetics of the different models as function of the adatom content that seems to be a crucial ingredient not only in the Si(111)-5x2/Au, but as well in other similar surface reconstructions. In STM images the adatoms can be observed as bright, irregular protrusions distributed quite randomly on the surface. We find that our model becomes less favorable than an earlier model proposed by Erwin [67], when the adatom content is very high. As we pointed out, all this implies that the adatoms play a very important role when determining the correct atomic level geometry of the Si(111)-5x2/Au surface reconstruction.

In Chap. 5 we studied the Si(111)-4x1/In reconstruction [39–57, 72–79]. A reasonable model for the atomic geometry of this surface at room temperature already exists that has been tested with *ab-initio* calculations and reproduces very well the experimental data. This geometry consists of two parallel indium zigzag-wires embedded in the silicon substrate. However, the experiments show that the Si(111)-4x1/In features a metal-insulator transition as the temperature is lowered from $\sim$ 300 K down to $\sim$ 130 K. Atomic-level geometry for this low-temperature phase has not yet been fully established. This phase-transition manifests itself both in the photoemission, where gaps open simultaneously in the surface bands, and in the STM images, where the symmetry is lowered to 8×2. We studied this phenomena - its origin lying in the coupling and distortion of the indium wires - by using a simplified model: we kept the two zigzag In wires as in the real surface model and substituted the neighboring Si atoms in the substrate by hydrogen. We verified that this simplified model is able to capture the essential behaviour of electrons and found out that two classes of surface bands can be found: (i) two bands associated with states within the In-wires and (ii) a band associated with the interaction between the two wires (coming from unsaturated In dangling-bonds). We found out that a shear-distortion, as proposed earlier by Gonzalez, et. al. [78] where the zigzag-wires slide with one respect to another, opens a gap in the interaction band. This gap-opening modifies the filling of the two remaining bands in such a way that the Peierls-distortion in them becomes favorable. We also studied the possible Peierls-distortions that can take place

within the zigzag-wires and found out that one of them is optimal. All the observations are consistent with the experimental data and might be important in understanding similar surface reconstructions featuring monatomic double-wires.

Chap. 6 studies the Si(557)/Au reconstruction [26–38, 69–71] that could be considered as the most well-known and widely studied quasi one-dimensional, gold-induced surface reconstruction in vicinal Si(111). For this surface reconstruction there exists an atomic-level geometry that seems to explain quite well the experimental data, the most important feature being the parabolic band that has its origin in the Si-Au bonds. However, there was a characteristic feature in the photoemission spectra - a splitting of the parabolic band - that was interpreted in various different ways in the past, including the Luttinger-liquid behaviour, just to name one. As we showed in Chap. 6, this splitting is probably due to the spin-orbit interaction. This observation has also been backed-up by a very recent photoemission experiment [62]. We also addressed the metal-insulator transition and the accompanying periodicity doubling in the STM images as the temperature is lowered. We assigned this behaviour to the freezing of dynamical fluctuations that have their origin in the atoms at the step-edge of the silicon terraces of the Si(557) surface: in the equilibrium configuration of the model geometry, the step-edge atoms are in alternating up-down positions along the step-edge. We studied the energy landscape as a function of the structural distortion and found a double energy-minimum; if the relative height of the atoms is h then there is a minimum at h_0 and at $-h_0$. As the temperature is increased, the atoms should move between the configurations h_0 and $-h_0$ and visit configurations such as $h = 0$ (atoms at the same height) quite often. In low temperatures the atoms are "freezed" at $-h_0$ or h_0 and this explains the periodicity doubling seen in the STM images. Based on a detailed analysis of the band structure we concluded that the configurations with h=0 are metallic, while those with $h = h_0$ or $h = -h_0$ are semiconducting. The metal-insulator transition is then observed because the system is more likely to visit configurations with $h \approx 0$ as the temperature is higher, while, again freezing to a semiconducting configurations at low temperatures.

We tested this hypothesis by producing theoretical scanning-tunneling microscopy, scanning-tunneling spectroscopy and projected density of states data at different values of h and comparing them to the experimental data. Low temperature data were produced with values $h = h_0$ and the high temperature data were mimicked with configurations $h \approx 0$. In each one of these cases the results were very satisfactory.

We also made *ab-initio* molecular dynamics simulations to see if the step-edge fluctuation actually takes place. We found out that the step-edge indeed fluctuates as we thought and that it is accompanied with other vibrational modes that contribute to the metallicity of the system. These are, for example, the fluctuation of the Si-Au bond angles.

In Chap. 7 we made an extensive study of the Si(553)/Au reconstruction [1, 58–64]. This reconstruction has been found only very recently and a plausible geometrical model that would reproduce the experimental data has not yet been proposed. This reconstruction features a quite unique electronic spectra, having two proximal half-filled and another $\sim \frac{1}{4}$ filled band. This makes this system very interesting, because a fractionally filled band with a such a small filling would be ideal to create the Luttinger liquid, because it might avoid the Mott-Hubbard metal-insulator transition. We searched for the lowest total energy model for this surface reconstruction systematically and based our search on analogies with the Si(557)/Au and other similar systems, considering building blocks found on them, such as surface dislocations and the honeycomb chains. We also developed a systematic notation that allowed us to enumerate

and generate automatically all physically reasonable surface topologies for this class of surface reconstructions. It included a step-by-step refining of the *ab-initio* calculations, allowing for a considerable reduction of the time used for structural relaxations. After using this systematic scheme to try a large number (210) of candidates for the atomic-level geometry for the Si(553)/Au surface, we end up with few structures that are most stable in the terms of the total energy and also reproduce reasonably well the electronic spectra and the STM images when compared to the experimental data.

The theory behind the LDA+U method and its implementation into SIESTA were described in Chap. 8. We first discussed the origin behind the failure of the LDA approximation to treat localized electrons. After this we considered how this could be corrected by using the Hartree-Fock method and derived the formulas of the standard, rotationally invariant LDA+U scheme due to Anisimov, et. al. [153] and also considered the possibility to calculate U by *ab-initio* calculations. Then, in Sec. 8.5, we described the new program switches used to control the LDA+U method and after this, in Sec. 8.6 tested our implementation of the LDA+U method by doing calculations of the FeO compound. For FeO, we were able to reproduce earlier results by Mazin, et. al. [160], where the FeO is seen to develop a gap when the LDA+U method is used. We also tested the rotational invariance of the method, but failed to get a reasonable value for the Hubbard-parameter U using *ab-initio* calculations only. This last aspect must be studied in detail in future.

In Sec. 8.7 we studied the effect of the LDA+U on *ab-initio* calculations of the Sr_2VO_4 compound [80–82]. As we discussed in the same chapter, this compound might be important in understanding the high-T_c superconductors. According to the standard LDA calculations, this compound is metallic, although in the experiments it is observed to be semiconducting. We showed, by studying charged VO_4 layers, how using the LDA+U, the symmetry of the vanadium d-orbitals in the layer can be broken and a gap can opened in the electronic structure, this way obtaining an electronic spectra that is in accordance with the experiment. This was also shown to be true in the case of the whole Sr_2VO_4 compound.

Finally, I believe that the work presented in this thesis has contributed to the fundamental understanding of the quasi one-dimensional metal-induced silicon surface reconstructions. Since these surfaces might be important from a technological point of view, a point that was discussed in Sec. 3.1, the results obtained in this thesis might be an important, although small, building block in the future exploitation of these surfaces.

The LDA+U is quite simple, semi-empirical, yet very efficient method for correcting some well-known pathologies of the LDA, and the implementation presented in this thesis will be included in the future distributions of the SIESTA program package.

Bibliography

[1] J. N. Crain, J. L. McChesney, F. Zheng, M. C. Gallagher, P. C. Snijders, M. Bissen, C. Gundelach, S. C. Erwin, and F. J. Himpsel, "Chains of gold atoms with tailored electronic states," *Phys. Rev. B*, vol. 69, p. 125401, 2004.

[2] H. E. Bishop and J. C. Riviere, "Segregation of gold to the silicon (111) surface observed by Auger emission spectroscopy and by LEED," *J. Phys. D*, vol. 2, p. 1635, 1969.

[3] H. Lipson and K. E. Singer, "Disorder in a film of gold deposited on silicon: investigation by low-energy electron diffraction," *J. Phys. C*, vol. 7, p. 12, 1974.

[4] G. Lelay and J. P. Faurie, "AES study of the very first stages of condensation of gold films on silicon (111) surfaces," *Surf. Sci.*, vol. 69, p. 295, 1977.

[5] L. E. Berman, B. W. Batterman, and J. M. Blakely, "Structure of submonolayer gold on silicon (111) from x-ray standing-wave triangulation," *Phys. Rev. B*, vol. 38, no. 8, pp. 5397–5405, Sep 1988.

[6] A. A. Baski, J. Nogami, and C. F. Quate, "Si(111)-5x1-Au reconstruction as studied by scanning tunneling microscopy," *Phys. Rev. B*, vol. 41, no. 14, pp. 10 247–10 249, May 1990.

[7] T. Hasegawa, K. Takata, S. Hosaka, and S. Hosoki, "Au-induced reconstructions of the Si(111) surface," *J. Vac. Sci. Technology A*, vol. 8, pp. 241–244, 1990.

[8] E. Bauer, "The Si(111)-(5x1) Au structure," *Surf. Sci. Lett.*, vol. 250, pp. L379–L382, 1991.

[9] C. Schamper, W. Moritz, H. Schulz, R. Feidenhans'l, M. Nielsen, F. Grey, and R. L. Johnson, "Static lattice distortions and the structure of Au/Si(111)-5x2: An x-ray-diffraction study," *Phys. Rev. B*, vol. 43, no. 14, pp. 12 130–12 133, May 1991.

[10] J. D. O'Mahony, C. H. Patterson, J. F. McGilp, F. M. Leibsle, P. Weightman, and C. F. J. Flipse, "The Au-induced 5 ÃŮ 2 reconstruction on Si(111)," *Surf. Sci. Lett.*, vol. 277, pp. L57–L62, 1992.

[11] J. D. O'Mahony, J. F. McGilp, C. F. J. Flipse, P. Weightman, and F. M. Leibsle, "Nucleation and evolution of the Au-induced 5x2 structure on vicinal Si(111)," *Phys. Rev. B*, vol. 49, no. 4, pp. 2527–2535, Jan 1994.

[12] I. R. Collins, J. T. Morgan, P. T. Andrews, R. Cosso, J. D. O'Mahony, J. F. McGlip, and G. Margaritondo, "Angle-resolved photoemission from an unusual quasi-one-dimensional metallic system: a single domain Au-induced 5x2 reconstruction of Si(111)," *Surf. Sci.*, vol. 325, pp. 45–49, 1995.

[13] R. Plass and L. D. Marks, "Submonolayer Au on Si(111) phase diagram," *Surf. Sci.*, vol. 380, p. 497, 1997.

[14] L. D. Marks and R. Plass, "Atomic Structure of Si(111)-(5x2)-Au from High Resolution Electron Microscopy and Heavy-Atom Holography," *Phys. Rev. Lett.*, vol. 75, no. 11, pp. 2172–2175, Sep 1995.

[15] T. Hasegawa, S. Hosaka, and S. Hosoki, "Domain growth of Si(111)-5 ÃŮ 2 Au by high-temperature STM," *Surf. Sci.*, vol. 357-358, pp. 858–862, 1996.

[16] I. G. Hill and A. B. McLean, "Role of Si adatoms in the Si(111)-(5x2)-Au quasi-one-dimensional system," *Phys. Rev. B*, vol. 55, no. 23, pp. 15 664–15 668, Jun 1997.

[17] J. R. Power, P. Weightman, and J. D. O'Mahony, "Strong optical anisotropy of the single-domain 5x2-Au reconstruction on vicinal Si(111)," *Phys. Rev. B*, vol. 56, no. 7, pp. 3587–3590, Aug 1997.

[18] R. Losio, K. N. Altmann, and F. J. Himpsel, "Continuous Transition from Two- to One-Dimensional States in Si(111)-5x2/Au," *Phys. Rev. Lett.*, vol. 85, no. 4, pp. 808–811, Jul 2000.

[19] K. N. Altmann, J. N. Crain, A. Kirakosian, J.-L. Lin, D. Y. Petrovykh, F. J. Himpsel, and R. Losio, "Electronic structure of atomic chains on vicinal Si(111)-Au," *Phys. Rev. B*, vol. 64, no. 3, p. 035406, Jun 2001.

[20] R. Bennewitz, J. N. Crain, A. Kirakosian, J. L. Lin, J. L. McChesney, D. Y. Petrovykh, and F. J. Himpsel, "Atomic scale memory at a silicon surface," *Nanotechnology*, vol. 13, p. 499, 2002.

[21] A. Kirakosian, J. N. Crain, J.-L. Lin, J. L. McChesney, D. Y. Petrovykh, F. J. Himpsel, and R. Bennewitz, "Silicon adatoms on the Si(111)5x2-Au surface," *Surf. Sci.*, vol. 532-535, pp. 928–933, 2003.

[22] A. Kirakosian, R. Bennewitz, F. Himpsel, and L. Bruch, "Correlations in a one-dimensional lattice fluid on Si(111)-(5x2)-Au," *Phys. Rev. B*, vol. 67, no. 20, p. 205412, May 2003.

[23] I. Matsuda, M. Hengsberger, F. Baumberger, T. Greber, H. W. Yeom, and J. Osterwalder, "Reinvestigation of the band structure of the Si(111)5x2-Au surface," *Phys. Rev. B*, vol. 68, no. 19, p. 195319, Nov 2003.

[24] J. L. McChesney, J. N. Crain, V. Pérez-Dieste, F. Zheng, M. C. Gallagher, M. Bissen, C. Gundelach, and F. J. Himpsel, "Electronic stabilization of a 5x4 dopant superlattice on Si(111)5x2-Au," *Phys. Rev. B*, vol. 70, p. 195430, 2004.

[25] H. S. Yoon, S. J. Park, J. E. Lee, C. N. Whang, and I. W. Lyo, "Novel Electronic Structure of Inhomogeneous Quantum Wires on a Si Surface," *Phys. Rev. Lett.*, vol. 92, p. 96801, 2004.

[26] M. Jalochowski, M. Strozak, and R. Zdyb, "Gold-induced ordering on vicinal Si(111)," *Surf. Sci.*, vol. 375, pp. 203–209, 1997.

[27] P. Segovia, D. Purdie, M. Hengsberger, and Y. Baer, "Observation of spin and charge collective modes in one-dimensional metallic chains," *Nature*, vol. 402, pp. 504–507, 1999.

[28] R. Losio, K. N. Altmann, A. Kirakosian, J.-L. Lin, D. Y. Petrovykh, and F. J. Himpsel, "Band Splitting for Si(557)-Au: Is It Spin-Charge Separation?" *Phys. Rev. Lett.*, vol. 86, no. 20, pp. 4632–4635, May 2001.

[29] I. K. Robinson, P. A. Bennett, and F. J. Himpsel, "Structure of Quantum Wires in Au/Si(557)," *Phys. Rev. Lett.*, vol. 88, no. 9, p. 096104, Feb 2002.

[30] J. R. Ahn, H. W. Yeom, H. S. Yoon, and I.-W. Lyo, "Metal-Insulator Transition in Au Atomic Chains on Si with Two Proximal Bands," *Phys. Rev. Lett.*, vol. 91, no. 19, p. 196403, Nov 2003.

[31] J. R. Ahn, H. W. Yeom, E. S. Cho, and C. Y. Park, "Electronic transition of Au-induced atomic chains on Si(5 5 12): A strong similarity with the Au/Si(5 5 7) system," *Phys. Rev. B*, vol. 69, p. 233311, 2004.

[32] H. Okino, R. Hobara, I. Matsuda, T. Kanagawa, S. Hasegawa, J. Okabayashi, S. Toyoda, and M. Oshima, "Nonmetallic transport of a quasi-one-dimensional metallic Si(557)-Au surface," *Phys. Rev. B*, vol. 70, p. 113404, 2004.

[33] H. W. Yeom, J. R. Ahn, H. S. Yoon, I.-W. Lyo, H. Jeong, and S. Jeong, "Real-space investigation of the metal-insulator transition of Si(557)-Au," *Phys. Rev. B*, vol. 72, p. 35323, 2005.

[34] M. Krawiec, T. Kwapiński, and M. Jalochowski, "Double nonequivalent chain structure on a vicinal Si(557)-Au surface," *Phys. Rev. B*, vol. 73, p. 75415, 2006.

[35] J. A. Lipton-Duffin, J. M. MacLeod, and A. B. McLean, "Detection of a Fermi-level crossing in Si(557)-Au with inverse photoemission," *Phys. Rev. B*, vol. 73, p. 245418, 2006.

[36] T. Nagao, S. Yaginuma, T. Inaoka, and T. Sakurai, "One-Dimensional Plasmon in an Atomic-Scale Metal Wire," *Phys. Rev. Lett.*, vol. 97, p. 116802, 2006.

[37] M. Schöck, C. Sürgers, and H. v. Löhneysen, "Atomically resolved tunneling spectroscopy on Si(557)-Au," *Europhys. Lett.*, vol. 74, pp. 473–478, 2006.

[38] T. K. Rügheimer, T. Fauster, and F. J. Himpsel, "Unoccupied electronic states in atomic chains on Si(557)-Au: Time-resolved two-photon photoemission investigation," *Phys. Rev. B.*, vol. 75, p. 121401(R), 2007.

[39] J. Nogami, S.-i. Park, and C. F. Quate, "Indium-induced reconstructions of the Si(111) surface studied by scanning tunneling microscopy," *Phys. Rev. B*, vol. 36, no. 11, pp. 6221–6224, Oct 1987.

[40] T. Abukawa, M. Sasaki, F. Hisamatsu, T. Goto, T. Kinoshita, A. Kakizaki, and S. Kono, "Surface electronic structure of a single-domain Si(111)4x1-In surface: a synchrotron radiation photoemission study," *Surf. Sci.*, vol. 325, p. 33, 1995.

[41] J. Kraft, M. G. Ramsey, and F. P. Netzer, "Surface reconstructions of In on Si(111)," *Phys. Rev. B*, vol. 55, no. 8, pp. 5384–5393, Feb 1997.

[42] A. A. Saranin, A. Zotov, K. V. Ignatovich, V. G. Lifshits, T. Numata, O. Kubo, H. Tani, M. Katayama, and K. Oura, "Structural model for the Si(111)-4x1-In reconstruction," *Phys. Rev. B*, vol. 56, no. 3, pp. 1017–1020, Jul 1997.

[43] O. Bunk, G. Falkenberg, J. H. Zeysing, L. Lottermoser, R. L. Johnson, M. Nielsen, F. Berg-Rasmussen, J. Baker, and R. Feidenhans'l, "Structure determination of the indium-induced Si(111)-4x1 reconstruction by surface x-ray diffraction," *Phys. Rev. B*, vol. 59, no. 19, pp. 12 228–12 231, May 1999.

[44] I. G. Hill and A. B. McLean, "Strongly Anisotropic Band Dispersion of an Image State Located above Metallic Nanowires," *Phys. Rev. Lett.*, vol. 82, no. 10, pp. 2155–2158, Mar 1999.

[45] H. W. Yeom, S. Takeda, E. Rotenberg, I. Matsuda, K. Horikoshi, J. Schaefer, C. M. Lee, S. D. Kevan, T. Ohta, T. Nagao, and S. Hasegawa, "Instability and Charge Density Wave of Metallic Quantum Chains on a Silicon Surface," *Phys. Rev. Lett.*, vol. 82, no. 24, pp. 4898–4901, Jun 1999.

[46] C. Kumpf, O. Bunk, J. H. Zeysing, Y. Su, M. Nielsen, R. L. Johnson, R. Feidenhans'l, and K. Bechgaard, "Low-Temperature Structure of Indium Quantum Chains on Silicon," *Phys. Rev. Lett.*, vol. 85, no. 23, pp. 4916–4919, Dec 2000.

[47] S. V. Ryjkov, T. Nagao, V. G. Lifshits, and S. Hasegawa, "Phase transition and stability of Si(1 1 1)8x2-In surface phase at low temperatures," *Surf. Sci.*, vol. 488, pp. 15–22, 2001.

[48] K. Fleischer, S. Chandola, N. Esser, W. Richter, and J. F. McGilp, "Phonon and polarized reflectance spectra from Si(111)-(4x1)In: Evidence for a charge-density-wave driven phase transition," *Phys. Rev. B*, vol. 67, no. 23, p. 235318, Jun 2003.

[49] G. Lee, S.-Y. Yu, H. Kim, J.-Y. Koo, H.-I. Lee, and D. W. Moon, "Absolute In coverage and bias-dependent STM images of the Si(111)4x1-In surface," *Phys. Rev. B*, vol. 67, no. 3, p. 035327, Jan 2003.

[50] S. Mizuno, Y. O. Mizuno, and H. Tochihara, "Structural determination of indium-induced Si(111) reconstructed surfaces by LEED analysis: $(\sqrt{3}\times\sqrt{3})R30^\circ$ and (4×1)," *Phys. Rev. B*, vol. 67, no. 19, p. 195410, May 2003.

[51] S. Wang, W. Lu, W. G. Schmidt, and J. Bernholc, "Nanowire-induced optical anisotropy of the Si(111)-In surface," *Phys. Rev. B*, vol. 68, no. 3, p. 035329, Jul 2003.

[52] J. R. Ahn, J. H. Byun, H. Koh, E. Rotenberg, S. D. Kevan, and H. W. Yeom, "Mechanism of Gap Opening in a Triple-Band Peierls System: In Atomic Wires on Si," *Phys. Rev. Lett.*, vol. 93, p. 106401, 2004.

[53] G. Lee, S.-Y. Yu, H. Kim, and J.-Y. Koo, "Defect-induced perturbation on Si(111)4x1-In: Period-doubling modulation and its origin," *Phys. Rev. B*, vol. 70, p. 121304, 2004.

[54] S. J. Park, H. W. Yeom, S. H. Min, D. H. Park, and I.-W. Lyo, "Direct Evidence of the Charge Ordered Phase Transition of Indium Nanowires on Si(111)," *Phys. Rev. Lett.*, vol. 93, p. 106402, 2004.

[55] S. Kurata and T. Yokoyama, "Interchain coupling of degenerated quasi-one-dimensional indium chains on Si(111)," *Phys. Rev. B*, vol. 71, p. 121306, 2005.

[56] H. W. Yeom, "Comment on "Soft Phonon, Dynamical Fluctuations, and a Reversible Phase Transition: Indium Chains on Silicon"," *Phys. Rev. Lett.*, vol. 97, p. 189701, 2006.

[57] J. R. Ahn, J. H. Byun, J. K. Kim, and H. W. Yeom, "Absence of dynamic fluctuation in metallic In chains on Si(111): Core-level and valence-band photoemission study," *Phys. Rev. B*, vol. 75, p. 033313, 2007.

[58] J. N. Crain, A. Kirakosian, K. N. Altmann, C. Bromberger, S. C. Erwin, J. L. McChesney, J.-L. Lin, and F. J. Himpsel, "Fractional Band Filling in an Atomic Chain Structure," *Phys. Rev. Lett.*, vol. 90, no. 17, p. 176805, May 2003.

[59] J. R. Ahn, P. G. Kang, K. D. Ryang, and H. W. Yeom, "Coexistence of Two Different Peierls Distortions within an Atomic Scale Wire: Si(553)-Au," *Phys. Rev. Lett.*, vol. 95, p. 196402, 2005.

[60] J. N. Crain and D. T. Pierce, "End States in One-Dimensional Atom Chains," *Science*, vol. 307, pp. 703–706, 2005.

[61] S. K. Ghose, I. K. Robinson, P. A. Bennett, and F. J. Himpsel, "Structure of double row quantum wires in Au/Si(5 5 3)," *Surf. Sci.*, vol. 581, pp. 199–206, 2005.

[62] I. Barke, F. Zheng, T. K. R$'$ugheimer, and F. J. Himpsel, "Experimental Evidence for Spin-Split Bands in a One-Dimensional Chain Structure," *Phys. Rev. Lett.*, vol. 97, p. 226405, 2006.

[63] J. N. Crain, M. D. Stiles, J. A. Stroscio, and D. T. Pierce, "Electronic Effects in the Length Distribution of Atom Chains," *Phys. Rev. Lett.*, vol. 96, p. 156801, 2006.

[64] P. C. Snijders, S. Rogge, and H. H. Weitering, "Competing Periodicities in Fractionally Filled One-Dimensional Bands," *Phys. Rev. Lett.*, vol. 96, p. 076801, 2006.

[65] S. C. Erwin, "New Structural Model for the Alkali-Induced Si(111)-(3x1) Reconstruction from First Principles," *Phys. Rev. Lett.*, vol. 75, no. 10, pp. 1973–1976, Sep 1995.

[66] S. C. Erwin and H. H. Weitering, "Theory of the Honeycomb Chain-Channel Reconstruction of M/Si(111)- 3x1," *Phys. Rev. Lett.*, vol. 81, no. 11, pp. 2296–2299, Sep 1998.

[67] S. C. Erwin, "Self-Doping of Gold Chains on Silicon: A New Structural Model for Si(111)-(5x2)-Au," *Phys. Rev. Lett.*, vol. 91, no. 20, p. 206101, Nov 2003.

[68] M. H. Kang and J. Y. Lee, "Theoretical investigation of the Au/Si(111)-(5x2) surface structure," *Surf. Sci.*, vol. 531, pp. 1–7, 2003.

[69] D. Sánchez-Portal, J. D. Gale, A. García, and R. M. Martin, "Two distinct metallic bands associated with monatomic Au wires on the Si(557)-Au surface," *Phys. Rev. B*, vol. 65, no. 8, p. 081401, Feb 2002.

[70] D. Sánchez-Portal and R. M. Martin, "First principles study of the Si(5 5 7)-Au surface," *Surf. Sci.*, vol. 532-535, pp. 655–660, 2003.

[71] D. Sánchez-Portal, S. Riikonen, and R. M. Martin, "Role of Spin-Orbit Splitting and Dynamical Fluctuations in the Si(557)-Au Surface," *Phys. Rev. Lett.*, vol. 93, p. 146803, 2004.

[72] J.-H. Cho, D.-H. Oh, K. S. Kim, and L. Kleinman, "Weakly correlated one-dimensional indium chains on Si(111)," *Phys. Rev. B*, vol. 64, no. 23, p. 235302, Nov 2001.

[73] R. H. Miwa and G. P. Srivastava, "Atomic geometry, electronic structure and image state for the Si(111)-In(4x1) nanowire," *Surf. Sci.*, vol. 473, p. 123, 2001.

[74] J. Nakamura, S. Watanabe, and M. Aono, "Anisotropic electronic structure of the Si(111)-4x1 In surface," *Phys. Rev. B*, vol. 63, no. 19, p. 193307, Apr 2001.

[75] F. Bechstedt, A. Krivosheeva, J. Furthmüller, and A. A. Stekolnikov, "Vibrational properties of the quasi-one-dimensional In/Si(111)-4x1 system," *Phys. Rev. B*, vol. 68, no. 19, p. 193406, Nov 2003.

[76] J.-H. Cho, J.-Y. Lee, and L. Kleinman, "Electronic structure of one-dimensional indium chains on Si(111)," *Phys. Rev. B*, vol. 71, p. 81310, 2005.

[77] C. González, J. Ortega, and F. Flores, "Metal-insulator transition in one-dimensional In-chains on Si(111): combination of a soft shear distortion and a double-band Peierls instability," *New J. of Phys.*, vol. 7, p. 100, 2005.

[78] C. González, F. Flores, and J. Ortega, "Soft Phonon, Dynamical Fluctuations, and a Reversible Phase Transition: Indium Chains on Silicon," *Phys. Rev. Lett.*, vol. 96, p. 136101, 2006.

[79] C. Gonzalez, F. Flores, and J. Ortega, "González, Ortega and Flores Reply," *Phys. Rev. Lett.*, vol. 97, p. 189702, 2006.

[80] M. Cyrot, B. Lambert-Andron, J. Soubeyroux, M. Rey, P. Dehauht, F. Cyrot-Lackmann, G. Fourcaudot, J. Beille, and J. Tholence, "Properties of a new perovskite oxide Sr_2VO_4," *J. Sol. State Chem.*, vol. 85, pp. 231–325, 1990.

[81] A. Nozaki, H. Yoshikawa, T. Wada, H. Yamauchi, and S. Tanaka, "Layered perovskite compounds $Sr_{n+1}V_nO_{3n+1}$ (n=1, 2, 3, and ∞)," *Phys. Rev. B*, vol. 43, no. 1, pp. 181–185, Jan 1991.

[82] Y. Imai, I. Solovyev, and M. Imada, "Electronic Structure of Strongly Correlated Systems Emerging from Combining Path-Integral Renormalization Group with the Density-Functional Approach," *Phys. Rev. Lett.*, vol. 95, p. 176405, 2005.

[83] R. M. Dreizler and E. K. U. Gross, *Density functional theory*. Springer, 1990.

[84] D. Sanchez-Portal, P. Ordejon, E. Artacho, and J. M. Soler, "Density-functional method for very large systems with LCAO basis sets," *Int. J. Quantum Chem.*, vol. 65, pp. 453–461, 1997.

[85] E. Artacho, D. Sánchez-Portal, P. Ordejón, A. García, and J. M. Soler, "Linear-Scaling ab-initio Calculations for Large and Complex Systems," *Phys. Stat. Solidi (b)*, vol. 215, pp. 809–817, 1999.

[86] J. M. Soler, E. Artacho, J. D. Gale, A. García, J. Junquera, P. Ordejón, and D. Sánchez-Portal, "The SIESTA method for ab initio order-N materials simulation," *J. of Phys.: Condensed Matter*, vol. 14, pp. 2745–2779, 2002.

[87] P. Hohenberg and W. Kohn, "Inhomogeneous Electron Gas," *Phys. Rev.*, vol. 136, no. 3B, pp. B864–B871, Nov 1964.

[88] W. Kohn and L. J. Sham, "Self-Consistent Equations Including Exchange and Correlation Effects," *Phys. Rev.*, vol. 140, no. 4A, pp. A1133–A1138, Nov 1965.

[89] E. Anglada, J. M. Soler, J. Junquera, and E. Artacho, "Systematic generation of finite-range atomic basis sets for linear-scaling calculations," *Phys. Rev. B*, vol. 66, no. 20, p. 205101, Nov 2002.

[90] D. Sanchez-Portal, E. Artacho, and J. M. Soler, "Projection of plane-wave calculations into atomic orbitals," *Solid State Communications*, vol. 95, pp. 685–690, 1995.

[91] N. Ashcroft and N. Mermin, *Solid State Physics*. Saunders College, 1976.

[92] H. J. Monkhorst and J. D. Pack, "Special points for Brillouin-zone integrations," *Phys. Rev. B*, vol. 13, no. 12, pp. 5188–5192, Jun 1976.

[93] N. Troullier and J. L. Martins, "Efficient pseudopotentials for plane-wave calculations," *Phys. Rev. B*, vol. 43, no. 3, pp. 1993–2006, Jan 1991.

[94] L. Kleinman and D. M. Bylander, "Efficacious Form for Model Pseudopotentials," *Phys. Rev. Lett.*, vol. 48, no. 20, pp. 1425–1428, May 1982.

[95] J. P. Perdew and A. Zunger, "Self-interaction correction to density-functional approximations for many-electron systems," *Phys. Rev. B*, vol. 23, no. 10, pp. 5048–5079, May 1981.

[96] J. P. Perdew, K. Burke, and M. Ernzerhof, "Generalized Gradient Approximation Made Simple," *Phys. Rev. Lett.*, vol. 77, no. 18, pp. 3865–3868, Oct 1996.

[97] H. Häkkinen, M. Moseler, and U. Landman, "Bonding in Cu, Ag, and Au Clusters: Relativistic Effects, Trends, and Surprises," *Phys. Rev. Lett.*, vol. 89, no. 3, p. 033401, Jun 2002.

[98] O. F. Sankey and D. J. Niklewski, "Ab initio multicenter tight-binding model for molecular-dynamics simulations and other applications in covalent systems," *Phys. Rev. B*, vol. 40, no. 6, pp. 3979–3995, Aug 1989.

[99] J. Tersoff and D. R. Hamann, "Theory of the scanning tunneling microscope," *Phys. Rev. B*, vol. 31, no. 2, pp. 805–813, Jan 1985.

[100] R. S. Mulliken, "Electronic Population Analysis on LCAO–MO Molecular Wave Functions. II. Overlap Populations, Bond Orders, and Covalent Bond Energies," *J. Chem. Phys.*, vol. 23, p. 1841, 1955.

[101] S. Riikonen and D. Sanchez-Portal, "First-principles study of the atomic and electronic structure of the Si(111)/Au-5x2 surface reconstruction," *Phys. Rev. B.*, vol. 71, p. 235423, 2005.

[102] S. Riikonen and D. Sánchez-Portal, "Structural models for Si(553)-Au atomic chain reconstruction," *Nanotechnology*, vol. 16, pp. S218–S223, 2005.

[103] S. Riikonen and D. Sánchez-Portal, "Interplay between electronic and atomic structures in the Si(557)-Au reconstruction from first principles," *Physical Review B (Condensed Matter and Materials Physics)*, vol. 76, no. 3, p. 035410, 2007. [Online]. Available: http://link.aps.org/abstract/PRB/v76/e035410

[104] T. Giamarchi, *Quantum Physics in One Dimension*. Clarendon Press, Oxford, 2004.

[105] S. Tomonaga, "Remarks on Bloch's Method of Sound Waves applied to Many-Fermion Problems," *Prog. Theor. Phys.*, vol. 5, p. 544, 1950.

[106] J. M. Luttinger, "An Exactly Soluble Model of a Many-Fermion System," *J. Math. Phys.*, vol. 4, p. 1154, 1963.

[107] Peierls, *Quantum Theory of Solids*. Oxford University Press, Oxford, 1955.

[108] A. N. Rubtsov, J. Hlinka, and T. Janssen, "Crossover between a displacive and an order-disorder phase transition," *Phys. Rev. E*, vol. 61, no. 1, pp. 126–131, Jan 2000.

[109] S. Riikonen, A. A. Fernandez, and D. Sanchez-Portal, "Metal-insulator transition in the In/Si(111) surface," *Surf. Sci.*, vol. 600, p. 3821, 2006.

[110] D. Haneman, "Surface Structures and Properties of Diamond-Structure Semiconductors," *Phys. Rev.*, vol. 121, no. 4, pp. 1093–1100, Feb 1961.

[111] K. Takayanagi, Y. Tanishiro, M. Takahashi, and S. Takahashi, "Structural analysis of Si(111)-7x7 by UHV-transmission electron diffraction and microscopy," *J. Vac. Sci. Technol. A*, vol. 3, pp. 1502–1506, 1985.

[112] ——, "Structure analysis of Si(111)-7x7 reconstructed surface by transmission electron diffraction," *Surf. Sci.*, vol. 164, p. 367, 1985.

[113] A. A. Baski, S. C. Erwin, and L. J. Whitman, "The structure of silicon surfaces from (001) to (111)," *Surf. Sci.*, vol. 392, p. 69, 1997.

[114] K. C. Pandey, "New pi-Bonded Chain Model for Si(111)-2x1 Surface," *Phys. Rev. Lett.*, vol. 47, no. 26, pp. 1913–1917, Dec 1981.

[115] J. E. Northrup and M. L. Cohen, "Reconstruction Mechanism and Surface-State Dispersion for Si(111)-(2×1)," *Phys. Rev. Lett.*, vol. 49, no. 18, pp. 1349–1352, Nov 1982.

[116] ——, "Total energy of the adatom and pyramidal-cluster models for Si(111)," *Phys. Rev. B*, vol. 29, no. 4, pp. 1966–1969, Feb 1984.

[117] R. D. Meade and D. Vanderbilt, "Adatoms on Si(111) and Ge(111) surfaces," *Phys. Rev. B*, vol. 40, no. 6, pp. 3905–3913, Aug 1989.

[118] G. Kresse and J. Hafner, "Ab initio molecular dynamics for liquid metals," *Phys. Rev. B*, vol. 47, no. 1, pp. 558–561, Jan 1993.

[119] G. Kresse and J. Furthmüller, "Efficient iterative schemes for ab initio total-energy calculations using a plane-wave basis set," *Phys. Rev. B*, vol. 54, no. 16, pp. 11 169–11 186, Oct 1996.

[120] J. Junquera, O. Paz, D. Sánchez-Portal, and E. Artacho, "Numerical atomic orbitals for linear-scaling calculations," *Phys. Rev. B*, vol. 64, no. 23, p. 235111, Nov 2001.

[121] J. E. Northrup, "Origin of surface states on Si(111)(7x7)," *Phys. Rev. Lett.*, vol. 57, no. 1, p. 154, Jul 1986.

[122] K. Reuter and M. Scheffler, "Composition, structure, and stability of RuO2(110) as a function of oxygen pressure," *Phys. Rev. B*, vol. 65, no. 3, p. 035406, Dec 2001.

[123] S. LaShell, B. A. McDougall, and E. Jensen, "Spin Splitting of an Au(111) Surface State Band Observed with Angle Resolved Photoelectron Spectroscopy," *Phys. Rev. Lett.*, vol. 77, no. 16, pp. 3419–3422, Oct 1996.

[124] L. Petersen and P. Hedegård, "A simple tight-binding model of spin-orbit splitting of sp-derived surface states," *Surf. Sci.*, vol. 459, p. 49, 2000.

[125] S. Datta and B. Das, "Electronic analog of the electro-optic modulator," *Appl. Phys. Lett.*, vol. 56, pp. 665–667, 1990.

[126] P. Středa and P. Šeba, "Antisymmetric Spin Filtering in One-Dimensional Electron Systems with Uniform Spin-Orbit Coupling," *Phys. Rev. Lett.*, vol. 90, no. 25, p. 256601, Jun 2003.

[127] W. Häusler, "Rashba precession in quantum wires with interaction," *Phys. Rev. B*, vol. 63, no. 12, p. 121310, Mar 2001.

[128] M. Governale and U. Zülicke, "Spin accumulation in quantum wires with strong Rashba spin-orbit coupling," *Phys. Rev. B*, vol. 66, no. 7, p. 073311, Aug 2002.

[129] M. Rohlfing, P. Krüger, and J. Pollmann, "Efficient scheme for GW quasiparticle band-structure calculations with applications to bulk Si and to the Si(001)-(2x1) surface," *Phys. Rev. B*, vol. 52, no. 3, pp. 1905–1917, Jul 1995.

[130] M. Rohlfing and S. G. Louie, "Optical Reflectivity of the Si(111)-(2x1) Surface - The Role of the Electron-Hole Interaction," *Phys. Stat. Solidi (a)*, vol. 175, pp. 17 – 22, 1999.

[131] J. Avila, A. Mascaraque, E. G. Michel, M. C. Asensio, G. LeLay, J. Ortega, R. Pérez, and F. Flores, "Dynamical Fluctuations as the Origin of a Surface Phase Transition in Sn/Ge(111)," *Phys. Rev. Lett.*, vol. 82, no. 2, pp. 442–445, Jan 1999.

[132] S. R. J.M. Perez-Mato, I. Etxebarria and S. Ivantchev, "The Rhodes-Wohlfarth parameter as assessment of the displacive degree in ferroelectrics: The case of the ϕ^4 model," *Eur. Phys. J. B*, vol. 12, pp. 331–334, 1999.

[133] T. Aruga, "Surface Peierls transition on Cu(001) covered with heavier p-block metals," *Surf. Sci. Rep.*, vol. 61, pp. 283–302, 2006.

[134] R. M. Martin, *Electronic Structure: Basic Theory and Practical Methods*. Cambridge University Press, Cambridge, UK, 2004.

[135] A. V. Melechko, J. Braun, H. H. Weitering, and E. W. Plummer, "Two-Dimensional Phase Transition Mediated by Extrinsic Defects," *Phys. Rev. Lett.*, vol. 83, no. 5, p. 999, Aug 1999.

[136] S. Kirkpatrick, J. C. D. Gelatt, and M. P. Vecchi, "Optimization by Simulated Annealing," *Science*, vol. 220, no. 4598, p. 671, May 1983.

[137] V. Černý, "Thermodynamical approach to the traveling salesman problem: An efficient simulation algorithm," *Journal of Optimization Theory and Applications*, vol. 45, no. 1, pp. 41–45, Jan 1985.

[138] K. Binder, Ed., *The Monte Carlo Method in Condensed Matter Physics*. Springer Berlin, 1992, vol. 71.

[139] D. M. Deaven and K. M. Ho, "Molecular Geometry Optimization with a Genetic Algorithm," *Phys. Rev. Lett.*, vol. 75, no. 2, pp. 288–291, Jul 1995.

[140] K. F. Man, K. S. Tang, and S. Kwong, *Genetic Algorithms*. Springer-Verlag, Berlin, 1999.

[141] V. E. Bazterra, O. Ona, M. C. Caputo, M. B. Ferraro, P. Fuentealba, and J. C. Facelli, "Modified genetic algorithms to model cluster structures in medium-size silicon clusters," *Phys. Rev. A*, vol. 69, p. 53202, 2004.

[142] C. V. Ciobanu and C. Predescu, "Reconstruction of silicon surfaces: A stochastic optimization problem," *Physical Review B*, vol. 70, no. 8, p. 085321, 2004.

[143] R. M. Briggs and C. V. Ciobanu, "Evolutionary approach for finding the atomic structure of steps on stable crystal surfaces," *Physical Review B (Condensed Matter and Materials Physics)*, vol. 75, no. 19, p. 195415, 2007. [Online]. Available: http://link.aps.org/abstract/PRB/v75/e195415

[144] When the maximum difference between the output and input value of each element of the density matrix in a self-consistent cycle is smaller than DM.Tolerance, a self-consistent solution is assumed to have been achieved. See the manual of the SIESTA code in http://www.uam.es/siesta.

[145] F. J. Himpsel, P. M. Marcus, R. Tromp, I. P. Batra, M. R. Cook, F. Jona, and H. Liu, "Structure analysis of Si(111)2x1 with low-energy electron diffraction," *Phys. Rev. B*, vol. 30, no. 4, pp. 2257–2259, Aug 1984.

[146] R. M. Tromp, L. Smit, and J. F. van der Veen, "Structure determination of the Si(111)-(2x1) surface with channeling and blocking," *Phys. Rev. B*, vol. 30, no. 10, pp. 6235–6237, Nov 1984.

[147] G. Xu, B. Deng, Z. Yu, S. Y. Tong, M. A. V. Hove, F. Jona, and I. Zasada, "Atomic structure of the cleaved Si(111) - (2x1) surface refined by dynamical LEED," *Physical Review B (Condensed Matter and Materials Physics)*, vol. 70, no. 4, p. 045307, 2004.

[148] F. Ancilotto, W. Andreoni, A. Selloni, R. Car, and M. Parrinello, "Structural, electronic, and vibrational properties of Si(111)-2x1 from ab initio molecular dynamics," *Phys. Rev. Lett.*, vol. 65, no. 25, pp. 3148–3151, Dec 1990.

[149] M. Zitzlsperger, R. Honke, P. Pavone, and U. SchrÃűder, "Ab initio calculation of the structure, the electronic states and the phonon dispersion of the Si(111)-(2x1) surface," *Surf. Sci.*, vol. 377-379, pp. 108–111, Apr 1997.

[150] V. I. Anisimov, J. Zaanen, and O. K. Andersen, "Band theory and Mott insulators: Hubbard U instead of Stoner I," *Phys. Rev. B*, vol. 44, no. 3, pp. 943–954, Jul 1991.

[151] V. I. Anisimov and O. Gunnarsson, "Density-functional calculation of effective Coulomb interactions in metals," *Phys. Rev. B*, vol. 43, no. 10, pp. 7570–7574, Apr 1991.

[152] V. I. Anisimov, I. V. Solovyev, M. A. Korotin, M. T. Czyżyk, and G. A. Sawatzky, "Density-functional theory and NiO photoemission spectra," *Phys. Rev. B*, vol. 48, no. 23, pp. 16 929–16 934, Dec 1993.

[153] V. I. Anisimov, F. Aryasetiawan, and A. I. Lichtenstein, "First-principles calculations of the electronic structure and spectra of strongly correlated systems: the LDA+ U method," *J. Phys.: Condens. Matter*, vol. 9, pp. 767–808, 1997.

[154] E. W. Weisstein, "Wigner 3j-Symbol," From MathWorld–A Wolfram Web Resource. http://mathworld.wolfram.com/Wigner3j-Symbol.html.

[155] M. Cococcioni and S. de Gironcoli, "Linear response approach to the calculation of the effective interaction parameters in the LDA + U method," *Phys. Rev. B*, vol. 71, p. 35105, 2005.

[156] A. K. McMahan, R. M. Martin, and S. Satpathy, "Calculated effective Hamiltonian for La_2CuO_4 and solution in the impurity Anderson approximation," *Phys. Rev. B*, vol. 38, no. 10, pp. 6650–6666, Oct 1988.

[157] O. Gunnarsson, O. K. Andersen, O. Jepsen, and J. Zaanen, "Density-functional calculation of the parameters in the Anderson model: Application to Mn in CdTe," *Phys. Rev. B*, vol. 39, no. 3, pp. 1708–1722, Jan 1989.

[158] W. E. Pickett, S. C. Erwin, and E. C. Ethridge, "Reformulation of the LDA+U method for a local-orbital basis," *Phys. Rev. B*, vol. 58, no. 3, pp. 1201–1209, Jul 1998.

[159] P. H. Dederichs, S. Blügel, R. Zeller, and H. Akai, "Ground States of Constrained Systems: Application to Cerium Impurities," *Phys. Rev. Lett.*, vol. 53, no. 26, pp. 2512–2515, Dec 1984.

[160] I. I. Mazin and V. I. Anisimov, "Insulating gap in FeO: Correlations and covalency," *Phys. Rev. B*, vol. 55, no. 19, pp. 12 822–12 825, May 1997.